



MAX-PLANCK-GESELLSCHAFT



Cell type specific transcriptomic characterization of myelin abnormalities

DISSERTATION

for the award of the degree

Doctor rerum naturalium (Dr. rer. nat.)

of the Georg-August-Universität Göttingen

within the doctoral program Biology

of the Georg-August University School of Science (GAUSS)

submitted by

Ting Sun

from Beijing, P.R. China

Göttingen, 2021



Doctoral thesis Committee

Prof. Dr. Klaus-Armin Nave (First reviewer)

Department of Neurogenetics

Max Planck Institute of Experimental Medicine, Göttingen

Prof. Dr. Dr. Hannelore Ehrenreich (Second reviewer)

Clinical Neuroscience

Max Planck Institute of Experimental Medicine, Göttingen

Prof. Dr. Michael Werner Sereda

Molecular and Translational Neurology

Max Planck Institute of Experimental Medicine, Göttingen

Further members of the examination board

Prof. Dr. Susann Boretius

Functional Imaging Laboratory

German Primate Center, Göttingen

Prof. Dr. Martin Göpfert

Department of Cellular Neurobiology

University of Göttingen, Göttingen

Dr. Johannes Söding

Computational Biology

Max Planck Institute of Biophysical Chemistry, Göttingen

Date of submission of thesis: 06.09.2021

Date of oral examination: 13.10.2021

Acknowledgment

Every doctoral thesis has a long story behind it. This one, specifically, took six years, crossed the longest for 8,000 km, and traveled back and forth between two cities in Germany. So many people have helped for this story to have a splendid ending. Here, please allow me to acknowledge them with my sincere gratitude.

First, I would like to thank my supervisor, Prof. Dr. Klaus-Armin Nave. Our tutor and student relationship might not have begun with me being a myelin lover and him being interested in single-cell sequencing, but more of a little coincident. However, we soon found the passion to discuss and work on projects together. It was not only amazing to be able to work closely with such a great mind of science and get to learn the myelin world comprehensively, at the same time, Klaus also taught me how a top scientist would always maintain a high interest in new knowledge, stay supportive for his team, and keep aiming at the future.

Moreover, I want to thank my other thesis committee members, Prof. Dr. Dr. Hannelore Ehrenreich and Prof. Dr. Michael Sereda, and my bioinformatics teacher, Prof. Dr. Stefan Bonn. During my study, they offered me valuable opportunities and trust to carry projects. More importantly, when I felt lost for research directions, it was my thesis committee members and Stefan who protected me from distractions and helped me to rebuild the scientific focus which would benefit my career the most. Together, they showed me how to lead and help a student with genuine hearts.

During my study, I had the privilege to join an amazing group of colleagues. In science, I would specially thank Constanze and Stefan for their support of this thesis out of their pure love of research. The inspiring discussions with them have affected me profoundly and made me a much more independent thinker. For me, they were more than colleagues, but also my teachers, friends, and if I may wish, life-long collaborators.

In addition, I am grateful for the writing and experiment help, as well as emotional support from Andrew and Swati, the beautiful collaborations with Constanze, Stefan, Lena, and every member from the Werner group; the fun bioinformatics brainstorming with Agnes, Josefine, and Yu; and the wet-lab and dry-lab technical support from Uli, Annette, Ramona, Martin, and Hajo. What is also extremely important for me is that I have gained knowledge and qualities not only in science. Especially from dear Michaela, who has offered countless help for me to survive all the international student administrations and the shifts between two labs, her kindness, and reliable work have influenced me to become more considerate and professional.

While writing, I struggled a lot with where to put my acknowledgment to Maria and Tobi. On the one hand, Maria is my colleague and neuroscience ally, and both of them have always been my trustful life tutors. Although from the other perspective, there is so much more than that. I remember once upon a time, shortly before we became close neighbors, Hauke said it would be a nice thing to learn Ting at a whole new level. Well, I certainly hope this is verified to be true. In the end, I sincerely thank the arrangement of life, to bring you two into my life, become my family, and give me encouragement and strength to be a better person.

感谢我在国内的家人对我的支持。我的母亲，大姨和舅舅们，耐心的引导和照料我经历成长与叛逆。我所有的家人，思想豁达且崇尚科学，并且一贯平等的交流各自的价值观。你们教导我尊重各行各业，踏实工作而不去赚取虚名。如此耳濡目染，是督促我完成博士学习和追寻更高学术成就最好的动力。同时也感谢我一直以来的朋友和长辈们，对我没有因距离而疏远，反而时常关心挂念。谢谢你们长久的支持，让我远离家乡仍能感到温暖，也让我回家时总有家人与朋友可期。

Viel Liebe und Dank an meinen Freund Bastian, der ein wunderbarer Freund ist, der meine Arbeit und meine Zukunftspläne respektiert und unterstützt, und der immer bereit ist, seine Sicht der Welt mit mir zu teilen. Noch wichtiger ist, dass er mich zur Familie Zimmer gebracht hat, die mich herzlich aufgenommen hat und Deutschland wirklich zu meiner zweiten Heimat gemacht hat. Darüber hinaus haben die erstaunlichen Pflanzkünste der Familie mich, der ich 29 Jahre lang keine Pflanzen hatte, erfolgreich in einen Kleingärtner verwandelt.

Last yet important, thanks to all the friends I have met since I arrived in Germany for every lovely moment we have spent together. Special thanks to Niccoló, one of my very first friends in Göttingen who is a great neuroscientist, thanks to all your kind help that motivated me to step into research from a clinical background.

Thanks again to all of you for accompanying me on this exciting journey. If one day I have the chance to be recognized as a qualified scientist, a reliable ally, and a good friend, I can proudly tell that you are the ones who have guided me.

Table of contents

Acknowledgment.....	v
Abstract	x
List of Abbreviations	xi
Chapter 1: Introduction.....	1
1.1 Myelin in the central nervous system (CNS).....	1
1.1.1 Physiopathology of oligodendroglia and myelin	1
1.1.2 Cross talk between myelin and axon.....	3
1.1.3 Cell heterogeneity of oligodendroglia and beyond.....	4
1.1.4 Oligodendroglia and myelin as key players in neurological disorders	5
1.2 Revolution of high-resolution sequencing biotechnologies	7
1.2.1 First layer of dimensionality: the increase of data resolution	8
1.2.2 Second layer of dimensionality: the increase of data specificity	9
1.2.3 Third layer of dimensionality: the increase of data connectivity	11
1.3 Code to decode biological information, from a scRNA-seq perspective.....	12
1.3.1 Critical algorithms for scRNA-seq analysis	13
1.3.2 Batch effect correction and data integration at the single-cell level.....	14
Chapter 2: Scope of the thesis	17
2.1 Aim of Project I.....	17
2.2 Aim of Project II	17
Chapter 3: Project I.....	18
3.1 Overview of Project I	18
3.2 Original manuscript	20
Chapter 4: Project II	43
4.1 Overview of Project II	43
4.2 Original publication.....	45
Chapter 5: Discussion and conclusion.....	68
5.1 Study the upstream role of oligodendrocyte and myelin dysfunctions	68
5.2 The butterfly effect: split differences in MOL subpopulation profiles.....	69
5.3 A Hamlet question: no myelin or bad myelin?	71
5.4 Balance between cell subpopulation discovery and interpretation	72

5.5 Conclusion and open questions.....	73
References.....	75
Appendices.....	87
Appendix A. First co-authored publication:	88
Appendix B. CV and list of publications.....	107

Abstract

Myelin is indispensable for the fast and efficient transmission of electric signals along axons. The formation of myelin by oligodendrocytes in the central nervous system (CNS) is tightly regulated at the transcriptional level to achieve the required coordinated synthesis of myelin lipids and proteins. Disturbed oligodendroglial RNA profiles not only cause myelin abnormalities but also affect axon health and cause inflammation. Overlapping pathological features can be observed in other neurological disorders and in advanced brain aging. Together, this suggests that oligodendrocytes contribute to the onset and progression of CNS pathologies. However, to what degree oligodendrocytes and myelin abnormalities drive disease is unknown. Additionally, recent single-cell RNA sequencing (scRNA-seq) studies have revealed that oligodendrocytes are highly heterogeneous cells, which further increases the difficulty of defining the responsible oligodendroglial subpopulations and their corresponding signals.

In the first project, in-house generated *Plp1*^{-y}, *Cnp*^{-/-}, and *Foxg1-Cre Mbp*^{fl/fl} mutants were recruited for the single-cell resolution characterization of oligodendrocyte transcriptome changes induced by myelin deficiencies. Surprisingly, the absence of essential myelin genes led to a shift of the oligodendroglial transcriptional profiles towards distinct cellular states. However, such drastic subpopulation shifts did not result in catastrophic system failure but rather triggered mild responses in neurons, astrocytes, and microglia. Cell manifold modeling reconstructed mutant oligodendrocytes are caged at cell stages close to or within the range of physiological subpopulations. The project, therefore, discovered cell type- and subtype-specific transcription profiles of myelin mutant mice and the unexpected tight connectivities of oligodendrocyte molecular footprints in distinct myelin diseases.

In the second project, we aimed to understand how oligodendrocytes and myelin defects contribute to neurodegenerative diseases by crossbreeding our myelin mutant mice to mouse models of Alzheimer's disease (AD). Intriguingly, the mice with primary myelin dysfunctions showed elevated amyloid-beta (A β) plaque deposition. Mechanistically, myelin defects induced axonal swellings and likely enhanced local amyloid precursor protein (APP) processing. Moreover, by combining image analyses with scRNA-seq data, we inspected that microglia in myelin mutant mice are distracted from A β plaque removal, presumably due to the increasing engagement to myelin debris clearance. Conversely, in the absence of forebrain myelin, the deposition of A β plaques in AD models was delayed.

Overall, my thesis provides a systematic characterization and crosswise comparison of transcriptomic changes in mutant oligodendrocytes and discusses potential downstream effects as a result of myelin dysfunctions. This work thus provides a novel model to assist our understanding of myelinating oligodendrocytes in health and disease.

List of Abbreviations

CNS	C entral N ervous S ystem
MOL	M ature O ligodendrocyte
NFO	N ewly F ormed O ligodendrocyte
OPC	O ligodendrocyte P recursor C ell
scRNA-seq	single-cell R N A s equencing
snRNA-seq	single-nuclei R N A s equencing
AD	A lzheimer's D isease
Aβ	A myloid- b eta
APP	A myloid P recursor P rotein
MS	M ultiple S clerosis
PD	P arkinson's D isease
ALS	A myotrophic L ateral S clerosis
PMD	P elizaeus– M erzbacher D isease
VZ	V entricular Z one
PLP	P roteolipid P rotein
CNP	2'3'- C yclic- N ucleotide 3'- P osphodiesterase
MBP	M yelin B asic P rotein
MCT1	M onocarboxylate T ransporter 1
BBB	B lood- B rain B arrier
FACS	F luorescence- a ctivated C ell S orting
ST	S patial T ranscriptomics
EAE	E xperimental A utoimmune E ncephalomyelitis
MHC-I	M ajor H istocompatibility C omplex class I
MHC-II	M ajor H istocompatibility C omplex class II

Piezo1	Piezo Type Mechanosensitive Ion Channel Component 1
MRI	M agnetic R esonance I maging
TBI	T raumatic B rain I njury
NGS	N ext G eneration S equencing
SNP	S ingle N ucleotide P olymorphism
FISH	F luorescent I n S itu H ybridization
UMI	U nique M olecular I dentifier
PCA	P rincipal C omponent A nalysis
KNN	k -Nearest Neighbour
t-SNE	t - D istributed S tochastic N eighbor E mbedding
UMAP	U niform M anifold A pproximation and P rojection
CCA	C anonical C orrelation A nalysis
MNN	M utual N earest N eighbor
DAM	D isease- a ssociated M icroglia
WAM	W hite matter- a ssociated M icroglia
EM	E lectronic M icroscope

Chapter 1: Introduction

1.1 Myelin in the central nervous system (CNS)

Myelin is an insulating layer formed around the axon to ensure axon saltatory conduction. In the CNS, myelin is generated by a type of glial cell named oligodendrocyte. It is often considered that oligodendrocytes and myelin have high stability and that the unique compact architecture of myelin results in a slow turnover rate of lipids and proteins (Toyama et al. 2013; Tripathi et al. 2017; S. Ando et al. 2003). Subsequently, this stability seemingly allows myelin to provide steady maintenance to neuronal energy metabolism, as well as axon integrity (Thomas Philips 2017; Klaus-Armin Nave 2010b).

Dysfunctions of oligodendrocytes and myelin lead to myelin and axon abnormalities and reactive gliosis (Lappe-Siefke et al. 2003; Matthieu et al. 1980). Phenotypically similar abnormalities can be observed in the aging brain or the context of neurodegenerative disease to varying degrees (Ewa Papuć 2020; Safaiyan et al. 2016; Peters 2002). In recent years, an increasing amount of research has shown evidence that instead of being affected downstream, oligodendrocyte and myelin can be key contributors to the pathogenesis and progression of neurological disorders (Ettle, Schlachetzki, and Winkler 2016; Zhou et al. 2020). This, therefore, raised the scientific question of the current thesis, of how oligodendrocyte and myelin malfunctions induce the cascade of cell heterogeneity responses that may further promote neuropathology (Ettle, Schlachetzki, and Winkler 2016).

1.1.1 Journey to form myelin

In early development, oligodendrocyte precursor cells (OPCs) originate from the brain and spinal cord ventricular zones (VZs) and later migrate throughout the CNS before differentiating into myelin-forming oligodendrocytes (Dwight E. Bergles 2016; Monika Bradl 2010). The proliferation and migration of OPCs are tightly regulated by signals including growth factors (platelet-derived growth factor- α , fibroblast growth factor 2, bone morphogenetic proteins, etc), axonally produced factors (netrins, semaphorins, etc), as well as extracellular matrix proteins (N-cadherin, etc) (Klämbt 2009). As an interesting fact, OPCs derived from distinct anatomical regions undergo different competitive programs, whereas, in the spinal cord, the first wave OPCs remain as a source of the majority of mature oligodendrocytes (MOL); although in the forebrain, three waves of OPCs

sequentially originate from the medial ganglionic eminence and anterior entopeduncular area of the ventral forebrain, the lateral and/or caudal ganglionic eminences, and within the postnatal cortex, in which the first wave of the OPC population is nearly eliminated by adulthood (Dwight E. Bergles 2016; Kessaris et al. 2006; Richardson, Kessaris, and Pringle 2006). The reason for brain region-dependent OPC population arrangement, especially the rapid decay of first wave OPCs in the forebrain is not completely clear. Some proposed a special developmental/regulatory function of these OPCs (Ordaz et al. 2019), while other hypotheses include an evolutionary point of view (Richardson, Kessaris, and Pringle 2006). Nevertheless, the migration of OPCs is a lengthy but essential journey, not just for initiation of myelination, but the precursor cells are also one of the few that stay abundant in adulthood to assist CNS homeostasis (Monika Bradl 2010).

The following myelination onset is an orchestrated regulatory progress starting around birth. Among all intrinsic and extrinsic signals, neuronal electrical activity was shown to be critical for the commencement of myelination (Gyllenstein and Malmfors 1963; Call and Bergles 2021). Action potential firing leads to the release of factors such as adenosine, which inhibits OPC proliferation and triggers its differentiation into myelinating oligodendrocytes (Stevens et al. 2002). This dependence potentially also explains why axons with less than 0.2µm caliber diameters are normally not myelinated (Simons and Trajkovic 2006). In addition to axon activities, other key molecules involved in the onset of myelination contain transcription factors (Olig1/2, Sox10), extracellular matrix or cytoskeleton organization proteins (Actin, FYN, etc) (Kathryn K. Bercury 2015). Once engaged to a target axon, the pre-myelinating oligodendrocyte will lose its bipolarity and start generating myelin outgrowth (Kuhn et al. 2019).

Formation and maintenance of myelin require the coordinative synthesis of myelin-specific lipids and proteins. The highest abundant proteins in the myelin fraction include the transmembrane proteolipid protein (PLP) that contributes to myelin extracellular membrane adhesion, the cytoplasmic myelin basic protein (MBP) that is required for myelin membrane compaction (Harauz, Ladizhansky, and Boggs 2009), and the 2',3'-cyclic-nucleotide 3'-phosphodiesterase (CNP) which is important for the construction of noncompact myelin compartments (Ishii et al. 2009; Jahn, Tenzer, and Werner 2009). Besides this, recent proteomic and lipidomic measurements have uncovered many more molecules which are essential for building myelin compartments, including more than 700 lipid moieties and over 1,000 proteins (Gopalakrishnan et al. 2013). Of note, proteins involved in myelin showed high stability as previously suggested. In a study that used the c57BL/6N wild type mouse model, myelin proteome displayed only minor changes after six

hours of post mortem delay (Jahn et al. 2020). Until now, several studies have attempted to cross-compare myelin across vertebrates, especially between humans and mice for a better understanding and translation of disease research results (Ishii et al. 2009; Gopalakrishnan et al. 2013; Siems et al. 2021). Overall, the myelin content is predominantly similar between humans and mice, although species-dependent expression of lipids and proteins has been detected to varying degrees (Ishii et al. 2009; Gopalakrishnan et al. 2013). However, with the fast development of omic measurement approaches, data resolution is able to reach a new altitude, and more systematic comparisons across vertebrate myelin are still needed.

1.1.2 Cross talk between myelin and axon

The canonical function of the myelin sheath is considered to facilitate fast axon potential transmission and to support axon integrity (Baumann and Pham-Dinh 2001). The tightly compacted, lipid-rich myelin sheath prevents the excitable axonal membrane from being exposed to the extracellular space. Meanwhile, sodium channels located between two myelin segments, namely the node of Ranvier, maintains depolarization of the electrical impulse (Morell and Quarles 1999). This together secures the efficient conduction of axonal signals. On the other hand, axon and myelin undergo life-long cross-talk, which is vital for axon diameter regulation and long-term survival (Mikael Simons 2016). Evidence suggested that under lack of myelin-essential proteins such as PLP or CNP, mice showed normally assembled myelin, although developed swellings at myelinated axons in adulthood, which eventually leads to demyelination and loss of axon integrity (Griffiths et al. 1998; Lappe-Siefke et al. 2003). Interestingly, axons without myelin ensheathing, especially under severe dysmyelination situations such as in the *Mbp*^{-/-} shiverer mice, do not exhibit a swelling phenotype, suggesting more complex cell, axon, and myelin cross talks that need to be unfolded (Matthieu et al. 1980; Griffiths et al. 1998).

More recently, the metabolic support function of myelin towards the axons has been validated. In humans, the longest axons can be over a meter in length, which clearly can not be fully supported by the neuronal soma with micrometers of diameter. The large amount of energy consumed by the axon needs to be fueled along its path. As a close interaction partner to the axon, myelin is a readily obtainable resource of various types of metabolites (Klaus-Armin Nave 2010a; Thomas Philips 2017). In 2012, Fünfschilling et al. demonstrated oligodendrocytes are a highly efficient glycolytic cell type that shuttles their glycolysis products along the white matter tracts (Fünfschilling et al. 2012). Shortly after, this finding has been supported by another study conducted by Lee et al., which showed in addition to astrocyte, lactate transporter monocarboxylate transporter 1 (MCT1) is abundantly expressed in

oligodendrocytes. Its dysfunction resulted in phenotypically normal myelin but degenerated axons (Lee et al. 2012). These discoveries have since added another perspective to cell-axon energy couplings and raised many more questions, such as *where does the oligodendrocyte generate its lactate pool?* The obvious first potential source was via gap junction coupling between oligodendrocyte and astrocytes, which would allow myelin to route small metabolites through the blood-brain barrier (BBB) (Klaus-Armin Nave 2010a). Amazingly, a later study also postulated and proved the expression of NMDA receptors on oligodendroglial lineage cells that can respond to neuronal activity with increased Ca^{2+} influx, and therefore upregulate glucose uptake through glucose transporter 1 (GLUT1) (Saab et al. 2016).

It is intriguing to think about how two cellular compartments, the myelin, and the axon, can have such elegant and fine controlled cross talks. Yet, there are still lots of unsolved questions before this complex regulatory network can be fully understood. Among these, cell heterogeneity is one of the most fascinating but difficult topics that will be introduced in the following section.

1.1.3 Cell heterogeneity of oligodendroglia and beyond

The entire oligodendroglial lineage has presented a huge potential of heterogeneity (Tomassy, Dershowitz, and Arlotta 2016). Since their discovery, researchers have asked whether dorsally and ventrally derived OPCs give rise to different mature oligodendrocytes (MOL), hence resulting in different myelin? Do distinct anatomical regions induce diverse MOL profiles? And if oligodendroglial heterogeneity exists, what would be the functional read-out and downstream effect on their surrounding milieus? Already a century ago, Pio del Rio Hortega proposed four oligodendrocyte subpopulations based on their morphological characterizations (del Rio Hortega 1928; Tomassy, Dershowitz, and Arlotta 2016). However, these questions were not able to be sufficiently answered without the evolution of advanced omics measurements and imaging techniques.

A strong boost to the understanding of heterogeneous oligodendrocytes is the invention of high parallel single-cell RNA sequencing (scRNA-seq). In 2015, Marques et al. first used the Smart-seq2 platform (Picelli et al. 2013), which combines fluorescence-activated cell sorting (FACS) with multiple library indexes, collected over 5,000 single-oligodendrocyte, and revealed six distinct MOL populations that displayed proportion changes across different early developmental time points, as well as among 10 different brain regions (Marques et al. 2016). The initial conclusion of these MOL subsets was that MOL1 to MOL4 are presented in the juvenile mouse brain, whereas MOL5 and MOL6 are more dominant in the adult

brain. Although with increasing sequencing resolution, especially with the stepwise development of scRNA-seq platforms by integrating microfluidic devices (Macosko et al. 2015) and later to spatial transcriptomics (ST) (Ståhl et al. 2016), the spatial and temporal map of MOL subpopulations has been renewed. Surprisingly, the latest ST assessment showed different preferences of MOL compositions in cortical and the adjacent callosal region over brain development (Hilscher et al. 2021). It is still unclear what the functional specificities of previously defined MOL subpopulations are, although some evidence showed that in the spinal cord, there are apparent alterations mainly between MOL2 and MOL5/6 while responding to injury (Floriddia et al. 2020).

Oligodendroglial heterogeneity also exists among precursor cells. More interestingly, apart from single-cell level characterizations under brain homeostasis, OPCs retain higher adaptation to CNS environment changes. For instance, aged OPCs were shown to be less responsive to cell differentiation signals, but can be rejuvenated in scaffolds that mimic the neonate brain niche (Neumann et al. 2019; Segel et al. 2019). As another example, in animal models of brain inflammation such as experimental autoimmune encephalomyelitis (EAE), a proportion of OPCs showed transcriptomic modification by expression of major histocompatibility complex classes I and II (MHC-I and -II) (Falcão et al. 2018; Meijer et al., n.d.).

Taken together, it is evident that oligodendroglia is a dynamic and heterogeneous lineage of cells. Yet, how does this affect other cell populations? So far, most studies have focused on the influences from other cell types and the vasculature on oligodendroglia (Yalçın and Monje 2021). However, few studies also illustrated regulatory effects originated from oligodendroglia. For example, knockout of *Olig2* in dorsal OPCs lead to reduced corpus callosum myelination without affecting the overall cell number, suggesting functional differences between dorsal and ventral derived OPCs (Yue et al. 2006). Furthermore, following cuprizone-induced brain demyelination, hippocampal CA1 projection neurons showed retraction of dendritic spines and therefore reduced neuronal activity (Baltan et al. 2021). In addition to revealing the importance of oligodendroglia intrinsic signals in the CNS, these shreds of evidence also suggested the relevancy of cell heterogeneity. Although currently, the interpretation of oligodendrocyte subpopulation functions is restricted to our limited understanding of its regional and molecular specificities.

1.1.4 Oligodendroglia and myelin as key players in neurological disorders

For a long time, oligodendroglia and myelin were considered to be static, and their role was more of a ‘bystander’ in neurological disorders (Tripathi et al. 2017; Marsh et al., n.d.). However, as previously introduced, the turnover rate of lipid and

proteins may be slow in the compact myelin, but cellular communications between oligodendroglial lineage cells, myelin, axon, and other cell types are rapid and important (Klaus-Armin Nave 2010a; Mikael Simons 2016; Yalçın and Monje 2021). On top of that, a growing amount of researches has discovered obvious oligodendrocyte transcriptome profile changes under aging and neurodegenerative disease conditions, indicating potential predominant regulatory programs initiated by oligodendrocytes (Ximerakis et al. 2019; Jäkel et al. 2019; Mathys et al. 2019). Upon promoting OPC differentiation and myelination, mice with AD pathology (APP/PS1 model) showed a rescue in cognitive decline (J.-F. Chen et al. 2021). Linking to previous magnetic resonance imaging (MRI) analyses, human myelin levels increase continuously until ~50 years old before progressively declining (George Bartzokis et al. 2001). The myelination stability, however, was already achieved between the ages of 29 and 50 years in different cortical regions (Grydeland et al. 2018). Hence, myelin stability is seemingly lost prior to the onset of most neurodegenerative diseases.

Even in more acute scenarios, the etiology or crucial contributions to diseases that relate to myelin dysfunction can be presumed. One well-recognized risk factor for patients developing neurodegeneration is the disease history of stroke or traumatic brain injury (TBI), which causes white matter injury and myelin integrity loss (Taib et al. 2017; Gupta and Sen 2016). Regardless of age, it is imaginable that this damage of myelin leaves a pre-aging microenvironment in the brain which can further lead to irreversible neurodegeneration. It is of course arguable that TBI can cause critical phenotypes like axon injury, weakening of the BBB, which also makes the system more vulnerable to neurodegeneration. Though from a collective point of view, all injured compartments could co-regulate with each other, and in the end would form an impaired region where myelin damage stands as an important part (Gupta and Sen 2016).

Another early-onset neurological disorder, with unknown etiology, characterized by an inflammatory demyelination phenotype is MS. It is still mysterious how peripheral immune cells choose to enter the immune-privileged CNS and attack myelin. One of the hypotheses is molecular mimicry, where immune cells could acquire sequence or structural self-like peptides via defending certain viruses or bacterias (Libbey, McCoy, and Fujinami 2007). On the other hand, could a similar immune mimicry also occur from inside the CNS? Lately, Schirmer et al. showed that the brain resident immune cell microglia are capable of uptaking myelin transcripts into their nucleus (Schirmer et al. 2019). It is intelligible that in MS lesions, microglia are in charge of a mass amount of debris removal and therefore can take up transcripts that are locally translated in myelin. However, what is the initiation of the transcripts being imported to the nuclei? Guesses are that either

myelin transcripts can further regulate transcription, or microglia undergo procedures similar to the anti-viral responses. Considering most of the myelin clearance happens during the launch and peak growth of myelination that lasts until ~20 years of age in humans (Grydeland et al. 2018), it could be that the immune environment in the CNS is primed to be susceptible for myelin already at a young age.

By combining previous as well as renewed molecular evidence with the timing of myelin decline, one could well speculate another possibility of neurodegenerative disease onset and progression, that is: *Can oligodendrocyte and myelin dysfunctions be an upstream factor?* It is of course difficult to answer the question with approaches using human post mortem specimens, or corresponding disease mouse models, given that those samples and models mostly offer snapshots of complicated cell communication networks, and can hardly reflect oligodendrocyte and myelin driven effects. Thus, in this thesis, I utilized established myelin mutant mice that provide well-defined and traceable white matter pathologies to decipher signals which originate from oligodendrocytes and myelin malfunction.

1.2 Revolution of high-resolution sequencing biotechnologies

Myelination presents a fascinating biological process, that the precise but complicated cellular programs have made it solid and efficient, but at the same time vulnerable to pathological challenges. Dynamic heterogeneities of the cells have made the integration of research results even more difficult (“Diversity of Oligodendrocytes and Their Progenitors” 2017). In order to depict the molecular footprint of oligodendroglial and myelin dysfunction, it is necessary to recruit cutting-edge biotechnologies, especially high-throughput sequencing assays to assist the collection of data. Specifically in this thesis, high-resolution bulk and single-cell transcriptome sequencing were broadly applied to answer oligodendroglial and myelin-related biological questions.

The development of sequencing biotechnology went through an amazingly fast but tough revolution (“The Third Revolution in Sequencing Technology” 2018). Generally, the milestones of sequencing techniques are recognized by names of first-generation sequencing (i.e. Sanger sequencing), next-generation sequencing (NGS), and third-generation sequencing. Later, it was also extended to single-cell, or even single-cellular compartment sequencing resolutions (Hwang, Lee, and Bang 2018; Eng et al. 2019; Habib et al. 2017). Stepwise, the technique is trying to perfect itself by balancing lots of parameters, including base pair accuracy, sequencing length, data collection depth, and efficiency, etc. But ultimately, what the revolution has brought is facilitation to data dimensionalities, that covers data resolution,

specificity, and connectivity, which has made former impossible missions achievable.

1.2.1 First layer of dimensionality: the increase of data resolution

In biology, increasing data resolution does not simply mean performing more experiments. There are lots of cases where researchers need to sacrifice the quantity of samples in order to fit the limited time or the experimental setup (Holmes and Huber n.d.; “Good Data, Bad Data and Ugly Data” 2019). The capacity of an experimental technique is the prerequisite to big data generation. Sequencing techniques that target information hidden in billions of base pairs of genome and trillions of cells are obviously more in need of a high amount of data collection within a short period of time (Brown 2002).

The first generation sequencing, namely Sanger sequencing, was invented nearly 40 years ago by Frederick Sanger and his colleagues (Sanger, Nicklen, and Coulson 1977). The principle of Sanger sequencing is to employ dideoxynucleotides that truncate DNA replicate chain reactions and to generate oligonucleotide copies randomly terminated at the 5' end. By electrophoresis, copied fragments are separated based on their size, and the base pair sequence is reflected by the readout of 5' dideoxynucleotides from each fragment (Schoales 2015). The emergence of this method was a fundamental boost to sequencing resolution, and for the first time made genome-wide sequencing possible. However, it was soon obvious that first-generation sequencing is labor-intensive and expensive for revealing complete sequences of genomes (Schloss 2008). Its use was also limited to the assembly of transcriptomes, which is mainly to produce expressed sequence tags without exact sequence locations (Adams et al. 1991). During the first decade of the human genome project, it cost nearly US\$3 billion, and this propagated further invention of cheaper and faster sequencing methods (“The Third Revolution in Sequencing Technology” 2018).

From the 2000s, success in microarray and NGS techniques dramatically accelerated the progress of genome and transcriptome research (Nelson 2001; McGettigan 2013). Between the two, NGS is more widely applied even today, due to its more flexible performance that covers all genomic, transcriptomic, and epigenomic usages (Anderson and Schrijver 2010). The development of NGS was a joint effort from many organizations. As a most used principle, NGS fragments and adapts target sequencing material (genomic DNA, cDNA) to the glass bottom flow cell chip, applies local amplification, and gets the sequencing readout by simultaneously synthesizing fluorescently labeled nucleotides to the fragments (Anderson and Schrijver 2010). In this way, no post-amplification separation is

required, and a single run of the experiment can collect millions of reads with close to 99% sequence accuracy (Wang, Gerstein, and Snyder 2009; Anderson and Schrijver 2010). According to the national human genome research institute, the sequencing cost of each human genome compared to its highest time has been reduced by nearly 100,000 times (“The Cost of Sequencing a Human Genome” n.d.). But more importantly, what NGS has pushed forward significantly is the improvement of bioinformatics analysis pipelines. The sequenced fragments are often within hundreds of base pairs, and they would need to be ‘stitched’ back together to get the assembly or alignment of the genome/transcriptome (Huber et al. 2015; Van Verk et al. 2013). Typically in assembly, the stitching process tries to find continuous overlaps in short reads, and group them into bigger contigs to reconstruct the initial gene sequence (Miller, Koren, and Sutton 2010). Yet, this is challenging when dealing with sequences with highly repetitive regions (Salzberg and Yorke 2005). In fact, although the first complete human genome was announced in 2003, ~8% of the full sequence remained ambiguous or unfinished for decades because of the difficulty of sequencing reads assembly (Reardon 2021). Most recently, assisted by third-generation sequencing Nanopore that is capable of passing long, non-fragmented DNA/RNA through ion channels and read the sequence by observing changes of the channel shape, Nurk et al. have potentially filled the missing sequence gaps and updated the real complete human genome for the first time (Nurk et al. 2021).

It is still under debate whether the third generation sequencing technique, Nanopore, is suitable for the large-scale application of genome and transcriptome assessment. Until 2019, nanopore measurements struggled with a base pair accuracy of 80% (Noakes et al. 2019). Whilst earlier this year, Oxford Nanopore technology has published close to 100% sequencing accuracy in a new version of chemistry (“Accuracy” n.d.). Nevertheless, the technique is highly promising and with further evaluation can be of great help to complete genomes across species, as well as study disease related single nucleotide polymorphisms (SNPs) to a broader extent.

1.2.2 Second layer of dimensionality: the increase of data specificity

The evolution of sequencing technologies has massively increased the amount of data that can be collected at one time. However, most tissues are highly complex and consist of multiple cell types. In which case, regardless of how much data one could collect, it is always a mixture of transcripts from various populations of cells, and can not reflect the specific changes in the responding cell subsets. Being aware of this problem, researchers have attempted to get morphological or gene expression readouts at a single-cell level (Eberwine et al. 1992; Bengtsson et al. 2008; Tomassy et al. 2014). By manual cell selection, the first whole-transcriptome characterization

from single-cells in blastomeres was achieved by Tang and colleagues (Tang et al. 2009). However, the protocol was time consuming, and the number of collected cells barely reached 2,000, which is not favorable for research that targets complicated tissues such as the brain (Tang et al. 2009; Aldridge and Teichmann 2020). Developing experimental setups that can massively collect and separate single-cells for high-resolution sequencing has therefore become a pressing issue in the past decade.

“If I have seen further”, said Isaac Newton in a letter to his fellow scientist Robert Hooke, “it is by standing on the shoulder of giants.” This quote perfectly describes the ongoing development of the single-cell sequencing field. It is still hard to believe that within such a short time, the scale of single-cell level data collection has increased exponentially. Part of the reason is that despite the core of different platforms, the single-cell field has maximally adapted already established platforms such as FACS (Smart-seq2), microfluidic devices (Drop-seq), fluorescent in situ hybridization (FISH) (seqFISH), semipermeable membrane (Seq-Well), and connected them to NGS or imaging for cell-specific omic readout (Svensson, Vento-Tormo, and Teichmann 2018). Overall, to enable the tracing of transcripts to their original cell, all platforms have used the barcoding system combined with a unique molecular identifier (UMI). Both cell barcodes and UMIs are artificially synthesized oligonucleotides. Once hybridized to the transcripts, they will participate in the following steps of reverse transcription, amplification, and high resolution sequencing (Svensson, Vento-Tormo, and Teichmann 2018). From which, the barcode facilitates the recovery of cell identity and the UMI serves as a control of amplification artifact. Specifically, for each transcript, one UMI in a cell is only counted once (Hwang, Lee, and Bang 2018). In Seq-Fish, the barcoding system is also applied, but to the transcripts identification probes instead of to cells. The barcodes are fluorescently labeled and can be assessed by imaging (Eng et al. 2019).

Among all single-cell sequencing platforms, Drop-seq was one of the most selected in studies (Svensson, Vento-Tormo, and Teichmann 2018). The droplet-based setup can profile up to millions of cells or nuclei in one single experiment (Macosko et al. 2015; Habib et al. 2017) and has adapted to epigenetic assays including chromatin accessibility assessment (ATAC-seq) and histone modification (ChIP-seq) at the single-cell level (Grosselin et al. 2019; Meijer et al., n.d.). Moreover, cell surface proteins, such as immune cell epitopes, that are hard to be measured by transcriptome assays, can be ‘stained’ by barcoded antibodies and get sequenced together with the cell transcriptome to ensure the proper identification of cell populations (Stoeckius et al. 2017). One of the clear drawbacks, however, is that Drop-seq can only sequence from either the 3’ or 5’ end of the transcripts with a

length of several hundred base pairs (Kashima et al. 2020). Unable to sequence full-length transcripts, Drop-seq data is therefore not suitable for SNP or alternative splicing analysis.

1.2.3 Third layer of dimensionality: the increase of data connectivity

The constantly updated single-cell sequencing techniques could help answer research questions with great detail based on cell specificities. Yet, to better understand the dynamic biological system, the technique needs to further develop its latitude and restore as many connectivities as possible between collected data.

In the majority of the bulk or single-cell high-resolution sequencing techniques, the spatial information of cells in a tissue is lost. The interpretation of whether the responsive cells are located in a pathological region or adjacent healthy area is therefore difficult, and more dependent on labor-intensive pre-sequencing sorting or microdissections, as well as post-sequencing histology and biochemistry validations (Zeisel et al. 2015, 2018; Ayata et al. 2018; Jäkel et al. 2019; Grubman et al. 2021). For running costly assays like scRNA-seq on complex tissues such as the brain, some studies also choose to profile a relatively larger tissue area and hope to learn the spatial information via validating or analyzing potential marker genes (Schirmer et al. 2019; Zhou et al. 2020). Nevertheless, without a solid match between the spatial map of the tissue with its sequencing characterization, it is nearly impossible to restore the cell-cell connections.

Thus, two spatial transcriptomic assays, Visium and seqFISH, were generated to highly parallelly capture transcriptomes without losing the intact tissue (Ståhl et al. 2016; Eng et al. 2019). The Visium assay aims to preserve slices of tissues that can be placed on microchips loaded with territories of poly-T tailed oligonucleotides. Subsequently, the tissue slices will be fixed and permeabilized to release its mRNA molecules that can be captured by adjacent oligonucleotides on the microchip and be subjected to high-resolution sequencing. In order to map transcripts back to their spatial locations, the Visium chip standardizes the diameter of captured oligonucleotide territory to roughly 100um. As a result, the readout of the Visium assay is not exactly at a single-cell level, and can only get relative cell type modules using the deconvolution analysis pipeline (Ståhl et al. 2016; W.-T. Chen et al. 2020). What can reach a single-cell resolution and as well preserve the anatomical information is the seqFISH assay. As previously introduced, seqFISH uses fluorescently labeled nucleotides to barcode molecule probes that can hybridize in a given tissue in individual cells (Eng et al. 2019). This powerful assay can be applied for the detection of DNA, RNA, and proteins, although is considered to be more efficient for genetic research, considering the sensitivity of protein antibodies

vary significantly (Geldert, Huang, and Herr 2020). In an antibody-free manner, it is always more reliable to assess proteome and lipidome through high sensitivity mass spectrometry. Recently, proteomics and lipidomics measurements at single-cell resolution with retained spatial information were shown to be possible and went through promising tests, and approaches including matrix-assisted laser desorption/ionization mass spectrometry imaging, as well as deep learning orientated tissue microdissection (Capolupo et al. 2021; Mund et al. 2021).

Aside from restoring spatial information, in particular for developmental research, it is also critical to investigate cell fate and cell decision making. By combining the CRISPR-Cas9 gene-editing technique with the single-cell barcoding concept, guide RNAs with specific labels can be introduced in single cells that later can be sorted and traced for their triggered transcriptomic changes (Replogle et al. 2020). Furthermore, instead of one-time induction of genetic editing in a pool of cells, an inducible CRISPR-Cas9 system such as iTracer is capable of introducing DNA ‘scars’ at any given time point for better tracing of cell lineage footprints (Zafar, Lin, and Bar-Joseph 2019; He et al., n.d.). As a caveat, neither the inducible nor the non-inducible CRISPR system has perfect reconstruction accuracy and is frequently reported to give off-target effects (Zafar, Lin, and Bar-Joseph 2019; Jun et al. 2020; He et al., n.d.).

Acknowledging rich technologies that have enabled sequencing data to converge compositional and spatial cell information, continuous efforts are being invested into the construction of cell atlas for humans and other species (Rozenblatt-Rosen et al. 2017; Ando et al. 2020; The Tabula Muris Consortium). The challenge of material and data collection has prompted many organizations to work and publish in consortia fashion and brought more collaborative models for future scientific research (Ando et al. 2020).

1.3 Code to decode biological information, from a scRNA-seq perspective

It is of course an exciting era, where data can be collected on a scale of millions of cells, with tens of thousands of genes being profiled in each cell. However, this means even in the processed form, a single-cell resolution RNA sequencing data could appear as a numeric matrix with ultra-dimensionality (Lähnemann et al. 2020; Oskolkov 2021), which brings an obvious follow-up question: *how to process this huge amount of data?*

Nowadays, big data processing is exclusively handled by high-performance computing, i.e. to process data and perform complex calculations at high speed. Especially in the high-resolution sequencing field, for the purpose of maintaining the flexibility of adapting frequently updated analysis pipelines, computational

coding has become a helpful skill (Gatto and Christoforou 2014; Draghici 2016; Love et al. n.d.). Through coding, bioinformaticians try to maximally recover the realistic states of a biological system and filter the most relevant regulatory pathways. In this process, a decent amount of decisions need to be made for choosing the optimal algorithms that fit the type of data.

1.3.1 Critical algorithms for scRNA-seq analysis

One of the critical steps for high-resolution data processing is the reduction of dimensionality. For bulk assays, this is reflected by the steps of filtering outlier samples and non-detected genes, and the assessing of relative sample distances (Love et al. n.d.). In more complex data such as scRNA-seq, to process data without intensively laboring the computational system, dimensionality reduction of the expression matrix has become indispensable (Sun et al. 2019). Nearly all scRNA-seq processing pipelines implemented principal component analysis (PCA) in their initial steps, the algorithm aims at capturing most variability through the high dimensional data, and the selection of top principle components can summarize most of the data relevance. More importantly, by applying PCA and selecting the most representative principal components, the dimension of a scRNA-seq expression matrix that can contain up to 50,000 genes will be reduced to merely 10 to 50 principal components (Luecken and Theis 2019; Sun et al. 2019). However, PCA that focuses on the bulk structure of the data does not offer enough specificities to reveal cell heterogeneity. Therefore, typical scRNA-seq analysis utilizes the k-nearest neighbor (KNN) algorithm, combined with t-distributed stochastic neighbor embedding (t-SNE) or uniform manifold approximation and projection (UMAP), to embed and calculate closest cell neighbors and assemble them into clusters (Luecken and Theis 2019).

The unbiased clustering analysis has dominated the early stage scRNA-seq studies and has made vital contributions. In neuroscience alone, this algorithm has helped to reveal numerous characteristically and/or functionally relevant cell populations, including disease-associated microglia (DAM) (Keren-Shaul et al. 2017), MS enriched MAFG-driven astrocytes (Wheeler et al. 2020), MOL subpopulations (Marques et al. 2016), etc. Although later studies soon realized that overclustering of cells does not help further discovery of biologically valid cell subsets. Instead, a pressing issue was to solve the problem of how cells become disease-associated or vulnerable to certain environments (Lähnemann et al. 2020). Thus, the concept of pseudotime trajectory analysis emerged and was soon widely applied. By definition, pseudotime represents the relative positioning of cells along a reconstructed trajectory that quantifies cell activity and potentially reflects biological processes (Saelens et al. 2019; “Chapter 18 Trajectory Analysis” n.d.). Essentially,

pseudotime reconstruction is a matter of cell state connectivity and therefore can be calculated using a variety of algorithms (Saelens et al. 2019). Nevertheless, in most cases, reconstructed trajectory still depends on the annotation of cell clusters or subpopulations, and does not fully exploit the single-cell resolution.

The next milestone algorithm, RNA velocity, managed to recover the putative connectivities between single-cell data points. In a nutshell, the algorithm assumes a model of cellular state based on the ratio of spliced, unspliced, and degraded transcripts (La Manno et al. 2018; Bergen et al. 2020). The initial study has tested the assumption using multiple bulk and single-cell RNA sequencing datasets (La Manno et al. 2018). Subsequently, the highly reconstructed cell connectivities unlocked many more possibilities for further analysis and visualization of data (Lange et al. 2020). Among which, by assuming adjacent cell states are tightly linked, the Markov chain algorithm was applied and greatly helped discover cell fate determinative genes (Setty et al. 2019; Lange et al. 2020).

1.3.2 Batch effect correction and data integration at the single-cell level

It was noted for a long time that high-resolution sequencing data can hardly be cross-compared between different batches (Zhang, Parmigiani, and Johnson 2020). This potentially came from the accumulation of diverse parameter choices, such as the amount of input material, library preparation kit, sequencing depth, etc, from different experimenters. As a result, many experiments have been done repetitively.

In scRNA-seq, with the immense increase of data dimensionality, batch effects also create more distortion of biological signals. For example, a previous study that used scRNA-seq to detect cell subpopulation shifts from post mortem brain samples showed a specific astrocyte subset that was exclusively related to AD. Although it was later validated that these cells were solely contributed by one AD patient, and clustered because of a minor batch effect within the data (Grubman et al. 2019). In another case, single-oligodendroglial profiles were collected from the brains of wild-type animals and EAE mouse models, respectively (Falcão et al. 2018). However, cells from healthy or EAE animals showed minimal overlapping, which could also have been the influence of sequencing batch effect, rather than realistically reflecting a completely different oligodendroglial state under pathological conditions (Falcão et al. 2018).

Removal of batch effects from scRNA-seq experiments is a challenging task. The high amount of cells are originally collected for the purpose of reading cell heterogeneity that shall not be over-corrected by algorithms. On top of that, artificial effects can be introduced by single or multiple covariates (specific patient, sequencing platform and depth, dropout rate, cell cycle effect, etc) and each cell

might adapt to it to a different degree (Luecken and Theis 2019). Hence, every cell can be considered as a mini-experiment, and can not be treated in a linear way for batch effect correction (Forcato, Romano, and Biciato 2020). Thus, the upfront mission prior to batch effect removal and data integration is to find the joint features among the cells. Typically, this contains two categories of commonalities: first, the shared, highly variable genes in the given datasets that are supposed to reflect the heterogeneity of cells, even rare subpopulations; and second, subsets of cells that share preserved profile structures identified by mutual nearest neighbors (MNN) and will serve as integration anchors (Forcato, Romano, and Biciato 2020). In principle, most algorithms presuppose that at least one stable cell population is being shared among different batches of experiments and therefore attempt to use these common integration anchor cells to compute data in a shared low-dimensional space (Tran et al. 2020). Detection of integration anchors is assisted by highly variable genes, and its accuracy can be additionally elevated by firstly summarizing the data in a space with reduced dimensionality. This can be achieved by canonical correlation analysis (CCA) (represented by Seurat v3 and above), PCA (represented by Harmony), or other cell neighbor calculations (scNCA, etc) (Butler et al. 2018; Korsunsky et al. 2019; Gong et al., n.d.). Eventually, in the shared low-dimensional space, integration anchors are used for the evaluation of alignment vectors or weight of anchor connection edges to joint cells obtained from different batches (Butler et al. 2018; Tran et al. 2020; Forcato, Romano, and Biciato 2020). Alternatively, apart from anchor detection methods, other less common approaches for batch effect correction include non-negative matrix factorization (LIGER) or deep neural networks (scGen, scAlign) (Welch et al. 2019; Lotfollahi, Wolf, and Theis 2019; Johansen and Quon, n.d.).

Unlike bulk sequencing batch correction, nonlinear alignment of the scRNA-seq dataset parallelly seeks the common and specific features. As a result, the method is not restricted to merging transcriptomes but is also generally used for the integration of multimodal single-cell data (Stuart et al. 2019; Stuart and Satija 2019; Welch et al. 2019). Downstream to all applications, corrected data can be further embedded and visualized by its aligned expression profiles. However, the corrected expression values are returned from shared low-dimensional space and mainly mirror the relative positions of datasets, which should be treated with caution for statistical use (Forcato, Romano, and Biciato 2020; Lähnemann et al. 2020).

Fascinating as it is, mathematical algorithms can always gain another layer of charm when used for solving life science questions. As Joel E Cohen once summarized, ‘*mathematics is biology’s next microscope, only better*’ (Cohen 2004). The evolution of algorithm applications in bioinformatics not only helps decode biologically relevant information but also provides more possibilities for the

development of biotechnology. In this thesis, I will present several projects combining cutting-edge sequencing techniques and bioinformatics pipelines, to try to answer the question of whether oligodendrocyte and myelin dysfunction can be an upstream factor of onset and progression of neurological disorders.

Chapter 2: Scope of the thesis

The scope of this thesis includes two major projects (Project I and II) and one supporting project (Appendix A). Ultimately, the author aimed to investigate one question: *What are oligodendroglia and myelin dysfunction intrinsic signals, and how do they influence the CNS?*

2.1 Aim of Project I

In Project I, three myelin mutant mouse models, *Plp1^{-y}*, *Cnp^{-/-}*, and *Foxg1-Cre Mbp^{fl/fl}* were used to investigate upstream effects derived from oligodendrocyte and myelin dysfunctions. The *Plp1^{-y}* and *Cnp^{-/-}* lines presented different degrees of myelin instability, and *Foxg1-Cre Mbp^{fl/fl}* contributed a forebrain shiverer environment. The project used the snRNA-seq technique to characterize heterogeneous oligodendrocyte transcriptomic changes under these various conditions. Moreover, cutting-edge bioinformatics analysis pipelines were applied to reconstruct oligodendrocyte molecular footprints under mutant conditions, as well as to read their influences on other CNS cell populations.

2.2 Aim of Project II

Project II specifically discussed the potential upstream role of oligodendrocyte and myelin dysfunction in the context of AD. The study applied multiple genetically or biochemically induced myelin disruptions on top of an AD pathological background. Using a battery of experiments comprised of immunohistochemistry, light-sheet microscopy, fluorescent imaging, behaviour characterization, bulk and single-cell transcriptome sequencing, this project dedicatedly characterized and investigated the effects of oligodendrocyte and myelin dysfunctions on AD.

Chapter 3: Project I

Characterization of dysfunctional oligodendrocytes at single-cell resolution

3.1 Overview of Project I

With the advent of high-resolution genetic approaches, it became apparent that the perturbation of even a single gene can induce a series of changes in the gene expression network (Davidson and Peter 2015; Zavolan 2015). Our previous microarray data suggest that mouse models lacking myelin-related genes show highly unique, although partially overlapping bulk-level transcriptome profiles (Rossner). These data, however, lack single-cell resolution which allows for probing of cell-type and subtype-specific responses which could help to decipher the complex interplay between myelin defects, gliosis, and axonal damage in myelin mutant mice.

Therefore in project I, three well-characterized myelin mutant mouse strains, the *Cnp*^{-/-} mice that exhibit strong reactive gliosis accompanied with axon pathology (Lappe-Siefke et al. 2003), the *Plp1*^{-y} mice that show clear axon instability and swelling pathologies, and present milder microgliosis and astrogliosis compared to the *Cnp*^{-/-} (Griffiths et al. 1998), and the *Foxg1-Cre Mbp*^{fl/fl} mice that were generated as forebrain shiverer model, were utilized for highly parallel single-nuclei transcriptome sequencing to reveal the molecular footprint of CNS cells under myelin abnormality challenges. The three lines share one important feature, which is the initial dysfunction created by mutant oligodendrocytes and defective myelin. Hypothetically, considering the overlapping pathological features among the mutant mouse brains, myelin mutant oligodendrocytes could be expected to exhibit similar profile or subpopulation shifts.

However, through unbiased clustering, RNA velocity calculation, and integrative analysis with previously published data (Marques et al. 2016), a surprisingly departed, yet closely connected cell map was recovered from myelin mutants and corresponding WT mature oligodendrocytes (MOLs). In particular, *Foxg1-Cre Mbp*^{fl/fl} presented a novel juvenile MOL subpopulation MOL0, *Cnp*^{-/-} mainly expanded intermediate stage MOL4, and the *Plp1*^{-y} mutant upregulated relative proportion of the most mature stage MOL5/6. Astonishingly, each myelin mutant would concentratedly enlarge one particular MOL subpopulation to over 50% upon knockout of one essential myelin gene. In comparison to former studies that have reported cell subpopulation shifts, such as disease-associated microglia (DAM) and disease-associated astrocyte (DAA) in AD and aging, the activated cell

subpopulations were never at the dominant proportion; More importantly, both DAM and DAA were discovered as novel cell clusters at relatively distant locations from the homeostatic cells, which means their transcriptome profiles are largely shifted from the homeostatic stage (Keren-Shaul et al. 2017; Habib et al. 2017). However, the same situation apparently does not apply to oligodendrocytes. In myelin mutants, as well as in re-analyzed scRNA-seq data from the experimental autoimmune encephalomyelitis (EAE) mouse model (Wheeler et al. 2020), both chronic and acute myelin disruptions did not push the MOLs towards disconnected cell stages but rather resulted in MOL subpopulation alterations within or adjacent to physiological range.

Moreover, reconstruction of the cell manifold and recovery of cell state determinative gene signatures revealed that the observed MOL subpopulations are indeed tightly connected. Regardless of relative stages, MOLs are generally concentrated on the production and maintenance of myelin and aim to differentiate towards two putative end states, MOL2/3 and MOL5/6. This further determined that downstream effects from mutant oligodendrocytes are not as drastic. Among all studied mutants, *Cnp*^{-/-} exhibited the strongest reactive gliosis and inhibitory neuron gene expression changes. In addition to myelin deficiency, cell interaction analysis also suggested that the microgliosis in the *Cnp*^{-/-} mutant could have been caused by increased communications between MOL4 and reactive microglia subtypes. Of note, compared to neurological disorders that mainly activate DAM (Keren-Shaul et al. 2017; Hammond et al. 2019), the *Cnp*^{-/-} and *Foxg1-Cre Mbp*^{fl/fl} mice presented increased proportions of microglia that ingested myelin transcripts, namely the myelin transcripts enriched microglia (MyTE). Such myelin transcripts uptaken microglia have been described from a previous MS study (Schirmer et al. 2019). However, the proportion of MyTE was more obviously enriched in the recruited myelin mutants. More specifically, in the *Foxg1-Cre Mbp*^{fl/fl} model that cannot sufficiently form compact myelin in the forebrain, the percentage of MyTE exceeded 20%, implying myelin transcripts are not necessarily transported to the microglia cell soma and nuclei through the compact myelin.

In summary, project I delivered comprehensive transcriptomic characterizations of mutant oligodendrocytes. The surprisingly expanded MOL subpopulations of each mutant were collected and formed an informatic basis to rebuild the genetic signature path that underlies cell state transitions. Altogether, this hopefully provides a systematic model to investigate intrinsic signals in the event of oligodendrocyte and myelin dysfunction that are relevant for aging and neurological diseases.


3.2 Original manuscript

Sun, T.*, Depp, C.*, Berghoff, S. A., Spieth, L., Sasmita, A. O., ... & Nave, K. (2021). Characterization of dysfunctional oligodendrocytes at single-cell resolution. *Manuscript in preparation*.

Personal contribution to Project I

I was involved in the conceptualization, experimental design, and data analysis of the project. The sequencing analysis results were interpreted by me and my colleagues. Further, I have assembled the manuscript figures and wrote the manuscript text.

Characterization of dysfunctional oligodendrocytes at single-cell resolution

Ting Sun¹, Constanze Depp¹, Stefan A. Berghoff¹, Lena Spieth¹, Andrew Octavian Sasmita¹, Agnes A. Steixner-Kumar², Swati Subramanian¹, Sandra Göbbels¹, Wiebke Möbius^{1,3}, Hannelore Ehrenreich², Daniel Geschwind⁴, Riki Kawaguchi⁴, Klaus-Armin Nave ¹


¹Department of Neurogenetics, Max Planck Institute of Experimental Medicine, Göttingen, Germany

²Clinical Neuroscience, Max Planck Institute of Experimental Medicine, Göttingen, Germany

³Electron Microscopy Core Unit, Max Planck Institute of Experimental Medicine, Göttingen, Germany

⁴Program in Neurogenetics, Department of Neurology, David Geffen School of Medicine, University of California Los Angeles, Los Angeles, CA, USA

*shared first authorship

 corresponding, email: nave@em.mpg.de

Abstract

Oligodendrocytes form myelin and enable the efficient transmission of axon electronic impulses in the central nervous system (CNS). Dysfunctions of oligodendrocyte and myelin are paralleled by pathological hallmarks such as axon swelling and reactive gliosis in multiple sclerosis (MS) and leukodystrophies. How these pathological side-effects of oligodendrocyte dysfunction arise, however, is incompletely understood. Here, we performed single-nuclei transcriptome sequencing (snRNA-seq) of cortex and underlying white matter from knockout mouse models of the three most abundant myelin proteins (PLP1, MBP, CNP) that present with subtle oligodendrocyte dysfunctions. We recovered astonishingly distinct oligodendrocyte RNA profiles upon knockout of CNP, PLP1, and MBP. Cell manifold reconstruction, as well as integrative analysis with previously defined cell subpopulations, revealed that mutant oligodendrocytes are mostly trapped at specific cell states. The imbalanced oligodendrocyte subtype proportions in the mutant brain potentially shift crosstalk between oligodendrocytes and other cell populations. Our data, therefore, provides a single-cell perspective on the early stages of oligodendrocyte dysfunction with relevance to neurological disorders that present with myelin defects.

Introduction

As a key process in the development of the central nervous system (CNS) in higher vertebrates, myelination mediates rapid action potential conduction and provides axonal trophic support (Fünfschilling et al. 2012; Lee et al. 2012; Nave 2010b). Despite its conserved function of producing myelin, recent snRNA-sequencing has revealed the highly heterogeneous nature of the oligodendrocyte lineage across brain development and adulthood (Marques et al. 2016; Marisca et al. 2020). Lately, an increasing number of studies showed that oligodendrocytes launch early responses and show altered heterogeneities in neurological disorders not only restricted to the classical myelin disease MS (Falcão et al. 2018; Jäkel et al. 2019), but also during brain aging (Ximerakis et al. 2019), and Alzheimer's Disease (AD) (Zhou et al. 2020). This highlights that oligodendrocytes are key regulators of disease progression. However, under disease conditions, it is challenging to distinguish oligodendrocyte dysfunction driven effects.

Recent proteomics measurements have systematically unfolded the relative abundance of proteins from myelin fractions (Chen et al. 2021). Among which, the top three most abundant myelin proteins are the transmembrane proteolipid protein 1 (PLP1) which extracellularly stabilize myelin lamellar structures, the myelin basic protein (MBP) that intracellularly compacts myelin leaflets, and the 2'-3' cyclic nucleotide phosphodiesterase (CNP) that maintain non-compacted myelin areas. Removal of PLP1 and CNP from oligodendrocytes by genetic editing approach resulted in milder myelin structural defects, reactive gliosis, and axon swellings at various degrees (Klugmann et al. 1997; Lappe-Siefke et al. 2003; Griffiths et al. 1998). Without MBP function as seen in the

classical shiverer mutant leads to myelin cannot be compacted any large stretches of axons are not properly myelinated (Matthieu et al. 1980). Surprisingly, the latter mutant does not represent axonal swellings.

We here utilized *Cnp*⁺, *Plp1*^{+/y}, and a novel forebrain specific shiver (*Foxg1-Cre Mbp*^{fl}) mice and performed single-nuclei resolution transcriptomics sequencing to investigate the molecular footprint of dysfunction associated oligodendrocytes (DAO), as well as of other reactive cell populations, under primary myelin dysfunctions.

Results

Myelin mutants show minor overall cell proportion changes

Cortex and corpus callosum were microdissected from 3-month-old myelin mutant mouse models (*Cnp*⁺, *Plp1*^{+/y} and *Foxg1-Cre Mbp*^{fl}) and corresponding wild type (WT) animals. Tissues were subjected to nuclei isolation and then single-nuclei RNA sequencing (snRNA-seq) experiments (Fig.1A). In total 55,777 valid single-nuclei transcriptome profiles were recovered and embedded into distinct cell clusters that were later annotated into the neuron, oligodendrocyte precursor cell (OPC), newly formed oligodendrocyte (NFOL), mature oligodendrocyte (MOL), microglia, astrocyte, endothelial cell, and pericyte based on their corresponding marker genes (Fig.2B-C). Interestingly, when highlighting genotype distributions on the embedded two-dimensional space, cells from myelin mutants and WT animals did not show spatial separation among all cell populations except in MOLs (Fig.1D). Clearly, MOLs from different genotypes preferred distinct spatial locations. This, however, is unlikely caused by the experimental batch effect according to the homogeneous grouping of other cells, indicating divergent transcriptome profiles among myelin mutant MOLs (Fig.1D). Nevertheless, regardless of spatial locations, proportions of all annotated cell types showed only minor shifts. *Foxg1-Cre Mbp*^{fl} and *Cnp*⁺ showed the decreased trend of neuronal cell proportion and a relative expansion of the MOL cell population (Fig.1E).

Mature oligodendrocytes in myelin mutants are locked at distinct cell states

To confirm and further investigate potential MOL molecular profile diversities from the myelin mutants, oligodendrocyte lineage cells including OPC, NFOL, and MOL were subset for individual analysis (n = 8,951 cells). Astonishingly, embedding analysis revealed spatially dislocated MOL subpopulations from different genotypes (Fig.2A). Similar spatial separation was not observed in OPC or NFOL cell clusters. Considering *Plp1*, *Mbp* and *Cnp* are highly abundant transcripts in MOLs, and their encoded protein products together account for more than 70% of the total myelin proteome, here list different proportions of all genes (Jahn et al. 2020), it was comprehensible that removal of these genes can fundamentally alter the relative location of a cell profile on a high dimensional space. Thus, to control for the potential knockout effect of highly abundant genes, counts of *Plp1*, *Mbp*, and *Cnp* were removed from the oligodendroglia expression matrix for re-embedding and clustering analysis. Yet, MOL exhibited the same spatial disconnections among four genotypes regardless of the absence of *Plp1*, *Mbp*, and *Cnp* transcripts (Supplementary 1A). This together confirmed fundamental shifts of MOL profiles once the cell loses the expression of an essential gene.

We then asked the question if the MOL cell profile shifts are within a traceable physiological range. For which, an external single-oligodendrocyte RNA sequencing dataset from Marques et al. 2016 was recruited (n = 4,867 cells), given its well-characterized oligodendroglia subpopulations (Marques et al. 2016; Hilscher et al. 2021). Through data integration, the majority of clusters that have been detected in the current data (Supplementary Fig.1B) were well aligned to previously discovered oligodendrocyte subpopulations (Supplementary Fig.1C). Hence, the current data oligodendrocyte clusters were annotated to OPC, NFOL, MFOL2, MOL2/3, MOL4, and MOL5/6 according to co-localizations with the reference dataset (Fig.2B; Supplementary Fig.1C), and the expression of previously described marker genes (Fig.2C) (Marques et al. 2016; Hilscher et al. 2021). In addition, one novel MOL cluster that was nearly exclusively contributed by *Foxg1-Cre Mbp*^{fl} was annotated that we termed MOL0 (Fig.2B). Evidently, compared to the WT oligodendrocytes, each myelin mutant has specifically expanded one MOL subpopulation, that in specific, is the enlarged proportion of MOL5/6 in *Plp1*^{+/y} mutant, MOL4 in *Cnp*⁺, and MOL0 in *Foxg1-Cre Mbp*^{fl} (Fig.2B).

Shifted MOL states are tightly connected on the cell manifold

The efficient integration of the current study oligodendrocyte profiles with formerly identified oligodendrocyte subpopulations indicate that myelin mutant MOLs are mostly within the known physiological stages. Recent

studies have concluded MOL2/3 and MOL4 are at a more juvenile stage compared to MOL5/6, whereas in adulthood, MOL2/3 and MOL5/6 stay as abundant subtypes in the spinal cord and brain, respectively (Hilscher et al. 2021; Floriddia et al. 2020). In the traumatic spinal cord injury model, MOL2/3 and MOL5/6 showed equal contributions at the acute injury site, although MOL5/6 showed relative increases during the injury chronic phase (Floriddia et al. 2020). Conversely, from reanalysis of single-MOL RNA profiles from experimental autoimmune encephalomyelitis (EAE) mouse brain, similar MOL subpopulations were assigned to unbiasedly recognize cell clusters (Supplementary Fig.3A; Supplementary Table.4), and further cell proportion calculation revealed upregulation of MOL2/3 quantity at the disease priming and peak stages (Supplementary Fig.3B). Linking to a previous study which suggested knockout MOL2/3 specific marker gene, kallikrein-related peptidase 6 (*Klk6*), led to milder EAE pathology, this together reflected that oligodendrocyte state shifts can be essential for disease progression (Bando et al. 2018). However, it is still unclear how MOL regulates its gene expressions to respond to the different physiopathological conditions.

In the myelin mutant, cells are stuck at one particular MOL state instead of shifting MOL2/3 and MOL5/6 subpopulations. We, therefore, asked the next question, of whether the enriched cell subpopulations could assist the reconstruction of cell molecular footprints and reveal the underlying biological signatures of MOL subtypes. For this, RNA velocity, an assumption model that uses the profile of sliced, unspliced, and degraded transcript proportions to recover the cell manifold, was applied to the MOL subset. As a result, MOL cells that are embedded based on spliced transcript counts were shown to be tightly connected on a UMAP space (Fig.3A). The reconstructed cell manifold indicated that MOL0 is at the most juvenile stage, and MOL4 locates at an intermediate cell stage (Fig.3A). Next, reclustering analysis was applied for capturing most representing cell subpopulation clusters (Supplementary Fig.2A). Subsequently, cell terminal states were calculated using the Markov chain algorithm, where in accordance with previous research, MOL2/3 and MOL5/6 were separately recognized as end states of the MOLs. In addition, no clear profile transition was observed between MOL2/3 and MOL5/6 (Fig.3A), potentially explained the relative enriched OPC proportion in *Plp*^{-/-} which has more mature MOLs, as well as the decreased OPC proportion in *Foxg1-Cre Mbp*^{fl/fl} that has only juvenile MOLs (Fig.2B). Putatively, cells from the starting state have no clear path preference changing towards the end states (Supplementary Fig.2B).

At the expression level, the top 100 genes that are most relevant for cells to shift to terminal state 1 (MOL2/3 direction) or terminal state 2 (MOL5/6 direction) were extracted and visualized based on the latent time trajectory, respectively (Fig.3B). Notably, genes that are involved in the molecular footprint towards MOL2/3 include its previously defined marker *Klk6*, and additionally show regulations of the actin cytoskeleton (*Gsn*, *Tln2*, *Actn4*) and extracellular cell adhesion (*Adam19*, *Adam23*); Where molecular footprint towards MOL5/6 are shown to be related with trophic support (*Ptgds*), glutamate signaling (*Gria2*), voltage-gated channels regulation (*Scn8a*, *Kcna1*), and cell migration and proliferation (*Cerk*, *Lrp4*, *Ptn*). Expression fluctuations of *Ptgds*, *Plp1*, *Apoe*, and *Apod* were further supported by dynamic expression plot visualizations and the expressions from previously reported oligodendrocyte subpopulations (Fig.3C; Supplementary Fig.2C). Intriguingly, *Plp1* was shown to be required for the differentiation of cells towards MOL2/3 direction, but to a lesser extent towards MOL5/6 (Fig.3B), which potentially explained why phenotypically similar *Cnp*^{-/-} and *Plp1*^{-/-} mutants expanded distinct MOL subsets (Fig.2A-B). Moreover, the two MOL terminal states also showed different preferences of apolipoprotein expressions. Of which, MOL2/3 end states expressed higher *Apod*, where MOL5/6 end states showed more expression of *Apoe*. Recent studies showed *Apod* is required for myelin compaction and the stabilization of lysosomal functions, and its level was shown to be reduced in Multiple Sclerosis (MS) patient brains (García-Mateo et al. 2018; Navarro et al. 2018). On the other hand, *Apoe* plays an important role in cholesterol transport that is essential for myelination (Stoll et al. 1989; Li et al. 2020). The regulation of apolipoproteins might further reflect the functionality preferences of MOL cell states.

Reactive microgliosis elicited by CNP null oligodendrocytes

Previous characterizations of *Cnp*^{-/-} and *Plp1*^{-/-} mutants revealed a strong reactive gliosis, especially pronounced in white matter tracts. The phenotype is earlier observed, as well as more severe in the *Cnp*^{-/-} (Griffiths et al. 1998; Lappe-Siefke et al. 2003). However, without apparently disrupted myelin, the underlying mechanism of how primary oligodendrocyte profile disruptions trigger reactive gliosis is unclear. We therefore further investigated the microglia subset for unfolding possible cell crosstalks of oligodendrocytes and microglia.

From 1,898 single-microglia data points, four major subpopulations were identified, including homeostatic microglia with high expressions of checkpoint genes (*Cx3cr1*, *p2ry12*, *Hexb*), myelin transcript enriched microglia

(MyTE) that show a high quantity of myelin transcripts (*Mbp*, *Mog*, *Plp1*), brain border macrophages characterized by expression of *Mrc1* and *Ms4a7* (Hammond et al. 2019), and disease-associated microglia (DAM) that upregulate *Trem2*, *Spp1* and *ApoE* expressions (Keren-Shaul et al. 2017) (Fig.4A). At 3-month of age, *Plp1*^{-/-} mutant did not show a clear microglia subpopulation difference compared to WT. However, the *Cnp*^{-/-} exhibited obvious upregulation of both MyTE and DAM (Fig.4A). Compared to microglia activation, the reactive astrogliosis is less discernible in the *Cnp*^{-/-} (Supplementary Fig.4A-B).

Interestingly, *Foxg1-Cre Mbp*^{fl/fl} that cannot form compact myelin in the forebrain showed the largest elevation of the MyTE proportion among all genotypes (Fig.4A). Previously, Schirmer et al. had demonstrated that microglia can uptake myelin transcripts in MS (Schirmer et al. 2019). In this study, tissue microdissection was performed to collect both cortex and corpus callosum, the enriched white matter content potentially also enriched the capture of the myelin processing microglia. Under this condition, we discovered the MyTE proportion was already abundant in the WT brain. More importantly, the current data suggest myelin transcripts are not necessarily imported to microglia in compact myelin debris. Under an amyelination situation, MOLs stay at a juvenile stage and likely urge the synthesis of myelin essential lipids and proteins, thus downstream trigger microglia processing of non-compact myelin debris (Fig.4A).

Independent of myelin, oligodendrocyte cells have been shown to be able to modulate immune responses through the expression of immune receptors and the release of cytokines and chemokines (Peferoen et al. 2014; Jäkel et al. 2019). To understand if there are cell communications enhanced between specific MOL and microglia subpopulations, we recruited public available reference databases and queried the cell subpopulation profiles using the CellPhoneDB analysis pipeline. We observed increased cell-cell interactions between *Cnp*^{-/-} enriched MOL4 subpopulation and activated microglia cells (Fig.4B). The potential interaction partners between MOL4 and activated microglia underlie several signaling pathways, such as NRG-ErbB, glutamate signaling (*GRIN2A*, *GRIN2B*), and fibroblast growth factor signaling (Fig.4B).

Neurons show modest responses to myelin dysfunctions at early stages

In the CNS, myelin plays a vital role in axon integrity and trophic support (Nave 2010a, [b] 2010). Decay of myelinogenesis and loss of myelin integrity is one of the critical features of brain aging and is correlated with pathological hallmarks including axon damage and cognitive decline (Sams 2021). In the *Cnp*^{-/-} and *Plp1*^{-/-} mutants, the lack of essential proteins results in the unstable but morphologically normal-appearing myelin sheath. This chronic instability, however, apparently disrupted axonal support and developed pronounced axon swelling pathology (Lappe-Siefke et al. 2003; Griffiths et al. 1998). From the current data, we observed only minor reductions of neuron cell proportion in *Cnp*^{-/-} and *Foxg1-Cre Mbp*^{fl/fl} mutants (Fig.1E) highlighting no obvious cell death. Subset analysis of neurons also revealed no obvious shifts between excitatory and inhibitory neurons across all genotypes (Supplementary Fig.5A-C). Subsequently, differential gene expression (DGE) analysis of proportionally small although well myelinated inhibitory neurons (Micheva et al. 2016) was applied between the mutants and WT. The result shows *Foxg1-Cre Mbp*^{fl/fl} mutant that shows amyelination of cortical axons in the forebrain did not trigger significant transcriptome responses in inhibitory neurons (Supplementary Table.5). Phenotypically overlapping *Cnp*^{-/-} and *Plp1*^{-/-} mutants gave rise to inhibitory neuron differentially expressed genes (DEGs) that enriched similar biological function terms through gene ontology analysis (Supplementary Fig.5D; Supplementary Table.5). Of which, *Cnp*^{-/-} mutant exhibited more regulated genes, which are involved in cell morphogenesis (*Ptprd*, *Ephb1*), dendritic spine regulation (*Homer1*, *Sipa1l1*), and more importantly, synaptic signaling and neurotransmitter release (*Nrgn1*, *Erc2*, *Mctp1*, *Camk2a*, *Syt6*) (Supplementary Fig.5D; Supplementary Table.6).

Discussion

While appreciated a long time ago (Trotter, Wegescheide, and Garvey 1984), oligodendroglial heterogeneity became recently studiable at unprecedented detail with the invention of single-cell resolution sequencing and spatial transcriptomics approaches. A special interest lies in the characterizations of oligodendrocyte subpopulations in their pathological responses (Marques et al. 2016; Ximerakis et al. 2019; Jäkel et al. 2019; Hilscher et al. 2021). In the current study, we discovered that the homeostatic distribution of heterogeneous oligodendrocytes in the brain can be strongly disrupted by the lack of myelin essential proteins. Under such mutant conditions, MOLs would concentratedly adapt their transcriptome profiles towards one particular state. The drastic cell subpopulation shift, however, did not exceed much from previously described physiological

oligodendrocyte subtypes (Marques et al. 2016). Phenotypically, the imbalanced assembly of the oligodendrocyte population led to diverse, but overall chronic pathologies (Griffiths et al. 1998; Lappe-Siefke et al. 2003; Stassart et al. 2018). This suggests tight connectivities between oligodendrocyte subpopulations at the molecular level. Indeed, on both neighboring embedded UMAP and RNA velocity reconstructed cell manifolds, MOL subtypes are closely adjacent to each other. In which case, it differs from other cell types, such as microglia, that present fundamentally changed transcriptome profiles upon cell activations (Keren-Shaul et al. 2017; Hammond et al. 2019). To a certain extent, this might reflect the unique cell property of MOL, which is generally focused on the formation and maintenance of myelin, and at the side try to adapt to local microenvironments with slightly altered functional priorities ranging from myelin compaction, immune modulation, to axon trophic support.

The current data also enabled us to investigate the intra- and inter-cellular regulatory networks downstream of one particular MOL stage, which is relevant for decoding oligodendrocyte and myelin intrinsic signals in the context of neurological disorders (Wheeler et al. 2020; Zhou et al. 2020; Hilscher et al. 2021). It is obvious from previous studies, that defect myelin burdens the system by exhausting microglia (Safaiyan et al. 2016), activating phagocytotic astrocyte (Ponath et al. 2017), and promoting axonal organelle accumulations (Stassart et al. 2018). However, to what degree oligodendrocyte and myelin play a primary role in diseases is unclear (Braak and Del Tredici 2004; Ettl, Schlachetzki, and Winkler 2016). Here, our observation through MOL subpopulation shifts derived single-cell profile changes argues that even in brain homeostasis at young adulthood, microglia constantly process myelin debris that results in the presence of myelin transcripts in the microglia cells. Yet with stable myelin turnover or absence of compact myelin, microglia do not necessarily undergo cell activation to disease-associated phenotype. Under more challenging situations such as *Cnp*⁺, the myelinating cells are trapped at an immature stage, where microglia and astrocyte are both activated into inflammatory phenotypes through exposure to myelin and axon pathology, as well as potential direct signaling from the oligodendrocytes. In the long term, this might lead to overload and/or distraction of reactive cells and therefore contribute to the onset and progression of neurological disorders to various degrees.

References

- Bando, Yoshio, Yoshiaki Hagiwara, Yasuhiro Suzuki, Kosuke Yoshida, Yoko Aburakawa, Takashi Kimura, Chisato Murakami, et al. 2018. "Kallikrein 6 Secreted by Oligodendrocytes Regulates the Progression of Experimental Autoimmune Encephalomyelitis." *Glia* 66 (2): 359–78.
- Braak, Heiko, and Kelly Del Tredici. 2004. "Poor and Protracted Myelination as a Contributory Factor to Neurodegenerative Disorders." *Neurobiology of Aging*.
- Chen, Jing-Fei, Kun Liu, Bo Hu, Rong-Rong Li, Wendy Xin, Hao Chen, Fei Wang, et al. 2021. "Enhancing Myelin Renewal Reverses Cognitive Dysfunction in a Murine Model of Alzheimer's Disease." *Neuron*. <https://doi.org/10.1016/j.neuron.2021.05.012>.
- Ettl, Benjamin, Johannes C. M. Schlachetzki, and Jürgen Winkler. 2016. "Oligodendroglia and Myelin in Neurodegenerative Diseases: More Than Just Bystanders?" *Molecular Neurobiology* 53 (5): 3046–62.
- Falcão, Ana Mendanha, David van Bruggen, Sueli Marques, Mandy Meijer, Sarah Jäkel, Eneritz Agirre, Samudrata, et al. 2018. "Disease-Specific Oligodendrocyte Lineage Cells Arise in Multiple Sclerosis." *Nature Medicine* 24 (12): 1837–44.
- Floriddia, Elisa M., Tânia Lourenço, Shupe Zhang, David van Bruggen, Markus M. Hilscher, Petra Kukanja, João P. Gonçalves dos Santos, et al. 2020. "Distinct Oligodendrocyte Populations Have Spatial Preference and Different Responses to Spinal Cord Injury." *Nature Communications* 11 (1): 1–15.
- Fünfschilling, Ursula, Lotti M. Supplie, Don Mahad, Susann Boretius, Aiman S. Saab, Julia Edgar, Bastian G. Brinkmann, et al. 2012. "Glycolytic Oligodendrocytes Maintain Myelin and Long-Term Axonal Integrity." *Nature* 485 (7399): 517–21.
- García-Mateo, Nadia, Raquel Pascua-Maestro, Alberto Pérez-Castellanos, Concepción Lillo, Diego Sanchez, and Maria D. Ganfornina. 2018. "Myelin Extracellular Leaflet Compaction Requires Apolipoprotein D Membrane Management to Optimize Lysosomal-Dependent Recycling and Glycocalyx Removal." *Glia* 66 (3): 670–87.
- Griffiths, Ian, Matthias Klugmann, Thomas Anderson, Donald Yool, Christine Thomson, Markus H. Schwab, Armin Schneider, et al. 1998. "Axonal Swellings and Degeneration in Mice Lacking the Major Proteolipid of Myelin." *Science* 280 (5369): 1610–13.
- Hammond, Timothy R., Connor Dufort, Lasse Dissing-Olesen, Stefanie Giera, Adam Young, Alec Wysoker, Alec J. Walker, et al. 2019. "Single-Cell RNA Sequencing of Microglia throughout the Mouse Lifespan and in the Injured Brain Reveals Complex Cell-State Changes." *Immunity* 50 (1): 253–71.e6.
- Hilscher, Markus M., Christoffer Mattsson Langseth, Petra Kukanja, Chika Yokota, Mats Nilsson, and Gonçalo Castelo-Branco. 2021. "Spatial Cell Type Mapping of the Oligodendrocyte Lineage in the Mouse Juvenile and Adult CNS with In Situ Sequencing." *bioRxiv*. <https://doi.org/10.1101/2021.06.04.447052>.

- Jahn, Olaf, Sophie B. Siems, Kathrin Kusch, Dörte Hesse, Ramona B. Jung, Thomas Liepold, Marina Uecker, Ting Sun, and Hauke B. Werner. 2020. "The CNS Myelin Proteome: Deep Profile and Persistence After Post-Mortem Delay." *Frontiers in Cellular Neuroscience* 0. <https://doi.org/10.3389/fncel.2020.00239>.
- Jäkel, Sarah, Eneritz Agirre, Ana Mendanha Falcão, David van Bruggen, Ka Wai Lee, Irene Knuesel, Dheeraj Malhotra, Charles French-Constant, Anna Williams, and Gonçalo Castelo-Branco. 2019. "Altered Human Oligodendrocyte Heterogeneity in Multiple Sclerosis." *Nature* 566 (7745): 543–47.
- Keren-Shaul, Hadas, Amit Spinrad, Assaf Weiner, Orit Matcovitch-Natan, Raz Dvir-Szternfeld, Tyler K. Ulland, Eyal David, et al. 2017. "A Unique Microglia Type Associated with Restricting Development of Alzheimer's Disease." *Cell*. <https://doi.org/10.1016/j.cell.2017.05.018>.
- Klugmann, Matthias, Markus H. Schwab, Anja Pühlhofer, Armin Schneider, Frank Zimmermann, Ian R. Griffiths, and Klaus-Armin Nave. 1997. "Assembly of CNS Myelin in the Absence of Proteolipid Protein." *Neuron*. [https://doi.org/10.1016/s0896-6273\(01\)80046-5](https://doi.org/10.1016/s0896-6273(01)80046-5).
- Lappe-Siefke, Corinna, Sandra Goebbels, Michel Gravel, Eva Nicksch, John Lee, Peter E. Braun, Ian R. Griffiths, and Klaus-Armin Nave. 2003. "Disruption of Cnp1 Uncouples Oligodendroglial Functions in Axonal Support and Myelination." *Nature Genetics*. <https://doi.org/10.1038/ng1095>.
- Lee, Youngjin, Brett M. Morrison, Yun Li, Sylvain Lengacher, Mohamed H. Farah, Paul N. Hoffman, Yiting Liu, et al. 2012. "Oligodendroglia Metabolically Support Axons and Contribute to Neurodegeneration." *Nature* 487 (7408): 443–48.
- Li, Li, Rongwen Li, Alex Zacharek, Fengjie Wang, Julie Landschoot-Ward, Michael Chopp, Jieli Chen, and Xu Cui. 2020. "ABCA1/ApoE/HDL Signaling Pathway Facilitates Myelination and Oligodendrogenesis after Stroke." *International Journal of Molecular Sciences* 21 (12). <https://doi.org/10.3390/ijms21124369>.
- Marisca, Roberta, Tobias Hoche, Eneritz Agirre, Laura Jane Hoodless, Wenke Barkey, Franziska Auer, Gonçalo Castelo-Branco, and Tim Czopka. 2020. "Functionally Distinct Subgroups of Oligodendrocyte Precursor Cells Integrate Neural Activity and Execute Myelin Formation." *Nature Neuroscience* 23 (3): 363–74.
- Marques, Sueli, Amit Zeisel, Simone Codeluppi, David van Bruggen, Ana Mendanha Falcão, Lin Xiao, Huiliang Li, et al. 2016. "Oligodendrocyte Heterogeneity in the Mouse Juvenile and Adult Central Nervous System." *Science* 352 (6291): 1326–29.
- Matthieu, J-M, J. -M. Matthieu, H. Ginalski, R. L. Friede, S. R. Cohen, and D. P. Doolittle. 1980. "Absence of Myelin Basic Protein and Major Dense Line in CNS Myelin of the Mld Mutant Mouse." *Brain Research*. [https://doi.org/10.1016/0006-8993\(80\)90333-9](https://doi.org/10.1016/0006-8993(80)90333-9).
- Micheva, Kristina D., Dylan Wolman, Brett D. Mensh, Elizabeth Pax, Joann Buchanan, Stephen J. Smith, and Davi D. Bock. 2016. "A Large Fraction of Neocortical Myelin Ensheathes Axons of Local Inhibitory Neurons." *eLife* 5 (July). <https://doi.org/10.7554/eLife.15784>.
- Navarro, Ana, Beatriz Rioseras, Eva del Valle, Eva Martínez-Pinilla, Aurora Astudillo, and Jorge Tolivia. 2018. "Expression Pattern of Myelin-Related Apolipoprotein D in Human Multiple Sclerosis Lesions." *Frontiers in Aging Neuroscience* 0. <https://doi.org/10.3389/fnagi.2018.00254>.
- Nave, Klaus-Armin. 2010a. "Myelination and Support of Axonal Integrity by Glia." *Nature*. <https://doi.org/10.1038/nature09614>.
- . 2010b. "Myelination and the Trophic Support of Long Axons." *Nature Reviews. Neuroscience* 11 (4): 275–83.
- Peferoen, Laura, Markus Kipp, Paul van der Valk, Johannes M. van Noort, and Sandra Amor. 2014. "Oligodendrocyte-Microglia Cross-Talk in the Central Nervous System." *Immunology* 141 (3): 302–13.
- Ponath, Gerald, Sriram Ramanan, Mayyan Mubarak, William Housley, Seunghoon Lee, F. Rezan Sahinkaya, Alexander Vortmeyer, Cedric S. Raine, and David Pitt. 2017. "Myelin Phagocytosis by Astrocytes after Myelin Damage Promotes Lesion Pathology." *Brain: A Journal of Neurology* 140 (2): 399–413.
- Safaiyan, Shima, Nimal Kannaiyan, Nicolas Snaidero, Simone Brioschi, Knut Biber, Simon Yona, Aimee L. Edinger, Steffen Jung, Moritz J. Rossner, and Mikael Simons. 2016. "Age-Related Myelin Degradation Burdens the Clearance Function of Microglia during Aging." *Nature Neuroscience* 19 (8): 995–98.
- Sams, Eleanor Catherine. 2021. "Oligodendrocytes in the Aging Brain." *Neuronal Signaling* 5 (3). <https://doi.org/10.1042/NS20210008>.
- Schirmer, Lucas, Dmitry Velmeshev, Staffan Holmqvist, Max Kaufmann, Sebastian Werneburg, Diane Jung, Stephanie Vistnes, et al. 2019. "Neuronal Vulnerability and Multilineage Diversity in Multiple Sclerosis." *Nature* 573 (7772): 75–82.
- Stassart, Ruth M., Wiebke Möbius, Klaus-Armin Nave, and Julia M. Edgar. 2018. "The Axon-Myelin Unit in Development and Degenerative Disease." *Frontiers in Neuroscience* 12 (July): 467.
- Stoll, Guido, Hans Werner Mueller, Bruce D. Trapp, and John W. Griffin. 1989. "Oligodendrocytes but Not Astrocytes Express Apolipoprotein E after Injury of Rat Optic Nerve." *Glia*. <https://doi.org/10.1002/glia.440020306>.
- Trotter, J. L., C. L. Wegescheide, and W. F. Garvey. 1984. "Regional Studies of Myelin Proteins in Human Brain and Spinal Cord." *Neurochemical Research* 9 (1): 133–46.
- Wheeler, Michael A., Iain C. Clark, Emily C. Tjon, Zhaorong Li, Stephanie E. J. Zandee, Charles P. Couturier, Brianna R. Watson, et al. 2020. "MAFG-Driven Astrocytes Promote CNS Inflammation." *Nature* 578 (7796): 593–99.
- Ximerakis, Methodios, Scott L. Lipnick, Brendan T. Innes, Sean K. Simmons, Xian Adiconis, Danielle Dionne, Brittany A. Mayweather, et al. 2019. "Single-Cell Transcriptomic Profiling of the Aging Mouse Brain." *Nature Neuroscience* 22 (10): 1696–1708.

Zhou, Yingyue, Wilbur M. Song, Prabhakar S. Andhey, Amanda Swain, Tyler Levy, Kelly R. Miller, Pietro L. Poliani, et al. 2020. "Human and Mouse Single-Nucleus Transcriptomics Reveal TREM2-Dependent and TREM2-Independent Cellular Responses in Alzheimer's Disease." *Nature Medicine* 26 (1): 131–42.

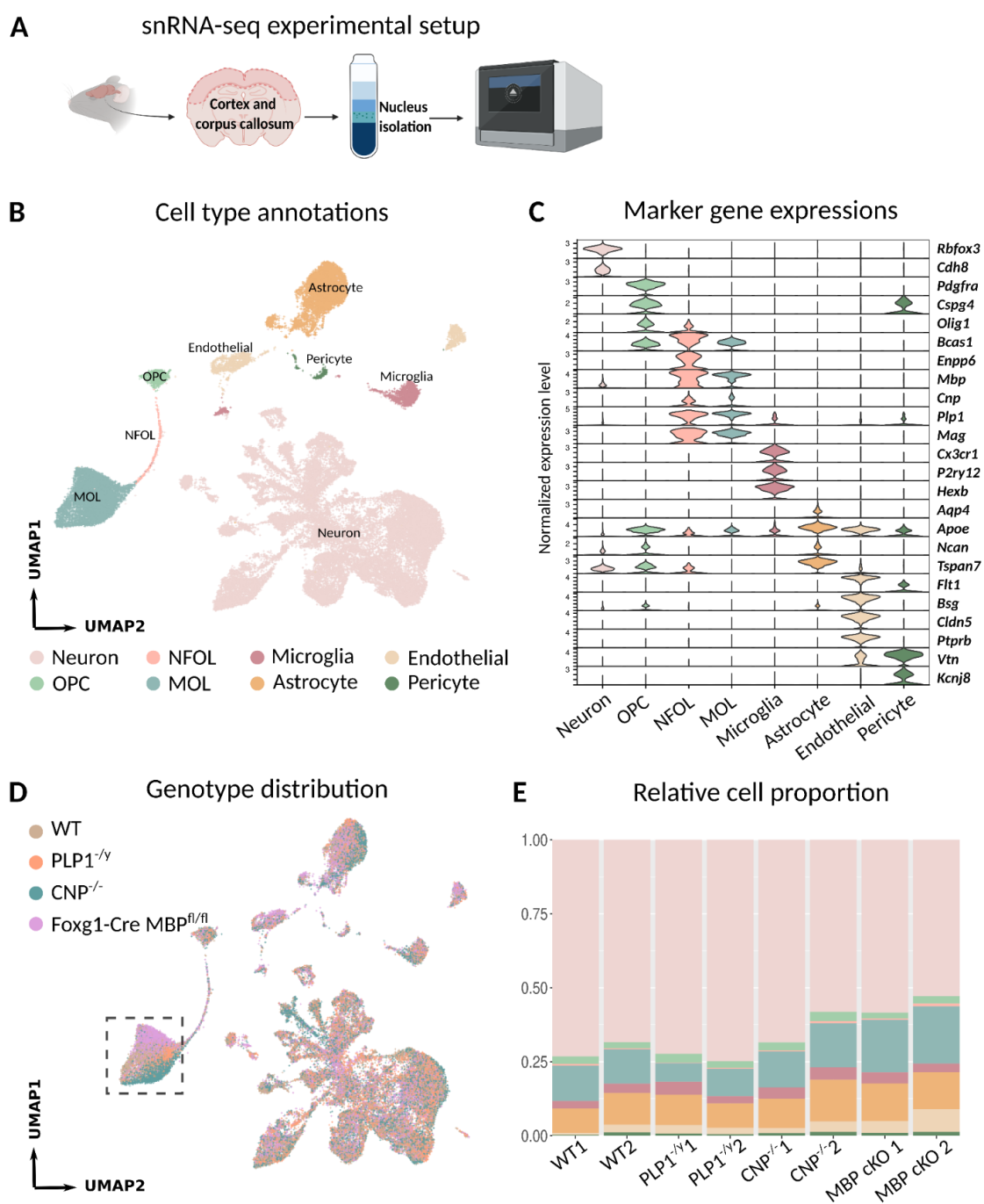
Figure 1

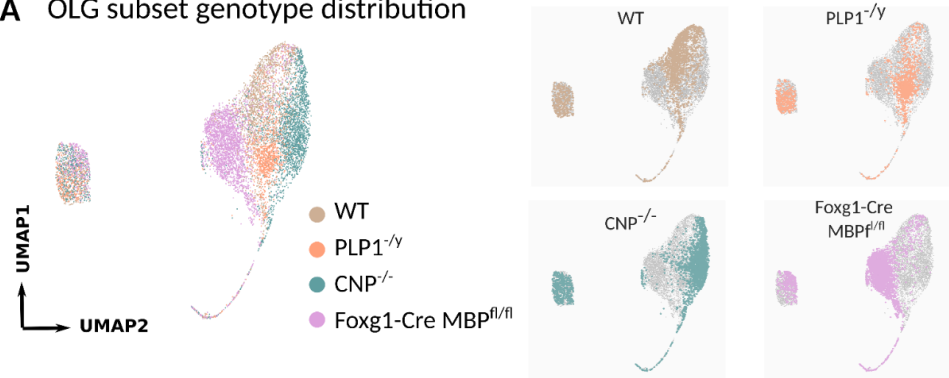
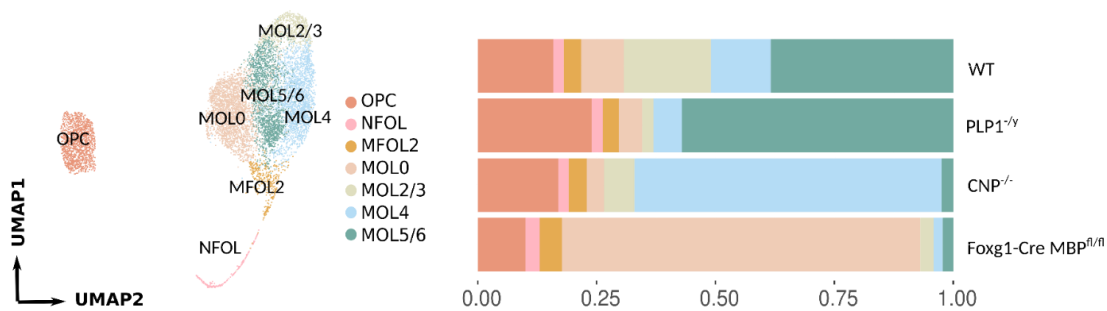
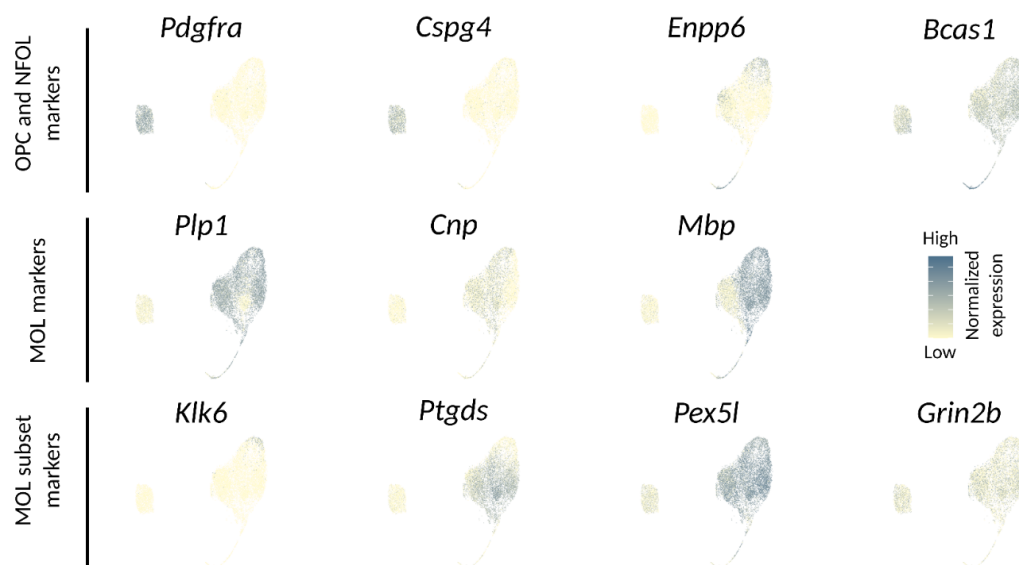
Figure 2**A** OLG subset genotype distribution**B** OLG subpopulations and proportion shifts**C** Marker gene expressions

Figure 3

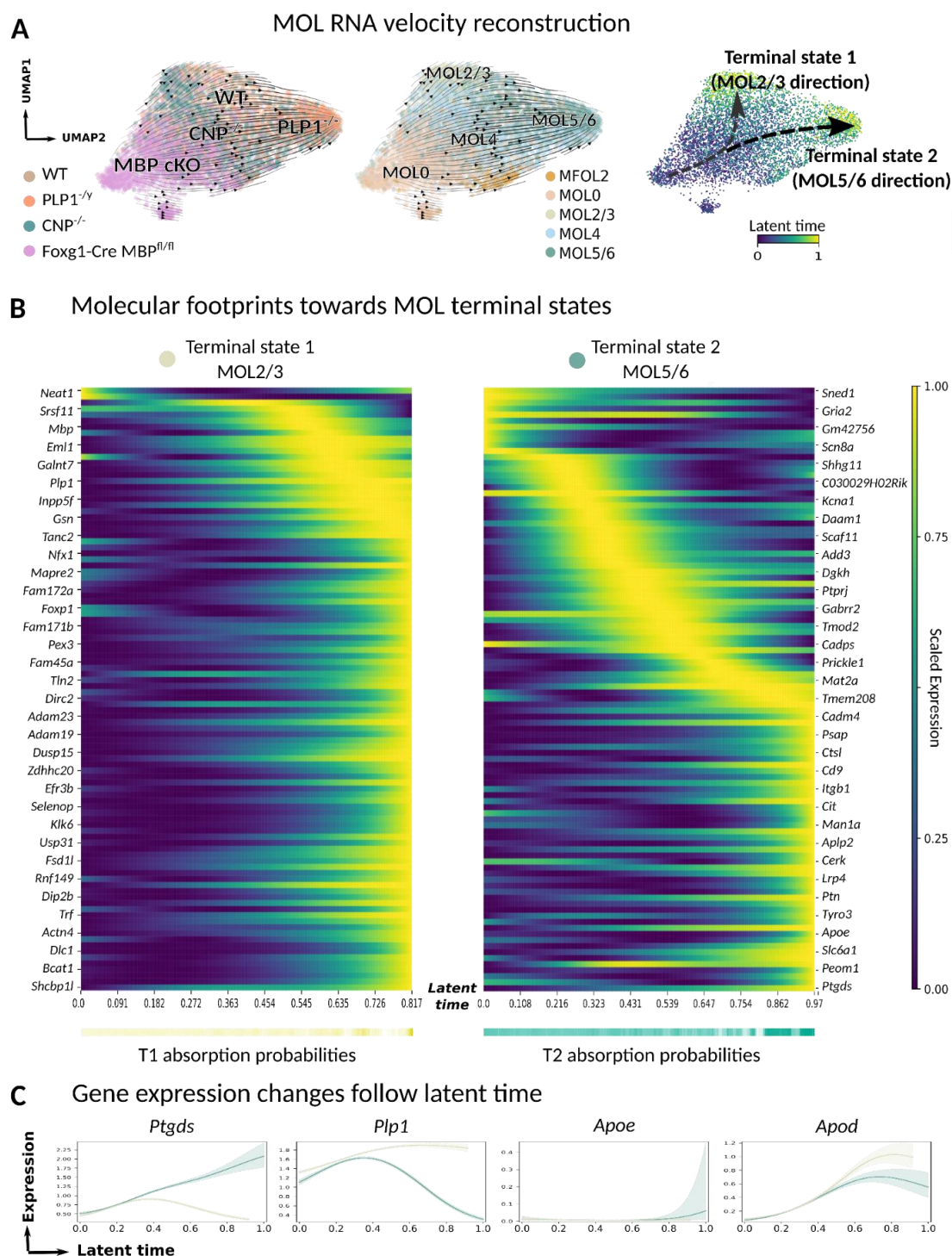
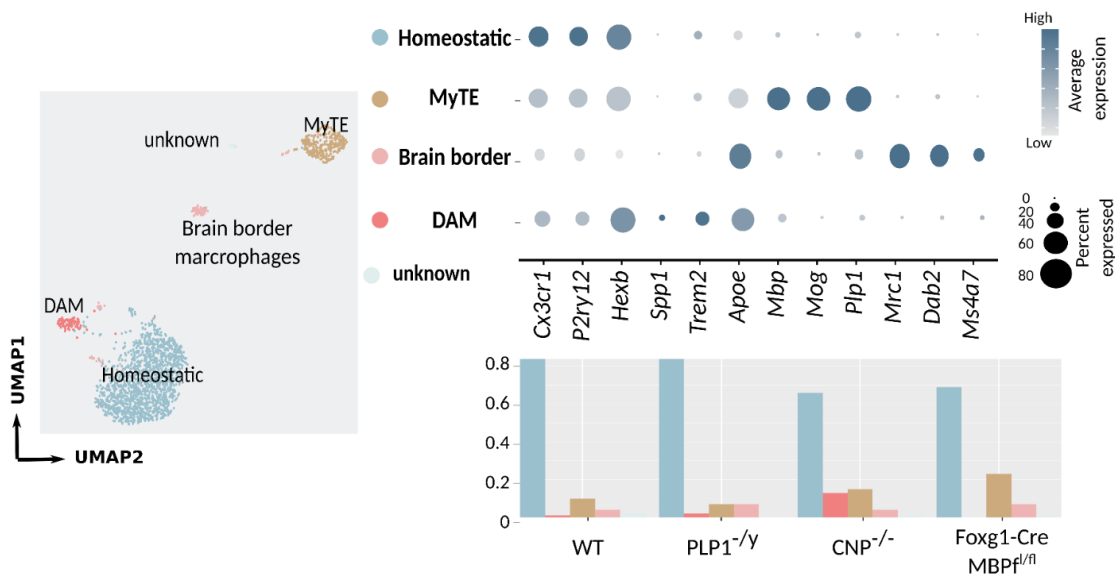
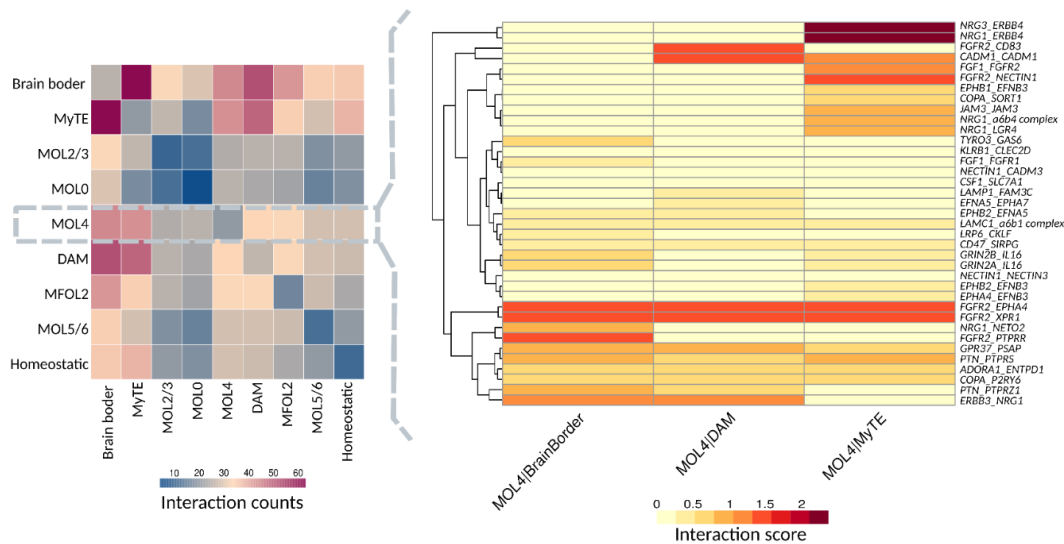


Figure 4

A Microglia subpopulation analysis



B Cell cross talk between MOL and microglia subpopulations



Main figure legends

Figure 1. Myelin mutant cortex and corpus callosum snRNA-seq

A Cortex and corpus callosum from 3-month-old mice brains were used for snRNA-seq experiment. In total, four genotypes including WT, *CNP^{-/-}*, *PLP1^{-/-}* and *Foxg1-Cre MBP^{fl/fl}* were recruited for the experiment, every genotype is sequenced in two replicates which contains material pooled from two animals. Collected brain tissues were subjected to iodixanol gradient nuclei isolation and snRNA-seq (10x Genomics). **B** UMAP represents annotated cell types of all nuclei ($n = 55,777$). **C** Identification of cell types were based on unbiasedly calculated cluster marker genes. Expression and distribution of top cell specific marker genes across different cell populations are shown in the violin plot. **D** single-nuclei RNA profiles from four genotypes distributed equally across cell types, but not in MOL (highlighted by dash line box). **E** Relative proportion of cells among experiment replicates do not show obvious alterations, although MOL proportion in *CNP^{-/-}* and *Foxg1-Cre MBP^{fl/fl}* exhibited a upregulation trend.

Figure 2. OLG subset analysis

A In total 8,951 annotated OLG lineage cells were subset for further analysis. Different genotypes distribute evenly among OPC and NFOL clusters, although occupy distinct spatial locations in the MOL population. **B** Clustering analysis of OLGs identified seven cell subpopulations (Supplementary Figure 1.B). Six subpopulations were annotated based on previous published data (Supplementary Figure 1.C), and one novel detected population is annotated as MOL0. Proportions of OLG subpopulations shift diversity in each myelin mutant model. **C** Featureplots show expression levels of OLG lineage and subpopulation marker genes.

Figure 3. MOL cell manifold reconstruction using RNA velocity

A RNA velocity analysis of MOLs ($n = 7,281$ cells) revealed putative cell manifolds on UMAP embedded by single-nuclei spliced RNA profiles. Color codes indicate different genotypes (left), cell subpopulations (middle), and position at latent time axis (right). Two cell terminal states, state 1 that ends at MOL2/3 subpopulation, and state 2 that ends at MOL5/6 subpopulation, were recognized by using cell terminal subclusters for calculation (Supplementary Figure 2.A). **B** Top 100 genes that are relevant for cell state transitions towards terminal state 1 (left) or terminal state 2 (right) are calculated by Markov Chain algorithm, respectively. Heatmaps show scaled expression values of genes over latent time (x-axis). Absorption probabilities represent cell state transition rate are shown under the heatmaps. **C** Dynamics of *Ptgds*, *Plp1*, *Apoe* and *Apod* gene expressions (y-axis) towards two terminal states are plotted along latent time (x-axis), colors of curves separate different terminal states.

Figure 4. Microglia subset analysis and interaction with MOL

A Microglia were extracted and individually analyzed. In total 1,898 cells were clustered into four major subpopulations including homeostatic, myelin transcript enriched (MyTE), disease-associated microglia (DAM), and brain border macrophages. Dotplot shows marker genes expression and positive expressed rate among microglia subpopulations. Barplot represents microglia subpopulation proportions changes across different genotypes. **B** Molecular interactions between MOL and microglia cell clusters were calculated using the CellPhoneDB toolkit; the amount of interactions between each pair of cell subpopulations are shown in the left heatmap, where MOL4 showed relatively enriched interactions with other microglia subtypes. Specific cell cross talk molecule pairs between MOL4 and microglia subtypes are visualized in the right heatmap, color scale represents interaction scores.

Material and Methods

Animal strains and tissue microdissection

Animal experiments were performed under approval by the local authority of German animal welfare practice regulations. Mice included in the study were housed in groups under 12 hours dark/light cycles. Tissue microdissection was performed using 3-month-old male mice across four genotypes, the wildtype, *Cnp^{-/-}*, *Plp1^{-/-}*, and *Foxg1-Cre Mbp^{fl/fl}*. Genotypes were confirmed by animal ear and tail biopsies genotyping before performing downstream experiments.

For tissue microdissection, animals were sacrificed by cervical dislocation to extract the whole brain into a prechilled 1x PBS buffer. Subsequently, the whole brain was coronally sliced and spread on an ice-cold glass plate, from which the cortical and corpus callosum regions from left and right hemispheres were carefully dissected, respectively. The microdissected tissue was directed frozen on dry ice and collected into pre-frozen 1.5 ml low-binding eppendorf tubes. Tissues collected from the animal's left hemisphere were subjected to the snRNA-seq experiment, where the right hemisphere samples were collected and stored as backups. All samples were stored under -80°C until further use.

Single-nuclei isolation

Microdissected left hemisphere cortex and corpus callosum tissue were pooled into two samples for each genotype, of which, the wild type group was pooled of c57BL/6J from *Cnp^{-/-}* and *Plp1^{-/-}* colony, respectively, and *Mbp^{fl/fl}*. For each pooled sample, tissue was kept frozen and subjected to 2ml of homogenization buffer as previously described (Depp et al., n.d.) and mechanically disrupted. Homogenized tissue was then passed through a 80um strainer to filter tissue debris. The filtered suspension was centrifuged for 1min under 100 rcf, and 400ul supernatant was transferred into a pre-chilled low-binding Eppendorf tube. Afterwards, nuclei were isolated by gradient centrifugation assay. In specific, the collected supernatant was diluted into 25% iodixanol concentration by adding 400ul pre-chilled 50% iodixanol solution that contains 480mM sucrose, and layered on top of 29% (middle) and 35% (bottom) iodixanol solutions. The gradient solutions were centrifuged for 20min under 3,000 rcf, where nuclei were collected at the band between the 29% and 35% iodixanol layers. Collected nuclei were then washed by a resuspension buffer that contains 1xPBS, 1% BSA, and 0.1U/ul RNase inhibitor. The isolated nuclei were immediately subjected to the snRNA-seq experiment.

snRNA-seq experiment

Freshly isolated nuclei were used for single-nuclei transcriptome library constructions using chromium single-cell 3' reagent kit (10x Genomics) according to the manufacturer's protocol. Around 15,000 nuclei were used for each reaction to target for recovery of 9,000 single-nuclei transcriptome profiles. Constructed single-nuclei RNA libraries were validated by the Agilent Bioanalyzer high sensitivity DNA chip (Agilent). Quality controlled library products were then sequenced by NovaSeq 6000 (Illumina).

Data alignment and pre-processing

Raw sequencing data in Fastq format were aligned and quality controlled using CellRanger v3.0.2 (10x Genomics), alignment was performed against reference transcriptome pre-mRNA (mm10). On average, each reaction was able to recover 7,716 droplets. Raw expression matrices from each sample were extracted from each sample and underwent individual quality control and droplet filters using R toolkit Seurat v3.2.3 (Stuart et al. 2019). In specific, cells with less than 500 total transcripts and less than 200 annotated genes were removed for further analysis. Moreover, cells exceeding the upper limit of transcripts detection rate are identified in individual samples and excluded from the following analysis (Supplementary Table.1).

After the individual sample filter, all matrices were merged for the next step analysis. Genes expressed in less than three cells were excluded from downstream calculations. Gene raw counts were represented by UMI values, which is normalized against the total amount of transcripts in each cell with a scale factor of 10,000, then transformed using log1p. To ensure efficient data processing, 3,000 variable genes that exhibit high cell-cell variations were detected for further analysis. Prior to dimensionality reductions, data was centered by scaling genes with a mean expression of 0 and a standard deviation of 1 across all cells.

Dimensionality reduction and cluster annotations

Data were summarized by linear dimensionality reduction using principal component analysis (PCA). For all 61,609 nuclei, the first 50 principal components (PCs) were selected for further data processing. Subsequently, non-linear dimensionality was performed for the data by utilizing the k-nearest neighbor (KNN) algorithm and visualized by Uniform Manifold Approximation and Projection (UMAP). Single-nuclei profiles were determined for closest neighbours in the reduced PCA space, and underwent unbiased cluster detection using resolution 0.5. As a result, 36 cell clusters were identified, and corresponding cluster-specific differentially expressed genes (DEGs)

were calculated using the Wilcoxon Rank Sum test (Supplementary Table.2). Major CNS cell types including neuron, oligodendroglia, astrocyte, microglia, endothelial cells, and pericyte were assigned to individual clusters. Cells with ambient markers were annotated as unclear and removed for further analysis. After removing unclear cell populations, the altered data expression matrix ($n = 55,777$ nuclei) was re-calculated for linear and non-linear dimensionality reduction, as well as for cell cluster visualization.

Cell subset analysis

Four cell types, oligodendrocyte, microglia, astrocyte, and neuron were subjected for subset analysis, respectively. Each cell population was extracted based on previous cell type annotations, and underwent re-normalization and scaling, and additionally dimensionality reductions and clustering analysis to identify cell subpopulations. In detail, oligodendroglia accounted for 8,951 nuclei, and the subset data was summarized by the first 15 PCs with 2,000 high variable genes, and clustered into seven subpopulations under resolution 0.5. In order to control gene knockout effects on data embedding and visualization, *Cnp*, *Plp1*, and *Mbp* counts were removed from the oligodendroglia expression matrix and subjected to the analysis pipeline using the exact same parameters. The seven subclusters recognized in the oligodendroglia subset were annotated by cluster marker genes, as well as integrative analysis with Marques et al. 2016 dataset (Marques et al. 2016). In other neuron and microglia subsets, subpopulations were purely detected by cluster marker genes, respectively. Specifically, neuron data subset ($n = 34,645$ nuclei) was summarized using the first 50 PCs and further clustered under resolution 0.5, where microglia data subset ($n = 1,898$ nuclei) was summarized using its first 20 PCs, and subpopulations were detected under cluster resolution 0.3. For astrocyte analysis, only *Cnp*⁺ and *Foxg1-Cre Mbp*^{fl} mutants and corresponding wild type profiles were subset for the purpose of support microglia subset analysis. The subset astrocyte data was reduced using the first 20 PCs, and data points were annotated for biological relevant subpopulations by integrating with the Habib et al. 2020 dataset (astrocyte subset) (Habib et al. 2020).

Differential gene expression statistics

Statistics analysis of differentially expressed genes were carried out by the MAST algorithm implemented in Seurat toolkit between the given cell groups. For MOLs, downsampling analysis was applied by comparing cells from every myelin mutant to WT. In detail, MAST analysis used 200 randomly selected cells from each compared genotype, and was repetitively applied for 50 times. All calculated results were then averaged for investigating the most stably differentially regulated genes in myelin mutant MOLs (Supplementary Table.3).

RNA velocity analysis

To reconstruct potential cell manifolds, single-nuclei RNA profiles from MOL were extracted and subjected to RNA velocity analysis. The alignment for separating spliced, unspliced and degraded RNA was done by the python package Velocity (La Manno et al. 2018) on top of each CellRanger aligned snRNA-seq raw data, and saved in .loom format. For the next step, loom files were translated to Seurat objects. Profiles were then merged and annotations from previous transcriptome analysis were matched to the new object that contains spliced and unspliced transcript counts. The MOL cells were subsetted for further velocity analysis. Alternatively, the embedding of the subset cells was performed only using sliced RNA profiles. Afterward, the object was saved in AnnData format (Wolf, Angerer, and Theis 2018) and continuous for velocity calculations using python package scVelo v0.2.3 (Bergen et al. 2020). Cell microstates were calculated based on the Markov Chain algorithm implemented in the python package CellRank v1.4.0 (Lange et al., n.d.).

External datasets reanalysis and integration

Data integration and cell subtype classification using integrated reference data were performed using the SCTransform pipeline implemented in Seurat v4.0.0 (Hao et al. 2021). Wheeler et al. 2020 dataset was recovered from the GEO database under accession number GSE130119 (Wheeler et al. 2020). MOL cells annotated in the corresponding dataset were subjected for reanalysis. In total 4,225 single-MOL profiles were collected, across five major groups including CFA control and four EAE pathological stages (priming, peak, remitting). Cell subclusters were calculated under resolution 0.8. For annotating identified subclusters, projection analysis was conducted by referring to the Marques et al. 2016 dataset (Marques et al. 2016) (Supplementary Table.4).

For external data integrative analysis with the current study, expression matrices from GSE75330 (Marques et al. 2016), GSE143758 (Habib et al. 2020) were accessed from GEO platform, and metadata matrices with cell subtype annotations were acquired upon contact to corresponding authors of the original publications. For oligodendroglia, subset profiles and objects recovered from GSE75330 were normalized using the SCTransform algorithm (Hafemeister and Satija 2019). Normalized matrices were then calculated for 3,000 shared integration genes, as well as for cell pairs that share stable expression structures as integration anchors for the alignment of

two expression matrices. Aligned data was downstream embedded using the first 20 PCs, and visualized for cell subpopulation overlapping. Similarly, the astrocyte subset from the current study was integrated with GSE143758 using the first 30 PCs after integration analysis based on shared 1,000 variable genes. However, since GSE143758 contains two different batches using distinct cell dissociation reagents, data integration was therefore applied based on experimental batches instead of different studies. To further confirm the detection of disease-associated astrocytes in the current study, projection analysis was performed for the astrocyte subset by referring to GSE143758.

Cell subpopulation crosstalk analysis

For analyzing cell-cell communication partners between MOL and microglia subpopulations, normalized expression matrices were firstly extracted from the analysis object. In order to suit for querying public databases that are mainly based on human studies, genes in extracted matrices were translated using R package biomaRt v2.42.1. Matrices with translated gene symbols were then input to the public repository CellPhoneDB v2.1.7 for the analysis of potential cell-cell interactions (Efremova et al. 2020).

Data and code availability

Raw single-cell RNA sequencing data are uploaded to the Gene expression Omnibus (GEO) under the SuperSeries accession number GSE178304. Analysis code can be accessed upon contact to the corresponding author.

Method References

- Bergen, Volker, Marius Lange, Stefan Peidli, F. Alexander Wolf, and Fabian J. Theis. 2020. "Generalizing RNA Velocity to Transient Cell States through Dynamical Modeling." *Nature Biotechnology* 38 (12): 1408–14.
- Depp, Constanze, Ting Sun, Andrew Octavian Sasmita, Lena Spieth, Stefan A. Berghoff, Agnes A. Steixner-Kumar, Swati Subramanian, et al. n.d. "Ageing-Associated Myelin Dysfunction Drives Amyloid Deposition in Mouse Models of Alzheimer's Disease." <https://doi.org/10.1101/2021.07.31.454562>.
- Efremova, Mirjana, Miquel Vento-Torres, Sarah A. Teichmann, and Roser Vento-Torres. 2020. "CellPhoneDB: Inferring Cell-cell Communication from Combined Expression of Multi-Subunit Ligand-receptor Complexes." *Nature Protocols* 15 (4): 1484–1506.
- Falcão, Ana Mendanha, David van Bruggen, Sueli Marques, Mandy Meijer, Sarah Jäkel, Eneritz Agirre, Samudiyata, et al. 2018. "Disease-Specific Oligodendrocyte Lineage Cells Arise in Multiple Sclerosis." *Nature Medicine* 24 (12): 1837–44.
- Habib, Naomi, Cristin McCabe, Sedi Medina, Miriam Varshavsky, Daniel Kitsberg, Raz Dvir-Szternfeld, Gilad Green, et al. 2020. "Disease-Associated Astrocytes in Alzheimer's Disease and Aging." *Nature Neuroscience* 23 (6): 701–6.
- Hafemeister, Christoph, and Rahul Satija. 2019. "Normalization and Variance Stabilization of Single-Cell RNA-Seq Data Using Regularized Negative Binomial Regression." *Genome Biology* 20 (1): 1–15.
- Hao, Yuhao, Stephanie Hao, Erica Andersen-Nissen, William M. Mauck 3rd, Shiwei Zheng, Andrew Butler, Maddie J. Lee, et al. 2021. "Integrated Analysis of Multimodal Single-Cell Data." *Cell* 184 (13): 3573–87.e29.
- Klugmann, Matthias, Markus H. Schwab, Anja Pühlhofer, Armin Schneider, Frank Zimmermann, Ian R. Griffiths, and Klaus-Armin Nave. 1997. "Assembly of CNS Myelin in the Absence of Proteolipid Protein." *Neuron*. [https://doi.org/10.1016/s0896-6273\(01\)80046-5](https://doi.org/10.1016/s0896-6273(01)80046-5).
- La Manno, Gioele, Ruslan Soldatov, Amit Zeisel, Emelie Braun, Hannah Hochgerner, Viktor Petukhov, Katja Lidschreiber, et al. 2018. "RNA Velocity of Single Cells." *Nature* 560 (7719): 494–98.
- Lange, Marius, Volker Bergen, Michal Klein, Manu Setty, Bernhard Reuter, Mostafa Bakhti, Heiko Lickert, et al. n.d. "CellRank for Directed Single-Cell Fate Mapping." <https://doi.org/10.1101/2020.10.19.345983>.
- Lappe-Siefke, Corinna, Sandra Goebbels, Michel Gravel, Eva Nicksch, John Lee, Peter E. Braun, Ian R. Griffiths, and Klaus-Armin Nave. 2003. "Disruption of Cnp1 Uncouples Oligodendroglial Functions in Axonal Support and Myelination." *Nature Genetics*. <https://doi.org/10.1038/ng1095>.
- Marques, Sueli, Amit Zeisel, Simone Codeluppi, David van Bruggen, Ana Mendanha Falcão, Lin Xiao, Huiliang Li, et al. 2016. "Oligodendrocyte Heterogeneity in the Mouse Juvenile and Adult Central Nervous System." *Science* 352 (6291): 1326–29.
- Matthieu, J-M, J. -M. Matthieu, H. Ginalski, R. L. Friede, S. R. Cohen, and D. P. Doolittle. 1980. "Absence of Myelin Basic Protein and Major Dense Line in CNS Myelin of the Mid Mutant Mouse." *Brain Research*. [https://doi.org/10.1016/0006-8993\(80\)90333-9](https://doi.org/10.1016/0006-8993(80)90333-9).
- Schirmer, Lucas, Dmitry Velmishev, Staffan Holmqvist, Max Kaufmann, Sebastian Werneburg, Diane Jung, Stephanie Vistnes, et al. 2019. "Neuronal Vulnerability and Multilineage Diversity in Multiple Sclerosis." *Nature* 573 (7772): 75–82.
- Stuart, Tim, Andrew Butler, Paul Hoffman, Christoph Hafemeister, Efthymia Papalexi, William M. Mauck, Yuhao Hao, Marlon Stoeckius, Peter Smibert, and Rahul Satija. 2019. "Comprehensive Integration of Single-Cell Data." *Cell*. <https://doi.org/10.1016/j.cell.2019.05.031>.

- Wheeler, Michael A., Iain C. Clark, Emily C. Tjon, Zhaorong Li, Stephanie E. J. Zandee, Charles P. Couturier, Brianna R. Watson, et al. 2020. "MAFG-Driven Astrocytes Promote CNS Inflammation." *Nature* 578 (7796): 593–99.
- Wolf, F. Alexander, Philipp Angerer, and Fabian J. Theis. 2018. "SCANPY: Large-Scale Single-Cell Gene Expression Data Analysis." *Genome Biology* 19 (1): 1–5.
- Ximerakis, Methodios, Scott L. Lipnick, Brendan T. Innes, Sean K. Simmons, Xian Adiconis, Danielle Dionne, Brittany A. Mayweather, et al. 2019. "Single-Cell Transcriptomic Profiling of the Aging Mouse Brain." *Nature Neuroscience* 22 (10): 1696–1708.
- Zhou, Yingyue, Wilbur M. Song, Prabhakar S. Andhey, Amanda Swain, Tyler Levy, Kelly R. Miller, Pietro L. Poliani, et al. 2020. "Human and Mouse Single-Nucleus Transcriptomics Reveal TREM2-Dependent and TREM2-Independent Cellular Responses in Alzheimer's Disease." *Nature Medicine* 26 (1): 131–42.

Acknowledgments

We acknowledge the rich input from all members of the Neurogenetics department at Max-Planck Institute of Experimental Medicine (MPI-EM), especially the intellectual discussions among the KAGS subgroup. We also thank Dr. Myriam and Sheldon Adelson Medical Foundation (AMRF) for their support of our laboratory work, especially for the snRNA-seq experiment in this study. The recovery of external scRNA-seq datasets was kindly supported by Dr. Gonalo Castelo-Branco and Dr. Naomi Habib.

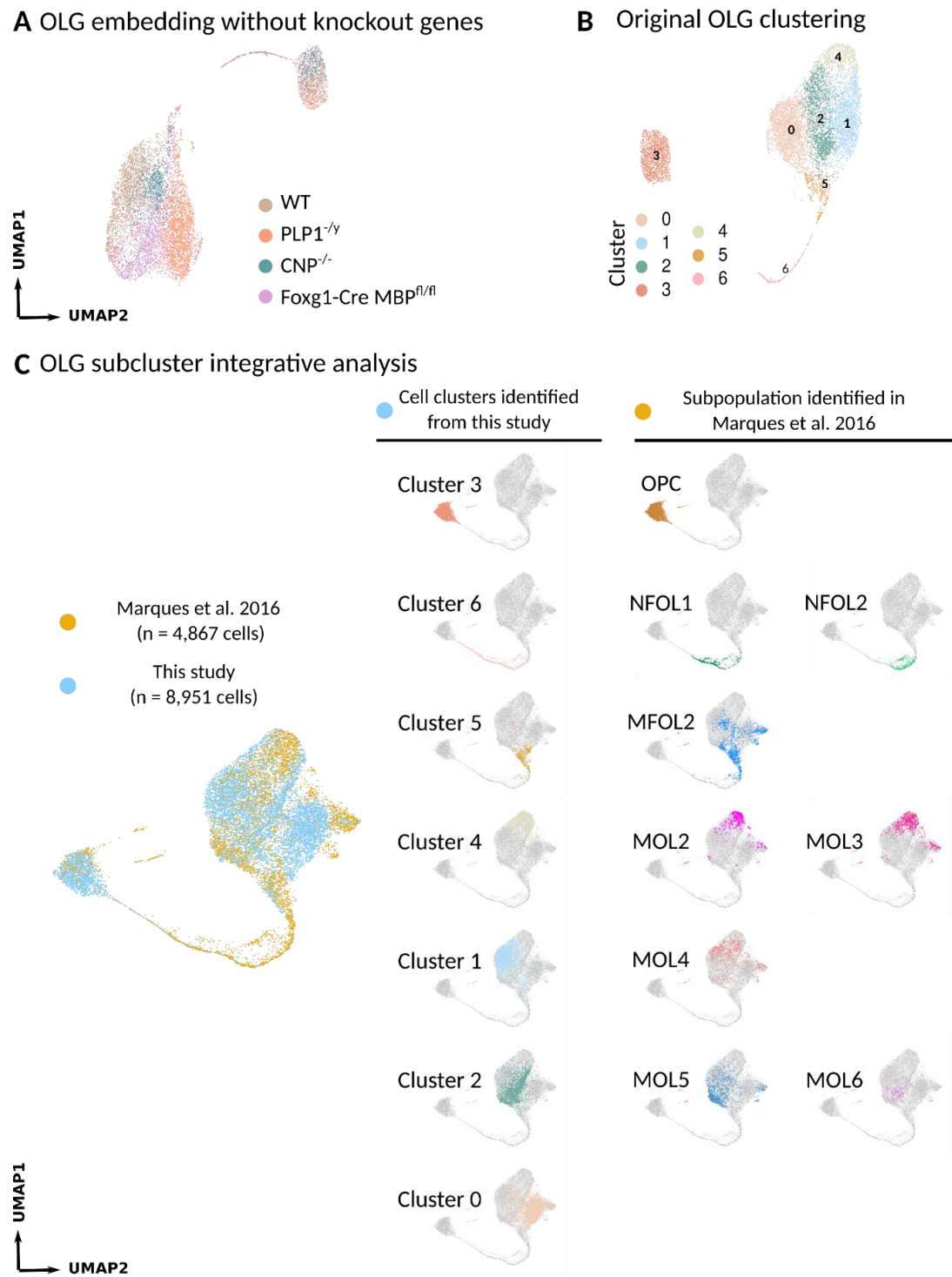
Author contributions

TS, CD, SB, and KAN designed the experiment. TS and CD conceptualized the study. TS designed and conducted snRNA-seq analysis pipelines. LS and AS contributed to animal organizations and tissue microdissection. AAS supported snRNA-seq analysis. SS and SG provided mice. HE provided conceptual input. DG and RK performed snRNA library construction and sequencing. TS and CD generated figures. TS, CD and KAN wrote the manuscript.

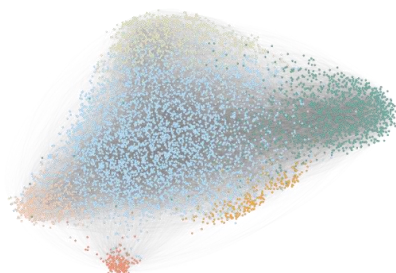
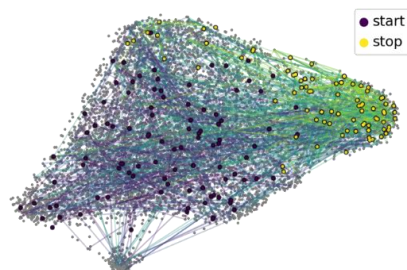
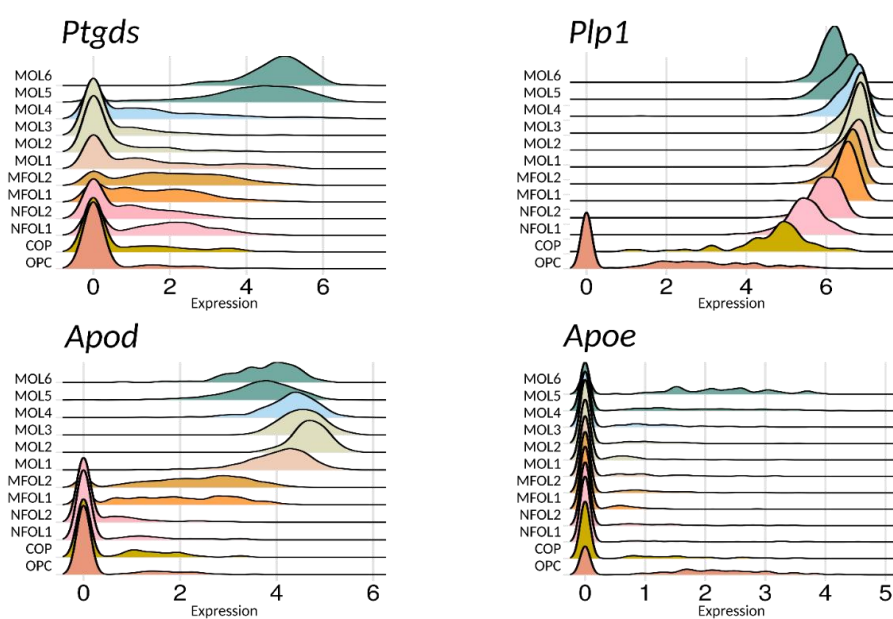
Correspondence

Correspondence and requests for materials, data, or code should be addressed to nave@em.mpg.de.

Supplementary Figure 1

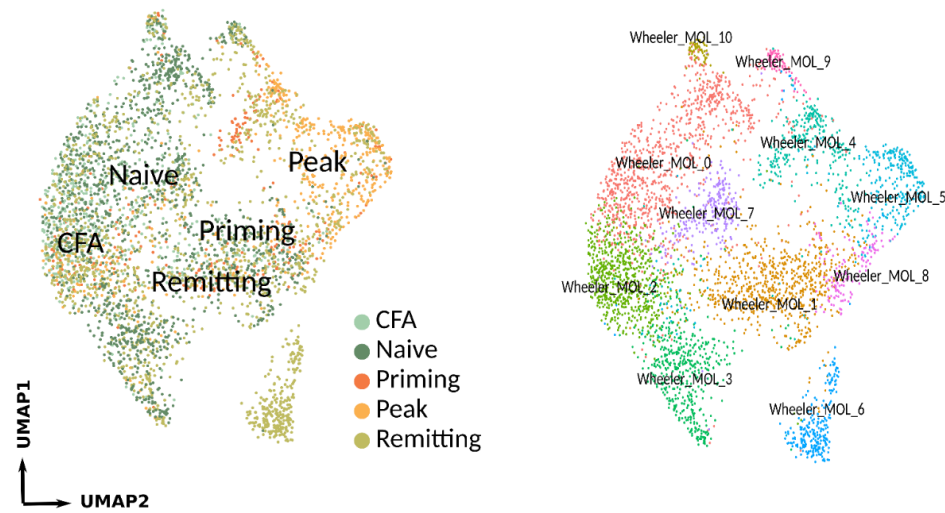


Supplementary Figure 2

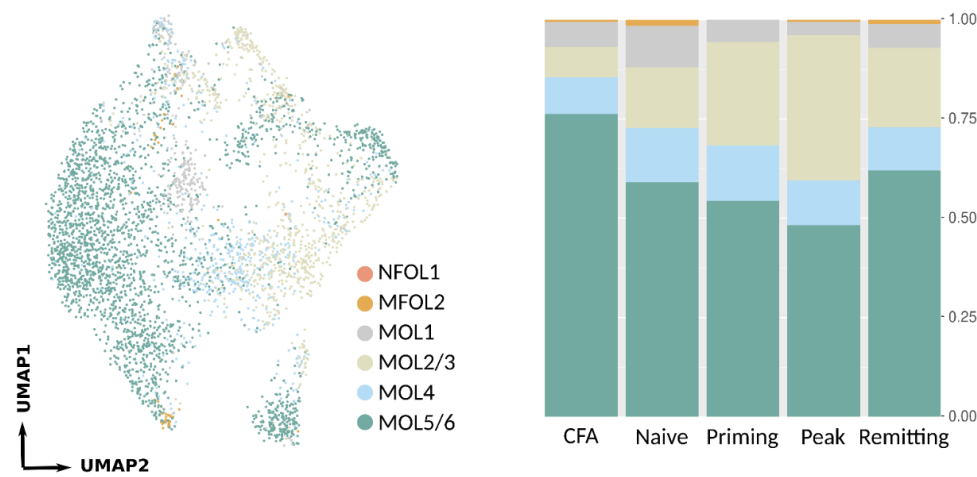
A Cell terminal clusters**B** Markov chain random walk**C** Marques et al. 2016 gene expression ridgeplots

Supplementary Figure 3

A MOL subset from Wheeler et al. 2020



B Wheeler et al. 2020 MOL subset annotation

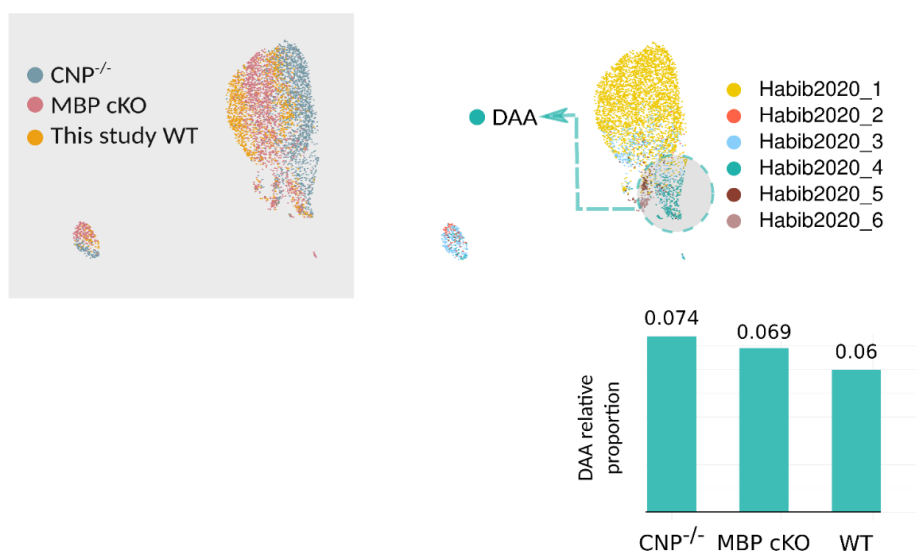


Supplementary Figure 4

A Astrocyte integrative analysis with Habib et al. 2020

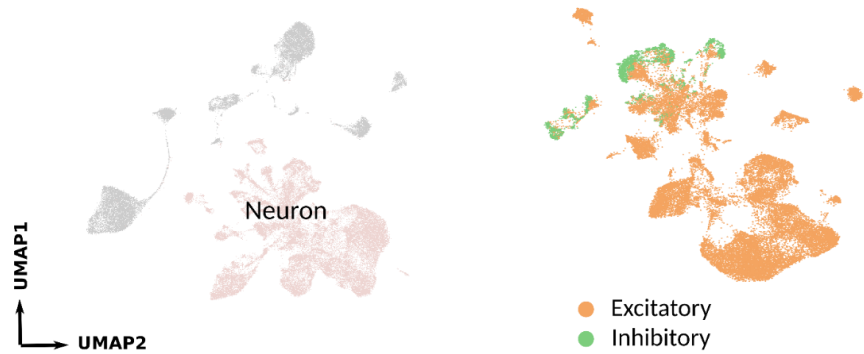


B Myelin mutant astrocyte DAA proportion

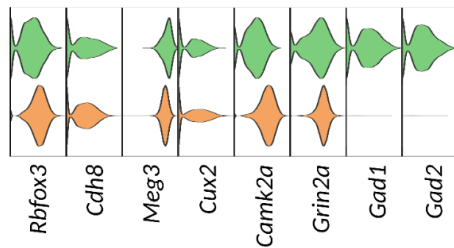


Supplementary Figure 5

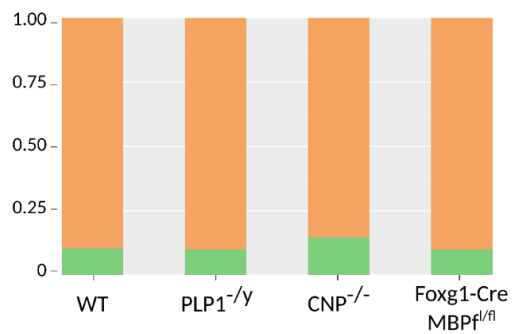
A Neuron subset analysis



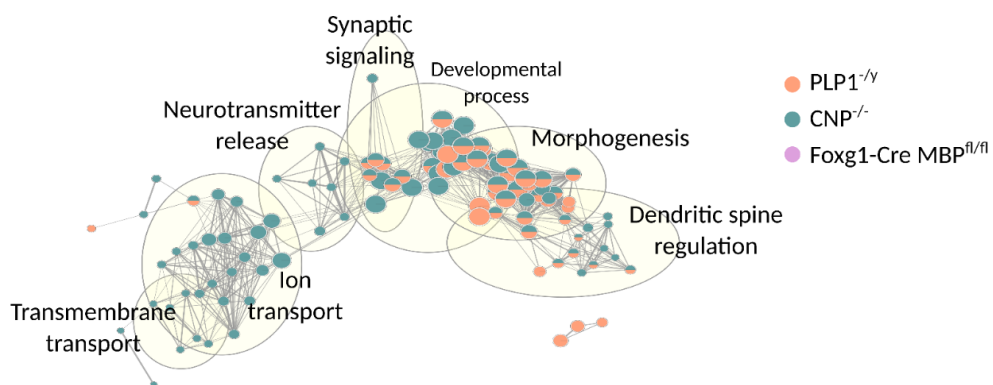
B Marker gene expression



C Relative proportions



D Inhibitory neuron DGE enriched GOBP terms



Supplementary Figure legends

Supplementary Figure 1. OLG subset validation analysis and subpopulation integrative annotation

A UMAP shows embedding of OLG cells after removal of *Cnp*, *Plp1* and *Mbp* expressions; spatial dislocations in MOL among different genotypes remains unchanged. **B** Original calculations of OLG clusters. **C** Integrative analysis of OLG cells from this study with Marques et al. 2016 dataset. In total 13,818 valid cell profiles were analyzed, and clusters detected in **B** were annotated to previously reported OLG subpopulations according to the colocalization of cells with the assistance of prediction scores.

Supplementary Figure 2. MOL RNA velocity structures and gene expression in Marques et al. 2016 OLG

A Terminal states calculation of MOLs was based on reclustering analysis on single-nuclei sliced RNA profile embedded UMAP. Structure plot shows clear separations between identified clusters that represent MOL subpopulations. **B** Plot shows 100 random walks on the Markov chain in UMAP embedding. **C** Ridgeplots show expression of *Ptgds*, *Plp1*, *Apod*, and *ApoE* over first reported OLG subpopulations from Marques et al 2016 dataset.

Supplementary Figure 3. Reanalysis of Wheeler et al. 2020 MOL subset

A MOLs from Wheeler et al. 2020 dataset (n = 4,225 cells) were extracted for subpopulation analysis. UMAPs show cells distributed unevenly according to their pathological stages (left) and can be clustered into 11 distinct subpopulations. **B** Subpopulations identified in **A** are annotated based on prediction scores when projecting to Marques et al. 2016 dataset (Supplementary Table.4). Barplot shows relative proportions of annotated cell subpopulations across disease stages.

Supplementary Figure 4. Astrocyte subset integrative analysis

A Astrocytes were subset and integrated with astrocyte profiles from Habib et al. 2020 dataset. Previous identified disease-associated astrocyte (DAA) showed in one concentrate cluster. Distribution of cells from each genotype is shown by highlighting UMAPs. **B** Astrocyte subset from this study is individually analyzed and embedded (left). Cell subtypes are annotated using prediction scores referring to Habib et al. 2020 astrocyte subpopulations. DAA is recognized in astrocytes from this study and highlighted in UMAP (middle). Relative proportion of DAA in each genotype is shown in barplot.

Supplementary Figure 5. Analysis for neuronal responses

A Left side UMAP shows highlighted neuron subset among all CNS cell types. Highlighted cells were subset and subjected to zoom-in analysis, where excitatory neurons and inhibitory neurons are recognized by marker gene expressions shown in **B** as a violin plot. **C** Barplot shows relative proportions of neuron subtypes across genotypes. **D** Network plot demonstrates GO (biological process) terms enriched by DGEs analysis in inhibitory neurons. DGE analysis was performed by comparing myelin mutant to WT.

Supplementary Table legends

Supplementary Table 1. snRNA-seq individual sample filter parameters

Supplementary Table 2. Clusters marker genes for all samples

Supplementary Table 3. Downsampling statistics results between myelin mutant and WT MOLs

Supplementary Table 4. GSE130119 MOL subpopulation projection analysis by referring Marque et al. dataset

Supplementary Table 5. DGE analysis for inhibitory neurons between myelin mutants and WT

Supplementary Table 6. GO biological process enrichment analysis of inhibitory neuron DEGs

Chapter 4: Project II

Ageing-associated myelin dysfunction drives amyloid deposition in mouse models of Alzheimer's disease

4.1 Overview of Project II

For a long time, AD research focused extensively on neuronal pathologies (Schirmer et al. 2019; Etle, Schlachetzki, and Winkler 2016; Onyango et al. 2021). In recent years, the role of glial cells in AD, especially microglia, has gathered increasing attention, which assisted the further understanding of disease mechanism, as well as proposed new potentials for therapeutic approaches (Keren-Shaul et al. 2017; Grubman et al. 2019; Zhou et al. 2020; Kleinberger et al. 2014; Habib et al. 2020). However, as a long-aware disease feature, myelin breakdown has always been considered a bystander in AD pathology (Bozzali et al. 2002; Jang et al. 2017). The concept of oligodendrocyte and myelin being more upstream drivers of AD pathology has only recently been more frequently discussed (George Bartzokis 2011; Braak and Del Tredici 2004; Etle, Schlachetzki, and Winkler 2016; G. Bartzokis 2004; Nasrabad et al. 2018). Lately, Chen et al. verified that the promotion of OPC differentiation and myelin renew was able to partially rescue the cognitive decline in AD mouse models (J.-F. Chen et al. 2021). Therefore, after the characterization of oligodendrocytes harboring myelin dysfunctions was incorporated in project I, a more specific but versatile question has been asked in project II: *How would such primarily induce oligodendrocytes and myelin dysfunctions influence AD pathology?*

To answer this question, mutant mouse models with chronically defective myelin (*Cnp*^{-/-} and *Plp1*^{-y}), acutely induced demyelination (EAE, cuprizone), or absence of forebrain myelin (*Emx-Cre Mbp*^{fl/fl}, *Foxg1-Cre Mbp*^{fl/fl}), were crossbred to mouse lines with AD backgrounds (5xFAD, APP^{NLGF}). Different from previous studies that focused on the promotion of myelin health, this project contributed more effort to the discussion of myelin dysfunction as an upstream parameter of AD disease onset and progression. As a result, A β deposits were significantly enhanced under early induced chronic or acute myelin deficiencies. Conversely, the absence of forebrain myelin considerably delayed the aggregation of A β plaques. These together, indicated primary dysfunctions of myelin can be a risk factor for AD. Considering previously characterized main pathological features in the *Cnp*^{-/-} and *Plp1*^{-y} mutants, enhanced axonal swelling, and reactive microgliosis, we hypothesized two underlying mechanisms of myelin dysfunctions promoting AD amyloidosis: Either increased metabolism of A β production at the axon swelling sites whereby

intracellular vesicles accumulate ,or by deriving malfunctioned microglia that can not sufficiently phagocytize A β peptides and plaques.

The validation of metabolism shifts of A β production in the AD mouse model with defective myelin was carried out by electronic microscopic (EM) imaging and biochemistry measurements. From which, vesicular structures were verified to be accumulated in *Cnp*^{-/-} axons by EM. More importantly, using antibodies that specifically target APP processing enzymes, as well as various sites of APP and A β peptides. We further revealed that the axonal swelling sites indeed hold an increased amount of β - and γ -secretase, cleaved APP fragments, and A β peptides, suggesting myelin dysfunction potentially promoted A β production and aggregation.

Microglia were known to play a central role in A β clearance (Ries and Sastre 2016). Previously, both *Cnp*^{-/-} and *Plp1*^{-/-} mutants were characterized with different levels of reactive microgliosis (Griffiths et al. 1998; Lappe-Siefke et al. 2003). These reactive microglia, however, are highly associated with myelin sheath and lose the corralling phenotype towards A β plaques when exposed to AD background, implying myelin deficiency possibly results in insufficient plaque detection and phagocytosis. Subsequently, we investigated corresponding microglia profile changes at the transcriptome level. Interestingly, instead of showing failure of cell activation, the microglia in *Cnp*^{-/-} are equipped with successfully activated RNA profiles that present upregulated DAM signature genes such as *Trem2*, *Spp1*, *Tyrobp* (Keren-Shaul et al. 2017). At the single-cell level, activated microglia in *Cnp*^{-/-} are identified in the same subpopulation cluster with AD-induced DAM (Zhou et al. 2020). On the other hand, these microglia also slightly differ from DAM by a comparably increased expression of lipid handling genes like *Apoe*, *Lpl*, and *Abca1*, which correlate with a recently reported microglia subtype, the white matter associated microglia (WAM), that is enriched in aged white matter (Safaiyan et al. 2021). According to previous studies, WAM and DAM are located at tightly connected cell stages. Yet, both cell subpopulations do not fully represent the state of myelin mutant microglia. In addition, it is also unclear whether the myelin distracted microglia could react to amyloid depositions once the myelin dysfunction is repaired.

In a nutshell, through stringent control of onset orders of myelin deficiency and AD pathology, project II revealed myelin dysfunctions as a potential upstream risk factor of AD. Mechanistically, abnormal myelin-induced axonal swellings potentially contributed to the promotion of A β production. At the same time, myelin debris can successfully activate microglia, although the reactive cells would rather engulf myelin and are distracted from A β plaques. Further investigations are still

required to understand the regulatory network that urged microglia to prioritize myelin instead of A β .

4.2 Original publication

Depp, C. *, Sun, T. *, Sasmita, A. O., Spieth, L., Berghoff, S. A., Steixner-Kumar, A. A., ... & Nave, K. (2021). Ageing-associated myelin dysfunction drives amyloid deposition in mouse models of Alzheimer's disease. *bioRxiv*.

Personal contribution to Project II

In this project, I contributed to the design and analysis of bulk and single-cell RNA sequencing experiments. Subsequently, I interpreted the sequencing analysis results, designed their visualizations, and summarized the corresponding parts in the manuscript text. Together with my colleague and my supervisor, we generated figures for the manuscript and edited the manuscript's text.

Ageing-associated myelin dysfunction drives amyloid deposition in mouse models of Alzheimer's disease

Constanze Depp^{1,2,3,4,5,6,7,8,9,10,11,12,13,14,15,16,17,18,19,20,21,22,23,24,25,26,27,28,29,30,31,32,33,34,35,36,37,38,39,40,41,42,43,44,45,46,47,48,49,50,51,52,53,54,55,56,57,58,59,60,61,62,63,64,65,66,67,68,69,70,71,72,73,74,75,76,77,78,79,80,81,82,83,84,85,86,87,88,89,90,91,92,93,94,95,96,97,98,99,100}, Ting Sun¹, Andrew Octavian Sasmita¹, Lena Spieth¹, Stefan A. Berghoff¹, Agnes A. Steixner-Kumar², Swati Subramanian¹, Wiebke Möbius^{1,3}, Sandra Göbbels¹, Gesine Saher¹, Silvia Zampar⁴, Oliver Wirths⁴, Maik Thalmann⁵, Takashi Saito^{6,7}, Takaomi Saito⁷, Dilja Krueger-Burg^{8,9}, Riki Kawaguchi⁹, Michael Willem¹⁰, Christian Haass¹⁰, Daniel Geschwind¹⁰, Hannelore Ehrenreich¹¹, Ruth Stassart^{11,1}, Klaus-Armin Nave^{12,13,14,15,16,17,18,19,20,21,22,23,24,25,26,27,28,29,30,31,32,33,34,35,36,37,38,39,40,41,42,43,44,45,46,47,48,49,50,51,52,53,54,55,56,57,58,59,60,61,62,63,64,65,66,67,68,69,70,71,72,73,74,75,76,77,78,79,80,81,82,83,84,85,86,87,88,89,90,91,92,93,94,95,96,97,98,99,100}

The prevalence of Alzheimer's disease (AD), the leading cause of dementia, shows a strict age-dependency, but why ageing constitutes the main risk factor for this disease is still poorly understood. Brain ageing affects oligodendrocytes¹ and the structural integrity of myelin sheaths², the latter associated with secondary neuroinflammation³. Since oligodendrocytes support axonal and neuronal health^{4,7}, we hypothesised that ageing-associated loss of myelin integrity could be an upstream risk factor for neuronal amyloid- β (A β) deposition, the primary neuropathological hallmark of AD. Here, we show that in AD mouse models different genetically induced defects of myelin integrity or demyelinating injuries are indeed potent drivers of amyloid deposition *in vivo*, quantified by whole brain light sheet microscopy. Conversely, the lack of myelin in the forebrain provides protection against plaque deposition. Mechanistically, we find that myelin dysfunction causes the accumulation of the A β producing machinery within axonal swellings and increases cortical amyloid precursor protein (APP) cleavage. Surprisingly, AD mice with dysfunctional myelin lack plaque-corralling microglia but show a disease-associated microglia (DAM)-like signature as revealed by bulk and single cell transcriptomics. These activated microglia, however, are primarily engaged with myelin, preventing the protective reactions of microglia to A β plaques. Our data suggest a working model, in which age-dependent structural defects of myelin promote plaque formation, directly and indirectly, and are thus an upstream AD risk factor. Improving oligodendrocyte health and myelin integrity could be a promising target to delay AD.

Main text

The pathology of AD is characterised by the deposition of A β plaques and neurofibrillary tangles primarily in cortex and hippocampus⁸. According to the 'amyloid hypothesis' of AD, the build-up of A β initiates a cascade of harmful events that lead to neuronal dysfunction⁹. More than lifestyle choices and genetic predisposition, old age is the primary risk factor for AD development, but exactly how brain ageing is linked to amyloid deposition is unclear¹⁰. Myelin, a spirally wrapped and compacted glial membrane, enhances axonal conduction speed¹¹ and its non-compacted regions allow oligodendrocytes to provide metabolic support to the neuronal compartment^{6,12}. The unique cellular architecture of myelin makes protein and lipid turnover challenging and slow¹³⁻¹⁵. This, together with the long lifetime of oligodendrocytes¹⁶ and age-dependent loss of epigenetic marks, might explain the structural deterioration of myelin with age². We speculated that the breakdown of myelin integrity in the ageing brain acts as driving force for A β deposition and tested this hypothesis in mouse models of amyloidosis, in which we introduced myelin dysfunction of various degrees by genetic and pharmacological manipulations.

Intracortical myelin decline in AD patients and mouse models

Macroscopic brain imaging studies have suggested that cortical myelin damage occurs in the preclinical phase of AD, i.e., prior to extensive amyloid deposition^{17,21}. Microscopic evidence of this, however, remains scarce. We therefore first studied intracortical myelin integrity in a small cohort of AD patients, focussing on the trans-entorhinal area by immunofluorescence analysis of myelin (Fig. 1a). We observed a striking decline of intracortical myelin density in autopsies from AD patients which were not limited to the immediate vicinity of plaques. Sites of myelin loss were also associated with increased numbers of Iba1⁺ microglia. Since human neuropathological correlations cannot distinguish between myelin loss being the cause or consequence of neuronal AD pathology such as axonal decay, we turned to two different experimental animal models of AD (5xFAD, APP^{NL-GF}). Here, we are in a position to ask whether loss of myelin can act as an upstream driver of amyloidosis

by combining AD mouse models with mice developing subtle genetically-induced myelin disintegration (Fig. 1b). Specifically, we employed null mutants of the myelin architectural proteins CNP and PLP1, that display rather minor structural myelin defects. Lack of CNP causes a collapse of cytosolic channels within the myelin sheath²² associated with axonal swellings²³. PLP1-deficient myelin lacks physical stability²⁴, reduces axonal energy metabolism²⁵ and causes axonopathy at higher age⁴. We first compared normal brain ageing of c57Bl6 wildtype mice with that of *Cnp* and *Plp1* null mutants on the same background. By immunostaining, *Cnp* and *Plp1* mice showed gliosis in grey and white matter at 6 months, qualitatively similar to aged wildtype mice (24-month-old), but more profound (Fig. 1c). Similar to AD patients, aged wildtype mice and more pronounced 6-month-old myelin mutants displayed significant reductions of intracortical myelin content, especially in the upper cortical layers (Fig. 1c).

Myelin dysfunction drives amyloid deposition in AD mouse models

To determine whether such ageing-associated myelin defects can drive amyloid deposition, we crossbred *Cnp*^{-/-} and *Plp1*^{-/-} mutants with commonly used mouse models of AD and analysed plaque burden in the resulting offspring (Fig. 1b). For this, we optimised a Congo Red *in toto* plaque staining and clearing protocol based on the iDISCO technique^{26,27} for light sheet microscopy (Fig. 1b, Extended data Fig. 1) to determine the amyloid plaque load of the entire brain in an unbiased fashion. Indeed, when compared to 5xFAD mice, both *Cnp*^{-/-} 5xFAD and *Plp1*^{-/-} 5xFAD double mutants showed striking increases of amyloid plaque load, as quantified in hippocampal white matter (alveus) and cortex at 6 months (Fig. 2a, b). In both models, the effects were expectedly strongest in the alveus, where A β was deposited in very small aggregates, indicating an increased formation of amyloid seeds. To exclude that these effects are specific to the 5xFAD model and APP overexpression, we validated our findings in crossbreedings of *Cnp*^{-/-} and the *App*^{PS2} knock-in model, in which the humanised triple-mutant APP is expressed under control of the endogenous *App* locus (Extended

¹Department of Neurogenetics, Max Planck Institute of Experimental Medicine, Göttingen, Germany ²Clinical Neuroscience, Max Planck Institute of Experimental Medicine, Göttingen, Germany ³Electron Microscopy Core Unit, Max Planck Institute of Experimental Medicine, Göttingen, Germany ⁴Department of Psychiatry and Psychotherapy, University Medical Center, Georg-August-University, Göttingen, Germany ⁵Georg-August-Universität Göttingen, Department of German Philology, Göttingen, Germany ⁶Department of Neurocognitive Science, Institute of Brain Science, Nagoya City University Graduate School of Medical Sciences, Nagoya, Aichi, Japan ⁷Laboratory for Proteolytic Neuroscience, RIKEN Center for Brain Science, Wako-shi, Saitama, Japan ⁸Department of Molecular Neurobiology, Max Planck Institute of Experimental Medicine, Göttingen, Germany ⁹Program in Neurogenetics, Department of Neurology, David Geffen School of Medicine, University of California Los Angeles, Los Angeles, CA, USA ¹⁰Chair of Metabolic Biochemistry, Biomedical Center (BMC), Faculty of Medicine, Ludwig-Maximilians-Universität München; Munich Cluster for Systems Neurology (SyNergy); German Center for Neurodegenerative Diseases, Munich, Germany ¹¹Paul-Flechsig-Institute of Neuropathology, University Clinic Leipzig, Leipzig, Germany ¹²shared first authorship ¹³corresponding email: depp@em.mpg.de, nave@em.mpg.de

data Fig.2). In both AD models, the increase in plaque load was observed at 6 months, but not yet at 3 months when myelin defects and reactive gliosis are only subtle in *Cnp^{-/-}* and *Pip1^{-/-}* mice (Extended data Fig.3a,b). We also investigated whether myelin dysfunction modifies 5xFAD behavioural deficits by performing behavioural testing in the Y-maze (YM) and the elevated plus maze (EPM) (Extended data Fig.4). In both paradigms, double mutant mice presented with hyperactivity that was less pronounced in single mutants. In the EPM, *Cnp^{-/-} 5xFAD* mice preferred the open arms, indicative of an abnormal lack of anxiety. Statistical analysis confirmed supra-additive effects (interactions) of 5xFAD and myelin mutant genotypes in many instances, also detectable in the hindlimb clasping test (Extended data Fig.4c,d). Myelin defects and amyloid pathology appear to synergistically worsen behavioural deficits indicative of disinhibition – a neuropsychiatric symptom also present in AD patients^{28,29}.

Acute demyelination drives amyloid deposition

To confirm that myelin dysfunction is an upstream driver of plaque pathology, we tested the effect of acute demyelination. Young adult 5xFAD mice were fed a cuprizone containing diet for 4 weeks, followed by a 4-week recovery period and the determination of plaque load via light sheet microscopy (Fig.2c). Interpreting this experiment is complicated, however, because the copper-chelating properties of cuprizone interfere with plaque core formation, which is copper-dependent³⁰. Indeed, in *in toto* light sheet microscopy cuprizone treatment seemingly ameliorated hippocampal and cortical A β pathology (Extended data Fig.3c). However, the amyloidosis-driving effect of demyelination prevailed over the inhibition by copper-chelation in most markedly demyelinated areas such as the hippocampal alveus. Here, less-compacted A β plaques in cuprizone treated 5xFAD could be well stained with anti-A β antibodies revealing a strong increase in small amyloid aggregates (Fig.2c).

Independent support of our working model was provided by AD mice challenged with experimental autoimmune encephalomyelitis (EAE). We immunised young 5xFAD animals with MOG peptide and analysed their brains and spinal cord 4 weeks later (Fig.2d). Unlike an earlier study with aged J20 and Tg2576 AD mice in which EAE reportedly reduced plaque load³¹, we found no such difference in amyloid deposition in younger 5xFAD-EAE mice (Extended data Fig.3d,e). However, in the spinal cord, where demyelinating EAE pathology massively unfolds, we identified small, atypical amyloid aggregates in the peri-lesion environment, which were absent from control 5xFAD mice (Fig.2d). We verified the presence of aggregated amyloid by staining spinal cord sections with the β -sheet dye Methoxy-04 (Me-04). Of note, in EAE spinal cord from wildtype animals, no such Me-04⁺ positive material was found, ruling out the non-specific detection of lipid deposits in demyelinated lesions (Fig.2d). Taken together, myelin defects – both chronic and acute – drive amyloid deposition in AD mouse models, which identifies dysfunctional myelin as an upstream risk factor for amyloid deposition.

Lack of myelin ameliorates amyloidosis in AD mouse models

Primate brains have more CNS myelin than smaller mammals³² and, compared to other apes, humans show a disproportional enlargement of prefrontal white matter³³. This raises the question whether the extent of cortical myelination *per se* could play a causal role in human AD. We, therefore, next asked the opposite question: what impact does the near complete absence of cortical myelin have on the course of amyloidosis in 5xFAD mice? To this end, we generated a line of forebrain-specific *shiverer* mice (*Emx-Cre Mbp^{fl/fl}*), in which cortical axons are largely unmyelinated, and crossed them to 5xFAD mice (Extended data Fig.5a). At 3 months of age, forebrain *shiverer* 5xFAD mice were strongly protected against amyloid deposition, both in hippocampus and cortex (Fig.2e). However, at 6 months this effect was largely lost, revealing a delay of plaque formation in the absence of myelin (Extended data Fig.5b). We conclude that myelin ensheathment and even more so

defective myelin is an upstream driving force of neuronal plaque deposition.

Myelin dysfunction shifts neuronal APP metabolism

How do myelin defects mechanistically drive amyloidosis? In theory, they could either promote APP processing and A β generation or interfere with A β removal (or a combination of both). We first investigated APP metabolism in *Cnp^{-/-} 5xFAD* mice. Axonal swellings that stain positive for APP are prominent features of ischemia, injury and myelin disorders and we speculated that these swellings contribute to the generation of A β in myelin mutant animals. Indeed, stalling axonal transport was shown to enhance amyloid production likely by increasing BACE1 and APP encounter in axonally transported vesicles³⁴⁻³⁷ and axons seem to be important sites of amyloid secretion³⁸⁻⁴⁰. Moreover, axonal swellings surrounding amyloid plaques (Fig.3a) are thought to be production sites of A β ^{41,42}. Plaque-independent axonal swellings in *Cnp^{-/-}* mice are enriched in vesicular structures likely of endosomal/lysosomal origin (Fig.3b). Using antibodies against APP processing enzymes and multiple APP/A β -specific antibodies (Fig.3a), we found that axonal swellings in *Cnp^{-/-} 5xFAD* brains accumulate β - and γ -secretase and consequently stain positive for β - and γ -cleaved APP fragments and A β (Fig.3c,d). We validated these findings by Western blot analysis of white matter and cortex and found elevated levels of BACE1 (statistically significant in white matter) (Fig.3e) in 6-month-old *Cnp^{-/-} 5xFAD*. When we investigated APP processing by immunoblotting, cortical APP metabolism was shifted towards an increased abundance of CTF- β and CTF- α fragments, but without changes to full length APP abundance or the α/β CTF ratio (Fig.3f). Together, these findings suggest that myelin defects enhance A β generation.

Myelin defects alter the microglial phenotype in AD mouse models

Glial cells play important roles in the clearance of myelin debris and amyloid peptides and microglia form barriers around amyloid plaques⁴³. Thus, we investigated how microglia react to amyloid plaques when additionally challenged with defective myelin. Despite pronounced gliosis throughout the brain in both *Cnp^{-/-} 5xFAD* and *Cnp^{-/-} APP^{K67}* mice, we noticed that cortical microglia failed to cluster around amyloid plaques (Fig.4a,b). Such a phenotype has been previously described in *Trem2* loss of function scenarios^{43,45}. We therefore asked if myelin dysfunction interferes with the upregulation of *Trem2* and the induction of the disease-associated microglia (DAM) signature, that is associated with a plaque corralling phenotype^{46,47}. Using magnetic activated cell sorting (MACS)-isolation of microglia and RNA sequencing (Fig.4c), principal component analysis (PCA) revealed that the transcriptome of *Cnp^{-/-} 5xFAD* microglia was dominated by the *Cnp^{-/-}* signature (Fig.4d). Extraction of the top 100 genes contributing to PC1 revealed 4 major gene clusters with different trajectories throughout the experimental groups (Fig.4e, Extended data Fig.6a). Homeostasis markers (*Cx3cr1*, *P2ry12*, *Tmem119*) that were downregulated in 5xFAD microglia were even further downregulated in *Cnp^{-/-}* and *Cnp^{-/-} 5xFAD* mice (Fig.4e,f). Conversely, DAM signature genes (*Clec7a*, *Gpnmb*, *Apoe*, *Spp1*, *Axl* and *Itgax*) were upregulated in 5xFAD microglia, and even further increased in *Cnp^{-/-}* and *Cnp^{-/-} 5xFAD* microglia (Fig.4e,f, Extended data Fig.6c) likely increased fraction of reactive microglia in the *Cnp^{-/-}* brain. Importantly, *Trem2* and *Tyrbp* showed an unaltered induction in *Cnp^{-/-} 5xFAD* mice (Fig.4e,f). We noticed that *Apoe*, a well-known factor in A β aggregation⁴⁸, was massively upregulated in *Cnp^{-/-}* and *Cnp^{-/-} 5xFAD* which is likely to lead to elevated APOE protein levels in the brain parenchyma of these mice. Indeed, using immunostainings, we found elevated levels of APOE in white matter and amyloid plaques in *Cnp^{-/-} 5xFAD* (Fig.4g).

The interpretation of bulk RNA-seq data is limited. To better understand the DAM-like microglial signature in *Cnp^{-/-}* mutants, we performed single nuclei RNA-sequencing (snRNA-seq) on cortical and callosal tissue from *Cnp^{-/-}* and wildtype mice (Fig.5a, Extended data Fig.7a,b). Cluster analysis identified 4 major microglia subpopulations, including one with high expression of DAM marker

genes (*Trem2*, *Lpl* and *Spp1*), which was only seen in *Cnp^{-/-}* mice (Fig.5b,c,d, Extended data Fig.7d). We next assessed similarities between this *Cnp^{-/-}*-associated DAM cluster and 5xFAD-associated DAM by integrating our dataset with the microglial snRNA-seq profile of Zhou et al⁴⁴ (Fig.5e). Indeed, *Cnp^{-/-}* DAM clustered with 5xFAD DAM (Fig.5e). Average expression analysis at the single cell level revealed that most DAM marker genes (including *ApoE*, *Lyz2* and *Axl*) were expressed at a similar level (Fig.5f). However, some genes (including *Ms4a7*, *Gpnmb* and *Lpl*) were highly induced in *Cnp^{-/-}* DAM, but only moderately so in 5xFAD DAM (Fig.5f). Importantly, *Trem2* was robustly upregulated in 5xFAD and to a lesser extent in *Cnp^{-/-}* DAM, suggesting that Aβ pathology is a stronger inducer of TREM2/TYROBP signalling (Fig.5f). We noted that genes of the *Ms4a* family were highly induced in microglia of *Cnp^{-/-}* 5xFAD mice, which is also a feature of some microglia in early development⁴⁰. The same *Ms4a* genes regulate the level of soluble TREM2 and modify AD risk⁵⁰. However, immunoblot analysis ruled out that myelin dysfunction affects TREM2 protein simply via increased *Ms4a* expression (Extended data Fig.8). In summary, our transcriptomic data suggest that microglia challenged by myelin dysfunction are still genetically equipped to react to amyloid plaques, but surprisingly fail to do so *in vivo*. We thus propose that microglia, once engaged in the clearance of defective myelin, are distracted from amyloid plaques. Indeed, *Cnp^{-/-}* microglia strongly express genes involved in phagocytosis (*Ctla4*, *C3*, *Itgax*), lysosomal function (*Spp1*, *Gpnmb*, *Lyz2*, *Pld3*, *Rab7b*) and lipid handling (*ApoE*, *Lpl*, *Lpl*, *Msr1*, *Apoc1*, *Apobec1*, *Abca1*) (Fig.4e,5f, Extended Data Fig.6c). Moreover, in *Cnp* mutants we validated by immunolabelling and the colocalization of PLP and IBA1 that microglia actively engulf myelin membranes (Fig.5g). Likewise, our snRNA-seq analysis identified a subpopulation of microglia that showed high level of "myelin RNA" (*Mobp*, *Plp1*, *Mbp*, *Mog* transcripts), which was further increased in *Cnp^{-/-}* microglia (Fig.5c,d, Extended data Fig.7c). This cell cluster likely represents microglia that had phagocytosed myelin (including oligodendroglial mRNA), as recently reported for snRNA-seq of multiple sclerosis autopsies⁵¹. We surmise that such microglial distraction not only leads to a faster build-up of amyloid in the brain, but that factors secreted by activated yet myelin-engaged microglia (such as APOE) may further fuel plaque seeding.

Ageing myelin is a risk factor for AD

Based on our findings, we propose a resulting working model for AD, in which myelin of the ageing forebrain well known to lose structural integrity² causes microglia to become engaged (as modelled in myelin mutant mice). This microglial activity interferes with the

ability to clear Aβ deposits and prevent plaque formation (Fig.5h). Simultaneously, ageing myelin loses its axon-supportive functions, which increases neuronal BACE1 and APP-CTF levels suggestive of enhanced Aβ production (Fig.5h). It is tempting to speculate that other well-known AD risk factors such as traumatic brain injury or cardiovascular diseases convey risk via negatively impacting myelin health or at least through similar mechanism i.e. microglia 'distraction'.

A critical role of myelin deterioration in the progression of AD has been previously hypothesised in light of correlative macroscopic brain imaging studies⁵², but necessarily lacked any evidence of causality. Our experimental findings in genetic models of AD can provide such a causal link with a molecular underpinning, and are fully in line with the prevailing amyloid hypothesis⁹ and the emerging role of neuroinflammation in disease progression⁵³. Moreover, we can position the well-documented loss of myelin integrity in the ageing primate brain as the most upstream initiator of AD pathology, which helps to explain why age is the major AD risk factor. Our working model is further supported by classical neuropathological observations by Braak & Braak⁵⁴ who pointed out the conspicuous temporal relationship with CNS myelination, which occurs the latest in those brain regions that are the first to develop AD pathology. Mechanistically, cortical ensheathment by oligodendrocytes is thin and may lack the robust myelinic channel architecture found in subcortical tracts that appear resistant to AD pathology and may overcome the axon shielding effects of myelin by providing glial metabolic support.

Only few studies have experimentally investigated oligodendrocytes and myelin in AD⁵⁵⁻⁶⁰. Nearly all have focussed on the effect of amyloid plaques and Aβ on oligodendrocytes and myelin, i.e., revealing secondary de- and hypomyelination. Similarly, scRNA-seq studies using human AD autopsy samples have identified myelin-related transcripts among the top altered clusters in AD patients^{46,61}. These findings are likely the downstream effects of overt Aβ and tau pathology on oligodendrocytes and their precursor cells in the latest stages of disease. Our discovery that age-dependent loss of myelin integrity can be a driver or risk factor of amyloid deposition not only changes our view on the role of oligodendrocytes in AD, together with the downstream effects of Aβ pathology causing demyelination, this closes a "vicious cycle" in the AD brain that may explain why a long prodromal phase is followed by a more rapid clinical progression. If further corroborated in humans, promoting myelin health should be considered as a target for the delay or prevention of AD.

References

- Shen, S., Liu, A., Li, J., Wolubah, C. & Casaccia-Bonnel, P. Epigenetic memory loss in aging oligodendrocytes in the corpus callosum. *Neurobiology of aging* **29**, 452-463 (2008).
- Bowley, M. P., Cabral, H., Rosene, D. L. & Peters, A. Age changes in myelinated nerve fibers of the cingulate bundle and corpus callosum in the rhesus monkey. *Journal of Comparative Neurology* **518**, 3046-3064 (2010).
- Safaiyan, S. et al. Age-related myelin degradation burdens the clearance function of microglia during aging. *Nature neuroscience* **19**, 995-998 (2016).
- Griffiths, I. et al. Axonal swellings and degeneration in mice lacking the major proteolipid of myelin. *Science* **280**, 1610-1613 (1998).
- Fünfschilling, U. et al. Glycolytic oligodendrocytes maintain myelin and long-term axonal integrity. *Nature* **485**, 517-521 (2012).
- Lee, Y. et al. Oligodendroglia metabolically support axons and contribute to neurodegeneration. *Nature* **487**, 443-448 (2012).
- Mukherjee, C. et al. Oligodendrocytes provide antioxidant defense function for neurons by secreting ferritin heavy chain. *Cell Metabolism* **32**, 259-272. e210 (2020).
- Braak, H. & Braak, E. Neuropathological staging of Alzheimer-related changes. *Acta neuropathologica* **82**, 239-259 (1991).
- Hardy, J. A. & Higgins, G. A. Alzheimer's disease: the amyloid cascade hypothesis. *Science* **256**, 184-186 (1992).
- Hou, Y. et al. Ageing as a risk factor for neurodegenerative disease. *Nature Reviews Neurology* **15**, 565-581 (2019).
- Cohen, C. C. et al. Saltatory conduction along myelinated axons involves a periaxonal nanocircuit. *Cell* **180**, 311-322. e315 (2020).
- Saab, A. S. et al. Oligodendroglial NMDA receptors regulate glucose import and axonal energy metabolism. *Neuron* **91**, 119-132 (2016).
- Toyama, B. H. et al. Identification of long-lived proteins reveals exceptional stability of essential cellular structures. *Cell* **154**, 971-982 (2013).
- Ando, S., Tanaka, Y., Toyoda, Y. & Kon, K. Turnover of myelin lipids in aging brain. *Neurochemical research* **28**, 5-13 (2003).
- Lüders, K. A. et al. Maintenance of high proteolipid protein level in adult central nervous system myelin is required to preserve the integrity of myelin and axons. *Glia* **67**, 634-649 (2019).
- Yeung, M. S. et al. Dynamics of oligodendrocyte generation and myelination in the human brain. *Cell* **159**, 766-774 (2014).
- Ringman, J. M. et al. Diffusion tensor imaging in preclinical and presymptomatic carriers of familial Alzheimer's disease mutations. *Brain* **130**, 1767-1776 (2007).
- Stricker, N. H. et al. Decreased white matter integrity in late-myelinating fiber pathways in Alzheimer's disease supports retrogenesis. *Neuroimage* **45**, 10-16 (2009).
- Dean, D. C. et al. Association of amyloid pathology with myelin alteration in preclinical Alzheimer disease. *JAMA neurology* **74**, 41-49 (2017).

- 20 Wang, Q. *et al.* Quantification of white matter cellularity and damage in preclinical and early symptomatic Alzheimer's disease. *NeuroImage: Clinical* **22**, 101767 (2019).
- 21 Araque Caballero, M. Á. *et al.* White matter diffusion alterations precede symptom onset in autosomal dominant Alzheimer's disease. *Brain* **141**, 3065-3080 (2018).
- 22 Snaidero, N. *et al.* Antagonistic functions of MBP and CNP establish cytosolic channels in CNS myelin. *Cell reports* **18**, 314-323 (2017).
- 23 Lappe-Siefke, C. *et al.* Disruption of Cnp1 uncouples oligodendroglial functions in axonal support and myelination. *Nature genetics* **33**, 366-374 (2003).
- 24 Klugmann, M. *et al.* Assembly of CNS myelin in the absence of proteolipid protein. *Neuron* **18**, 59-70 (1997).
- 25 Trevisiol, A. *et al.* Structural myelin defects are associated with low axonal ATP levels but rapid recovery from energy deprivation in a mouse model of spastic paraplegia. *PLoS biology* **18**, e3000943 (2020).
- 26 Renier, N. *et al.* iDISCO: a simple, rapid method to immunolabel large tissue samples for volume imaging. *Cell* **159**, 896-910 (2014).
- 27 Liebmann, T. *et al.* Three-dimensional study of Alzheimer's disease hallmarks using the iDISCO clearing method. *Cell reports* **16**, 1138-1152 (2016).
- 28 Keszyci, R. M., Fisher, D. W. & Dong, H. The hyperactivity-impulsivity-irritability-disinhibition-aggression-agitation domain in Alzheimer's disease: current management and future directions. *Frontiers in pharmacology* **10**, 1109 (2019).
- 29 Chung, J. A. & Cummings, J. L. Neurobehavioral and neuropsychiatric symptoms in Alzheimer's disease: characteristics and treatment. *Neurologic clinics* **18**, 829-846 (2000).
- 30 Cherny, R. A. *et al.* Treatment with a copper-zinc chelator markedly and rapidly inhibits β -amyloid accumulation in Alzheimer's disease transgenic mice. *Neuron* **30**, 665-676 (2001).
- 31 Frenkel, D., Maron, R., Burt, D. S. & Weiner, H. L. Nasal vaccination with a proteosome-based adjuvant and glatiramer acetate clears β -amyloid in a mouse model of Alzheimer disease. *The Journal of clinical investigation* **115**, 2423-2433 (2005).
- 32 Herculano-Houzel, S., Manger, P. R. & Kaas, J. H. Brain scaling in mammalian evolution as a consequence of concerted and mosaic changes in numbers of neurons and average neuronal cell size. *Frontiers in neuroanatomy* **8**, 77 (2014).
- 33 Schoenemann, P. T., Sheehan, M. J. & Glotzer, L. D. Prefrontal white matter volume is disproportionately larger in humans than in other primates. *Nature neuroscience* **8**, 242-252 (2005).
- 34 Stokin, G. B. *et al.* Axonopathy and transport deficits early in the pathogenesis of Alzheimer's disease. *Science* **307**, 1282-1288 (2005).
- 35 Gowrishankar, S., Wu, Y. & Ferguson, S. M. Impaired JIP3-dependent axonal lysosome transport promotes amyloid plaque pathology. *Journal of Cell Biology* **216**, 3291-3305 (2017).
- 36 Vagnoni, A. *et al.* Calsynenin-1 mediates axonal transport of the amyloid precursor protein and regulates A β production. *Human molecular genetics* **21**, 2845-2854 (2012).
- 37 Ye, X. & Cai, Q. Snapin-mediated BACE1 retrograde transport is essential for its degradation in lysosomes and regulation of APP processing in neurons. *Cell reports* **6**, 24-31 (2014).
- 38 Niederst, E. D., Reyna, S. M. & Goldstein, L. S. Axonal amyloid precursor protein and its fragments undergo somatodendritic endocytosis and processing. *Molecular biology of the cell* **26**, 205-217 (2015).
- 39 Buxbaum, J. D. *et al.* Alzheimer amyloid protein precursor in the rat hippocampus: transport and processing through the perforant path. *Journal of Neuroscience* **18**, 9629-9637 (1998).
- 40 Lazarov, O., Lee, M., Peterson, D. A. & Sisodia, S. S. Evidence that synaptically released β -amyloid accumulates as extracellular deposits in the hippocampus of transgenic mice. *Journal of Neuroscience* **22**, 9785-9793 (2002).
- 41 Gowrishankar, S. *et al.* Massive accumulation of luminal protease-deficient axonal lysosomes at Alzheimer's disease amyloid plaques. *Proceedings of the National Academy of Sciences* **112**, E3699-E3708 (2015).
- 42 Sadleir, K. R. *et al.* Presynaptic dystrophic neurites surrounding amyloid plaques are sites of microtubule disruption, BACE1 elevation, and increased A β generation in Alzheimer's disease. *Acta neuropathologica* **132**, 235-256 (2016).
- 43 Yuan, P. *et al.* TREM2 haploinsufficiency in mice and humans impairs the microglia barrier function leading to decreased amyloid compaction and severe axonal dystrophy. *Neuron* **90**, 724-739 (2016).
- 44 Zhou, Y. *et al.* Human and mouse single-nucleus transcriptomics reveal TREM2-dependent and TREM2-independent cellular responses in Alzheimer's disease. *Nature medicine* **26**, 131-142 (2020).
- 45 Parhizkar, S. *et al.* Loss of TREM2 function increases amyloid seeding but reduces plaque-associated ApoE. *Nature neuroscience* **22**, 191-204 (2019).
- 46 Keren-Shaul, H. *et al.* A unique microglia type associated with restricting development of Alzheimer's disease. *Cell* **169**, 1276-1290. e1217 (2017).
- 47 Krasemann, S. *et al.* The TREM2-APOE pathway drives the transcriptional phenotype of dysfunctional microglia in neurodegenerative diseases. *Immunity* **47**, 566-581. e569 (2017).
- 48 Huynh, T.-P. V., Davis, A. A., Ulrich, J. D. & Holtzman, D. M. Apolipoprotein E and Alzheimer's disease: the influence of apolipoprotein E on amyloid- β and other amyloidogenic proteins: Thematic Review Series: ApoE and Lipid Homeostasis in Alzheimer's Disease. *Journal of lipid research* **58**, 824-836 (2017).
- 49 Hammond, T. R. *et al.* Single-cell RNA sequencing of microglia throughout the mouse lifespan and in the injured brain reveals complex cell-state changes. *Immunity* **50**, 253-271. e256 (2019).
- 50 Deming, Y. *et al.* The MS4A gene cluster is a key modulator of soluble TREM2 and Alzheimer's disease risk. *Science translational medicine* **11** (2019).
- 51 Schirmer, L. *et al.* Neuronal vulnerability and multilineage diversity in multiple sclerosis. *Nature* **573**, 75-82 (2019).
- 52 Bartzokis, G. Age-related myelin breakdown: a developmental model of cognitive decline and Alzheimer's disease. *Neurobiology of aging* **25**, 5-18 (2004).
- 53 Heneka, M. T. *et al.* Neuroinflammation in Alzheimer's disease. *The Lancet Neurology* **14**, 388-405 (2015).
- 54 Braak, H. & Braak, E. Development of Alzheimer-related neurofibrillary changes in the neocortex inversely recapitulates cortical myelogenesis. *Acta neuropathologica* **92**, 197-201 (1996).
- 55 C. Schmued, L., Raymick, J., G. Paule, M., Dumas, M. & Sarkar, S. Characterization of myelin pathology in the hippocampal complex of a transgenic mouse model of Alzheimer's disease. *Current Alzheimer Research* **10**, 30-37 (2013).
- 56 Desai, M. K. *et al.* Early oligodendrocyte/myelin pathology in Alzheimer's disease mice constitutes a novel therapeutic target. *The American journal of pathology* **177**, 1422-1435 (2010).
- 57 Desai, M. K. *et al.* Triple-transgenic Alzheimer's disease mice exhibit region-specific abnormalities in brain myelination patterns prior to appearance of amyloid and tau pathology. *Glia* **57**, 54-65 (2009).
- 58 Mitew, S. *et al.* Focal demyelination in Alzheimer's disease and transgenic mouse models. *Acta neuropathologica* **119**, 567-577 (2010).
- 59 Roher, A. E. *et al.* Increased A β peptides and reduced cholesterol and myelin proteins characterize white matter degeneration in Alzheimer's disease. *Biochemistry* **41**, 11080-11090 (2002).
- 60 Chen, J.-F. *et al.* Enhancing myelin renewal reverses cognitive dysfunction in a murine model of Alzheimer's disease. *Neuron* (2021).
- 61 Mathys, H. *et al.* Single-cell transcriptomic analysis of Alzheimer's disease. *Nature* **570**, 332-337 (2019).

Figure 1 bioRxiv preprint doi: <https://doi.org/10.1101/2021.07.31.454562>; this version posted August 2, 2021. The copyright holder for this preprint (which was not certified by peer review) is the author/funder. All rights reserved. No reuse allowed without permission.

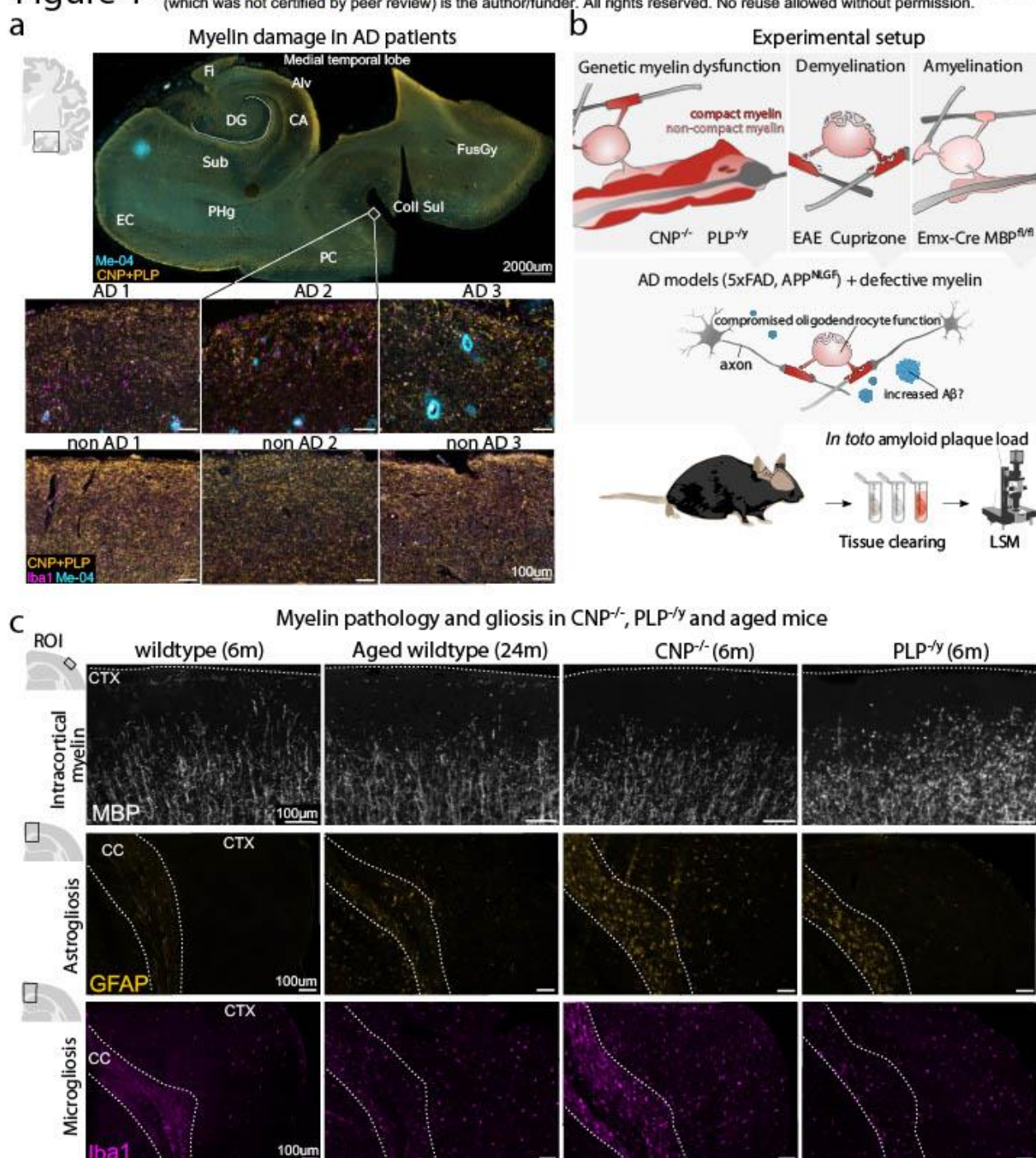


Figure 1. Myelin mutant animals show premature myelin integrity breakdown recapitulating myelin decline in ageing and AD

(a) Myelin damage in Alzheimer's disease (AD) patients in the medial temporal lobe visualised by immunolabelling against CNP and PLP1 to stain myelinated fibres, Iba1 to stain microglia and Methoxy-04 (Me-04) to stain amyloid- β plaques. Annotated overview image of the medial temporal lobe of one AD patient indicates the location of the closeups, which show upper cortical layers in the transentorhinal cortex in plaque+ individual AD patients and non-AD controls ($n=3$ per group). DG: Dentate Gyrus, FI: Fimbria, CA: Cornu Ammonis, Sub: Subiculum, EC: Entorhinal cortex, PHg: Parahippocampal gyrus, FusGy: Fusiform gyrus, Coll Sul: Collateral Sulcus. (b) Experimental setup to study the effect of myelin dysfunction on amyloid plaque load in AD mouse models. Models of genetic myelin dysfunction, acute demyelination and genetic amyelination were combined with the 5xFAD and APP^{NLGF} model of AD and effects on amyloid deposition were investigated in toto by tissue clearing and light sheet microscopy (LSM). (c) Myelin defects drive a premature ageing phenotype in mice. Panels show microscopic images of immunolabellings against MBP (Myelin), GFAP (Astroglia), IBA1 (Microglia) in 6-month-old wildtype, 24-month-old wildtype, 6-month-old CNP^{-/-} and 6-month-old PLP^{-/-} mice. Regions of interest (ROI) analysed are indicated on the left. Dashed lines in the upper panel marks pial surface. Dashed line in lower panels outline the corpus callosum. CC: Corpus callosum, CTX: Cortex.

Figure 2

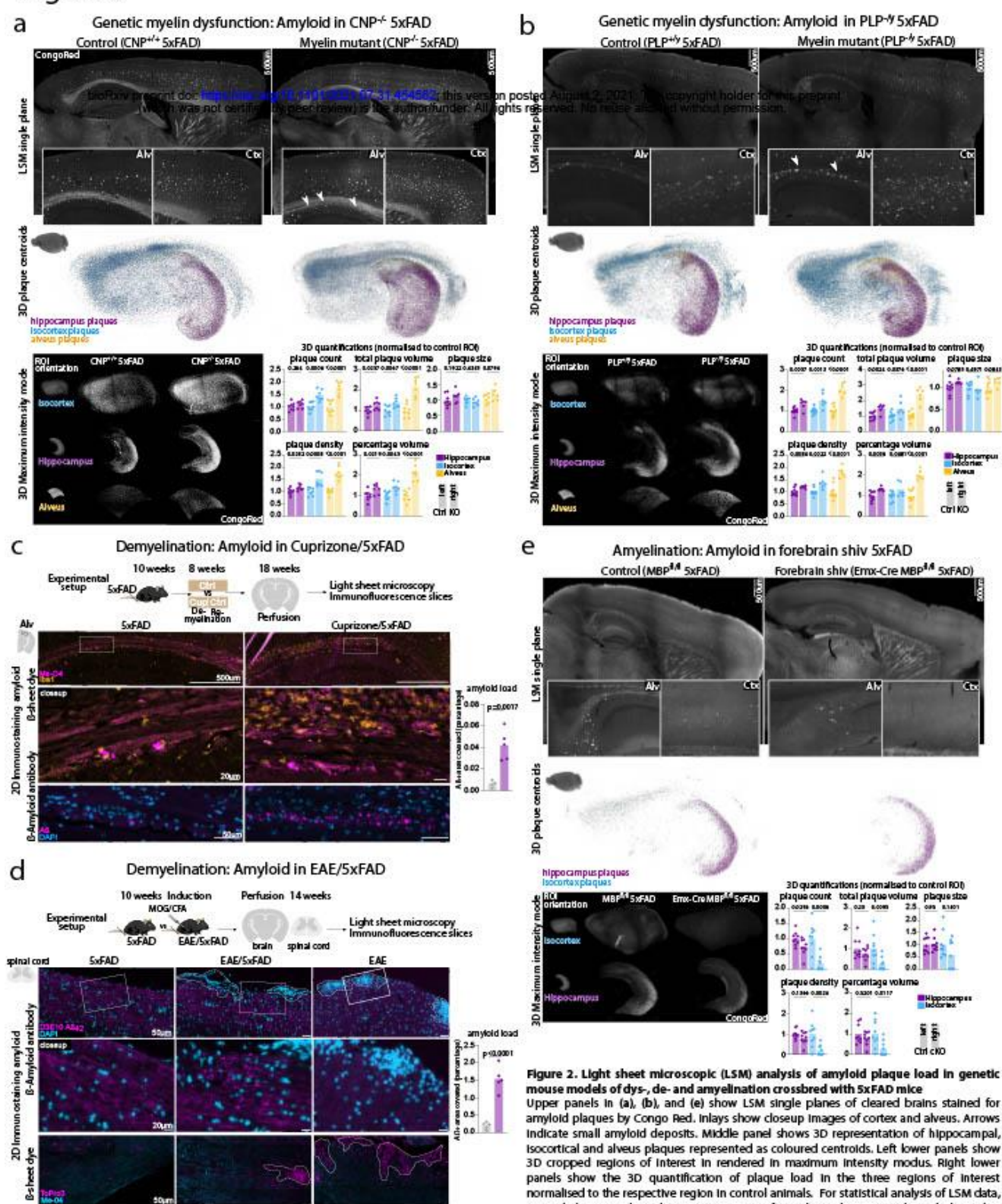


Figure 2. Light sheet microscopic (LSM) analysis of amyloid plaque load in genetic mouse models of dys-, de- and amyelination crossbred with 5xFAD mice

Upper panels in (a), (b), and (e) show LSM single planes of cleared brains stained for amyloid plaques by Congo Red. Insets show closeup images of cortex and alveus. Arrows indicate small amyloid deposits. Middle panel shows 3D representation of hippocampal, isocortical and alveus plaques represented as coloured centroids. Left lower panels show 3D cropped regions of interest in rendered in maximum intensity mode. Right lower panels show the 3D quantification of plaque load in the three regions of interest normalised to the respective region in control animals. For statistical analysis of LSM data, two-sided unpaired Student's t-test was performed. P-values are indicated above bar graphs. Dots represent single animals and bars represent mean. (a) In toto plaque load in 6-month-old CNP^{-/-} 5xFAD. n=8 for control, n=7 for mutant. (b) In toto plaque load in 6-month-old PLP^{-/-} 5xFAD mice. n=10 for control, n=6 for mutant. (c) Experimental setup to study effects of cuprizone-mediated demyelination on plaque deposition in 5xFAD mice. Middle panel shows 2D immunostaining against microglia (Iba1) and amyloid-β using the β-sheet dye Me-04 in the alveus of cuprizone-treated 5xFAD and control animals. Lower panel shows 2D immunostainings against amyloid and quantification of amyloid positive deposits in the alveus. Dots represent single animals and bars represent mean. Statistical analysis was performed using unpaired, two-sided Student's t-test. n=4 for control, n=5 for cuprizone treatment. (d) Experimental setup to study the effect of EAE-mediated demyelination on amyloid plaque load in 5xFAD animals. Lower panel shows 2D immunostainings against amyloid. EAE lesions are indicated by nuclei accumulations and marked by dashed lines. Lower panel shows β-sheet dye (Me-04) staining against amyloid plaques in EAE/5xFAD spinal cord. EAE control animals are shown to rule out unspecific staining of lesion sites in EAE. Quantification of amyloid positive deposits in the lesion environment is shown on the left. Dots represent single animals and bars represent mean. Statistical analysis was performed using unpaired, two-sided Student's t-test. n=5 for control, n=5 for EAE treatment. (e) In toto plaque load in 3-month-old forebrain shiv 5xFAD (Emx-Cre MBP^{+/+} 5xFAD). n=9 for control, n=9 for mutant.

Figure 3

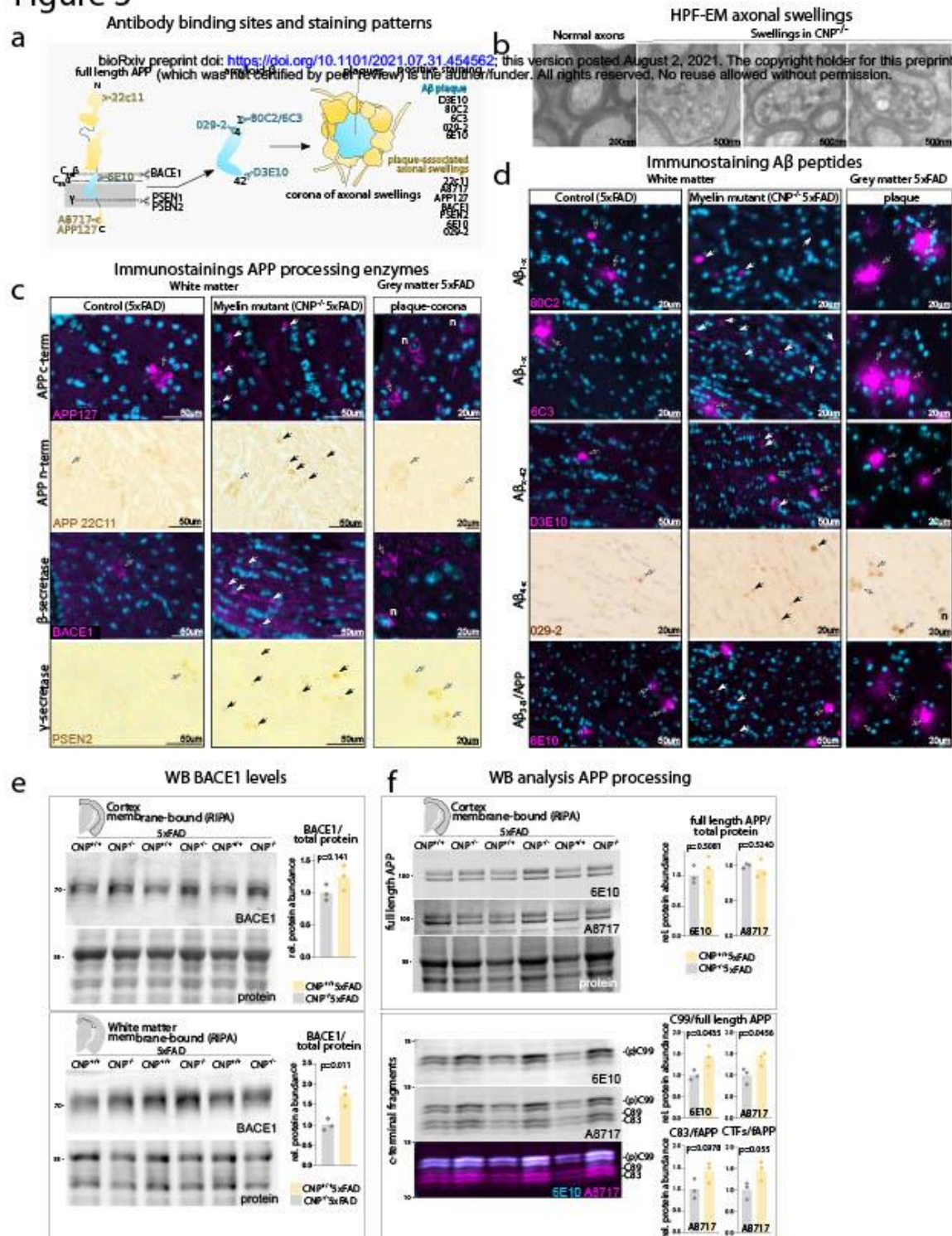


Figure 3. Myelin dysfunction alters APP processing (a) Schematic representation of binding sites and specificity of antibodies to APP and amyloid- β used in the following panels and typical staining observed (plaque-associated axonal swellings vs $A\beta$ plaque staining). Plaque-associated axonal swellings typically form a corona consisting of multiple swellings around amyloid plaques. (b) High pressure freezing EM of optic nerves from 6-month-old wildtype and $CNP^{-/-}$ optic nerves. Examples of (plaque-independent) axonal swellings in $CNP^{-/-}$ animals show abundant accumulation of endosomal/lysosomal structures and multivesicular bodies. (c) Fluorescent and chromogen immunostainings against APP and APP cleavage enzymes BACE1 (β -secretase) and Psen2 (as part of the γ -secretase complex) showing accumulation of APP, BACE1 and PSEN2 in plaque-independent axonal swellings in $CNP^{-/-}$ 5xFAD mice. Contoured arrows indicate plaque-associated axonal swellings as observed in $CNP^{-/-}$ mice. Non-contoured arrows indicate plaque-independent axonal swellings as observed in $CNP^{-/-}$ mice. (d) Fluorescent and chromogenic immunostainings against different species of $A\beta$ -peptides in $CNP^{-/-}$ 5xFAD vs 5xFAD control in the white matter. Contoured arrows indicate proper amyloid plaques, typically stained very intensely. Non-contoured arrows indicate swellings stained positive by the respective β -amyloid antibody, typically less intensely stained and of round structure. D3E10, 80C2 and 6C3 do not show cross-reactivity to full length APP and typically do not stain plaque-associated swellings, but stain swellings in $CNP^{-/-}$ 5xFAD mice. 029-2 and 6E10 antibody show certain cross-reactivity to full-length APP and also stain axonal swellings. (e) Fluorescent immunoblot analysis of BACE1 levels in micro-dissected cortex and white matter of $CNP^{-/-}$ 5xFAD and 5xFAD mice. P-value of unpaired, two-sided Student's t-test is indicated in the respective quantification bar plots. Dots represent lanes/single animals. n=3 for each group. (f) Fluorescent immunoblot analysis of APP fragmentation in the membrane-bound fraction of micro-dissected cortical tissue of $CNP^{-/-}$ 5xFAD and 5xFAD control mice. Quantification of band intensity is given on the right. fAPP levels were normalised against total protein fastgreen staining. CTF levels were normalised to fAPP levels. fAPP: full length APP. CTFs: c-terminal fragments. P-values of unpaired, two-tailed Student's t-test is indicated in the respective quantification bar plots. Dots represent lanes/single animals. n=3 for each group.

Figure 4

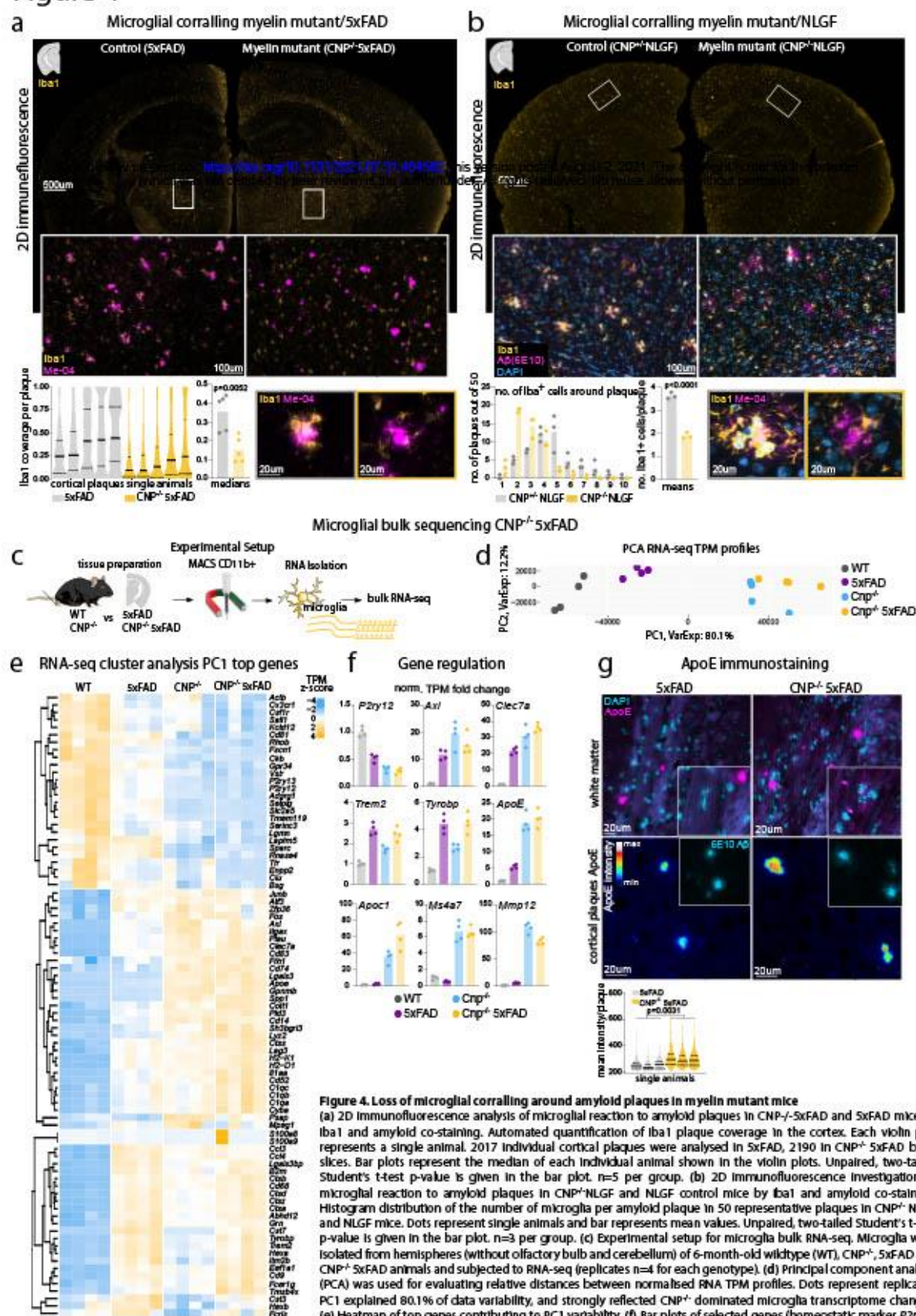


Figure 4. Loss of microglial corraling around amyloid plaques in myelin mutant mice

(a) 2D Immunofluorescence analysis of microglial reaction to amyloid plaques in CNP^{-/-}5xFAD and 5xFAD mice by Iba1 and amyloid co-staining. Automated quantification of Iba1 plaque coverage in the cortex. Each violin plot represents a single animal. 2017 individual cortical plaques were analysed in 5xFAD, 2190 in CNP^{-/-} 5xFAD brain slices. Bar plots represent the median of each individual animal shown in the violin plots. Unpaired, two-tailed Student's t-test p-value is given in the bar plot. n=5 per group. (b) 2D immunofluorescence investigation of microglial reaction to amyloid plaques in CNP^{-/-}NLGF and NLGF control mice by Iba1 and amyloid co-staining. Histogram distribution of the number of microglia per amyloid plaque in 50 representative plaques in CNP^{-/-} NLGF and NLGF mice. Dots represent single animals and bar represents mean values. Unpaired, two-tailed Student's t-test p-value is given in the bar plot. n=3 per group. (c) Experimental setup for microglia bulk RNA-seq. Microglia were isolated from hemispheres (without olfactory bulb and cerebellum) of 6-month-old wildtype (WT), CNP^{-/-} 5xFAD and CNP^{-/-} 5xFAD animals and subjected to RNA-seq (replicates n=4 for each genotype). (d) Principal component analysis (PCA) was used for evaluating relative distances between normalised RNA TPM profiles. Dots represent replicates. PC1 explained 80.1% of data variability, and strongly reflected CNP^{-/-} dominated microglia transcriptome changes. (e) Heatmap of top genes contributing to PC1 variability. (f) Bar plots of selected genes (homeostatic marker *P2ry12*, disease-associated microglia signature *Trem2*, *Tyrob*, *Axl*, *Clec7a* and differential regulated genes in CNP^{-/-} 5xFAD (*Apoc1*, *ApoE*, *M54a7*, *Mmp12*). Bar show normalised expression level. (g) Microscopic analysis of APOE levels in CNP^{-/-} 5xFAD and 5xFAD by immunofluorescence staining against ApoE. Upper panel shows strong APOE staining in amyloid plaques on both 5xFAD and CNP^{-/-} 5xFAD brains and speckled staining throughout the white matter in CNP^{-/-} mice indicative of elevated ApoE levels. Lower panel shows representative images of APOE plaque content in cortical plaques in 5xFAD and CNP^{-/-} 5xFAD mice, pseudo-coloured according to rainbow lookup table. Quantification shows violin plots of mean ApoE plaque content per plaque. Each violin plots represents a single animal (n=3 per genotype, 703 plaques for 5xFAD, 846 plaques for CNP^{-/-} 5xFAD). For statistical analysis, unpaired, two-tailed Student's t-test was performed.

Figure 5

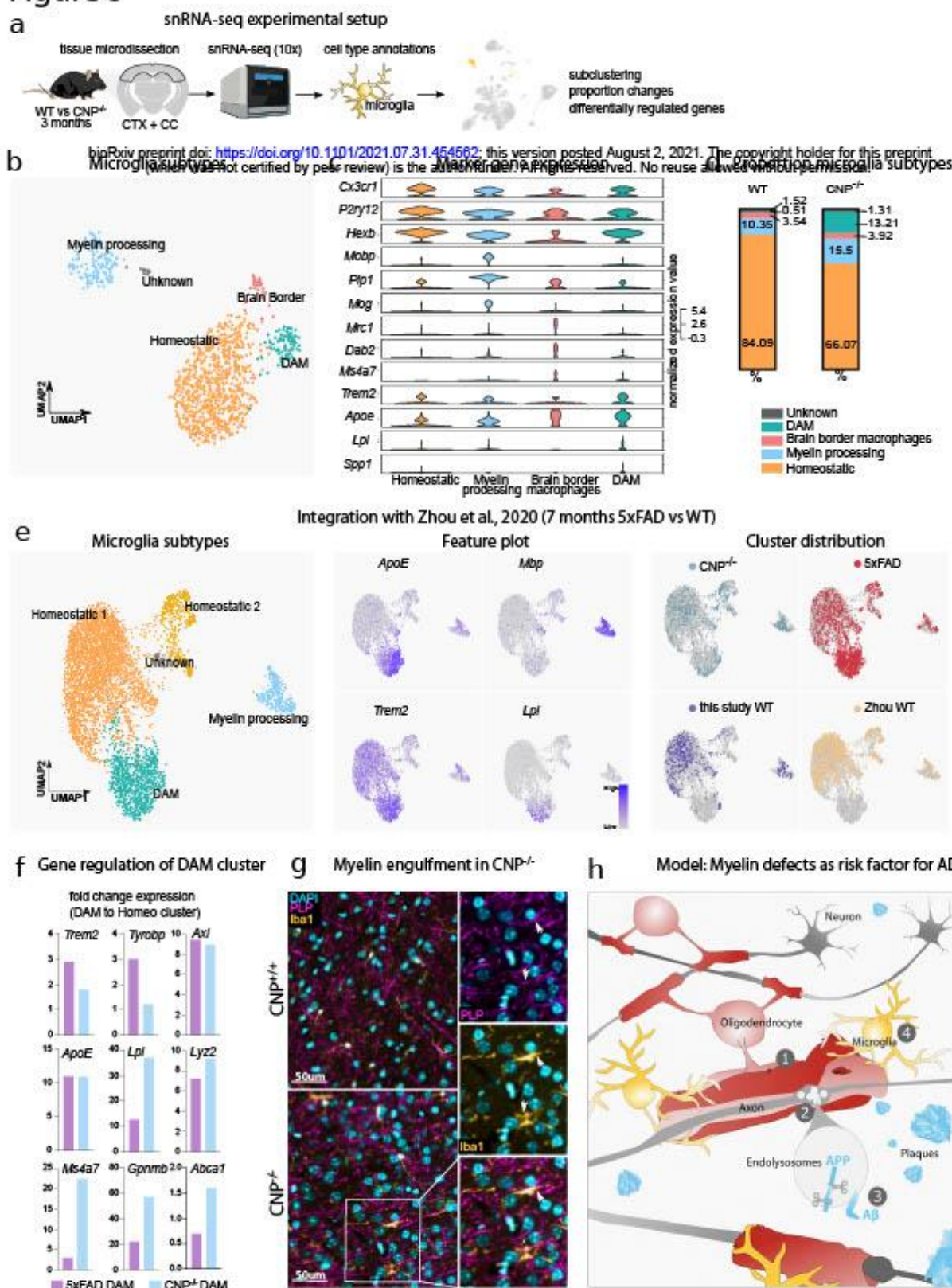


Figure 5. Myelin dysfunction induces DAM-like state as determined by snRNA-seq and distracts microglia from plaques

(a) Experimental setup for studying myelin dysfunction induced microglia profiles at the single cell level. Cortex and adjacent callosal white matter were microdissected from 3-month-old wildtype and $CNP^{-/-}$ mice and subjected to snRNA-seq (10x). Cell types were identified based on marker genes and microglia were subset for further analysis. (b) UMAP visualization of annotated microglia subtypes. (c) Violin plots showing marker gene expressions in each microglia subpopulation. (d) Bar plot shows distribution of microglia subpopulations in wildtype and $CNP^{-/-}$. (e) Integrative analysis of this study and 7-month-old 5x FAD and wildtype microglia snRNA-seq profiles from Zhou et al.³⁴ Feature plots showing normalized expression levels of $ApoE$, Mbp , $Trem2$ and Lpl for identification of microglia subclusters. Right panel showing genotype distribution among microglia subpopulations visualised in the UMAP space. (f) Bar plots representing average regulation levels of single genes in $CNP^{-/-}$ DAM and 5x FAD DAM. Regulation values are calculated by comparing gene average expression of DAM to the respective homeostatic microglia population. (g) Immunofluorescence analysis of myelin phagocytosis (PLP+) by microglia (Iba1+) in the cortex of $CNP^{-/-}$ mice. (h) Scheme illustrating a model of AD in which myelin dysfunction (1) induces axonal spheroids (2) where endolysosomes accumulate and $A\beta$ production is enhanced (3). Simultaneously, microglia become increasingly engaged with myelin and are distracted from amyloid plaques (4). All processes contribute to enhanced formation of amyloid plaques (5).

Material and Methods

Human tissue analysis

Case selection was performed from a pool of approximately 400 individuals, in which an autopsy with neuropathological evaluation was performed between 2018 and 2019 as a matter of routine procedure following death at the Leipzig University Hospital. In the individual contracts that govern medical treatment, all patients provided upon admission written consent to the scientific use of tissue removed and stored after any biopsy or during autopsy. Selection of patients was performed according to exclusion/inclusion criteria. Samples were anonymized and processed in a blinded manner. Selected patients were of mixed age and gender, between >60 years and <90 years of age, had a clinical history of dementia, and a NIA-AA score in neuropathological assessment between A2B3C2 and A3B2C2 (inclusion criteria) and did not suffer from another severe neurological disorder (exclusion criteria). In addition, control patients of the same age range without any clinical or neuropathological record of neurological disease were selected. No other criteria besides the described characteristics were applied. In total paraffin-embedded CNS tissue of 3 patients with moderate to pronounced AD neuropathological changes according to the NIA-AA (see above) and 3 control patients was histologically evaluated. In our analysis we used biopsies from the medial temporal lobe containing the hippocampal formation. We performed histological assessment for intracortical myelin content on the human tissue provided. For this, we sectioned paraffin blocks (5µm) and stained paraffin-sections for CNP, PLP, Iba1 and amyloid plaques simultaneously (see Histology for details).

Mouse strains and husbandry

Animal experiments were conducted in compliance with German animal welfare practices and approved by the local authorities (Landesamt für Verbraucherschutz und Lebensmittelsicherheit, Niedersachsen). Mice were group-housed in the local animal facility of the Max Planck Institute for Experimental Medicine under a 12-h dark/12-h light cycle and fed *ad libitum*. Both sexes were used throughout the study. Original mouse strains used to generate crossbreedings were: 5xFAD⁶², APPNLG⁶³, CNP⁴⁻²³, PLP⁴⁻²⁴, MBP⁶⁴, Emx-Cre⁶⁵. For analysis, either littermate controls were used or a corresponding control line from the initial F1 generation was generated. Age of animals is given in the respective figure legend. All animals were maintained on a C57BL/6 background. Genotyping was performed on clips derived from ear-marking according to standard protocols (see references for original mouse strains). Genotype was confirmed by re-genotyping on a tail biopsy upon sacrifice of the animal at the end of the respective experiment.

Demyelination models

As demyelination models, we employed cuprizone-intoxication and experimental autoimmune encephalomyelitis (EAE) and experiments were conducted as described previously⁶⁶. For cuprizone-mediated demyelination, male 14 weeks old 5xFAD mice were fed a powder diet containing 0.2% (w/w) cuprizone (Sigma-Aldrich) for 4 weeks followed by a 4-week recovery period on a normal pelleted food without cuprizone supplementation. Control 5xFAD received a standard diet without cuprizone. Animals were perfused at 18 weeks of age and brain tissue was analysed via light sheet microscopy and epifluorescence microscopy. For EAE experiments, 10-week-old 5xFAD mice were immunised against myelin oligodendrocyte glycoprotein (MOG) by subcutaneous injection of 200µg MOG peptide 35–55 in complete Freund's adjuvant (Mycobacterium tuberculosis at 3.75 mg/ml; BD) followed by injection of 500ng of pertussis toxin (Sigma) at day 1 and 3 post EAE induction (dpi 1 and 3). Animals were checked on a daily basis and a neurological disease score was determined according to the following parameters: 0 - normal; 0.5 - loss of tail tip tone; 1 - loss of tail tone; 1.5 - ataxia and mild walking deficits (slip off the grid); 2 - mild hind limb weakness, severe gait ataxia and twist of the tail causing rotation of the whole body; 2.5 - moderate hind limb weakness and inability to grip the grid with the hind paw but ability

to stay on an upright tilted grid; 3 - mild paraparesis and falls from an upright tilted grid; 3.5 - paraparesis of the hind limbs (legs strongly affected but move clearly); 4 - paralysis of the hind limbs and weakness in the forelimbs; 4.5 - forelimbs paralyzed; 5 - moribund or dead. Animals were perfused at 28 dpi at 14 weeks of age. All immunised 5xFAD animals developed EAE (Extended data Fig.3d). Brain and spinal cords were analysed by light sheet microscopy and epifluorescence microscopy.

Mouse behavioural testing

Hindlimb clasping was assessed by suspending the mouse on its tail for 5sec, carefully observing movement of the hindlimbs and scoring movement impairments according to a score from 0–4: 0 - no impairments, hindlimbs normally spread and moved; 1 - one hindlimb shows slightly less mobility; 2 - both hindlimbs show less mobility; 3 - both hindlimbs show reduced mobility and reduced spread; 4 - both hindlimbs show severely reduced movement and severely reduced spread. Videos were recorded. Animals were tested in the elevated plus (EPM) and Y-maze (YM) on consecutive days. In the EPM paradigm, animals were allowed to freely explore an elevated cross-shaped platform with two opposing enclosed arms and two opposing open arms for 5min without the experimenter present. In the YM paradigm, animals were allowed to explore a Y-shaped maze with enclosed arms for 8min without human interference. Videos were recorded and analysed using the Bloobserve Viewer behavioural analysis setup with automated tracking. Zones (Open arms, closed arms, centre) and object detection settings were optimised according to the maze type used. After the run, positional data, track length and full track images were exported. For the EPM, the time spent in both open arms was summed and plotted. For the YM, the order of arm entries was recorded, and the number of correct triads (consecutive visit of the three different arms) determined. The alternation index was calculated according to the formula: alternation index = number triads/number of arm entries-2. For a successful arm visit, animals had to enter an arm with their full body (excluding tail). For statistical analysis of the behavioural data, we report the results of several different type III ANOVAs that probed the main effects for the 5xFAD and myelin mutants as well as their interaction. All analyses were conducted in R (version 4.0.4, R Core Team 2021). The analyses of variance were computed with the *afex* package as reported in⁶⁷.

Tissue preparation

For microscopic analysis, animals were deeply anaesthetised or euthanised via CO₂ asphyxiation and subsequently transcardially perfused with ice-cold Hank's buffered salt solution (HBSS) and 4% paraformaldehyde (PFA) in 0.1M phosphate buffer, pH 7.4. Brains and spinal cord were removed and postfixed overnight in 4% PFA/phosphate buffer. Brains were washed once in PBS pH 7.4 and stored in PBS at 4°C until further use. For biochemical analysis of full brains, animals were killed by cervical dislocation, brain and spinal cord were extracted and fresh-frozen on dry-ice. Tissue was stored at -80°C until further use. For microdissection of subcortical white matter and cortical tissue, animals were sacrificed by cervical dislocation and the brain was quickly removed and submerged in ice-cold HBSS. The brain was inserted into a custom-made brain matrix and the brain was sliced coronally in ~1mm thick slices. Brain slices were spread onto an ice-cold glass plate and cortex and subcortical white matter were separated and excised from each individual brain slice. Tissue was immediately frozen on dry-ice and stored at -80°C until further use.

Whole tissue staining and clearing for light sheet microscopy

Fixed hemibrains and spinal cords were pretreated and permeabilised following a modified iDisco protocol^{26,27}. Briefly, tissues were dehydrated with an ascending concentration of methanol in PBS (50% 1x, 80% 1x, 100% 2x, 1 h each). Tissues were then bleached with a 1:1:4 ratio of H₂O₂:DMSO:methanol overnight at 4°C. Further dehydration followed with 100% methanol

incubation in 4°C (30 min), -20°C (3 h), and overnight storage at 4°C. Samples were incubated the following day in methanol with 20% DMSO before subjecting them to gradual rehydration in a descending methanol in PBS series (80% 1x, 50% 1x, 0% 1x, 1 h each). We then washed the tissues with a detergent mixture of 0.2% Triton X-100 in PBS (2x, 1 h) and permeabilised them overnight at 37°C in PBS with 0.2% Triton X-100, 20% DMSO, and 0.3 M glycine. After permeabilization, tissues were either stained with the Congo Red dye (Sigma Aldrich) for beta sheet structures within amyloid plaques or immunolabelled with antibodies of interest. For Congo Red staining, tissues were washed with PBS/0.2% Tween-20/10 mg/ml heparin/5mM sodium azide (PTwH) (2x, 1 h) before immersing them for 3 d at 37°C in 0.005% w/v Congo Red (100x stock solution in 50% ethanol). For immunolabelling, following tissue permeabilization and glycine treatment, samples were blocked in PBS with 0.2% Triton X-100, 10% DMSO and 6% goat serum (GS) for 3 d followed by washing in PTwH (2x, 1 h) and incubation in primary antibodies with the appropriate dilution factors (1:500, rabbit, anti-Iba, Wako) in PTwH with 0.2% Triton X-100, 5% DMSO and 3% GS for 14 d at 37°C. Upon completion of primary antibody labelling, tissues were washed in PTwH (6x, 10 min) and stored overnight at 37°C. For secondary antibody labelling, tissues were again incubated in secondary antibodies with the appropriate dilution factors (anti-rabbit Dylight 633, 1:500, Thermo-Fisher) in PTwH with 3% GS for 7 d at 37°C. Prior to clearing, spinal cords were fixed in 1.5% w/v Phytigel in water. Dyed or immunolabelled tissues were washed in PTwH (3x, 10 min each) before rehydration through an ascending concentration of methanol in PBS (20% 1x, 40% 1x, 60% 1x, 80% 1x, 100% 1x, 1 h each) and delipidation in a 1:2 mixture of methanol:dichloromethane (1x, 1 h 40 min). Lastly, samples were cleared by immersing them in ethyl cinnamate (Eci, Sigma-Aldrich) until transparent. All incubation steps were carried out at constant medium-speed rotation at the indicated temperatures. Samples were stored at room temperature in Eci until imaging.

In toto imaging of whole tissues and analysis/visualization

Cleared hemibrains and spinal cords were imaged *in toto* with a light sheet microscope setup (UltraMicroscope II, LaVision Biotec) equipped with a 2x objective lens, zoom body, and a corrected dipping cap. Samples were imaged being submerged in a sample chamber containing Eci. For all hemibrain imaging, hemibrains were mounted medial side-down on the sample holder to acquire sagittal images. Images were acquired in the mosaic acquisition mode with the following settings: 5 µm light sheet thickness, 20% sheet width, 0.154 sheet numerical aperture, 4 µm z-step size, 1000x1600 px field of view, 4x4 tiling, dual light sheet illumination, and 100 ms camera exposure time. Red fluorescence was recorded with 561 nm laser excitation at 80% laser power and a 585/40 emission filter. Far-red fluorescence was recorded with 640 nm laser excitation at 30% laser power and a 680/30 emission filter. Autofluorescence was recorded with 488 nm laser excitation at 50% and 525/20 nm emission filter. Images were imported into Vision4D v3.2 (Arivis) and stitched using the tile sorter setup. Partly, images were imported and stitched using the Imaris Importer and Stitcher v9.1 (Bitplane). Rendered whole hemibrains were then processed and three main regions of interest (ROIs) were manually annotated based on the sagittal Allen mouse brain atlas, namely isocortex, hippocampus, and alveus. All ROIs were first traced manually in 2D planes to automatically extrapolate the 3D ROIs. Cortical and hippocampal annotations were cropped with a medial cut-off of approximately ~0.4 mm and a lateral cut-off of ~4.4 mm which would span the dorsal isocortex and the entire hippocampal formation of one hemibrain. The lateral cut-off for the alveus ROI is the plane where the hippocampal formation appears in 2D. Next, we segmented amyloid plaques within the ROIs. For 3-month-old 5x FAD brain data, we typically used automated intensity thresholding. For 6-month-old 5x FAD data, plaques were segmented using the blob finder algorithm in Vision4D with the following parameters: 20 µm object size, 10-15% probability threshold, and 0% split sensitivity. Once segmentation has been performed, a stringent noise removal was performed by deleting objects with voxel sizes <10 from the object table. Objects were then critically reviewed and

any additional noise, which might include but are not restricted to blood vessels and nuclei, were manually removed from the dataset. For quantification of amyloid plaques in the APP^{tg} brains that typically stained much weaker for Congo Red, plaque segmentation was performed using the machine learning segmenter in Vision4D. Object parameters, namely volume, ROI volumes, were extracted for further quantification. For plaque visualization in the different ROIs, objects are represented in centroids and color-coded according to location.

Paraffin slices and histological stainings

Fixed hemibrains and spinal cords were subjected to dehydration steps (50% EtOH, 80% EtOH, 100% EtOH, 100% Isopropanol, 50% Isopropanol/50% Xylol, 2x 100% Xylol) followed by paraffinization on the STP 120 tissue processing machine (Leica microsystems). Samples were retrieved and embedded in paraffin blocks on the HistoStar embedding workstation (Eprelia). Paraffin-embedded blocks were sectioned coronally while spinal cords were sectioned longitudinally at 5 µm slice thickness, slices were mounted onto slides and dried overnight. Slides were deparaffinised at 60°C followed by incubation in xylol (100% 2x) and a 1:1 mixture of xylol and isopropanol (1x) for 10 min each. The slides were rehydrated in a descending ethanol series. This was followed by incubation in either acidic antigen retrieval solution (pH 6.0) or basic antigen retrieval solution (10mM Tris/1 mM EDTA pH10) (for 5 min and boiling for 10 min). The samples were cooled for 20 min and washed in distilled water for 1 min before a subsequent permeabilisation in 0.1% Triton X-100 in PBS. For Aβ antibody staining, samples were subjected to an extra antigen retrieval in 88% formic acid to loosen up the β-sheet structure for optimal antibody binding for 3 min. For plaque ApoE staining, formic acid treatment was even prolonged (10 min, fresh formic acid). This was followed by washes in PBS (2x, 5 min) and blocking with 10% GS in PBS for 1 h at RT. For chromogenic labelling, an additional step of inactivation of endogenous peroxidases was implemented prior to blocking by incubation in 3% H₂O₂. After blocking, slices were incubated in primary antibody solution (PBS/10%GS or PBS/5%BSA) overnight at 4°C in coverplates (Eprelia). Antibodies used in this study were: anti-Iba1 (rabbit, Wako; 1:1000); anti-Aβ-6E10 (mouse, Biolegend; 1:1000), anti-CNP (mouse, AMAB91072, Atlas; 1:1000), anti-PLP-clone aa3 (rat, culture supernatant; 1:200), anti-BACE1 (rabbit, ab183612, Abcam; 1:100), anti-MBP (rabbit, serum, custom Nave Lab; 1:1000), anti-GFAP (mouse, GA5, Leica, 1:200), anti-n-terminal APP (22c11, Merck; 1:1000), anti-c-terminal APP (rabbit, 127-003, Synaptic Systems; 1:1000), anti-Aβ₄₂-D3E10 (rabbit, Cell Signalling Technology; 1:1000), anti-Psen2 (rabbit, Abcam, 1:100), anti-ApoE D719N (rabbit, Cell Signalling Technology; 1:500), anti-Aβ₁₋₄₂ (mouse, 80C2, Synaptic Signalling, 1:200), anti-Aβ₁₋₄₂ (mouse, Moab2-6C3⁶⁸, Abcam, 1:200), anti-Aβ₁₋₄₂ (guinea pig, 029-2⁶⁹, Oliver Wirths, custom, 1:200). For immunofluorescence staining, samples were washed in PBS or Tris/2% Milk and incubated with the corresponding fluorescent secondary antibody diluted in PBS containing 10% goat serum for 2 h at RT in the dark. Fluorescently conjugated secondary antibodies used were: anti-mouse Alexa555 (donkey/goat, Thermo-Fisher; 1:1000), anti-mouse Dylight633 (donkey/goat, Thermo-Fisher; 1:1000), anti-rabbit Alexa555 (donkey/goat, Thermo-Fisher; 1:1000), anti-rabbit Dylight633 (donkey/goat, Thermo-Fisher; 1:1000). Amyloid plaques were stained by the β-sheet dye Methoxy-X04 (4 µg/ml in 50% ethanol, Tocris) for 30 min at RT and contrasting in 50% ethanol. Nuclei were either stained with DAPI (300nM, Thermo-Fisher) or ToPro3 (1:1000, Thermo-Fisher) in PBS for 5 min at RT. Slides were again washed in PBS and mounted with Aqua PolyMount mounting medium (PolySciences). For chromogenic labelling, the LSAB2 Kit (Dako) for rabbit/mouse and the DAB-Kit from Zytomed was used according to the manufacturers' protocols. Slides were then rinsed in water, dehydrated and mounted using Eukitt (Sigma-Aldrich).

Epifluorescence and brightfield microscopy

Epifluorescence microscopy was performed on a Zeiss Observer Z1 microscope equipped with Plan-Apochromat 20x/08 and Fluor

2.5x/0.12 objectives, a Colibri 5 LED light source (630nm, 555nm, 475nm 385nm excitation), 96 HE BFP, 90 HE DAPI/GFP/Cy3/Cy5, 38 GFP, 43 DsRed, 50 Cy5 Zeiss filter sets, a Axiocam MrM and a SMC900 motorized stage. For whole brain slice microscopy, a preview scan at 2.5x magnification was taken and focus support points were distributed and manually set for imaging at 20x magnification in the ZEN imaging software (Zeiss). Tiled images were stitched in ZEN. For visualisation, pseudocolours (cyan, magenta, yellow) were assigned to different channels, intensity was adjusted and images were exported in ZEN. Brightfield microscopy of DAB-stained slices was performed on a Zeiss Axiophot Imager.Z1 equipped with a Achromplan 4x/0.1, PlanFluar 20x/0.75 and Plan Neofluar 40x/0.75 objectives and a AxiocamMrc camera. For whole brain slice microscopy, a preview scan at 4x magnification was taken and focus support points were distributed and manually set for imaging at 40x magnification in the ZEN imaging software (Zeiss). Tiled images were stitched in ZEN. Brightness and contrast of RGB images were adjusted and images exported in ZEN.

2D microscopy quantification

2D image analysis was performed in Fiji (v1.53c)⁷⁰. For quantification of amyloid load, thresholding was performed to segment amyloid- β deposits (either stained by Methoxy-04 or amyloid- β plaques) and area positive was calculated in the respective region of interest. For analysis of the plaque corralling phenotype, in Iba1+/A β co-stainings individual plaques were segmented using thresholding and the Iba1+ area in each individual plaque was calculated using a Fiji macro-script. Iba1 coverage was expressed as percentage. For quantification of ApoE levels in plaques, ApoE positive plaques were segmented and the raw mean fluorescence per plaque was calculated.

High-pressure freezing electron microscopy

Sample preparation by high pressure-freezing and freeze substitution was performed as described⁷¹. In brief, optic nerves of 6-months-old Cnp^{-/-} and control wildtype mice were freshly dissected, immersed in 20% PVP in PBS and placed into HPF sample carriers (Wohlwend, Sennwald, Switzerland). After freezing using a HPM100 high pressure freezer (Leica Microsystems, Vienna, Austria), samples were embedded in EPON after freeze substitution using 0.1 % tannic acid in acetone followed by 2% OsO₄ and 0.1 % uranyl acetate in acetone. After polymerization, samples were sectioned with a UC7 ultramicrotome (Leica Microsystems, Vienna, Austria) and imaged with a LEO912 transmission electron microscope (Carl Zeiss Microscopy GmbH, Oberkochen, Germany) using an on-axis 2k CCD camera (TRS, Moorenweis, Germany).

Cell fractioning

For analysis of APP and Trem2 fragmentation, cell fractioning was performed prior to western blot analysis according to published protocols⁴⁵. In brief, tissue was homogenised in DEA-buffer (0.25% Diethylamine 50mM NaCl pH10) using the Precellys bead-milling method (Precellys soft tissue homogenising lysis kit, Bertin Instruments) and the soluble protein fraction was extracted via centrifugation (10min, 500g, 4°C) followed by ultracentrifugation (1h, 130 000g, 4°C). The membrane-bound fraction was solubilised in RIPA buffer (20mM Tris-HCl pH7.5, 150mM NaCl, 1%NP-40, 1%SDS, 2.5mM sodium pyrophosphate, 1mM Na₂EDTA) and cleaned via centrifugation (10min, 500g, 4°C) and ultra-centrifugation (1h, 130 000g, 4°C). RIPA insoluble material (containing plaque A β) was resuspended in ice-cold 70% formic acid in water, sonicated and ultracentrifuged (1h, 130 000g, 4°C). Supernatant was collected as formic acid fraction and neutralised with 1M Tris pH9.5. All buffers and solutions were supplemented with protease inhibitor cocktail (P8340, Merck). Fractions were stored at -80°C until further use.

SDS PAGE and Western blotting

To determine sample protein concentration, detergent compatible protein assays (Biorad) were carried out in duplicates. Sample was mixed with Laemmli sample buffer (2%SDS, 10% glycerol, 0.0025% bromophenol blue, 0.125M Tris-Cl, pH 6.8, 0.05M DTT) and equal

amount of protein (typically 20-30ug) were loaded per lane. For BACE1 western blotting, standard Tris-Glycine SDS-PAGE gels (8%) were used. For western blot analysis of APP and TREM2 fragmentation, Tris-Tricine SDS PAGE gels (10-20%, Novex, Thermo Fisher) were used. Gels were run at 100-120V for approximately 1h. For Tris-Glycine SDS-PAGE gels, proteins were transferred onto low fluorescent Immobilon-FL membrane (0.45 μ m por size, Merck) using the Biorad wet-blot system (1.15h, 500mA) and blot transfer buffer (25mM Tris, 190mM glycine) containing 20% MeOH. For Tris-Tricine SDS PAGE gels, proteins were transferred onto a low fluorescent PVDF membrane of lower pore size (0.2 μ m). Blots were washed in water and transferred protein was stained with Fastgreen for transfer quality-check and for normalisation purposes. For this, membranes were transferred to Fastgreen working solution (0.0005% Fastgreen FCF (Serva) in de-staining solution (30% Methanol, 7% mL glacial acetic acid, 63% H₂O) for 5min and briefly washed two times in de-staining solution. Membranes were imaged at a ChemoStar fluorescent imager (Intas) equipped with a 670 nm/20 nm excitation filter and near infrared emission collection. Membranes were rinsed in TBS with Tween (0.05%) until pH was neutral and blocked in 5% BSA in TBS-T for 1h at room temperature. Membranes were then incubated in primary antibodies in 5% BSA over night at 4°C on a rotating shaker. The following primary antibodies were used: anti-BACE1(1:1000, rabbit, D10E5, Cell Signalling Technologies), anti-n-terminal APP (1:1000, mouse, 22c11, Merck), anti-c-terminal APP (1:1000, rabbit, A8717, Merck), anti-APP/A β (1:1000, mouse, 6E10, Biologend), anti-c-terminal TREM2 (1:1000, rabbit, E7P8), Cell Signalling Technologies). Membranes were washed several times and membranes were incubated in secondary antibody solution (5% BSA in TBS-T). The following secondary antibodies were used: anti-rabbit IgG (H+L) DyLight 800 (1:1000, Thermo Fisher), anti-mouse IgG (H+L) DyLight 680 (1:1000, Thermo Fisher). For visualisation, membranes were scanned at an Odyssey platform (Licor). For quantification, background was subtracted from raw images and bands were analysed using Fiji (integrated density). Protein levels were normalised to fastgreen whole protein or in the case of APP and Trem2 cleavage to full length protein.

Magnetic activated cell sorting of microglia sorting and bulk RNA-sequencing

Microglia were isolated from mouse hemibrains (excluding cerebellum and olfactory bulb) via magnetic-activated cell sorting. Dissected tissues were enzymatically and mechanically dissociated using the Miltenyi Biotec adult brain dissociation kit according to manufacturer's protocol. Prior to microglial isolation via CD11b microglia microbeads and LS columns (Miltenyi Biotec), astrocytes (ACSA-2 microbeads) and oligodendrocytes (O4 microbeads) were removed to enhance purity of the microglial population. Isolated microglia were directly eluted in RLT lysis buffer and RNA was isolated using the RNeasy Micro Kit (Qiagen). In total, n = 4 replicates were used for each genotype (WT, Cnp^{-/-}, 5xTAD, Cnp^{-/-}5xTAD. RNA extracted from sorted mouse brain hemisphere microglia was eluted in 30 μ l nuclease-free water and subjected to 50 bp single-end mRNA sequencing using HiSeq 4000 (Illumina). Raw sequencing data were first evaluated by FASTQC v0.72 for quality, then aligned against the reference mouse genome GRCh38 using STAR v2.5.2b-2⁷² with default parameters. Gene raw counts of each sample were extracted using featureCounts v1.6.3⁷³ from aligned profiles for differential gene expression (DGE) analysis using DESeq2 v1.26.0⁷⁴ and converted to TPM value for sample distance calculation and visualization, as well as for gene expression pattern analysis. For DGE analysis, each pair of genotypes were calculated separately, and statistics results were summarised (SuppTable2). Gene targets with adjusted P-value < 0.05 were considered as significantly regulated. Using normalised TPM profiles, samples were embedded by principal component analysis (PCA) to assess distances.

Nucleus isolation and single-nuclei transcriptome sequencing

Cortex and corpus callosum from 3-month-old Cnp^{-/-} and WT controls were micro-dissected and subjected to single-nuclei transcriptome sequencing. For each genotype and replicate, the tissue of two

animals were pooled. Two replicates per genotype were sequenced. Nuclei were isolated according to previously published methods⁷⁵. Briefly, frozen tissue was transferred into 2ml of pre-chilled homogenization buffer (320mM sucrose, 0.1% NP40, 0.1mM EDTA, 5mM CaCl₂, 3mM Mg(Ac)₂, 10mM pH 7.8 Tris, 167uM β -mercaptoethanol and 1x protease inhibitor (Roche)). Tissue was carefully homogenised and filtered through a 80 μ m strainer, and further centrifuged for 1min under 100 rcf. For each sample, 400 μ l supernatant was collected into a pre-chilled 2ml low-binding Eppendorf tube, followed by adding 400 μ l 50% iodixanol solution (in 1x homogenization buffer containing 480mM sucrose) to reach a 25% iodixanol concentration. By layering 600 μ l of 29% iodixanol underneath the 25% iodixanol mixture, then 600 μ l of 35% iodixanol underneath the 29% iodixanol, two clear interfaces between different concentrations of buffers were created, and the tube was centrifuged for 20 min under 3000 rcf. After centrifugation, nuclei were collected from the band between the 29% and the 35% iodixanol layers and transferred to a fresh pre-chilled tube. Isolated nuclei were washed and resuspended in cold resuspension buffer (1xPBA, 1% BSA, 0.1U/ul RNase inhibitor) and further subjected to single-nuclei transcriptome libraries using the chromium single cell 3' reagent kit according to the manufacturer's instruction (10x Genomics). The constructed libraries were sequenced using Novaseq 6000 (Illumina). Raw snRNA-seq data were collected in Fastq format and first aligned to the reference profile pre-mRNA (ENSEMBL GRCh38) using CellRanger toolkit v3.0.2 (10x Genomics). Matrices containing UMI count of each gene in each nuclei were extracted for all samples, by filtering out nuclei with <200 detected genes and <500 total transcripts, as well as nuclei with outlier level transcripts quantity or gene detection rate identified according to individual sample sequencing depth (SuppTable3). Genes expressed in less than 3 cells were excluded for further analysis. Filtered expression matrices were combined, and UMI of each nucleus were normalised towards its total UMI counts with a scale factor of 10,000 and then log transformed.

Dimensionality reduction, clustering analysis and cell type annotation

The normalised UMI matrix of all samples was mainly analysed using the R package Seurat v3.2.3⁷⁶. High variable genes were calculated and scaled to support linear dimensionality reduction using PCA. For all cells, the first 50 PCs were used for further neighbouring embedding using uniform manifold approximation and projection (UMAP)⁷⁷, as well as for performing the clustering analysis (resolution=0.5) using K nearest neighbour (KNN) algorithm. Cluster marker genes were calculated using the MAST algorithm⁷⁸ to determine cluster cell type annotations. Clusters with undefined cell identities were removed from further analysis. To perform cell type specific analysis for microglia the corresponding cell population was firstly subset and reduced for its dimensionality using PCA. Similarly, selected top PCs were used for UMAP embedding and clustering analysis, with cluster marker genes calculated by MAST. Specific parameters used for analysing microglia can be found in (SuppTable3).

External data integrative analysis

Integrative analysis was carried out between CNP^{-/-} and GSE140511⁴⁴. More specifically, microglia from Cnp^{-/-} and corresponding controls were integrated with microglia profiles from 7-month-old WT, 5xFAD from GSE140511, to unravel the disease associated microglia (DAM) subpopulation. Integrative analysis was conducted using the SCTransform pipeline implemented in the Seurat toolkit. The batch effect corrected data underwent PCA dimensionality reduction, neighbouring embedding and unbiased clustering. Corresponding parameters for different datasets integration are listed in (SuppTable3).

Data visualisation

Images were exported from the respective imaging or bioinformatic software (ZEN 2011 blue edition, Zeiss; Vision4D Arivis; Fiji; R) and

final figures were assembled in Inkscape (v1.1, www.inkscape.org). Graphs were created in Prism 8.0 (Graphpad).

Data availability

All raw sequencing data, as well as raw and processed counts matrices have been uploaded to the Gene expression Omnibus (GEO)⁷⁹ under the SuperSeries accession number GSE178304. External datasets recruited for analysis were accessed through accession numbers listed in material and method.

Code availability

Packages involved in data analysis pipelines are listed in material and method. The code used for bulk and single-nuclei transcriptome sequencing is available on GitHub https://github.com/TSun-tech/AD_MyeloidMutant.git. More detailed information is available upon contacting the corresponding authors. Custom-made Fiji scripts for analysis of plaque-correlation are available on request.

Methods References

- 62 Oakley, H. *et al.* Intraneuronal β -amyloid aggregates, neurodegeneration, and neuron loss in transgenic mice with five familial Alzheimer's disease mutations: potential factors in amyloid plaque formation. *Journal of Neuroscience* **26**, 10129-10140 (2006).
- 63 Saito, T. *et al.* Single App knock-in mouse models of Alzheimer's disease. *Nature neuroscience* **17**, 661-663 (2014).
- 64 Meschkat, M. *et al.* White matter integrity requires continuous myelin synthesis at the inner tongue. *bioRxiv* (2020).
- 65 Gorski, J. A. *et al.* Cortical excitatory neurons and glia, but not GABAergic neurons, are produced in the Emx1-expressing lineage. *Journal of Neuroscience* **22**, 6309-6314 (2002).
- 66 Berghoff, S. A. *et al.* Microglia facilitate repair of demyelinated lesions via post-squalene sterol synthesis. *Nature neuroscience* **24**, 47-60 (2021).
- 67 Singmann, H. *et al.* afex: analysis of factorial experiments. R package version 0.16-1. *R Package Version 0.16.1* (2016).
- 68 Youmans, K. L. *et al.* Intraneuronal A β detection in 5xFAD mice by a new A β -specific antibody. *Molecular neurodegeneration* **7**, 1-14 (2012).
- 69 Wirths, O. *et al.* N-truncated A β 4-x peptides in sporadic Alzheimer's disease cases and transgenic Alzheimer mouse models. *Alzheimer's research & therapy* **9**, 1-12 (2017).
- 70 Schindelin, J. *et al.* Fiji: an open-source platform for biological-image analysis. *Nature methods* **9**, 676-682 (2012).
- 71 Weil, M.-T., Ruhwedel, T., Meschkat, M., Sadowski, B. & Möbius, W. in *Oligodendrocytes: Methods and protocols* 343-375 (2019).
- 72 Dobin, A. *et al.* STAR: ultrafast universal RNA-seq aligner. *Bioinformatics* **29**, 15-21 (2013).
- 73 Liao, Y., Smyth, G. K. & Shi, W. featureCounts: an efficient general purpose program for assigning sequence reads to genomic features. *Bioinformatics* **30**, 923-930 (2014).
- 74 Love, M. I., Huber, W. & Anders, S. Moderated estimation of fold change and dispersion for RNA-seq data with DESeq2. *Genome biology* **15**, 1-21 (2014).
- 75 Corces, M. R. *et al.* An improved ATAC-seq protocol reduces background and enables interrogation of frozen tissues. *Nature methods* **14**, 959-962 (2017).
- 76 Stuart, T. *et al.* Comprehensive integration of single-cell data. *Cell* **177**, 1888-1902. e1821 (2019).
- 77 McInnes, L., Healy, J. & Melville, J. Umap: Uniform manifold approximation and projection for dimension reduction. *arXiv preprint arXiv:1802.03426* (2018).
- 78 Finak, G. *et al.* MAST: a flexible statistical framework for assessing transcriptional changes and characterizing heterogeneity in single-cell RNA sequencing data. *Genome biology* **16**, 1-13 (2015).
- 79 Barrett, T. *et al.* NCBI GEO: archive for functional genomics data sets—update. *Nucleic acids research* **41**, D991-D995 (2012).

Acknowledgements

We thank the animal care takers and veterinarians of the animal facility at the Max-Planck-Institute for Experimental Medicine (MPI-EM). We thank Anette Fahrenholz and Katharina Overhoff for technical assistance. We thank members of the Department for Neurogenetics at the MPI-EM and the KAGS subgroup for helpful discussions and input. C.D. was supported by a Boehringer Ingelheim Fonds PhD fellowship. Work in KAN's laboratory was supported by by

bioRxiv preprint doi: <https://doi.org/10.1101/2021.07.31.454562>; this version posted August 2, 2021. The copyright holder for this preprint (which was not certified by peer review) is the author/funder. All rights reserved. No reuse allowed without permission.

the Dr. Myriam and Sheldon Adelson Medical Foundation (AMRF) and an ERC Advanced Grant (MyelinANO).

Author contributions

CD and KAN conceptualised and designed the study. CD and AOS performed microscopy and biochemical experiments. TSun planned and analysed bulk RNA-seq and snRNA-seq experiments. LS, SB, GS helped perform acute demyelination experiments. AAS helped analysing snRNA-seq experiments. SS provided mice. WM performed electron microscopic analysis and generated mice. SZ and OW helped analyse A β generation in axonal swellings. MT performed statistical analysis of behavioural data. TSaito and TSaido provided APP NLGF mice. DKB helped performing behavioural experiments. RK and DG performed snRNA-seq. MW and CH helped perform biochemical analysis of APP processing and provided critical experimental advice. RS provided human autopsy material. HE provided conceptual input. CD and TSun created figures. CD, TSun and KAN wrote the manuscript.

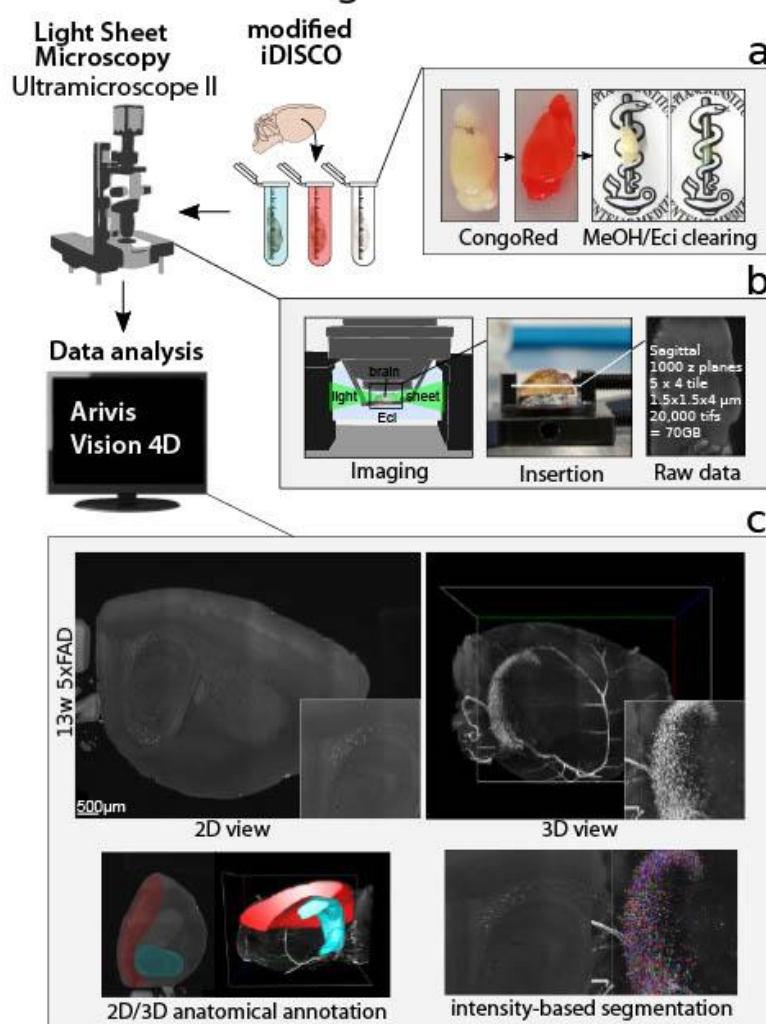
Competing Interest

Authors declare no competing interests.

Correspondence

Correspondence and requests for materials, data or code should be addressed to depp@em.mpg.de or nave@em.mpg.de.

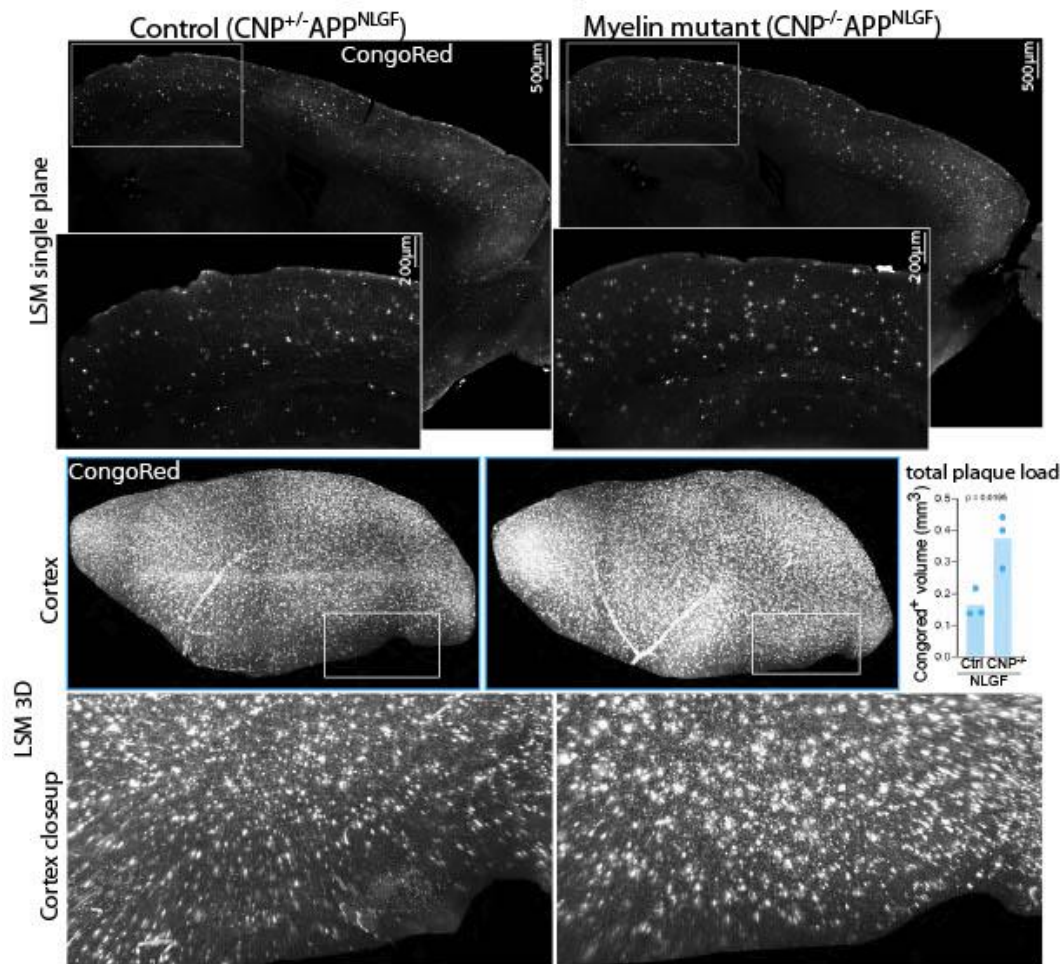
Extended Data Figure 1

**Extended Data Figure 1. Assessment of *in toto* amyloid burden by light sheet microscopy**

(a) Brains were subjected to *in toto* staining with the β -sheet dye Congo Red according to a modified iDISCO protocol (see Material and Methods) followed by clearing in Ethylcinnamate (Eci). (b) Cleared brains were imaged on an Ultramicroscope II (LaVision-Biotech) light sheet setup to obtain sagittal optical slices. (c) Raw data were visualised and analysed in Arivis Vision 4D using manual region of interest annotation for hippocampus and cortex and automated plaque segmentation (intensity-thresholding: 3-month-old 5xFAD, blobfinder algorithm: 6-month-old 5xFAD, machine learning: 6-month-old APP^{MLGF}).

Extended Data Figure 2

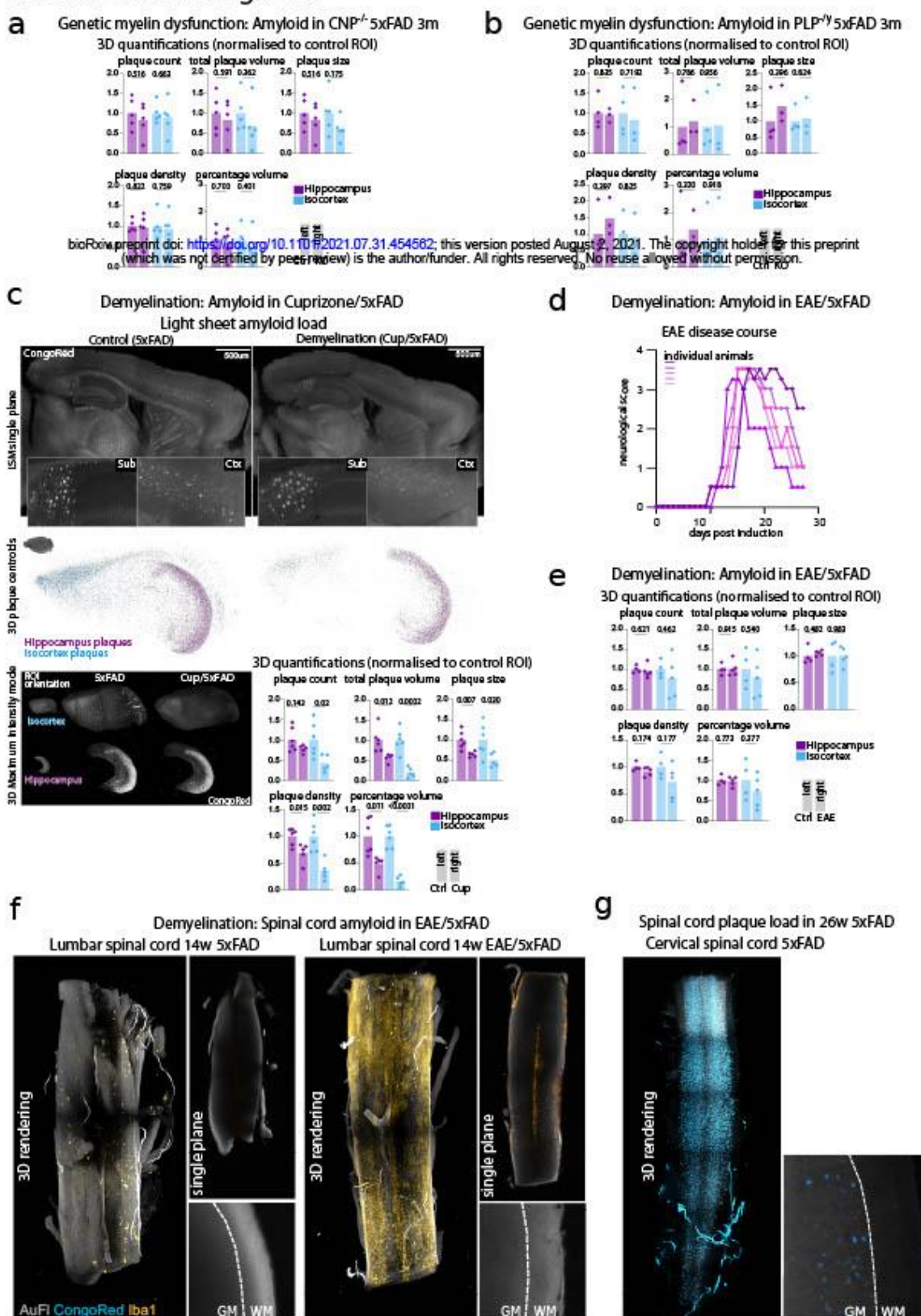
Light sheet amyloid load



Extended Data Figure 2. Light sheet microscopic analysis of amyloid plaque load in CNP^{-/-}App^{NLGF}

CNP^{-/-}App^{NLGF} brains show enhanced plaque deposition at 6-month of age when compared to CNP^{+/+}App^{NLGF} controls. Upper panel shows LSM single plane and a closeup of a cortical region. Middle panel shows 3D maximum intensity projection of the cropped isocortical region of interest. Plaque burden was quantified using machine-learning based segmentation of amyloid plaques. Lower panel shows the closeup indicated in the middle panel. Dots represent single animals and bars depict mean. Unpaired, two-tailed Student's t-test was performed for statistical analysis.

Extended Data Figure 3

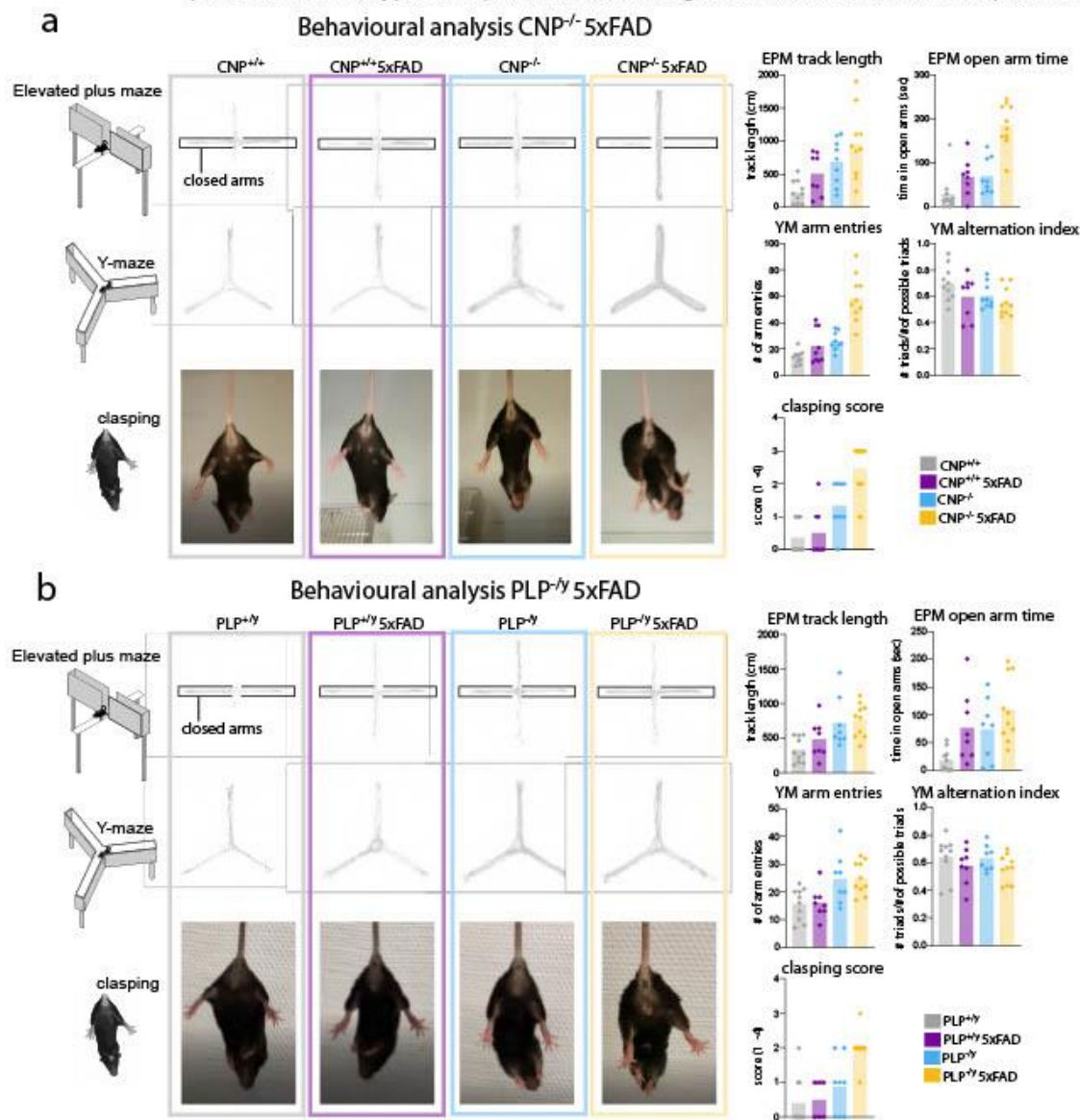


Extended Data Figure 3. Microscopic analysis of plaque changes induced by dys- or acute demyelination (Main Figure 2 extended)

(a) Quantifications of light sheet microscopic analysis of 3-months-old CNP^{-/-} 5xFAD mice. n=5 for control, n=5 for KO. (b) Quantifications of light sheet microscopic analysis of 3-months-old PLP^{-/-} 5xFAD mice. n=4 for control, n=3 for KO. (c) Light sheet microscopic analysis of amyloid plaque load in cuprizone-fed 5xFAD mice. Upper panel shows LSM single plane of Congo Red stained brains and closeups of the subiculum and a cortical region. Middle panel shows 3D distribution of isocortical and hippocampal plaques represented as centroids. Lower panel shows 2D maximum intensity projection of cropped regions of interest. Lower right shows 3D quantifications of plaque burden parameters in hippocampus and isocortex. n=6 for control, n=5 for Cup. (d) Neurological scoring shows successful EAE induction in 5xFAD animals with typical disease onset at around day 10 post induction. Lines represent single animals. n=5. (e) 3D quantifications of plaque burden in the brain of EAE/5xFAD animals. n=4 for control, n=5 for EAE. (f) Light sheet microscopic analysis of plaque burden in the lumbar spinal cord of EAE/5xFAD mice. No typical grey matter plaques could be detected in either 14 weeks old 5xFAD controls or EAE/5xFAD mice. The lumbar spinal cord was heavily affected by EAE lesions as visualised by Iba1 staining. (g) As positive control for successful detection of spinal cord plaques, a cervical spinal cord of a 6-month-old 5xFAD animal is shown. Throughout the panels, dots represent single animals and bars depict mean. Unpaired, two-tailed Student's t-test was performed for statistical analysis.

Extended Data Figure 4

bioRxiv preprint doi: <https://doi.org/10.1101/2021.07.31.454562>; this version posted August 2, 2021. The copyright holder for this preprint (which was not certified by peer review) is the author/funder. All rights reserved. No reuse allowed without permission.



Statistical analysis

C

Two-way-ANOVA Behavioural Testing CNP^{-/-} 5xFAD

	Parameter	F(1,33)	p	partial η^2	η^2 90% CI
EPM Track Length	5xFAD	35.02	< .001	0.51	[0.31, 0.65]
	CNP ^{-/-}	24.57	< .001	0.43	[0.21, 0.59]
	CNP ^{-/-} 5xFAD	8.94	0.005	0.21	[0.04, 0.40]
EPM Open Arm Time	5xFAD	34.25	< .001	0.51	[0.30, 0.65]
	CNP ^{-/-}	29.67	< .001	0.47	[0.26, 0.62]
	CNP ^{-/-} 5xFAD	6.89	0.013	0.17	[0.02, 0.36]
YM Alternation Index	5xFAD	0.82	0.372	0.02	[0.00, 0.16]
	CNP ^{-/-}	0.02	0.876	7.54E-04	[0.00, 0.05]
	CNP ^{-/-} 5xFAD	0.64	0.429	0.02	[0.00, 0.15]
YM Arm Entries	5xFAD	36.15	< .001	0.52	[0.32, 0.66]
	CNP ^{-/-}	43.91	< .001	0.57	[0.38, 0.70]
	CNP ^{-/-} 5xFAD	15.62	< .001	0.32	[0.12, 0.50]
Clasping Score	5xFAD	12.11	0.001	0.27	[0.08, 0.45]
	CNP ^{-/-}	42.73	< .001	0.56	[0.37, 0.69]
	CNP ^{-/-} 5xFAD	5.78	0.022	0.15	[0.01, 0.34]

d

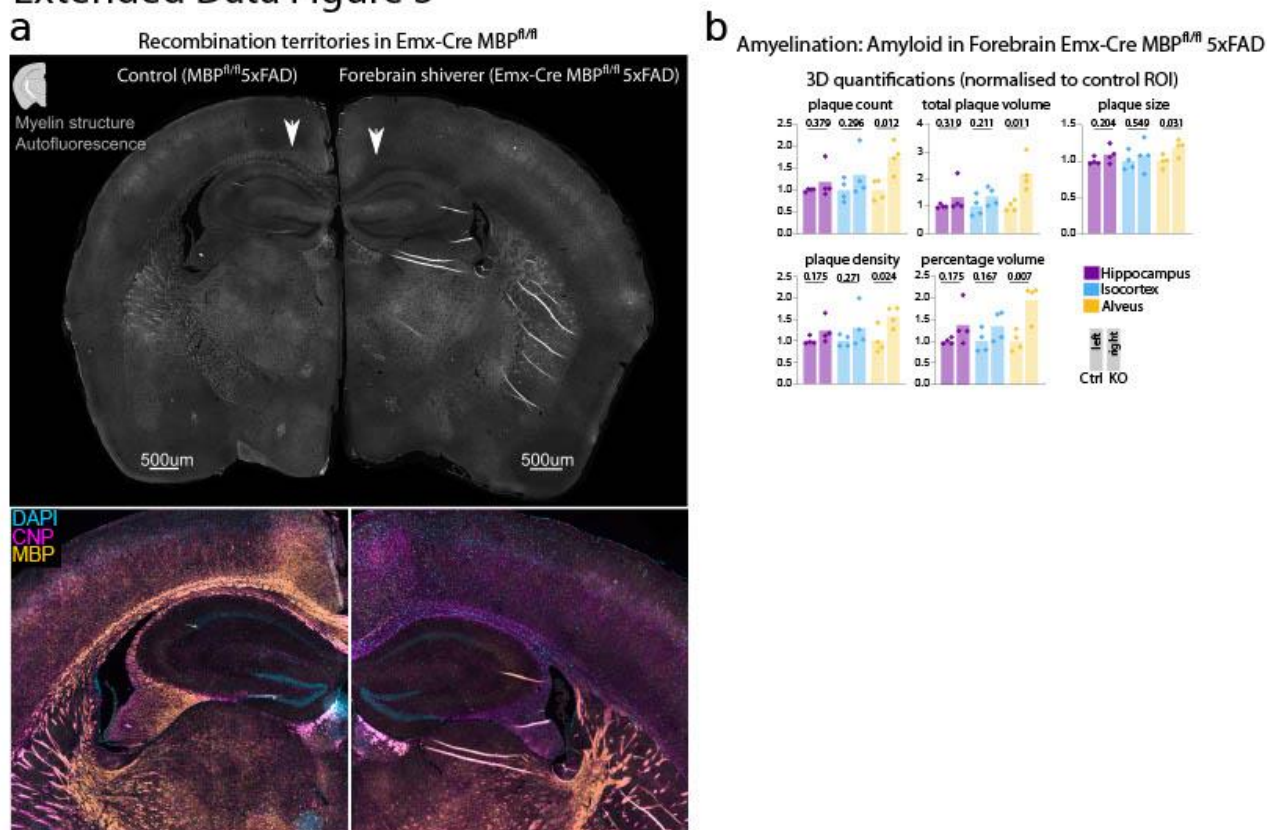
Two-way-ANOVA Behavioural Testing PLP^{-/-} 5xFAD

	Parameter	F(1,32)	p	partial η^2	η^2 90% CI
EPM Track Length	5xFAD	2.45	0.127	0.07	[0.00, 0.25]
	PLP ^{-/-}	13.74	< .001	0.3	[0.10, 0.49]
	PLP ^{-/-} 5xFAD	0.36	0.554	0.01	[0.00, 0.13]
EPM Open Arm Time	5xFAD	9.19	0.005	0.22	[0.05, 0.42]
	PLP ^{-/-}	6.5	0.016	0.17	[0.02, 0.36]
	PLP ^{-/-} 5xFAD	0.45	0.506	0.01	[0.00, 0.14]
YM Alternation Index	5xFAD	3.09	0.089	0.09	[0.00, 0.27]
	PLP ^{-/-}	0.12	0.733	3.68E-03	[0.00, 0.10]
	PLP ^{-/-} 5xFAD	0.03	0.86	9.94E-04	[0.00, 0.06]
YM Arm Entries	5xFAD	0.4	0.534	0.01	[0.00, 0.14]
	PLP ^{-/-}	16.45	< .001	0.34	[0.13, 0.52]
	PLP ^{-/-} 5xFAD	3.16E-05	0.996	9.89E-07	[0.00, 0.00]
Clasping Score	5xFAD	11.32	0.002	0.26	[0.07, 0.45]
	PLP ^{-/-}	20.89	< .001	0.4	[0.18, 0.56]
	PLP ^{-/-} 5xFAD	5.63	0.024	0.15	[0.01, 0.34]

Extended Data Figure 4. Myelin-dysfunction exacerbates behavioural deficits in 5xFAD mice

Behavioural analysis of mice in the elevated plus maze (EPM), Y maze (YM) and the claspings test. Middle panels show representative tracks in the respective maze and representative image of the claspings test. Right panel shows quantifications of behavioural parameters. Dots represent single animals, bars depict mean. (a) Behavioural analysis of CNP^{-/-} 5xFAD female mice. n=9 for CNP^{+/+}, n=8 CNP^{+/+} 5xFAD, n=9 for CNP^{-/-}, n=9 CNP^{-/-} 5xFAD (b) Behavioural analysis of PLP^{-/-} 5xFAD male mice. n=10 for PLP^{+/+}, n=8 PLP^{+/+} 5xFAD, n=8 for PLP^{-/-}, n=10 PLP^{-/-} 5xFAD (c,d) For statistical analysis, several different type III ANOVAs were performed for each behavioural test that probed the main effects for the 5xFAD genotype and the myelin-mutant genotype as well as their interaction.

Extended Data Figure 5

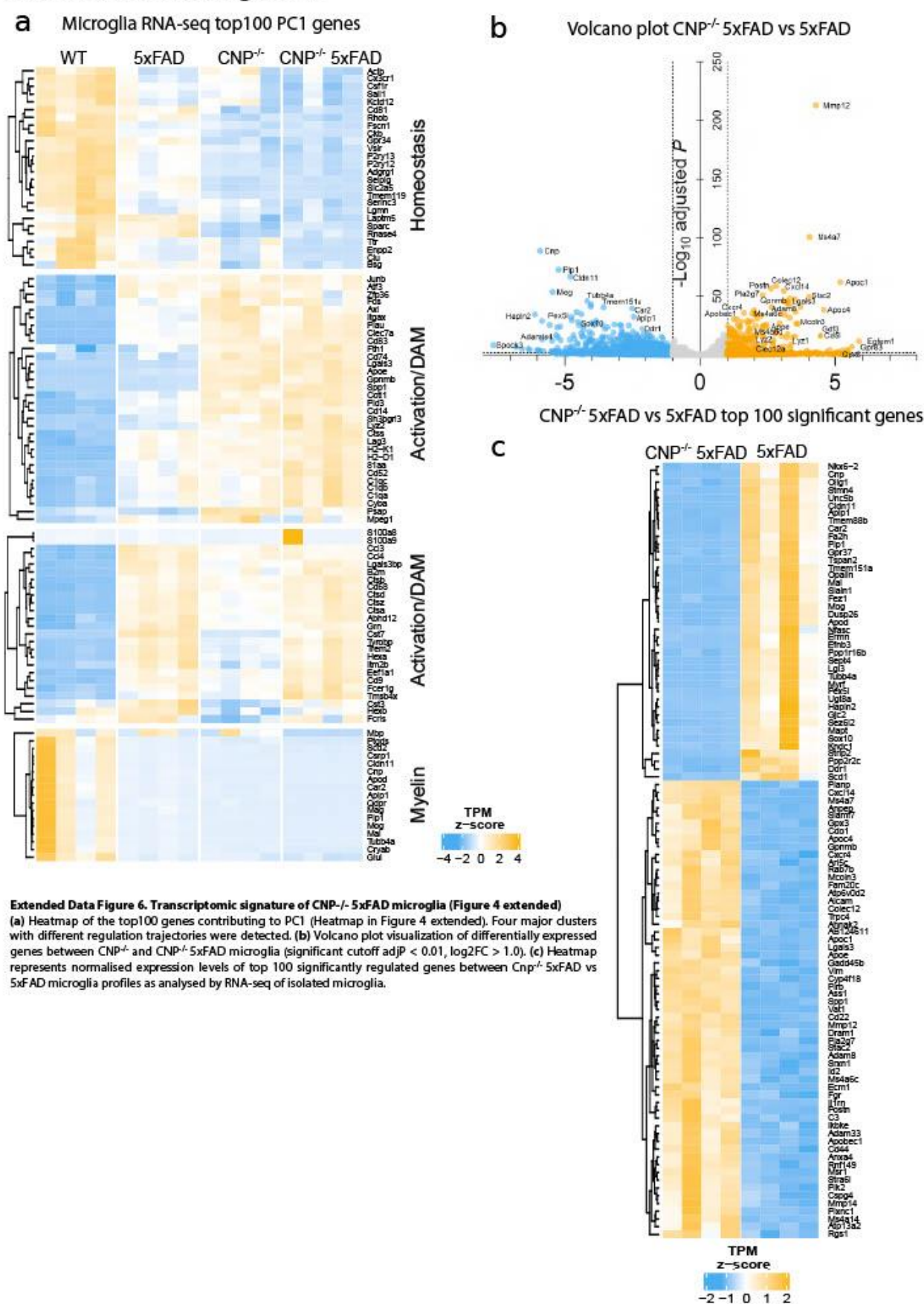


Extended Data Figure 5. Recombination territories and plaque load in 6-month-old forebrain shiverer/5xFAD mice

(a) Basic characterisation of myelination patterns in Emx-Cre MBP^{fl/fl} 5xFAD mice. Autofluorescence shows clear lack of myelinated profiles in corpus callosum (arrows) while thalamus and striatum show normal myelin profiles. Lower panel show closeup images of anti-CNP and MBP co-immunolabelling in Emx-Cre MBP^{fl/fl} 5xFAD. Lack of myelin compaction (MBP-CNP⁺) throughout cortex, hippocampus and subcortical white matter. Compaction of myelin is unaffected in other brain regions such as thalamus and striatum (MBP-CNP⁺). (b) Quantification of light sheet microscopic analysis of plaque load in 6-month-old Emx-Cre MBP^{fl/fl} 5xFAD mice. Dots represent single animals, bar depicts mean. Unpaired, two-sided Student's t-test was performed for statistical analysis for each ROI. n=4 for WT and cKO.

Extended Data Figure 6

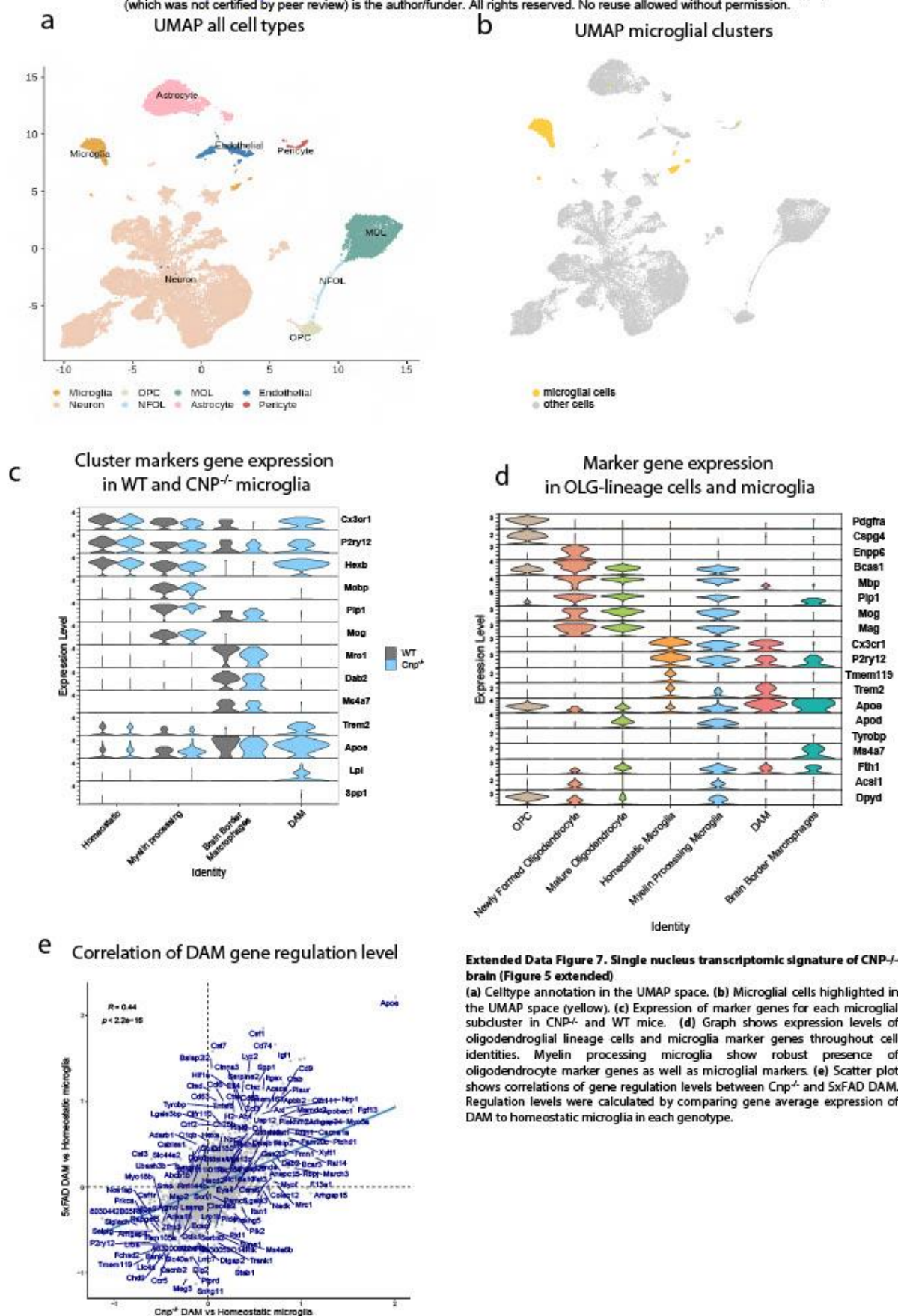
(which was not certified by peer review) is the author/funder. All rights reserved. No reuse allowed without permission.

Extended Data Figure 6. Transcriptomic signature of CNP^{-/-} 5xFAD microglia (Figure 4 extended)

(a) Heatmap of the top100 genes contributing to PC1 (Heatmap in Figure 4 extended). Four major clusters with different regulation trajectories were detected. (b) Volcano plot visualization of differentially expressed genes between CNP^{-/-} and CNP^{-/-} 5xFAD microglia (significant cutoff adj *P* < 0.01, log₂FC > 1.0). (c) Heatmap represents normalised expression levels of top 100 significantly regulated genes between CNP^{-/-} 5xFAD vs 5xFAD microglia profiles as analysed by RNA-seq of isolated microglia.

Extended Data Figure 7

bioRxiv preprint doi: <https://doi.org/10.1101/2021.07.31.454562>; this version posted August 2, 2021. The copyright holder for this preprint (which was not certified by peer review) is the author/funder. All rights reserved. No reuse allowed without permission.

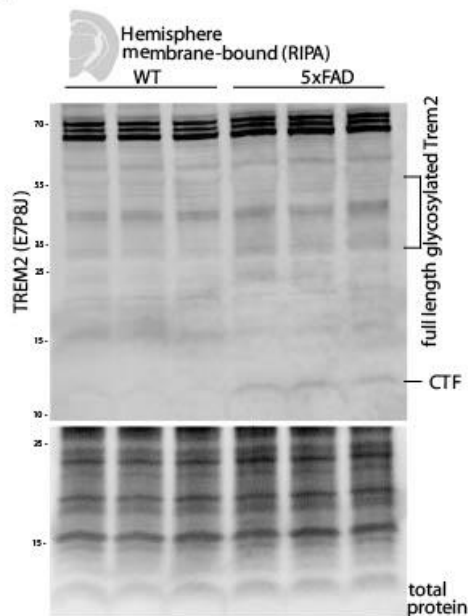


Extended Data Figure 7. Single nucleus transcriptomic signature of CNP^{-/-} brain (Figure 5 extended)

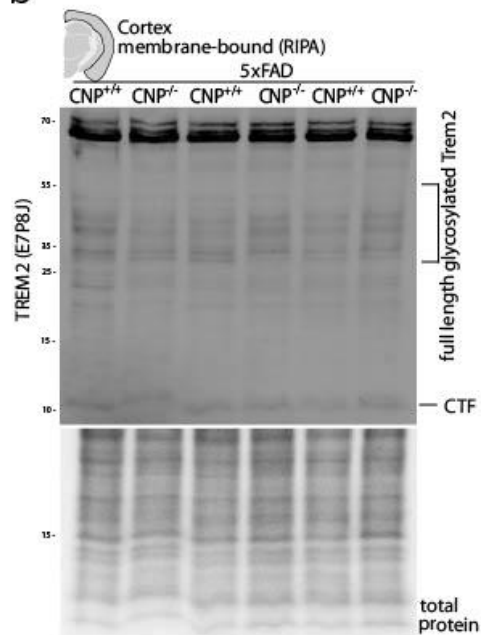
(a) Celltype annotation in the UMAP space. (b) Microglial cells highlighted in the UMAP space (yellow). (c) Expression of marker genes for each microglial subcluster in CNP^{-/-} and WT mice. (d) Graph shows expression levels of oligodendroglial lineage cells and microglia marker genes throughout cell identities. Myelin processing microglia show robust presence of oligodendrocyte marker genes as well as microglial markers. (e) Scatter plot shows correlations of gene regulation levels between CNP^{-/-} and 5xPAD DAM. Regulation levels were calculated by comparing gene average expression of DAM to homeostatic microglia in each genotype.

Extended Data Figure 8

a



b

**Extended Data Figure 8. Trem2 cleavage is not altered in CNP^{-/-} 5xFAD mice**

(a) Western blot analysis of Trem2 levels in WT vs 5xFAD mice shows clear induction of full length Trem2 (30-60kDa, glycosylated forms) and enhanced Trem2 cleavage (~12kDa) in 5xFAD mice. n=3 per group. Lanes present single animals. (b) Western blot analysis of Trem2 levels in CNP^{-/-} 5xFAD and 5xFAD mice shows no differences in Trem2 cleavage. Total protein fastgreen staining is shown as loading control. n=3 per group. Lanes present single animals.

Chapter 5: Discussion and conclusion

5.1 Study the upstream role of oligodendrocyte and myelin dysfunctions

The core question of this thesis: *if and how oligodendrocyte and myelin dysfunction can be an upstream risk factor for CNS pathologies*, was raised based on decades of extensive studies on aging and neurological diseases. In many pathological characterizations, across brain aging, AD, PD, MS, TBI, ALS, myelin macro and micro structural health were reported to be challenged (Hill, Li, and Grutzendler 2018; Nasrabady et al. 2018; Jang et al. 2017; Ettle, Schlachetzki, and Winkler 2016; Sams 2021; Dean et al. 2016; Alizadeh, Dyck, and Karimi-Abdolrezaee 2015; Berginström et al. 2020). Naturally, myelin damage was concluded as a hallmark in aging and many CNS diseases (Figure 1). Yet, if we consider the dynamics of myelination in humans, where the decline starts at an age of around 50 years, it is generally before the typical onset of neurodegenerative (George Bartzokis 2011). Hypothetically, relatively early myelin breakdown could gradually vulnerate the CNS environment to eventually succumb to the provocations of genetic or environmental disease risk factors (Braak and Del Tredici 2004; G. Bartzokis 2004; Ettle, Schlachetzki, and Winkler 2016).

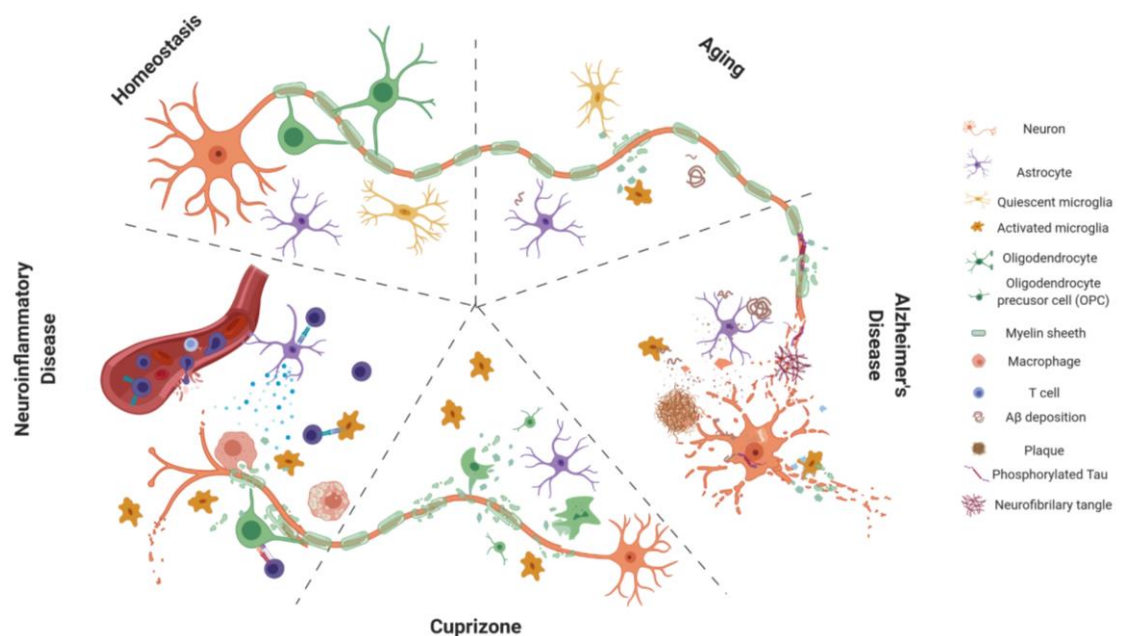


Figure 1. Schematic figure of physiopathological features in homeostatic, aging, AD, cuprizone treated, or neuroinflammation disease brain. In all pathological states, myelin health is influenced. In the cuprizone model, oligodendrocytes also undergo apoptosis. Created with BioRender.com.

To verify an upstream role of oligodendrocyte and myelin dysfunctions in the context of disease is a challenging task. Numerous animal models have been established to mimic neurological disease or primary oligodendropathy. Although disease models normally lack control of the pathology onset orders. Whereas in primary oligodendropathy models such as EAE or cuprizone, demyelination is acutely induced and would trigger intense neuroinflammation, which is not suitable for studying the effect of chronic myelin damage (Torkildsen et al. 2008; Constantinescu et al. 2011). Luckily, in order to study myelin-associated protein functions, mutant mouse lines with varying degrees of myelin dysfunction were generated. Among the myelin mutant models, some show chronic myelin instabilities without severely influencing the overall myelin sheath morphology. These models provide a viable environment to study myelin dysfunction-derived CNS changes (K-A Nave 1994; Klaus-Armin Nave and Werner 2014; Stassart et al. 2018).

Thus, in this thesis, mouse models with chronic defective myelination were widely applied for the investigation of oligodendrocyte and myelin intrinsic pathological signals. Different from previous studies that focused on phenotypic changes, projects in this thesis first concentrated on deciphering the gene regulatory networks in the mutants in a celltype-specific and high-resolution manner, and second exposed the mutant environments to the most well researched neurodegenerative disease, Alzheimer's Disease (AD). From this, molecular footprints underlying myelin dysfunction-associated phenotypes were unfolded, which shed light on further mechanistically untangling the vicious cycles observed in aging and brain diseases.

5.2 The butterfly effect: split differences in MOL subpopulation profiles

One of the key discoveries from project I is the unusually shifted MOL subpopulations among different myelin mutants. As the project already discussed, ever since data integrative analysis was effectively used for high-resolution data batch effects correction, such enlargement of one specific subpopulation was not reported from various CNS cell types, including oligodendrocyte under spinal cord injury condition (Keren-Shaul et al. 2017; Schirmer et al. 2019; Hammond et al. 2019; Grubman et al. 2019; Zhou et al. 2020; Habib et al. 2020; Floriddia et al. 2020). Even more interestingly, the expanded MOL subpopulation is different in each recruited myelin mutant. It was absolutely puzzling how this could have happened, and what it meant as a reflection of oligodendrocyte cell properties.

An important inspiration to interpret this result came from the analysis work of microglia RNA profiles for project II. There, an activated microglia subtype, DAM, was discovered in the *Cnp*^{-/-} mutant model. Verification of the DAM population was

conducted by integrative analysis with publicly available snRNA-seq datasets of 5xFAD mouse brains (Zhou et al. 2020). However, when comparing specific gene expressions to the 5xFAD DAM, the *Cnp*^{-/-} DAM showed a slight upregulation of genes related to lipid handling and lowered expression of *Trem2* and *Tyrobp* which are important for DAM differentiation. The upregulation of *Abca1* and *Lpl* in the *Cnp*^{-/-} DAM partially overlaps with white matter-associated microglia (WAM) that has been described by Safaiyan and colleagues (Safaiyan et al. 2021). WAM was initially identified to have a very similar RNA profile to DAM and may represent a precursor stage of microglia prior to their conversion to DAM. Taken together, this suggests that myelin mutant DAM is situated at an even more intermediate stage between WAM and DAM.

To a certain extent, concentrated shifts of MOL subpopulations in myelin mutants presented a similar situation with the fine-tuned microglia gene signatures and cell states in aging, AD, and *Cnp*^{-/-} DAMs. Indeed, using state-of-the-art analysis approaches, all identified MOL subpopulations were positioned on a tightly connected manifold, indicating these subpopulations are well related and connected. What shall be kept in mind is that the recruited myelin mutants might exhibit chronic pathological phenotypes. But, at the molecular level, oligodendrocytes in these mutants actually get non-trivial challenges. The null expression of CNP, PLP1, or MBP means a loss of one of the top three myelin-essential proteins. Yet, mutant MOLs would mediate transcriptome profiles within a close range of cell homeostasis. Even under more severe system hits, such as EAE and spinal cord injury, MOLs still adapt subpopulation proportions within the physiological existent subtypes (Floriddia et al. 2020; Wheeler et al. 2020).

Nevertheless, amazingly, the split differences of MOL subpopulations potentially prompted way more obvious functional diversities like triggering a butterfly effect, that might be involved in the construction or contribution to traceable features including myelin spatial and temporal heterogeneities, local de- and re-myelination, and diverse ensheathment of axons (Marques et al. 2016; Micheva et al. 2016; Tomassy, Dershowitz, and Arlotta 2016; Call and Bergles 2021; Floriddia et al. 2020; Li et al. 2020). How MOLs can be so closely regulated at the transcriptome level and whether there are master regulators that control/restrict the cell profiles are still open questions that require further investigation. Moreover, certain shifts, such as to the subcluster MOL4 which was enriched in the *Cnp*^{-/-} mutant, showed enhanced interactions with activated microglia subpopulations. Along with the imaging analysis of *Cnp*^{-/-} 5xFAD mouse brains, it is also unclear whether direct MOL and microglia cell crosstalks contributed to the distraction of microglia to myelin engulfment rather than plaque corralling.

5.3 A Hamlet question: no myelin or bad myelin?

From an evolutionary point of view, myelin was a novel invention in higher vertebrates concomitant with the acquisition of hinged jaw, i.e. the gnathostoma, for the purpose of increasing the propagation of nerve action potentials (Zalc 2006). In the big picture, myelin is definitely a successful development for vertebrates (Zalc 2006; Klaus-Armin Nave and Werner 2021). Besides its major function of ensheathing axons and enabling saltatory signal propagation, myelination by oligodendrocytes also provides critical structural and trophic support to the axons and actively participates in cellular communications (Klaus-Armin Nave and Werner 2014; Klaus-Armin Nave 2010b, [a] 2010; Stassart et al. 2018; Safaiyan et al. 2016; Domingues et al. 2016). Although inevitably, the myelination process and the maintenance of compact myelin require a whole new set of energy supply and regulatory controls (Macklin and Rasband 2012). Disturbance of myelin generation and maintenance could therefore result in a cascade of pathological changes (Braak and Del Tredici 2004; Stassart et al. 2018).

Interestingly, in cases where oligodendrocyte and myelin are malfunctioning, many signs suggested that it probably would have been easier if the system can temporarily remove the burden of handling disturbed myelin, or myelin-associated molecules. Typically in Pelizaeus-Merzbacher disease (PMD), an X-linked hypomyelination disease caused by mutations in the *Plp1* gene, missense mutations generating misfolded proteins would lead to more severe phenotypes compared to nonsense mutation or deletion of the *Plp1* (Yamamoto and Shimojima 2013). In the corresponding animal models, suppression of *Plp1* expression in *Plp1^{ip}*, a severe point-mutation PMD mouse model, showed amelioration of the disease phenotypes (Eliott et al. 2020).

Obviously, complete loss of compact myelin does not benefit the system. Such as in the shiverer mouse model, where the absence of MBP leads to amyelinated axons and shows severe pathology with a short lifespan (Readhead and Hood 1990; Readhead et al. 1987). However, when only forebrain myelin is missing such as in the *Emx-Cre Mbp^{fl/fl}* and *Foxg1-Cre Mbp^{fl/fl}* mutants, animals do not exhibit strong phenotypes. In addition, the absence of compact myelin in the forebrain significantly delayed A β plaque depositions in the cortical region. At the transcriptome level, the dysmyelination did not trigger aggressive gliosis. Instead, microglia in *Foxg1-Cre Mbp^{fl/fl}* mutant cortex and corpus callosum showed elevated uptake of myelin transcripts which was potentially caused by the constant attempt of oligodendrocytes producing new but non-compacted myelin. Conversely, plaque load in the *Cnp^{-/-} 5xFAD* and *Plp^{-/-} 5xFAD* mutant brains was significantly increased compared to normal 5xFAD. Considering that defect myelin influences axonal vesicle transport leading to axonal swellings (Stassart et al. 2018; Bartzokis 2011),

it is attractive to assume and verify that increases in plaque load are in part caused by alteration in local APP metabolism at the myelin dysfunction induced-swelling site. In parallel, in the more severe *Cnp*^{-/-} 5xFAD mutant, activated microglia are distracted by myelin perturbations and can not handle A β plaques efficiently. Under acute demyelination like MS, not only myelin is actively attacked by microglia and peripheral immune cells, OPCs and MOLs were also shown to express genes related to the immune receptors MHC-I and MHC-II which could further worsen the inflammatory environment (Falcão et al. 2018; Jäkel et al. 2019; Meijer et al., n.d.).

Taken together, the presence of myelin is of course essential for the overall normal function of the brain. Although, one could argue that the temporary removal of problematic myelin or myelin-associated molecules might help/ be sufficient to put a brake on the vicious cycle of pathologies. A similar concept was proposed for microglia, where depletion and repopulation of microglia at correct time points showed beneficial effects in the context of diseases, as well as in myelin mutants (Coleman, Zou, and Crews 2020; Elmore et al. 2018; Spangenberg et al. 2019; Garcia-Agudo et al. 2019). However, a controversial result of microglia depletion in a spinal cord injury model suggested that the role of the cell and its products should be carefully evaluated before applying removal therapy (Fu et al. 2020). Furthermore, treatment for oligodendrocyte and myelin is apparently a more difficult task compared to microglia depletion due to the unique compacted structure of myelin. For this, precise recognition of pathological responsible cell subpopulation, gene regulation, and even spatial location would be required in future investigations.

5.4 Balance between cell subpopulation discovery and interpretation

High-resolution, especially single-cell level transcriptome sequencing brought evolutionary development in neuroscience research (Mayer et al. 2019). Whilst at the same time, it dramatically increased the amount of collected data and until now still challenges the canonical way of bioinformatic analysis (Lähnemann et al. 2020). From several samples to hundreds of thousands of cells, scRNA-seq data reached ultra dimensionality and complicated the analysis pipeline in a way that can not only rely on linear approaches (Oskolkov 2021). Non-linear dimensionality reduction was widely applied for the purpose of revealing novel or disease-responsive cell subpopulations. In the beginning, this workflow helped the discovery of several important cell subpopulations, including DAM, immunological oligodendrocyte, MS vulnerable astrocytes and neurons (Keren-Shaul et al. 2017; Jäkel et al. 2019; Wheeler et al. 2020; Schirmer et al. 2019). However, it soon became clear that neighboring embedding and clustering work with relative profile distances, can segregate as many clusters as the analysis resolution requires.

Determination of optimal cluster numbers is one of the solutions to control the analysis process (Patil and Baidari 2019; Alade 2018). On the other hand, integrative analysis using previous studies could offer more anchor points between the *in silico* calculations and biologically relevant information (Stuart et al. 2019; Butler et al. 2018). Indeed in this thesis, in addition to close evaluation of dataset-specific embedding parameters, multiple high-quality external datasets were recruited for interpreting the potential shifts of biological relevant cell subpopulations. It also became clear that to correlate cell subpopulations across single-cell resolution datasets that used different platforms and sequencing setups, simply matching the subpopulation marker genes is a suboptimal approach compared to integrating datasets in a common low-dimensional space based on the unbiased calculation of their shared features (Stuart et al. 2019; Butler et al. 2018).

More interestingly, several recent research, including projects of this thesis, showed subpopulations with split different profiles from previously reported cell subsets (Safaiyan et al. 2021; Schirmer et al. 2019; Zhou et al. 2020; Habib et al. 2020). From a biological standpoint, such inch-perfect connections of cellular profiles are actually more realistic. However, even with the advent of scRNA-seq, each cell is only able to be sequenced for a limited amount of transcripts which is far from the real ‘whole transcriptome’. Therefore, it is imaginable that the footprint of transcriptome regulations was lost or disconnected at the parts which are dependent on low-expressed genes. To tackle this problem, new models, represented by pseudotime analysis and RNA velocity, which aim at recovering the cell connectivities, were developed (Amezquita et al. 2020; La Manno et al. 2018; Bergen et al. 2020; Lange et al. 2020). Especially using the RNA velocity model, the connections between each single-cell data point can be evaluated. But as a downside, the projection of cell velocity is still borrowing one of the embedded cell maps (PCA, t-SNE, UMAP), and disconnections on such maps will also be adapted to the velocity calculation. Recently, Atta et al. proposed RNA-velocity informed embedding of cell profiles, which improved the accuracy of cell manifold recoveries (Atta, Sahoo, and Fan, n.d.).

5.5 Conclusion and open questions

In conclusion, this thesis systematically investigated and characterized the tightly connected transcriptomic footprints of oligodendrocytes under healthy and mutant conditions. Moreover, in this study, downstream effects caused by abnormalities in oligodendrocyte and myelin on other cell types in the brain were analyzed. Overall, the projects provided base models to study the primary role of oligodendrocyte and myelin dysfunctions in the context of aging and neurological diseases.

Additionally, apart from the open questions that have been addressed in the thesis, there are some more interesting points that are worth investigating in the future. Of which, one of the major concerns is the translation of research results from mouse models to real human aging or disease conditions. As a future direction, comprehensive analyses would be applied to human and mouse single-cell resolution data with the focus on cross-comparing the heterogeneous responses of oligodendrocytes across different CNS pathologies. Last but not least, changes in the aging brain and under pathological conditions are highly complicated and involve cooperative responses from different cell types. Therefore, using the advantage of already detected cell heterogeneities, it is crucial to revisit the explorations of inter-and intra-cellular interaction networks to solve the enigmas of brain disorders.

References

- “Accuracy.” n.d. Accessed August 10, 2021. <http://nanoporetech.com/accuracy>.
- Adams, M., J. Kelley, J. Gocayne, M. Dubnick, M. Polymeropoulos, H. Xiao, C. Merrill, et al. 1991. “Complementary DNA Sequencing: Expressed Sequence Tags and Human Genome Project.” *Science*. <https://doi.org/10.1126/science.2047873>.
- Alade, Tola. 2018. “Tutorial: How to Determine the Optimal Number of Clusters for K-Means Clustering.” Cambridge Spark. May 27, 2018. <https://blog.cambridgespark.com/how-to-determine-the-optimal-number-of-clusters-for-k-means-clustering-14f27070048f>.
- Aldridge, Sarah, and Sarah A. Teichmann. 2020. “Single Cell Transcriptomics Comes of Age.” *Nature Communications* 11 (1): 1–4.
- Alizadeh, Arsalan, Scott M. Dyck, and Soheila Karimi-Abdolrezaee. 2015. “Myelin Damage and Repair in Pathologic CNS: Challenges and Prospects.” *Frontiers in Molecular Neuroscience* 0. <https://doi.org/10.3389/fnmol.2015.00035>.
- Amezquita, Robert A., Aaron T. L. Lun, Etienne Becht, Vince J. Carey, Lindsay N. Carpp, Ludwig Geistlinger, Federico Marini, et al. 2020. “Orchestrating Single-Cell Analysis with Bioconductor.” *Nature Methods* 17 (2): 137–45.
- Anderson, Matthew W., and Iris Schrijver. 2010. “Next Generation DNA Sequencing and the Future of Genomic Medicine.” *Genes*. <https://doi.org/10.3390/genes1010038>.
- Ando, Susumu, Yasukazu Tanaka, Yuriko Toyoda, and Kazuo Kon. 2003. “Turnover of Myelin Lipids in Aging Brain.” *Neurochemical Research* 28 (1): 5–13.
- Ando, Yoshinari, Andrew Tae-Jun Kwon, and Jay W. Shin. 2020. “An Era of Single-Cell Genomics Consortia.” *Experimental & Molecular Medicine* 52 (9): 1409–18.
- “A Single-Cell Transcriptomic Atlas Characterizes Ageing Tissues in the Mouse.” 2020. *Nature* 583 (7817): 590–95.
- Atta, Lyla, Arpan Sahoo, and Jean Fan. n.d. “VeloViz: RNA-Velocity Informed Embeddings for Visualizing Cellular Trajectories.” <https://doi.org/10.1101/2021.01.28.425293>.
- Ayata, Pinar, Ana Badimon, Hayley J. Strasburger, Mary Kaye Duff, Sarah E. Montgomery, Yong-Hwee E. Loh, Anja Ebert, et al. 2018. “Epigenetic Regulation of Brain Region-Specific Microglia Clearance Activity.” *Nature Neuroscience* 21 (8): 1049–60.
- Baltan, Selva, Safdar S. Jawaid, Anthony M. Chomyk, Grahame J. Kidd, Jacqueline Chen, Harsha D. Battapady, Ricky Chan, Ranjan Dutta, and Bruce D. Trapp. 2021. “Neuronal Hibernation Following Hippocampal Demyelination.” *Acta Neuropathologica Communications* 9 (1): 1–15.
- Bartzokis, G. 2004. “Age-Related Myelin Breakdown: A Developmental Model of Cognitive Decline and Alzheimer’s Disease.” *Neurobiology of Aging* 25 (1). <https://doi.org/10.1016/j.neurobiolaging.2003.03.001>.
- Bartzokis, George. 2011. “Alzheimer’s Disease as Homeostatic Responses to Age-Related Myelin Breakdown.” *Neurobiology of Aging* 32 (8): 1341–71.
- Bartzokis, George, Mace Beckson, Po H. Lu, Keith H. Nuechterlein, Nancy Edwards, and Jim Mintz. 2001. “Age-Related Changes in Frontal and Temporal Lobe Volumes in Men: A Magnetic Resonance Imaging Study.” *Archives of General Psychiatry* 58 (5): 461–65.
- Baumann, Nicole, and Danielle Pham-Dinh. 2001. “Biology of Oligodendrocyte and Myelin in the Mammalian Central Nervous System.” *Physiological Reviews*.

- <https://doi.org/10.1152/physrev.2001.81.2.871>.
- Bengtsson, Martin, Martin Hemberg, Patrik Rorsman, and Anders Ståhlberg. 2008. "Quantification of mRNA in Single Cells and Modelling of RT-qPCR Induced Noise." *BMC Molecular Biology* 9 (July): 63.
- Bergen, Volker, Marius Lange, Stefan Peidli, F. Alexander Wolf, and Fabian J. Theis. 2020. "Generalizing RNA Velocity to Transient Cell States through Dynamical Modeling." *Nature Biotechnology* 38 (12): 1408–14.
- Berginström, Nils, Peter Nordström, Lars Nyberg, and Anna Nordström. 2020. "White Matter Hyperintensities Increases with Traumatic Brain Injury Severity: Associations to Neuropsychological Performance and Fatigue." *Brain Injury: [BI]* 34 (3): 415–20.
- Bozzali, M., A. Falini, M. Franceschi, M. Cercignani, M. Zuffi, G. Scotti, G. Comi, and M. Filippi. 2002. "White Matter Damage in Alzheimer's Disease Assessed in Vivo Using Diffusion Tensor Magnetic Resonance Imaging." *Journal of Neurology, Neurosurgery, and Psychiatry* 72 (6): 742–46.
- Braak, Heiko, and Kelly Del Tredici. 2004. "Poor and Protracted Myelination as a Contributory Factor to Neurodegenerative Disorders." *Neurobiology of Aging*.
- Brown, Terence A. 2002. "The Human Genome." In *Genomes. 2nd Edition*. Wiley-Liss.
- Butler, Andrew, Paul Hoffman, Peter Smibert, Efthymia Papalexi, and Rahul Satija. 2018. "Integrating Single-Cell Transcriptomic Data across Different Conditions, Technologies, and Species." *Nature Biotechnology* 36 (5): 411–20.
- Call, Cody L., and Dwight E. Bergles. 2021. "Cortical Neurons Exhibit Diverse Myelination Patterns That Scale between Mouse Brain Regions and Regenerate after Demyelination." *Nature Communications* 12 (1): 4767.
- Capolupo, Laura, Irina Khven, Luigi Mazzeo, Galina Glousker, Francesco Russo, Jonathan Paz Montoya, Sylvia Ho, et al. 2021. "Sphingolipid Control of Fibroblast Heterogeneity Revealed by Single-Cell Lipidomics." *bioRxiv*. <https://doi.org/10.1101/2021.02.23.432420>.
- "Chapter 18 Trajectory Analysis." n.d. Accessed August 12, 2021. <https://github.com/Bioconductor/OrchestratingSingleCellAnalysis>.
- Chen, Jing-Fei, Kun Liu, Bo Hu, Rong-Rong Li, Wendy Xin, Hao Chen, Fei Wang, et al. 2021. "Enhancing Myelin Renewal Reverses Cognitive Dysfunction in a Murine Model of Alzheimer's Disease." *Neuron*. <https://doi.org/10.1016/j.neuron.2021.05.012>.
- Chen, Wei-Ting, Ashley Lu, Katleen Craessaerts, Benjamin Pavie, Carlo Sala Frigerio, Nikky Corthout, Xiaoyan Qian, et al. 2020. "Spatial Transcriptomics and In Situ Sequencing to Study Alzheimer's Disease." *Cell* 182 (4): 976–91.e19.
- Cohen, Joel E. 2004. "Mathematics Is Biology's Next Microscope, Only Better; Biology Is Mathematics' Next Physics, Only Better." *PLoS Biology* 2 (12): e439.
- Coleman, Leon G., Jian Zou, and Fulton T. Crews. 2020. "Microglial Depletion and Repopulation in Brain Slice Culture Normalizes Sensitized Proinflammatory Signaling." *Journal of Neuroinflammation* 17 (1): 1–20.
- Constantinescu, Cris S., Nasr Farooqi, Kate O'Brien, and Bruno Gran. 2011. "Experimental Autoimmune Encephalomyelitis (EAE) as a Model for Multiple Sclerosis (MS)." *British Journal of Pharmacology*. <https://doi.org/10.1111/j.1476-5381.2011.01302.x>.
- Davidson, Eric H., and Isabelle S. Peter. 2015. "Gene Regulatory Networks." *Genomic Control Process*. <https://doi.org/10.1016/b978-0-12-404729-7.00002-2>.
- Dean, Douglas C., III, Jitka Sojkova, Samuel Hurley, Steven Kecskemeti, Ozioma Okonkwo, Barbara B. Bendlin, et al. 2016. "Alterations of Myelin Content in

- Parkinson's Disease: A Cross-Sectional Neuroimaging Study." *PloS One* 11 (10). <https://doi.org/10.1371/journal.pone.0163774>.
- "Diversity of Oligodendrocytes and Their Progenitors." 2017. *Current Opinion in Neurobiology* 47 (December): 73–79.
- Domingues, Helena S., Camila C. Portugal, Renato Socodato, and João B. Relvas. 2016. "Oligodendrocyte, Astrocyte, and Microglia Crosstalk in Myelin Development, Damage, and Repair." *Frontiers in Cell and Developmental Biology* 0. <https://doi.org/10.3389/fcell.2016.00071>.
- Draghici, Sorin. 2016. *Statistics and Data Analysis for Microarrays Using R and Bioconductor*. CRC Press.
- Dwight E. Bergles, William D. Richardson. 2016. "Oligodendrocyte Development and Plasticity." *Cold Spring Harbor Perspectives in Biology* 8 (2). <https://doi.org/10.1101/cshperspect.a020453>.
- Eberwine, J., H. Yeh, K. Miyashiro, Y. Cao, S. Nair, R. Finnell, M. Zettel, and P. Coleman. 1992. "Analysis of Gene Expression in Single Live Neurons." *Proceedings of the National Academy of Sciences*. <https://doi.org/10.1073/pnas.89.7.3010>.
- Elitt, Matthew S., Lilianne Barbar, H. Elizabeth Shick, Berit E. Powers, Yuka Maeno-Hikichi, Mayur Madhavan, Kevin C. Allan, et al. 2020. "Suppression of Proteolipid Protein Rescues Pelizaeus-Merzbacher Disease." *Nature* 585 (7825): 397–403.
- Elmore, Monica R. P., Lindsay A. Hohsfield, Enikő A. Kramár, Lilach Soreq, Rafael J. Lee, Stephanie T. Pham, Allison R. Najafi, et al. 2018. "Replacement of Microglia in the Aged Brain Reverses Cognitive, Synaptic, and Neuronal Deficits in Mice." *Aging Cell*. <https://doi.org/10.1111/ace.12832>.
- Eng, C. L., M. Lawson, Q. Zhu, R. Dries, N. Koulana, Y. Takei, J. Yun, et al. 2019. "Transcriptome-Scale Super-Resolved Imaging in Tissues by RNA seqFISH." *Nature* 568 (7751). <https://doi.org/10.1038/s41586-019-1049-y>.
- Ettle, Benjamin, Johannes C. M. Schlachetzki, and Jürgen Winkler. 2016. "Oligodendroglia and Myelin in Neurodegenerative Diseases: More Than Just Bystanders?" *Molecular Neurobiology* 53 (5): 3046.
- Ewa Papuč, Konrad Rejdak. 2020. "The Role of Myelin Damage in Alzheimer's Disease Pathology." *Archives of Medical Science: AMS* 16 (2): 345.
- Falcão, Ana Mendanha, David van Bruggen, Sueli Marques, Mandy Meijer, Sarah Jäkel, Eneritz Agirre, Samudyata, et al. 2018. "Disease-Specific Oligodendrocyte Lineage Cells Arise in Multiple Sclerosis." *Nature Medicine* 24 (12): 1837–44.
- Floriddia, Elisa M., Tânia Lourenço, Shupe Zhang, David van Bruggen, Markus M. Hilscher, Petra Kukanja, João P. Gonçalves Dos Santos, et al. 2020. "Distinct Oligodendrocyte Populations Have Spatial Preference and Different Responses to Spinal Cord Injury." *Nature Communications* 11 (1): 5860.
- Forcato, Mattia, Oriana Romano, and Silvio Bicciato. 2020. "Computational Methods for the Integrative Analysis of Single-Cell Data." *Briefings in Bioinformatics* 22 (3). <https://doi.org/10.1093/bib/bbaa042>.
- Fu, Haitao, Yanpeng Zhao, Die Hu, Song Wang, Tengbo Yu, and Licheng Zhang. 2020. "Depletion of Microglia Exacerbates Injury and Impairs Function Recovery after Spinal Cord Injury in Mice." *Cell Death & Disease*. <https://doi.org/10.1038/s41419-020-2733-4>.
- Fünfschilling, Ursula, Lotti M. Supplie, Don Mahad, Susann Boretius, Aiman S. Saab, Julia Edgar, Bastian G. Brinkmann, et al. 2012. "Glycolytic Oligodendrocytes Maintain Myelin and Long-Term Axonal Integrity." *Nature* 485 (7399): 517–21.
- Garcia-Agudo, Laura Fernandez, Hana Janova, Lea E. Sandler, Sahab Arinrad, Agnes A.

- Steixner, Imam Hassouna, Evan Balmuth, et al. 2019. “Genetically Induced Brain Inflammation by Deletion Transiently Benefits from Microglia Depletion.” *FASEB Journal: Official Publication of the Federation of American Societies for Experimental Biology* 33 (7): 8634–47.
- Gatto, Laurent, and Andy Christoforou. 2014. “Using R and Bioconductor for Proteomics Data Analysis.” *Biochimica et Biophysica Acta* 1844 (1 Pt A): 42–51.
- Geldert, Alisha, Haiyan Huang, and Amy E. Herr. 2020. “Probe-Target Hybridization Depends on Spatial Uniformity of Initial Concentration Condition across Large-Format Chips.” *Scientific Reports* 10 (1): 1–12.
- Gong, Wuming, Bhairab N. Singh, Pruthvi Shah, Satyabrata Das, Joshua Theisen, Sunny Chan, Michael Kyba, et al. n.d. “A Novel Algorithm for the Collective Integration of Single Cell RNA-Seq during Embryogenesis.” <https://doi.org/10.1101/543314>.
- “Good Data, Bad Data and Ugly Data.” 2019. *Nature Microbiology* 4 (2): 209–209.
- Gopalakrishnan, Gopakumar, Anshul Awasthi, Wiam Belkaid, Omar De Faria Jr, Dalinda Liazoghli, David R. Colman, and Ajit S. Dhaunchak. 2013. “Lipidome and Proteome Map of Myelin Membranes.” *Journal of Neuroscience Research* 91 (3): 321–34.
- Griffiths, I., M. Klugmann, T. Anderson, D. Yool, C. Thomson, M. H. Schwab, A. Schneider, et al. 1998. “Axonal Swellings and Degeneration in Mice Lacking the Major Proteolipid of Myelin.” *Science* 280 (5369): 1610–13.
- Grosselin, Kevin, Adeline Durand, Justine Marsolier, Adeline Poitou, Elisabetta Marangoni, Fariba Nemati, Ahmed Dahmani, et al. 2019. “High-Throughput Single-Cell ChIP-Seq Identifies Heterogeneity of Chromatin States in Breast Cancer.” *Nature Genetics* 51 (6): 1060–66.
- Grubman, Alexandra, Gabriel Chew, John F. Ouyang, Guizhi Sun, Xin Yi Choo, Catriona McLean, Rebecca K. Simmons, et al. 2019. “A Single-Cell Atlas of Entorhinal Cortex from Individuals with Alzheimer’s Disease Reveals Cell-Type-Specific Gene Expression Regulation.” *Nature Neuroscience* 22 (12): 2087–97.
- Grubman, Alexandra, Xin Yi Choo, Gabriel Chew, John F. Ouyang, Guizhi Sun, Nathan P. Croft, Fernando J. Rossello, et al. 2021. “Transcriptional Signature in Microglia Associated with A β Plaque Phagocytosis.” *Nature Communications* 12 (1): 1–22.
- Grydeland, Håkon, Petra E. Vértés, František Váša, Rafael Romero-Garcia, Kirstie Whitaker, Aaron F. Alexander-Bloch, Atle Bjørnerud, et al. 2018. “Waves of Maturation and Senescence in Micro-Structural MRI Markers of Human Cortical Myelination over the Lifespan.” *Cerebral Cortex* 29 (3): 1369–81.
- Gupta, Rajaneesh, and Nilkantha Sen. 2016. “Traumatic Brain Injury: A Risk Factor for Neurodegenerative Diseases.” *Reviews in the Neurosciences*. <https://doi.org/10.1515/revneuro-2015-0017>.
- Gyllenstein, L., and T. Malmfors. 1963. “Myelinization of the Optic Nerve and Its Dependence on Visual Function--a Quantitative Investigation in Mice.” *Journal of Embryology and Experimental Morphology* 11 (March): 255–66.
- Habib, Naomi, Inbal Avraham-Davidi, Anindita Basu, Tyler Burks, Karthik Shekhar, Matan Hofree, Sourav R. Choudhury, et al. 2017. “Massively Parallel Single-Nucleus RNA-Seq with DroNc-Seq.” *Nature Methods* 14 (10): 955–58.
- Habib, Naomi, Cristin McCabe, Sedi Medina, Miriam Varshavsky, Daniel Kitsberg, Raz Dvir-Szternfeld, Gilad Green, et al. 2020. “Disease-Associated Astrocytes in Alzheimer’s Disease and Aging.” *Nature Neuroscience* 23 (6): 701–6.
- Hammond, Timothy R., Connor Dufort, Lasse Dissing-Olesen, Stefanie Giera, Adam Young, Alec Wysoker, Alec J. Walker, et al. 2019. “Single-Cell RNA Sequencing of Microglia throughout the Mouse Lifespan and in the Injured Brain Reveals

- Complex Cell-State Changes.” *Immunity* 50 (1): 253–71.e6.
- Harauz, George, Vladimir Ladizhansky, and Joan M. Boggs. 2009. “Structural Polymorphism and Multifunctionality of Myelin Basic Protein.” *Biochemistry* 48 (34): 8094–8104.
- He, Zhisong, Tobias Gerber, Ashley Maynard, Akanksha Jain, Rebecca Petri, Malgorzata Santel, Kevin Ly, et al. n.d. “Lineage Recording Reveals Dynamics of Cerebral Organoid Regionalization.” <https://doi.org/10.1101/2020.06.19.162032>.
- Hill, Robert A., Alice M. Li, and Jaime Grutzendler. 2018. “Lifelong Cortical Myelin Plasticity and Age-Related Degeneration in the Live Mammalian Brain.” *Nature Neuroscience* 21 (5): 683–95.
- Hilscher, Markus M., Christoffer Mattsson Langseth, Petra Kukanja, Chika Yokota, Mats Nilsson, and Gonçalo Castelo-Branco. 2021. “Spatial Cell Type Mapping of the Oligodendrocyte Lineage in the Mouse Juvenile and Adult CNS with in Situ Sequencing.” *bioRxiv*. <https://doi.org/10.1101/2021.06.04.447052>.
- Holmes, Susan, and Wolfgang Huber. n.d. “13 Design of High Throughput Experiments and Their Analyses.” Accessed August 10, 2021. <https://web.stanford.edu/class/bios221/book/>.
- Huber, Wolfgang, Vincent J. Carey, Robert Gentleman, Simon Anders, Marc Carlson, Benilton S. Carvalho, Hector Corrada Bravo, et al. 2015. “Orchestrating High-Throughput Genomic Analysis with Bioconductor.” *Nature Methods* 12 (2): 115–21.
- Hwang, Byungjin, Ji Hyun Lee, and Duhee Bang. 2018. “Single-Cell RNA Sequencing Technologies and Bioinformatics Pipelines.” *Experimental & Molecular Medicine* 50 (8): 1–14.
- Ishii, Akihiro, Ranjan Dutta, Greg M. Wark, Sun-Il Hwang, David K. Han, Bruce D. Trapp, Steven E. Pfeiffer, and Rashmi Bansal. 2009. “Human Myelin Proteome and Comparative Analysis with Mouse Myelin.” *Proceedings of the National Academy of Sciences of the United States of America* 106 (34): 14605–10.
- Jahn, Olaf, Sophie B. Siems, Kathrin Kusch, Dörte Hesse, Ramona B. Jung, Thomas Liepold, Marina Uecker, Ting Sun, and Hauke B. Werner. 2020. “The CNS Myelin Proteome: Deep Profile and Persistence After Post-Mortem Delay.” *Frontiers in Cellular Neuroscience* 14 (August): 239.
- Jahn, Olaf, Stefan Tenzer, and Hauke B. Werner. 2009. “Myelin Proteomics: Molecular Anatomy of an Insulating Sheath.” *Molecular Neurobiology* 40 (1): 55–72.
- Jäkel, Sarah, Eneritz Agirre, Ana Mendanha Falcão, David van Bruggen, Ka Wai Lee, Irene Knuesel, Dheeraj Malhotra, Charles Ffrench-Constant, Anna Williams, and Gonçalo Castelo-Branco. 2019. “Altered Human Oligodendrocyte Heterogeneity in Multiple Sclerosis.” *Nature* 566 (7745): 543–47.
- Jang, Hyemin, Hunki Kwon, Jin-Ju Yang, Jinwoo Hong, Yeshin Kim, Ko Woon Kim, Jin San Lee, et al. 2017. “Correlations between Gray Matter and White Matter Degeneration in Pure Alzheimer’s Disease, Pure Subcortical Vascular Dementia, and Mixed Dementia.” *Scientific Reports* 7 (1): 1–9.
- Johansen, Nelson, and Gerald Quon. n.d. “scAlign: A Tool for Alignment, Integration and Rare Cell Identification from scRNA-Seq Data.” <https://doi.org/10.1101/504944>.
- Jun, Soyeong, Hyeonseob Lim, Honggu Chun, Ji Hyun Lee, and Duhee Bang. 2020. “Single-Cell Analysis of a Mutant Library Generated Using CRISPR-Guided Deaminase in Human Melanoma Cells.” *Communications Biology* 3 (1): 1–12.
- Kashima, Yukie, Yoshitaka Sakamoto, Keiya Kaneko, Masahide Seki, Yutaka Suzuki, and Ayako Suzuki. 2020. “Single-Cell Sequencing Techniques from Individual to

- Multiomics Analyses.” *Experimental & Molecular Medicine* 52 (9): 1419–27.
- Kathryn K. Bercury, Wendy B. Macklin. 2015. “Dynamics and Mechanisms of CNS Myelination.” *Developmental Cell* 32 (4): 447.
- Keren-Shaul, Hadas, Amit Spinrad, Assaf Weiner, Orit Matcovitch-Natan, Raz Dvir-Szternfeld, Tyler K. Ulland, Eyal David, et al. 2017. “A Unique Microglia Type Associated with Restricting Development of Alzheimer’s Disease.” *Cell*. <https://doi.org/10.1016/j.cell.2017.05.018>.
- Kessaris, Nicoletta, Matthew Fogarty, Palma Iannarelli, Matthew Grist, Michael Wegner, and William D. Richardson. 2006. “Competing Waves of Oligodendrocytes in the Forebrain and Postnatal Elimination of an Embryonic Lineage.” *Nature Neuroscience*. <https://doi.org/10.1038/nn1620>.
- Klämbt, Christian. 2009. “Modes and Regulation of Glial Migration in Vertebrates and Invertebrates.” *Nature Reviews. Neuroscience* 10 (11): 769–79.
- Kleinberger, Gernot, Yoshinori Yamanishi, Marc Suárez-Calvet, Eva Czirr, Ebba Lohmann, Elise Cuyvers, Hanne Struyfs, et al. 2014. “TREM2 Mutations Implicated in Neurodegeneration Impair Cell Surface Transport and Phagocytosis.” *Science Translational Medicine* 6 (243): 243ra86.
- Korsunsky, Ilya, Nghia Millard, Jean Fan, Kamil Slowikowski, Fan Zhang, Kevin Wei, Yuriy Baglaenko, Michael Brenner, Po-Ru Loh, and Soumya Raychaudhuri. 2019. “Fast, Sensitive and Accurate Integration of Single-Cell Data with Harmony.” *Nature Methods* 16 (12): 1289–96.
- Kuhn, Sarah, Laura Gritti, Daniel Crooks, and Yvonne Dombrowski. 2019. “Oligodendrocytes in Development, Myelin Generation and Beyond.” *Cells* 8 (11). <https://doi.org/10.3390/cells8111424>.
- Lähnemann, David, Johannes Köster, Ewa Szczurek, Davis J. McCarthy, Stephanie C. Hicks, Mark D. Robinson, Catalina A. Vallejos, et al. 2020. “Eleven Grand Challenges in Single-Cell Data Science.” *Genome Biology* 21 (1): 1–35.
- La Manno, Gioele, Ruslan Soldatov, Amit Zeisel, Emelie Braun, Hannah Hochgerner, Viktor Petukhov, Katja Lidschreiber, et al. 2018. “RNA Velocity of Single Cells.” *Nature* 560 (7719): 494–98.
- Lange, Marius, Volker Bergen, Michal Klein, Manu Setty, Bernhard Reuter, Mostafa Bakhti, Heiko Lickert, et al. 2020. “CellRank for Directed Single-Cell Fate Mapping.” *bioRxiv*. <https://doi.org/10.1101/2020.10.19.345983>.
- Lappe-Siefke, Corinna, Sandra Goebbels, Michel Gravel, Eva Nicksch, John Lee, Peter E. Braun, Ian R. Griffiths, and Klaus-Armin Nave. 2003. “Disruption of Cnp1 Uncouples Oligodendroglial Functions in Axonal Support and Myelination.” *Nature Genetics* 33 (3): 366–74.
- Lee, Youngjin, Brett M. Morrison, Yun Li, Sylvain Lengacher, Mohamed H. Farah, Paul N. Hoffman, Yiting Liu, et al. 2012. “Oligodendroglia Metabolically Support Axons and Contribute to Neurodegeneration.” *Nature* 487 (7408): 443–48.
- Libbey, Jane E., Lori L. McCoy, and Robert S. Fujinami. 2007. “Molecular Mimicry in Multiple Sclerosis.” *International Review of Neurobiology* 79: 127.
- Li, Li, Rongwen Li, Alex Zacharek, Fengjie Wang, Julie Landschoot-Ward, Michael Chopp, Jieli Chen, and Xu Cui. 2020. “ABCA1/ApoE/HDL Signaling Pathway Facilitates Myelination and Oligodendrogenesis after Stroke.” *International Journal of Molecular Sciences* 21 (12). <https://doi.org/10.3390/ijms21124369>.
- Lotfollahi, Mohammad, F. Alexander Wolf, and Fabian J. Theis. 2019. “scGen Predicts Single-Cell Perturbation Responses.” *Nature Methods* 16 (8): 715–21.
- Love, Michael I., Simon Anders, Vladislav Kim, and Wolfgang Huber. n.d. “RNA-Seq Workflow: Gene-Level Exploratory Analysis and Differential Expression.”

- Accessed August 11, 2021.
<https://www.bioconductor.org/packages/devel/workflows/vignettes/rnaseqGene/inst/doc/rnaseqGene.html>.
- Luecken, Malte D., and Fabian J. Theis. 2019. "Current Best Practices in Single-Cell RNA-Seq Analysis: A Tutorial." *Molecular Systems Biology* 15 (6): e8746.
- Macklin, Wendy B., and Matthew N. Rasband. 2012. "Formation and Maintenance of Myelin." *Basic Neurochemistry*. <https://doi.org/10.1016/b978-0-12-374947-5.00031-6>.
- Macosko, Evan Z., Anindita Basu, Rahul Satija, James Nemesh, Karthik Shekhar, Melissa Goldman, Itay Tirosh, et al. 2015. "Highly Parallel Genome-Wide Expression Profiling of Individual Cells Using Nanoliter Droplets." *Cell* 161 (5): 1202–14.
- Marques, Sueli, Amit Zeisel, Simone Codeluppi, David van Bruggen, Ana Mendanha Falcão, Lin Xiao, Huiliang Li, et al. 2016. "Oligodendrocyte Heterogeneity in the Mouse Juvenile and Adult Central Nervous System." *Science* 352 (6291): 1326–29.
- Marsh, Samuel E., Tushar Kamath, Alec J. Walker, Lasse Dissing-Olesen, Timothy R. Hammond, Adam M. H. Young, Abdulraouf Abdulraouf, et al. n.d. "Single Cell Sequencing Reveals Glial Specific Responses to Tissue Processing & Enzymatic Dissociation in Mice and Humans." <https://doi.org/10.1101/2020.12.03.408542>.
- Mathys, Hansruedi, Jose Davila-Velderrain, Zhuyu Peng, Fan Gao, Shahin Mohammadi, Jennie Z. Young, Madhvi Menon, et al. 2019. "Single-Cell Transcriptomic Analysis of Alzheimer's Disease." *Nature* 570 (7761): 332–37.
- Matthieu, J. M., H. Ginalski, R. L. Friede, S. R. Cohen, and D. P. Doolittle. 1980. "Absence of Myelin Basic Protein and Major Dense Line in CNS Myelin of the Mld Mutant Mouse." *Brain Research* 191 (1): 278–83.
- Mayer, Simone, Shokoufeh Khakipour, Maxim A. Drömer, and Daniel A. Cozetto. 2019. "Single-Cell RNA-Sequencing in Neuroscience." *Neuroforum* 25 (4): 251–58.
- McGettigan, Paul A. 2013. "Transcriptomics in the RNA-Seq Era." *Current Opinion in Chemical Biology* 17 (1): 4–11.
- Meijer, Mandy, Eneritz Agirre, Mukund Kabbe, Cassandra A. van Tuijn, Abeer Heskol, Ana Mendanha Falcão, M. Ryan Corces, et al. n.d. "A Primed Immune Transcriptional Program Is Activated in Oligodendroglia in Multiple Sclerosis." <https://doi.org/10.1101/2020.07.21.213876>.
- Micheva, Kristina D., Dylan Wolman, Brett D. Mensh, Elizabeth Pax, Joann Buchanan, Stephen J. Smith, and Davi D. Bock. 2016. "A Large Fraction of Neocortical Myelin Ensheathes Axons of Local Inhibitory Neurons." *eLife* 5 (July). <https://doi.org/10.7554/eLife.15784>.
- Mikael Simons, Klaus-Armin Nave. 2016. "Oligodendrocytes: Myelination and Axonal Support." *Cold Spring Harbor Perspectives in Biology* 8 (1). <https://doi.org/10.1101/cshperspect.a020479>.
- Miller, Jason R., Sergey Koren, and Granger Sutton. 2010. "Assembly Algorithms for next-Generation Sequencing Data." *Genomics*. <https://doi.org/10.1016/j.ygeno.2010.03.001>.
- Monika Bradl, Hans Lassmann. 2010. "Oligodendrocytes: Biology and Pathology." *Acta Neuropathologica* 119 (1): 37.
- Morell, Pierre, and Richard H. Quarles. 1999. "The Myelin Sheath." In *Basic Neurochemistry: Molecular, Cellular and Medical Aspects. 6th Edition*. Lippincott-Raven.
- Mund, Andreas, Fabian Coscia, Réka Hollandi, Ferenc Kovács, András Kriston, Andreas-David Brunner, Michael Bzorek, et al. 2021. "AI-Driven Deep Visual

- Proteomics Defines Cell Identity and Heterogeneity.” *bioRxiv*.
<https://doi.org/10.1101/2021.01.25.427969>.
- Nasrabady, Sara E., Batool Rizvi, James E. Goldman, and Adam M. Brickman. 2018. “White Matter Changes in Alzheimer’s Disease: A Focus on Myelin and Oligodendrocytes.” *Acta Neuropathologica Communications* 6 (1): 1–10.
- Nave, K-A. 1994. “Neurological Mouse Mutants and the Genes of Myelin.” *Journal of Neuroscience Research*. <https://doi.org/10.1002/jnr.490380602>.
- Nave, Klaus-Armin. 2010a. “Myelination and the Trophic Support of Long Axons.” *Nature Reviews. Neuroscience* 11 (4): 275–83.
- . 2010b. “Myelination and Support of Axonal Integrity by Glia.” *Nature* 468 (7321): 244–52.
- Nave, Klaus-Armin, and Hauke B. Werner. 2014. “Myelination of the Nervous System: Mechanisms and Functions.” *Annual Review of Cell and Developmental Biology*. <https://doi.org/10.1146/annurev-cellbio-100913-013101>.
- . 2021. “Ensheathment and Myelination of Axons: Evolution of Glial Functions.” *Annual Review of Neuroscience* 44 (July): 197–219.
- Nelson, N. J. 2001. “Microarrays Have Arrived: Gene Expression Tool Matures.” *Journal of the National Cancer Institute* 93 (7): 492–94.
- Neumann, Björn, Roey Baror, Chao Zhao, Michael Segel, Sabine Dietmann, Khalil S. Rawji, Sarah Foerster, et al. 2019. “Metformin Restores CNS Remyelination Capacity by Rejuvenating Aged Stem Cells.” *Cell Stem Cell* 25 (4): 473–85.e8.
- Noakes, Matthew T., Henry Brinkerhoff, Andrew H. Laszlo, Ian M. Derrington, Kyle W. Langford, Jonathan W. Mount, Jasmine L. Bowman, et al. 2019. “Increasing the Accuracy of Nanopore DNA Sequencing Using a Time-Varying Cross Membrane Voltage.” *Nature Biotechnology* 37 (6): 651–56.
- Nurk, Sergey, Sergey Koren, Arang Rhie, Mikko Rautiainen, Andrey V. Bzikadze, Alla Mikheenko, Mitchell R. Vollger, et al. 2021. “The Complete Sequence of a Human Genome.” *bioRxiv*. <https://doi.org/10.1101/2021.05.26.445798>.
- Onyango, Isaac G., Gretsén V. Jauregui, Mária Čarná, James P. Bennett, Jr, and Gorazd B. Stokin. 2021. “Neuroinflammation in Alzheimer’s Disease.” *Biomedicines* 9 (5). <https://doi.org/10.3390/biomedicines9050524>.
- Orduz, David, Najate Benamer, Domiziana Ortolani, Eva Coppola, Lisa Vigier, Alessandra Pierani, and María Cecilia Angulo. 2019. “Developmental Cell Death Regulates Lineage-Related Interneuron-Oligodendroglia Functional Clusters and Oligodendrocyte Homeostasis.” *Nature Communications* 10 (1): 1–13.
- Oskolkov, Nikolay. 2021. “Genomics New Clothes - Towards Data Science.” Towards Data Science. February 11, 2021. <https://towardsdatascience.com/genomics-new-clothes-6301ab9798a7>.
- Patil, Channamma, and Ishwar Baidari. 2019. “Estimating the Optimal Number of Clusters K in a Dataset Using Data Depth.” *Data Science and Engineering* 4 (2): 132–40.
- Peters, A. 2002. “The Effects of Normal Aging on Myelin and Nerve Fibers: A Review.” *Journal of Neurocytology* 31 (8-9). <https://doi.org/10.1023/a:1025731309829>.
- Picelli, Simone, Åsa K. Björklund, Omid R. Faridani, Sven Sagasser, Gösta Winberg, and Rickard Sandberg. 2013. “Smart-seq2 for Sensitive Full-Length Transcriptome Profiling in Single Cells.” *Nature Methods* 10 (11): 1096–98.
- Readhead, Carol, and Leroy Hood. 1990. “The Dysmyelinating Mouse Mutations Shiverer (shi) and Myelin Deficient (shi Mld).” *Behavior Genetics* 20 (2): 213–34.
- Readhead, C., B. Popko, N. Takahashi, H. D. Shine, R. A. Saavedra, R. L. Sidman, and L. Hood. 1987. “Expression of a Myelin Basic Protein Gene in Transgenic Shiverer

- Mice: Correction of the Dysmyelinating Phenotype." *Cell* 48 (4): 703–12.
- Reardon, Sara. 2021. "A Complete Human Genome Sequence Is Close: How Scientists Filled in the Gaps." *Nature* 594 (7862): 158–59.
- Replogle, Joseph M., Thomas M. Norman, Albert Xu, Jeffrey A. Hussmann, Jin Chen, J. Zachery Cogan, Elliott J. Meer, et al. 2020. "Combinatorial Single-Cell CRISPR Screens by Direct Guide RNA Capture and Targeted Sequencing." *Nature Biotechnology* 38 (8): 954–61.
- Richardson, William D., Nicoletta Kessaris, and Nigel Pringle. 2006. "Oligodendrocyte Wars." *Nature Reviews. Neuroscience* 7 (1): 11–18.
- Ries, Miriam, and Magdalena Sastre. 2016. "Mechanisms of A β Clearance and Degradation by Glial Cells." *Frontiers in Aging Neuroscience* 0. <https://doi.org/10.3389/fnagi.2016.00160>.
- Rio Hortega, Pio del. 1928. *Tercera aportación al conocimiento morfológico e interpretación funcional de la oligodendrología*.
- Rozenblatt-Rosen, Orit, Michael J. T. Stubbington, Aviv Regev, and Sarah A. Teichmann. 2017. "The Human Cell Atlas: From Vision to Reality." *Nature* 550 (7677): 451–53.
- Saab, Aiman S., Iva D. Tzvetavona, Andrea Trevisiol, Selva Baltan, Payam Dibaj, Kathrin Kusch, Wiebke Möbius, et al. 2016. "Oligodendroglial NMDA Receptors Regulate Glucose Import and Axonal Energy Metabolism." *Neuron* 91 (1): 119–32.
- Saelens, Wouter, Robrecht Cannoodt, Helena Todorov, and Yvan Saeys. 2019. "A Comparison of Single-Cell Trajectory Inference Methods." *Nature Biotechnology* 37 (5): 547–54.
- Safaiyan, Shima, Simon Besson-Girard, Tuğberk Kaya, Ludovico Cantuti-Castelvetri, Lu Liu, Hao Ji, Martina Schifferer, et al. 2021. "White Matter Aging Drives Microglial Diversity." *Neuron* 109 (7): 1100–1117.e10.
- Safaiyan, Shima, Nirmal Kannaiyan, Nicolas Snaidero, Simone Brioschi, Knut Biber, Simon Yona, Aimee L. Edinger, Steffen Jung, Moritz J. Rossner, and Mikael Simons. 2016. "Age-Related Myelin Degradation Burdens the Clearance Function of Microglia during Aging." *Nature Neuroscience* 19 (8): 995–98.
- Salzberg, Steven L., and James A. Yorke. 2005. "Beware of Mis-Assembled Genomes." *Bioinformatics* 21 (24): 4320–21.
- Sams, Eleanor Catherine. 2021. "Oligodendrocytes in the Aging Brain." *Neuronal Signaling* 5 (3). <https://doi.org/10.1042/NS20210008>.
- Sanger, F., S. Nicklen, and A. R. Coulson. 1977. "DNA Sequencing with Chain-Terminating Inhibitors." *Proceedings of the National Academy of Sciences of the United States of America* 74 (12): 5463–67.
- Schirmer, Lucas, Dmitry Velmeshev, Staffan Holmqvist, Max Kaufmann, Sebastian Werneburg, Diane Jung, Stephanie Vistnes, et al. 2019. "Neuronal Vulnerability and Multilineage Diversity in Multiple Sclerosis." *Nature* 573 (7772): 75–82.
- Schloss, Jeffery A. 2008. "How to Get Genomes at One Ten-Thousandth the Cost." *Nature Biotechnology* 26 (10): 1113–15.
- Schoales, Jeremy. 2015. "How Does Sanger Sequencing Work?" June 17, 2015. <https://www.thermofisher.com/blog/behindthebench/how-does-sanger-sequencing-work/>.
- Segel, Michael, Björn Neumann, Myfanwy F. E. Hill, Isabell P. Weber, Carlo Viscomi, Chao Zhao, Adam Young, et al. 2019. "Niche Stiffness Underlies the Ageing of Central Nervous System Progenitor Cells." *Nature* 573 (7772): 130–34.
- Setty, Manu, Vaidotas Kisieliovas, Jacob Levine, Adam Gayoso, Linas Mazutis, and Dana Pe'er. 2019. "Characterization of Cell Fate Probabilities in Single-Cell Data

- with Palantir.” *Nature Biotechnology* 37 (4): 451.
- Siems, Sophie B., Olaf Jahn, Laura J. Hoodless, Ramona B. Jung, Dörte Hesse, Wiebke Möbius, Tim Czopka, and Hauke B. Werner. 2021. “Proteome Profile of Myelin in the Zebrafish Brain.” *Frontiers in Cell and Developmental Biology* 9 (April): 640169.
- Simons, Mikael, and Katarina Trajkovic. 2006. “Neuron-Glia Communication in the Control of Oligodendrocyte Function and Myelin Biogenesis.” *Journal of Cell Science* 119 (21): 4381–89.
- “Single-Cell Transcriptomic Analysis of Oligodendrocyte Lineage Cells.” 2017. *Current Opinion in Neurobiology* 47 (December): 168–75.
- Spangenberg, Elizabeth, Paul L. Severson, Lindsay A. Hohsfield, Joshua Crapser, Jiazhong Zhang, Elizabeth A. Burton, Ying Zhang, et al. 2019. “Sustained Microglial Depletion with CSF1R Inhibitor Impairs Parenchymal Plaque Development in an Alzheimer’s Disease Model.” *Nature Communications*. <https://doi.org/10.1038/s41467-019-11674-z>.
- Ståhl, Patrik L., Fredrik Salmén, Sanja Vickovic, Anna Lundmark, José Fernández Navarro, Jens Magnusson, Stefania Giacomello, et al. 2016. “Visualization and Analysis of Gene Expression in Tissue Sections by Spatial Transcriptomics.” *Science* 353 (6294): 78–82.
- Stassart, Ruth M., Wiebke Möbius, Klaus-Armin Nave, and Julia M. Edgar. 2018. “The Axon-Myelin Unit in Development and Degenerative Disease.” *Frontiers in Neuroscience* 0. <https://doi.org/10.3389/fnins.2018.00467>.
- Stevens, Beth, Stefania Porta, Laurel L. Haak, Vittorio Gallo, and R. Douglas Fields. 2002. “Adenosine: A Neuron-Glial Transmitter Promoting Myelination in the CNS in Response to Action Potentials.” *Neuron* 36 (5): 855–68.
- Stoeckius, Marlon, Christoph Hafemeister, William Stephenson, Brian Houck-Loomis, Pratip K. Chattopadhyay, Harold Swerdlow, Rahul Satija, and Peter Smibert. 2017. “Simultaneous Epitope and Transcriptome Measurement in Single Cells.” *Nature Methods* 14 (9): 865–68.
- Stuart, Tim, Andrew Butler, Paul Hoffman, Christoph Hafemeister, Eftymia Papalexi, William M. Mauck, III, et al. 2019. “Comprehensive Integration of Single-Cell Data.” *Cell* 177 (7): 1888.
- Stuart, Tim, and Rahul Satija. 2019. “Integrative Single-Cell Analysis.” *Nature Reviews. Genetics* 20 (5): 257–72.
- Sun, Shiquan, Jiaqiang Zhu, Ying Ma, and Xiang Zhou. 2019. “Accuracy, Robustness and Scalability of Dimensionality Reduction Methods for Single-Cell RNA-Seq Analysis.” *Genome Biology* 20 (1): 1–21.
- Svensson, Valentine, Roser Vento-Tormo, and Sarah A. Teichmann. 2018. “Exponential Scaling of Single-Cell RNA-Seq in the Past Decade.” *Nature Protocols* 13 (4): 599–604.
- Taib, Toufik, Claire Leconte, Juliette Van Steenwinckel, Angelo H. Cho, Bruno Palmier, Egle Torsello, Rene Lai Kuen, et al. 2017. “Neuroinflammation, Myelin and Behavior: Temporal Patterns Following Mild Traumatic Brain Injury in Mice.” *PloS One* 12 (9): e0184811.
- Tang, Fuchou, Catalin Barbacioru, Yangzhou Wang, Ellen Nordman, Clarence Lee, Nanlan Xu, Xiaohui Wang, et al. 2009. “mRNA-Seq Whole-Transcriptome Analysis of a Single Cell.” *Nature Methods* 6 (5): 377–82.
- “The Cost of Sequencing a Human Genome.” n.d. Accessed August 10, 2021. <https://www.genome.gov/about-genomics/fact-sheets/Sequencing-Human-Genome-cost>.

- “The Third Revolution in Sequencing Technology.” 2018. *Trends in Genetics: TIG* 34 (9): 666–81.
- Thomas Philips, Jeffrey D. Rothstein. 2017. “Oligodendroglia: Metabolic Supporters of Neurons.” *The Journal of Clinical Investigation* 127 (9): 3271.
- Tomassy, Giulio Srubek, Daniel R. Berger, Hsu-Hsin Chen, Narayanan Kasthuri, Kenneth J. Hayworth, Alessandro Vercelli, H. Sebastian Seung, Jeff W. Lichtman, and Paola Arlotta. 2014. “Distinct Profiles of Myelin Distribution along Single Axons of Pyramidal Neurons in the Neocortex.” *Science* 344 (6181): 319–24.
- Tomassy, Giulio Srubek, Lori Bowe Dershowitz, and Paola Arlotta. 2016. “Diversity Matters: A Revised Guide to Myelination.” *Trends in Cell Biology* 26 (2): 135–47.
- Torkildsen, Ø., L. A. Brunborg, K-M Myhr, and L. Bø. 2008. “The Cuprizone Model for Demyelination.” *Acta Neurologica Scandinavica*. <https://doi.org/10.1111/j.1600-0404.2008.01036.x>.
- Toyama, Brandon H., Jeffrey N. Savas, Sung Kyu Park, Michael S. Harris, Nicholas T. Ingolia, John R. Yates 3rd, and Martin W. Hetzer. 2013. “Identification of Long-Lived Proteins Reveals Exceptional Stability of Essential Cellular Structures.” *Cell* 154 (5): 971–82.
- Tran, Hoa Thi Nhu, Kok Siong Ang, Marion Chevrier, Xiaomeng Zhang, Nicole Yee Shin Lee, Michelle Goh, and Jinmiao Chen. 2020. “A Benchmark of Batch-Effect Correction Methods for Single-Cell RNA Sequencing Data.” *Genome Biology* 21 (1): 1–32.
- Tripathi, Richa B., Martyna Jackiewicz, Ian A. McKenzie, Eleni Kougioumtzidou, Matthew Grist, and William D. Richardson. 2017. “Remarkable Stability of Myelinating Oligodendrocytes in Mice.” *Cell Reports* 21 (2): 316.
- Van Verk, Marcel C., Richard Hickman, Corné M. J. Pieterse, and Saskia C. M. Van Wees. 2013. “RNA-Seq: Revelation of the Messengers.” *Trends in Plant Science* 18 (4): 175–79.
- Wang, Zhong, Mark Gerstein, and Michael Snyder. 2009. “RNA-Seq: A Revolutionary Tool for Transcriptomics.” *Nature Reviews. Genetics* 10 (1): 57–63.
- Welch, Joshua D., Velina Kozareva, Ashley Ferreira, Charles Vanderburg, Carly Martin, and Evan Z. Macosko. 2019. “Single-Cell Multi-Omic Integration Compares and Contrasts Features of Brain Cell Identity.” *Cell* 177 (7): 1873–87.e17.
- Wheeler, Michael A., Iain C. Clark, Emily C. Tjon, Zhaorong Li, Stephanie E. J. Zandee, Charles P. Couturier, Brianna R. Watson, et al. 2020. “MAFG-Driven Astrocytes Promote CNS Inflammation.” *Nature* 578 (7796): 593–99.
- Ximerakis, Methodios, Scott L. Lipnick, Brendan T. Innes, Sean K. Simmons, Xian Adiconis, Danielle Dionne, Brittany A. Mayweather, et al. 2019. “Single-Cell Transcriptomic Profiling of the Aging Mouse Brain.” *Nature Neuroscience* 22 (10): 1696–1708.
- Yalçın, Belgin, and Michelle Monje. 2021. “Microenvironmental Interactions of Oligodendroglial Cells.” *Developmental Cell*. <https://doi.org/10.1016/j.devcel.2021.06.006>.
- Yamamoto, Toshiyuki, and Keiko Shimojima. 2013. “Pelizaeus-Merzbacher Disease as a Chromosomal Disorder.” *Congenital Anomalies* 53 (1): 3–8.
- Yue, Tao, Kendy Xian, Edward Hurlock, Mei Xin, Steven G. Kernie, Luis F. Parada, and Q. Richard Lu. 2006. “A Critical Role for Dorsal Progenitors in Cortical Myelination.” *The Journal of Neuroscience: The Official Journal of the Society for Neuroscience* 26 (4): 1275–80.
- Zafar, Hamim, Chieh Lin, and Ziv Bar-Joseph. 2019. “Single-Cell Lineage Tracing by Integrating CRISPR-Cas9 Mutations with Transcriptomic Data.” *bioRxiv*.

- <https://doi.org/10.1101/630814>.
- Zalc, Bernard. 2006. "The Acquisition of Myelin: A Success Story." *Novartis Foundation Symposium* 276: 15–21; discussion 21–25, 54–57, 275–81.
- Zavolan, Mihaela. 2015. "Inferring Gene Expression Regulatory Networks from High-Throughput Measurements." *Methods*. <https://doi.org/10.1016/j.ymeth.2015.07.006>.
- Zeisel, Amit, Hannah Hochgerner, Peter Lönnerberg, Anna Johnsson, Fatima Memic, Job van der Zwan, Martin Häring, et al. 2018. "Molecular Architecture of the Mouse Nervous System." *Cell* 174 (4): 999–1014.e22.
- Zeisel, Amit, Ana B. Muñoz-Manchado, Simone Codeluppi, Peter Lönnerberg, Gioele La Manno, Anna Juréus, Sueli Marques, et al. 2015. "Brain Structure. Cell Types in the Mouse Cortex and Hippocampus Revealed by Single-Cell RNA-Seq." *Science* 347 (6226): 1138–42.
- Zhang, Yuqing, Giovanni Parmigiani, and W. Evan Johnson. 2020. "ComBat-Seq: Batch Effect Adjustment for RNA-Seq Count Data." *NAR Genomics and Bioinformatics* 2 (3). <https://doi.org/10.1093/nargab/lqaa078>.
- Zhou, Yingyue, Wilbur M. Song, Prabhakar S. Andhey, Amanda Swain, Tyler Levy, Kelly R. Miller, Pietro L. Poliani, et al. 2020. "Human and Mouse Single-Nucleus Transcriptomics Reveal TREM2-Dependent and TREM2-Independent Cellular Responses in Alzheimer's Disease." *Nature Medicine* 26 (1): 131–42.

Appendices

Appendix A. First co-authored publication:

Original publication

Berghoff, S.*, Spieth, L.*, Sun, T.*, Hosang, L., Depp, C., Sasmita, A., ... & Saher, G. (2021). Neuronal cholesterol synthesis is essential for repair of chronically demyelinated lesions in mice. *bioRxiv*.

Personal contribution

I have contributed to the collection, evaluation, and integrative analysis of external datasets that supported this publication. Specifically, I performed detailed analysis on the collected neuron, astrocyte, oligodendrocyte single-cell transcriptome profiles, respectively, with the focus on cholesterol synthesis gene regulatory pathways. In addition, I was involved in the interpretation and visualization of analysis results for the manuscript, as well as assisted in the curation of the manuscript draft.

Neuronal cholesterol synthesis is essential for repair of chronically demyelinated lesions in mice

Stefan A. Berghoff^{1*}, Lena Spieth^{1#}, Ting Sun^{1,2#}, Leon Hosang³, Constanze Depp¹, Andrew O. Sasmita¹, Martina H. Vasileva¹, Patricia Scholz⁴, Yu Zhao², Dilja Krueger-Burg⁵, Sven Wichert⁶, Euan R Brown⁷, Kyriakos Michael⁷, Klaus-Armin Nave¹, Stefan Bonn², Francesca Odoardi³, Moritz Rossner⁶, Till Ischebeck^{4,8}, Julia M. Edgar^{1,9}, and Gesine Saher^{1*}

Astrocyte-derived cholesterol supports brain cells under physiological conditions. However, in demyelinating lesions, astrocytes downregulate cholesterol synthesis and the cholesterol that is essential for remyelination has to originate from other cellular sources. Here, we show that repair following acute versus chronic demyelination involves distinct processes. In particular, we found that in chronic myelin disease, when recycling of lipids is often defective, de novo neuronal cholesterol synthesis is critical for regeneration. By gene expression profiling, genetic loss of function experiments and comprehensive phenotyping, we provide evidence that neurons increase cholesterol synthesis in chronic myelin disease models and MS patients. In mouse models, neuronal cholesterol facilitated remyelination specifically by triggering OPC proliferation. Our data contribute to the understanding of disease progression and have implications for therapeutic strategies in MS patients.

Introduction

During normal brain development, cholesterol is produced locally by de novo synthesis involving neurons, oligodendrocytes, microglia, and astrocytes (Berghoff et al., 2021; Camargo et al., 2012; Fünfschilling et al., 2012; Saher et al., 2005). Neuronal cholesterol is essential for neurite outgrowth and synapse formation during neurogenesis (Fünfschilling et al., 2012; Mauch et al., 2001) but the highest rates of cholesterol synthesis in the brain are achieved by oligodendrocytes during postnatal myelination (Dietschy, 2009). The resulting cholesterol-rich myelin enwraps, shields, and insulates axons to enable rapid conduction of neuronal impulses. Myelin also provides support to axons, potentially by mobilizing oligodendroglial lipids (Kassmann et al., 2007; Saab and Nave, 2017). In the adult brain, cholesterol synthesis is attenuated to low steady-state levels (Dietschy and Turley, 2004).

Destruction of lipid-rich myelin in demyelinating diseases such as multiple sclerosis (MS) likely impairs neuronal function by disrupting the fine-tuned axon-myelin unit (Stassart et al., 2018). Remyelination is

considered crucial for limiting axon damage and slowing progressive clinical disability. Statin-mediated inhibition of the cholesterol synthesis pathway impairs remyelination (Miron et al., 2009). Previously, we showed that following an acute demyelinating episode, oligodendrocytes import cholesterol for new myelin membrane synthesis from damaged myelin that has been recycled by phagocytic microglia (Berghoff et al., 2021). In contrast, de novo oligodendroglial cholesterol synthesis contributes to remyelination only following chronic demyelination (Berghoff et al., 2021; Voskuhl et al., 2019). Notably, we and others showed that astrocytes reduce expression of cholesterol synthesis genes following demyelination (Berghoff et al., 2021; Itoh et al., 2018). As astrocytes are considered to support neurons by providing cholesterol in ApoE-containing lipoproteins in the healthy brain (Dietschy, 2009), the lack of this support in the diseased brain contributes to the disruption of CNS cholesterol homeostasis. Neuronal activity leads to OPC proliferation during development and likely also after demyelination (Bacmeister et al., 2020; Gibson et al., 2014; Marisca et al., 2020). However, neuronal responses to myelin degeneration with regard to cholesterol metabolism, and the contribution of

¹ Department of Neurogenetics, Max Planck Institute of Experimental Medicine, Göttingen, Germany; ² Institute for Medical Systems Biology, Center for Molecular Neurobiology Hamburg, Hamburg, Germany; ³ Institute for Neuroimmunology and Multiple Sclerosis Research, University Medical Center Göttingen, Göttingen, Germany; ⁴ Department of Plant Biochemistry, Albrecht-von-Haller-Institute for Plant Sciences and Göttingen Center for Molecular Biosciences (GZMB), University of Göttingen, Göttingen, Germany; ⁵ Department of Molecular Neurobiology, Max Planck Institute of Experimental Medicine, Göttingen, Germany; ⁶ Department of Psychiatry and Psychotherapy, University Hospital, LMU Munich, Munich, Germany; ⁷ School of Engineering and Physical Sciences, Institute of Biological Chemistry, Biophysics and Bioengineering, James Naysmith Building, Heriot Watt University, Edinburgh, UK; ⁸ Service Unit for Metabolomics and Lipidomics, Göttingen Center for Molecular Biosciences (GZMB), University of Göttingen, Göttingen, Germany; ⁹ Axi-glial Group, Institute of Infection, Immunity and Inflammation, College of Medical Veterinary and Life Sciences, University of Glasgow, Glasgow, UK; *Correspondence: saher@em.mpg.de, berghoff@em.mpg.de

neuronal cholesterol to remyelination, remains unknown.

Here, using mice with cell type-specific inactivation of cholesterol synthesis and models of myelin disease, we assess neuronal versus glial cholesterol metabolism. We compare white and grey matter CNS regions and isolated brain cells in the healthy adult brain and during remyelination. We show that active myelin disease is associated with downregulated expression of cholesterol metabolism in neurons. Surprisingly, during chronic myelin disease, neurons increase cholesterol synthesis. Similarly, neurons in MS brain upregulate a gene profile related to cholesterol synthesis and metabolism in non-lesion areas. Finally, neuronal cholesterol synthesis contributes to remyelination following experimental demyelination. Our data support the essential role of cholesterol synthesis in neurons for remyelination, a role that is likely relevant for MS disease progression.

Results

Loss of *Fdft1* in neurons alters white matter cholesterol metabolism

In the adult brain, neuronal synthesis as well as horizontal cholesterol transfer from glial cells meets neuronal cholesterol demands. To evaluate neuronal versus glial cholesterol metabolism, we acutely isolated neurons, astrocytes and oligodendrocytes from brain tissue that contained cortex or subcortical white matter of adult mice (Figure 1A). The abundance of neuronal mRNA transcripts related to cholesterol metabolism was compared with oligodendrocyte and astrocyte profiles obtained previously (Berghoff *et al.*, 2021). As expected, neurons showed low steady-state expression levels of cholesterol synthesis genes (*Hmgcr*, *Fdft1*, *Cyp51*, *Dhcr24*) compared to oligodendrocytes and astrocytes (Figure 1B, Table S1). In contrast, several gene transcripts related to cholesterol import (*Apob*, *Scarb1*, *Lrp1*), storage (*Soat1*) and brain export (*Cyp46a1*) were higher in relative abundance. To assess the relevance of cell type-specific cholesterol synthesis, we genetically inactivated squalene synthase (SQS, *Fdft1* gene), an essential enzyme of the sterol biosynthesis pathway, in adult oligodendrocytes (OLcKO, *Plp1-CreERT2*), OPCs (OPCcKO, *CSPG4::CreERT2*), astrocytes (AcKO, *GLAST::CreERT2*), or neurons (NcKO, *CaMKII-Cre*) (Figure 1C, S1A-B) (Berghoff *et al.*, 2021; Fünfschilling *et al.*, 2012; Saher *et al.*, 2005). Comparable to oligodendroglial and astrocyte conditional mutants (Berghoff *et al.*, 2021), loss of cholesterol synthesis in neurons did not affect peripheral serum cholesterol level or body weight

(Figure S1C). In an open field test, neuronal, astrocyte or OPC mutants appeared similar to controls (Figure 1D, S1D-E), whereas OLcKO animals showed signs of anxiety, which were enhanced in OPC/OL double mutants (Figure S1F). Notably, these behavioral changes occurred in the absence of overt myelin / oligodendrocyte deficits (Figure S1G), which were also not observed in the other conditional mutants (Berghoff *et al.*, 2021; Fünfschilling *et al.*, 2012).

Next, we evaluated the impact of conditional loss of squalene synthase / cholesterol synthesis for cholesterol homeostasis by gene transcription profiling of cortex or subcortical white matter (corpus callosum) from the conditional cholesterol synthesis mutants and respective controls. In the cortex, conditional inactivation of cholesterol synthesis in neurons or oligodendrocytes resulted in moderate upregulation of cholesterol synthesis genes, possibly to compensate for the loss of cholesterol synthesis in the affected cell type (Figure 1E, Table S2, S3). In contrast, in all conditional mutants we observed a moderate but consistent downregulation of expression related to cholesterol metabolism in white matter (Figure 1E-F, S1H). Here, reduced expression of genes associated with horizontal cholesterol transfer such as *Abca1*, *Apoe* and *Lcat* was noted in all conditional mutants, particularly in AcKO animals (Figure 1F). In agreement, sterol profiling revealed only moderate alteration in conditional mutants (Figure S2A).

Surprisingly, comparison of significant transcript changes in conditional mutants revealed a marked downregulation of genes related to the blood-brain barrier (BBB) in corpus callosum samples of OLcKO and NcKO mice. This was accompanied by upregulation of few inflammatory mediators with profiles being unique to each mutant (Figure 1E-F). Interestingly, biochemical quantification of BBB permeability revealed that reduced tight junction gene expression was paralleled by increased CNS influx of the small molecular weight BBB tracer NaFI (376 Da) in OLcKO and NcKO brains. Perhaps surprisingly, given the role of astrocytes in BBB formation, this was not the case in AcKO animals (Figure 1F, S1D, SB-C).

In summary, genetic elimination of cholesterol synthesis in oligodendrocytes, neurons and astrocytes leads to altered transcriptional expression of genes related to cholesterol metabolism in grey and white matter. These data confirm that all cell types contribute to cholesterol homeostasis in the adult brain by cell autonomous cholesterol synthesis. Of note, in cortex but also corpus callosum of neuronal *Fdft1* mutants,

Fdft1 expression was significantly reduced and the abundance of cholesterol synthesis intermediates was attenuated (Figure 1E, S2A). This suggests axonal localization of cholesterol synthesis transcripts *in vivo*, contrary to neurons in compartmentalized culture (Vance et al., 2000).

Myelin disease leads to increased cholesterol synthesis in neurons

Experimental demyelination is associated with axonal pathology (Berghoff et al., 2017b; Nikic et al., 2011), and chronic loss of myelin in multiple sclerosis patients leads to persistent disabilities. Even subtle myelin defects can lead to axonal damage, myelin instability and glial activation, as observed in null mutants of the myelin-specific genes *Plp1* (proteolipid protein 1) and *Cnp1* (2',3'-cyclic-nucleotide 3'-phosphodiesterase) (Edgar et al., 2009; Edgar et al., 2004; Lappe-Siefke et al., 2003; Trevisiol et al., 2020). To assess neuronal responses to mild alterations in myelin integrity, we combined the well-characterized *Plp1* and *Cnp1* knockout mice with Thy1-EYFPnuc transgenes to label neuronal nuclei, predominantly of callosal projection neurons (CPN) (Wehr et al., 2006). Despite the axonal pathology, CPN loss was not a feature of *Plp1* and *Cnp1* mutants up to 12 months of age as quantified by EYFPnuc+ cell counting (Figure S2D). We then isolated CPN from cortical layer five by fluorescence-directed laser microdissection at various ages (1, 3, 6 and 12 month) for transcriptional profiling (Figure 2A). Neuronal identity of Thy1-EYFPnuc+ cells isolated from cortical layer five was verified by cell type-specific marker gene expression (Figure S2E). Transcriptional profiling revealed 412 differentially expressed genes in neurons from *Cnp1* knockout mice and 104 genes from *Plp1* knockout mice compared to Thy1-EYFPnuc controls (adj. p-val<0.001, Benjamin-Hochberg correction, at least 1.8-fold changed expression) (Figure S2F). Surprisingly, by gene set enrichment analysis (GSEA) the gene set "cholesterol metabolism" was upregulated in CPNs of both mutants (Figure 2B). This included genes involved in cholesterol synthesis (*Hmgcr*, *Fdft1*, *Cyp51*, *Dhcr24*) and transport (*Ldlr*, *ApoE*) (Figure 2C).

Considering the possibility that neuronal upregulation of genes related to cholesterol metabolism is a general response to chronic myelin alterations, we analyzed transcriptional profiles of isolated cortical neurons following acute experimental autoimmune encephalomyelitis (EAE) induction and following acute-phase (6 weeks cuprizone) and chronic-phase remyelination (chronic demyelination for 12 weeks

followed by two weeks of cuprizone withdrawal, 12+2 weeks) (Figure 2D). During acute disease (EAE or 6 weeks cuprizone), neurons consistently downregulated gene expression related to cholesterol metabolism (Figure 2E). In contrast, during remyelination following chronic demyelination in the cuprizone model, expression of genes involved in cholesterol synthesis (*Hmgcr*, *Fdft1*, *Dhcr24*) and transport (*Vldlr*, *ApoE*) were increased (Figure 2E). To test whether the upregulation of cholesterol synthesis genes was functionally relevant, we determined the abundance of cholesterol by GC/MS in the chronic demyelination/remyelination paradigm. Cholesterol as well as several precursors of the cholesterol synthesis pathway were increased 4-5 fold in isolated neurons (Figure 2F), suggesting enhanced cholesterol synthesis in neurons during remyelination in this paradigm.

Increased cholesterol synthesis gene expression in neurons from MS patients

We next determined whether increased neuronal expression of cholesterol synthesis genes is relevant in human MS and used single-nuclei gene expression profiles from MS patients and healthy control tissue from two recent studies (GSE118257 and GSE124335). We separately merged expression profiles of neurons, oligodendrocytes and astrocytes as annotated in each study (Figure 3A-B, S3A-C). Although the disease history of the MS tissue samples is unknown, we categorized MS samples in two subsets. One comprises the different stages of active MS lesions (termed "lesion"). The other subset (termed "non-lesion") contains normal-appearing MS tissue that was derived from areas adjacent to active lesions. Neuronal nuclei contributed considerably to each of the MS subsets (3122 lesion, 3547 non-lesion). Next, we performed pairwise comparisons of expression profiles separately, in neurons, oligodendrocytes or astrocytes, focusing on cholesterol metabolism.

As expected, lesion-derived astrocytes showed significantly reduced transcript levels of several genes related to cholesterol synthesis (*HMGCR*, *FDFT1*, *DHCR7*, *DHCR24*), while this gene set was not differentially regulated in non-lesion-derived astrocytes (Figure 3C). In contrast to astrocytes, both oligodendrocytes and neurons in MS lesions, increased expression of apolipoproteins including *APOE*, indicating active participation in local lipid transport in areas of active disease. Moreover, MS oligodendrocytes upregulated genes associated with cholesterol synthesis and metabolism, most markedly

in lesions. This confirms the relevance of cholesterol availability for oligodendrocytes in myelin disease (Berghoff *et al.*, 2017b; Berghoff *et al.*, 2021; Voskuhl *et al.*, 2019) and potentially reflects ongoing remyelination or attempts to remyelinate. Notably, neurons in MS lesions showed reduced transcript levels of genes associated with cholesterol synthesis including the rate-limiting enzyme of this process, *HMGCR* (Figure 3C). In contrast, in non-lesion MS tissue, neurons upregulated this gene set, suggesting increased neuronal cholesterol synthesis in normal-appearing MS tissue areas.

Neuronal *Fdft1* ablation impairs remyelination following chronic cuprizone

The contrasting expression of neuronal cholesterol synthesis genes in lesion versus non-lesion areas of MS brain and in acute versus chronic-phase remyelination in mouse models prompted us to test the importance of this finding for lesion repair. To explore whether loss of neuronal cholesterol synthesis affects remyelination efficiency, NcKO animals were challenged with acute and chronic demyelination paradigms using EAE and cuprizone. We evaluated disease expression, remyelination (Gallyas), oligodendrocyte differentiation (CAII), number of oligodendrocyte lineage cells (Olig2) and gliosis (GFAP, Iba1, MAC3).

As anticipated, loss of neuronal cholesterol synthesis did not affect acute-phase remyelination in cuprizone treated mice (Figure 4A-B, S4A-C, Video1) or pathology following immune mediated myelin degeneration (Figure 4C-E). However, after cuprizone-induced chronic demyelination, we observed reduced oligodendrocyte density and impaired remyelination in both the corpus callosum and cortex of NcKO animals compared to controls (Figure 4F-H, S4A-C). Defective repair of chronically demyelinated lesions in NcKO animals occurred without affecting gliosis, neuronal degeneration (NeuN+ cell number, FluoroJade, TUNEL) or axonal stress (APP+ spheroids) (Figure S4D-F). The degree of sustained hypomyelination in NcKO animals was comparable to mutants with inactivated cholesterol synthesis in OPCs (NcKO 53±5% of controls, OPCcKO 55±3%; Figure 4I). Further, both conditional mutants displayed comparable defects in motor performance after chronic cuprizone administration (Figure S4G). However, in contrast to oligodendroglial mutants that showed normal OPC densities, the loss of neuronal cholesterol synthesis caused a reduction of Olig2/PCNA+ proliferating OPCs in the corpus callosum (Figure 4G,

I, J). Interestingly, cholesterol administration enhanced OPC proliferation and differentiation in myelinating co-cultures, but only OPC proliferation was impaired by abolishing neuronal activity (Figure 4K, S4H). Together, these findings raise the possibility that elevating neuronal cholesterol synthesis is essential for OPC proliferation and differentiation to facilitate remyelination.

Discussion

Complete functional recovery from demyelinating episodes and prevention of persistent disabilities is the ultimate goal of multiple sclerosis (MS) therapies. In addition to decreasing the rate of demyelinating events and dampening pathological inflammation, the support of remyelination has come into focus in MS drug development (Plemel *et al.*, 2017). Repair following immune-mediated degeneration of oligodendrocytes and destruction of myelin involves the resolution of inflammation, OPC migration, proliferation and differentiation (Reich *et al.*, 2018). Tissue regeneration is achieved by synthesis of lipid- and cholesterol-rich myelin membranes by newly differentiated oligodendrocytes and oligodendrocytes that survived the immune attack (Franklin *et al.*, 2020). Remyelination contributes to neuroprotection, the restoration of impulse conduction and may facilitate (re)establishing neural circuits (Bacmeister *et al.*, 2020).

Disparate repair processes during acute and chronic myelin disease

With respect to lipid metabolism, repair after an acute demyelinating episode differs markedly from repair in chronic myelin disease or after repeated demyelinating events. Tissue remodeling and repair after an acute demyelinating attack is coordinated by microglial/macrophage activation and lipid recycling (Berghoff *et al.*, 2021; Cunha *et al.*, 2020; Miron *et al.*, 2013). Correspondingly, acute-phase remyelination is independent of squalene synthase / *Fdft1* inactivation in oligodendrocytes, OPCs, astrocytes, or neurons (this study and Berghoff *et al.*, 2021).

In chronic myelin disease, myelin debris is largely cleared from demyelinated lesions. Correspondingly, in chronically demyelinated lesions in cuprizone-treated mice (Berghoff *et al.*, 2017b) and in chronically inactive lesions in MS patients (Hess *et al.*, 2020) predominantly lipid-laden foamy microglia/macrophages remain. This suggests that lipid recycling by microglia could be inefficient in chronically demyelinated lesions. These lipid trafficking defects in microglia could not only impede remyelination but also

aggravate axonal damage, as observed in TREM2 mutants (Cantoni et al., 2015).

As cholesterol is essential for myelin formation (Saher et al., 2005), these findings underscore the necessity of local de novo synthesis. This is supported by the observation that statin-mediated inhibition of cholesterol synthesis blocks remyelination (Miron et al., 2009). However, astrocytes, which provide cholesterol in the healthy brain, fail as a local cholesterol source in myelin disease as they strongly downregulate its synthesis both in mouse models (Berghoff et al., 2021; Borggrewe et al., 2021; Itoh et al., 2018) and MS lesions (this study). We hypothesize that chronic myelin disease depletes neuronal and oligodendroglial cholesterol levels, which triggers cell-autonomous cholesterol synthesis by feedback regulation. In agreement, the cholesterol for remyelination originates at least partially from de novo oligodendroglial synthesis (Berghoff et al., 2021; Jurevics et al., 2002; Voskuhl et al., 2019). The finding that dietary cholesterol supplementation also supports myelin repair (Berghoff et al., 2017b; Saher et al., 2012) suggests that endogenous cholesterol synthesis is insufficient for complete remyelination. In the current study, we provide evidence that neuronal cholesterol synthesis is essential for repair of chronically demyelinated lesions.

Neuronal cholesterol synthesis during remyelination

Following chronic demyelination, we found impaired remyelination in both white and grey matter of animals lacking neuronal cholesterol synthesis. This is in agreement with the increased neuronal expression of cholesterol synthesis genes in human non-lesion MS tissue and following chronic experimental demyelination. In neuronal mutants of cholesterol synthesis, but not in corresponding oligodendroglial mutants, we showed a marked reduction in the density of oligodendrocyte lineage cells. This finding points to an inference with repair that precedes myelin membrane synthesis, likely in OPC proliferation and oligodendrocyte differentiation.

What is the mechanism by which regeneration of chronically demyelinated white matter tracts such as the corpus callosum benefits from neuronal cholesterol synthesis? Neuronal electrical activity triggers OPC proliferation and oligodendrocyte differentiation during development and after demyelination through unknown signals (Demerens et al., 1996; Marisca et al., 2020; Mitew et al., 2018; Ortiz et al., 2019). The hyperactivity of cortical neurons observed after acute demyelination

(Bacmeister et al., 2020) could offset conduction deficits of demyelinated white matter tracts (Crawford et al., 2009). This could lead to synaptic vesicle release from callosal axons (Almeida et al., 2020; Pfeiffer et al., 2019) and provide the endogenous signal to white matter OPCs to proliferate and initiate repair. We observed that neuronal cholesterol plays a role in this process. In cultured OPCs, short term pharmacological inhibition of cholesterol synthesis induces OPC differentiation (Miron et al., 2007). It is possible that reducing cellular cholesterol levels in OPCs decreases the probability of receiving neuronal input via neurotransmitter channels (Korinek et al., 2020). In agreement, we showed that administration of cholesterol facilitates OPC proliferation (this study). However, OPC proliferation was amplified only, when cholesterol was supplied in the context of neuronal activity. It is possible that neurotransmitter release occurs concomitant with release of neuronal cholesterol. This could be a means to prevent (premature) OPC differentiation and to generate sufficient numbers of oligodendrocyte lineage cells to accomplish repair.

In addition, cholesterol-depleted denuded axons as in chronic lesions of NcKO mice are likely more fragile as suggested from increased plasma membrane tether forces of cholesterol synthesis mutant neurons (Fünfschilling et al., 2012). Especially when electrically hyperactive, impaired stability of axonal membranes could increase axon damage and the probability of conduction blocks. Moreover, cholesterol is essential for the biogenesis and exocytosis of synaptic vesicles (Linetti et al., 2010; Thiele et al., 2000). This is compatible with the observation that cholesterol synthesis deficient neurons show reduced spontaneous activity in culture (Fünfschilling et al., 2012).

Several studies have highlighted the importance of cholesterol availability for developmental OPC proliferation, oligodendrocyte differentiation and myelin membrane synthesis (Mathews and Appel, 2016; Saher et al., 2012; Zhao et al., 2016). The finding that administration of dietary cholesterol during chronic-phase remyelination increases the density of proliferating OPCs (Berghoff et al., 2017b) suggests that the entire oligodendrocyte lineage can benefit from externally administered cholesterol. It is possible that neurons increase cholesterol production not only to fulfill their own cholesterol demands but also to support oligodendrocytes to synthesize myelin. Indeed, cholesterol synthesis in callosal axons would position the lipid optimally to supply proliferating OPCs and

newly differentiating oligodendrocytes for remyelination. This suggestion is reinforced by the observation that electrically hyperactive neurons in demyelinated lesions release lipids as ApoE-containing lipoproteins (Ioannou et al., 2019; Xu et al., 2006). Our data show that increased expression of neuronal cholesterol synthesis genes is paralleled by strongly elevated expression of ApoE. Thus, following chronic demyelination, neurons could export cholesterol via ApoE to support myelination by oligodendrocytes in a lipid-poor environment. Although we have not measured neuronal activity in demyelinated conditional mutants, we speculate that *Fdft1* mutant neurons produce less activity-dependent pro-repair signals to local OPCs than controls.

Taken together, our data show that loss of neuronal cholesterol synthesis strongly impairs remyelination with relevance for human MS disease. Our study confirms distinct cell type-specific roles in brain cholesterol biogenesis and import during remyelination and provides an additional explanation for disease progression related to age-associated decline of cholesterol synthesis (Berghoff *et al.*, 2021; Scalfari, 2019; Thelen et al., 2006). Further studies are needed to design therapeutic strategies that stimulate cholesterol synthesis in affected neuronal populations.

Figure 1

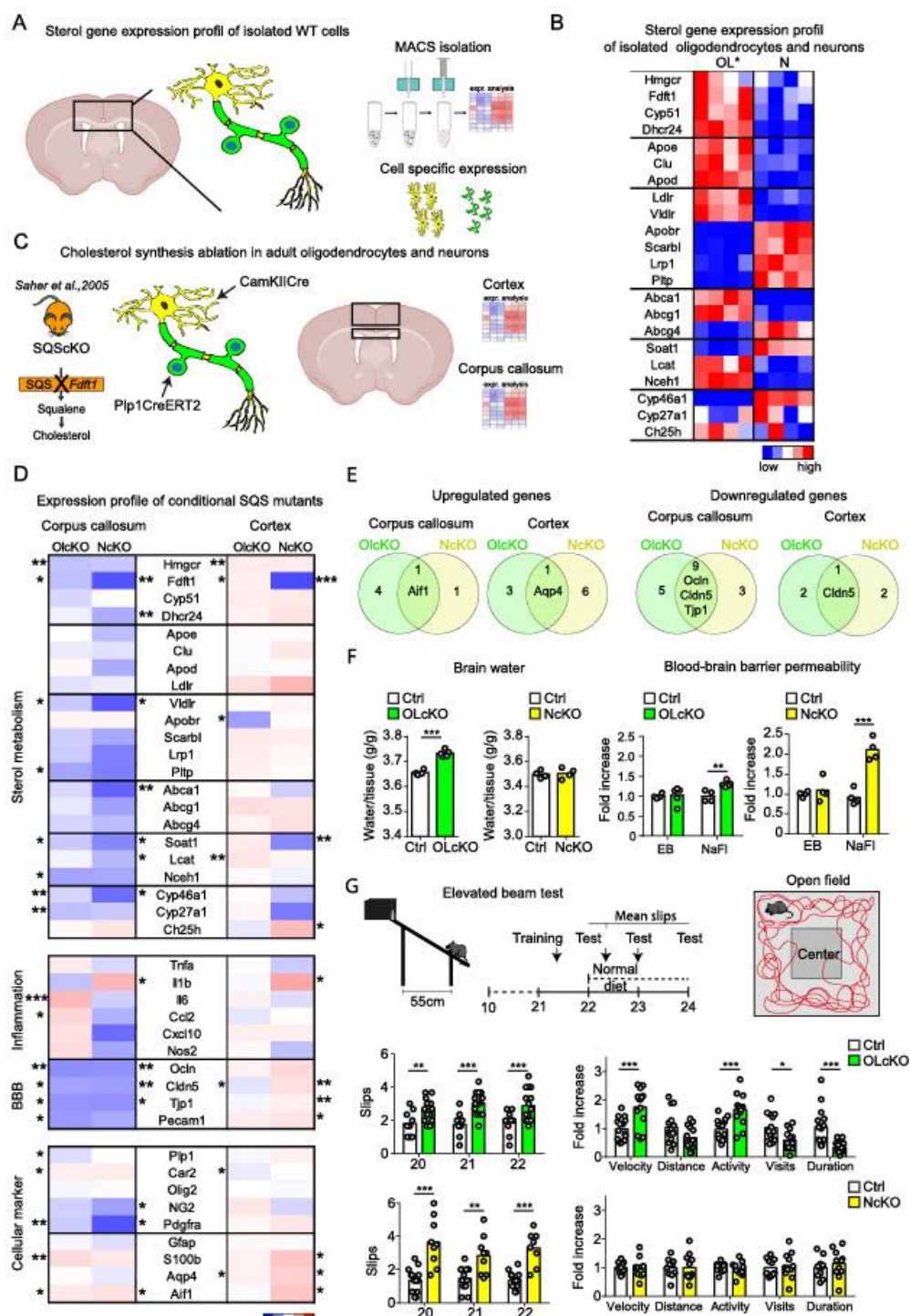
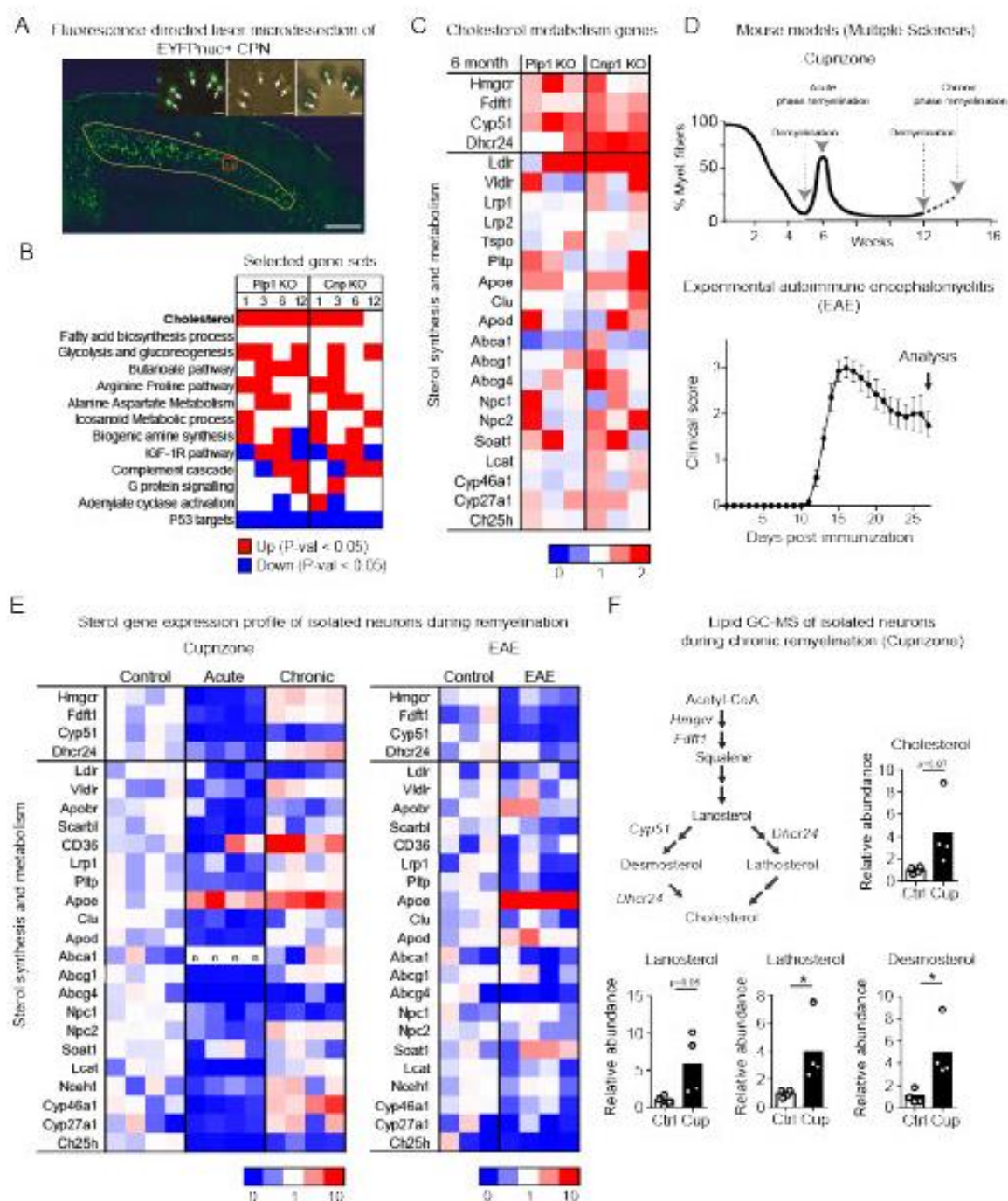


Figure 2

**Figure 2. Expression of genes related to cholesterol metabolism in neurons of genetic and experimental myelin disease models**

(A) Representative fluorescent micrographs depicting the isolation of EYFP^{huc+} callosal projection neurons (CPN) from the primary motor and somatosensory cortex (yellow line) of PLP-KO and CNP-KO mutants (scale 200 μ m). Insets show the tissue before and after laser microdissection, and isolated neurons (scale 20 μ m). (B) Selected gene sets in microdissected neurons from PLP-KO and CNP-KO mutants compared to controls (1, 3, 6, 12 months of age). Significantly up-regulated and down-regulated gene sets (P-val<0.05) are indicated in red and blue, respectively. (C) Gene expression profile of genes related to cholesterol metabolism in callosal projection neurons from PLP-KO and CNP-KO mutants at 6 month of age. Heat maps show fold expression of biological replicates (n=3) normalized to controls (Table S5). (D) Time points of analysis related to the course of demyelination/remyelination in the cuprizone model and the clinical score of EAE-induced animals analyzed in (E). (E) Gene expression profile of genes related to cholesterol metabolism in isolated neurons following acute (6 weeks) and chronic (12w+2w) cuprizone challenge (left) and following EAE (right). Heat maps show fold expression normalized to controls (Table S6-S7). Each square represents an individual animal (n=3-4). (F) Cholesterol synthesis pathway with major enzymes and sterol intermediates. Mean relative abundance of sterol intermediates in isolated neurons from chronic cuprizone-treated mice (n=4) compared to untreated controls (n=3), measured by GC-MS (two-sided Student's t-test).

Figure 3

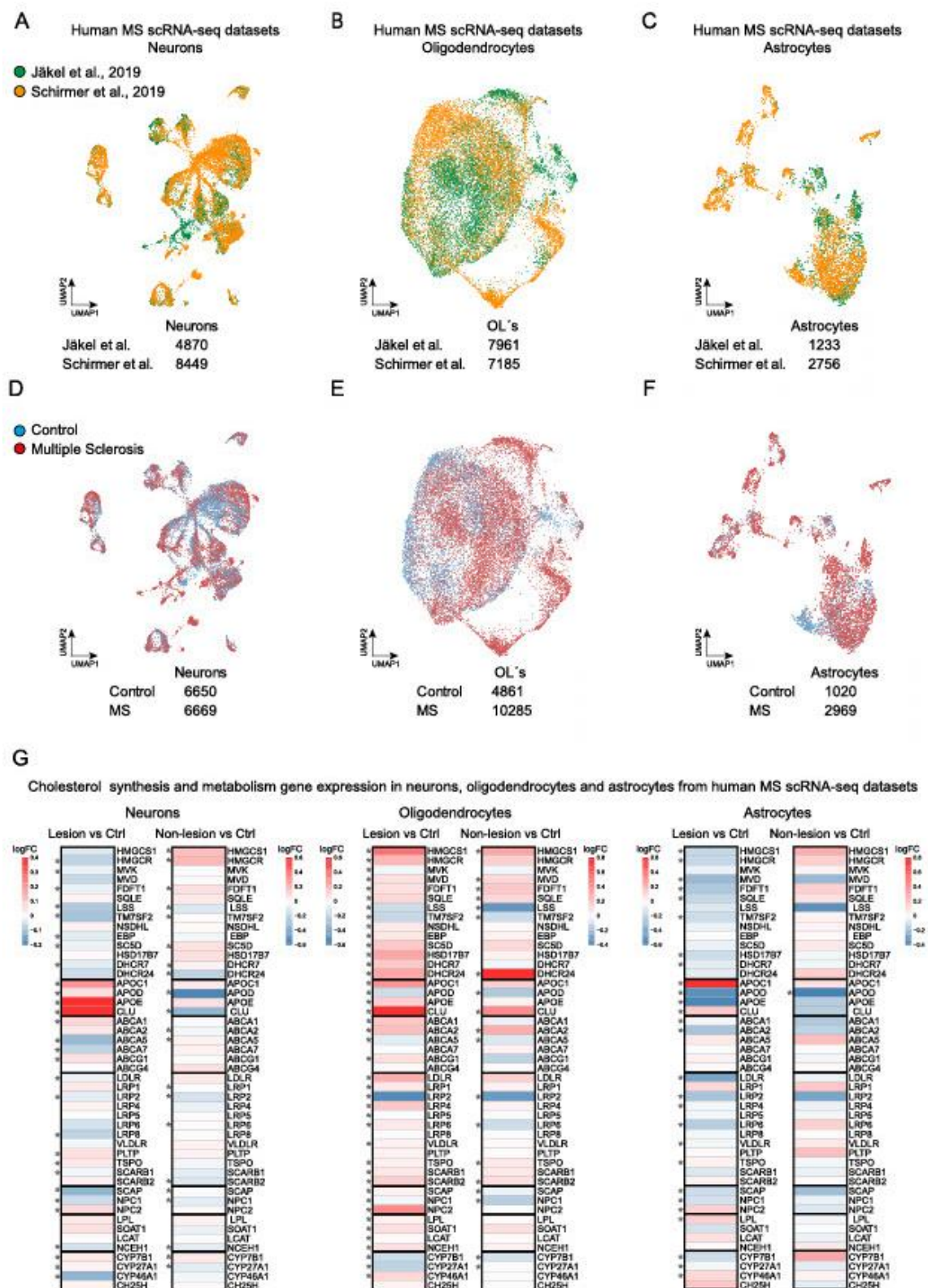
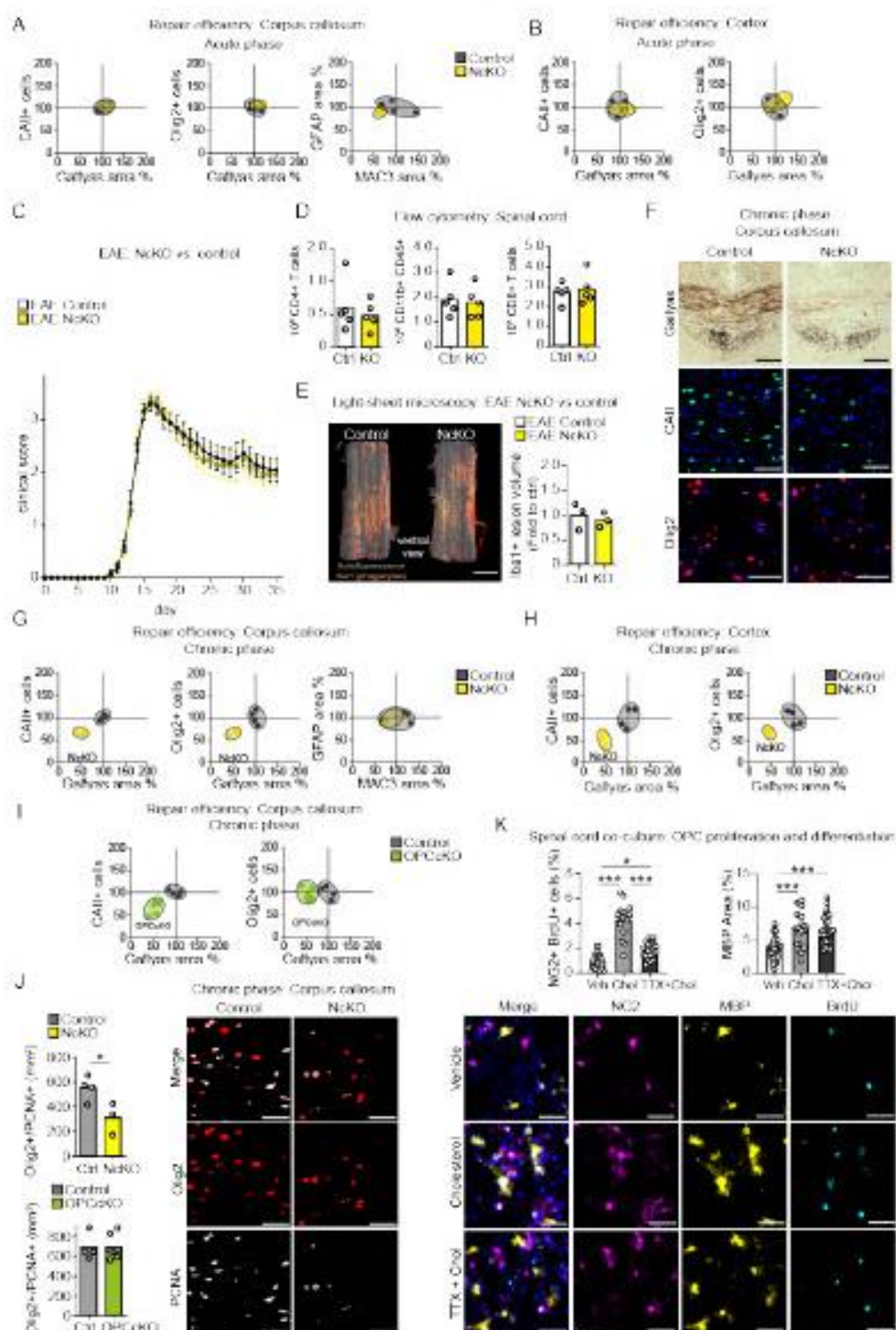


Figure 3. Gene expression related to cholesterol metabolism in neurons, oligodendrocytes and astrocytes from patients with MS
(A) UMAP (Uniform Manifold Approximation and Projection) of neurons, oligodendrocytes and astrocytes from human MS snRNAseq datasets according to dataset (GSE118257, GSE124335). (B) UMAP projection of neurons, oligodendrocytes and astrocytes from human MS snRNAseq datasets according to patient samples identity (GSE118257, GSE124335). (C) Heat map of mean gene expression related to cholesterol metabolism in cellular subsets comparing control and MS (lesion and non-lesion) samples. Data represent log₂fold changes (logFC) and p-value (Wilcoxon Rank Sum test, two sided).

Figure 4

**Figure 4. Neuronal *Fdft1* ablation impairs remyelination following chronic cuprizone**

(A-B) Repair efficiency and gliosis in the corpus callosum (A) and cortex (B) during acute cuprizone (8 weeks) in NcKO (n=4 animals) compared to controls (n=4, set to 100%) based on histochemical stainings for myelin (Gallyas), oligodendrocytes (CAII), oligodendrocyte lineage cells (Olig2), microgliosis (MAC3) and astroglisis (GFAP), shown as 95% confidence ellipses with individual data points. (C) Mean clinical EAE score \pm SEM of control and NcKO mice (n=11). (D) Flow cytometric quantification of inflammatory cells of EAE animals in (C, n=5). (E) Representative light sheet microscopy with quantification of lumbar spinal cord from NcKO and controls 35d after EAE induction, stained for Iba1+ phagocytes (n=3). (F) Representative micrographs of the corpus callosum of control and NcKO animals following chronic cuprizone challenge (12w+2w) illustrating myelination (Gallyas), oligodendrocytes (CAII), and oligodendrocyte lineage cells (Olig2). (G-H) Repair efficiency and gliosis in the corpus callosum (G) and cortex (H) during chronic cuprizone (12w+2w) in NcKO mice compared to controls (n=4, set to 100%). (I) Repair efficiency in the corpus callosum during chronic cuprizone (12w+2w) in OPC cholesterol mutants (OPCcKO, n=7) compared to controls (n=4, set to 100%). (J) Representative micrographs of Olig2/PCNA double labeling in the corpus callosum with quantification of NcKO (n=3) and OPCcKO (n=7) mutants compared to controls (n=4) following chronic remyelination (12w+2w; two-sided Student's t-test). **p<0.01, *p<0.05, scales 50 μ m, 1 mm (E). (K) Mean OPC proliferation (NG2+, BrdU+) and oligodendrocyte differentiation (MBP+) in spinal cord cultures at 17 days *in vitro* (n=18-31 images from 2-3 cultures) in the presence of cholesterol (10 μ g/ml) with or without inhibition of neuronal activity by TTX (1 μ M). Data show the mean number of NG2+ BrdU+ positive cells normalized to DAPI+ cell density and the mean MBP-positive area with individual values (one-way ANOVA with Sidak's post-test; Scale 50 μ m).

Materials and Methods

Animals

All animal studies were performed in compliance with the animal policies of the Max Planck Institute of Experimental Medicine, and were approved by the German Federal State of Lower Saxony. Animals were group-housed (3-5 mice) with 12 hour dark/light cycle and had access to food and water ad libitum. Adult male and female C57BL/6N mice (8-10 weeks of age) or cholesterol synthesis mutants (8-10 weeks of age) were taken for all experiments. Male mice were subjected to cuprizone experiments. Female mice were used for non-induced pathology experiments. Animals of same gender were randomly assigned to experimental groups (3-12 mice). Cholesterol synthesis mutants in this study were generated by crossbreeding cell type-specific Cre-driver lines (see Key Resources table) with mice harboring squalene synthase floxed mice (*Fdft1^{fllox/fllox}*). Conditional mutants were compared with the respective Cre or homozygous floxed controls, i.e. CaMKII-Cre::*Fdft1^{fllox/fllox}* mutants and *Fdft1^{fllox/fllox}* controls, Plp1-CreERT2::*Fdft1^{fllox/fllox}* mutants and *Fdft1^{fllox/fllox}* controls, Cspg4/NG2^{CreERT2/+}::*Fdft1^{fllox/fllox}* and Cspg4/NG2^{CreERT2/+} controls, GLAST^{CreERT2/+}::*Fdft1^{fllox/fllox}* mutants and GLAST^{CreERT2/+} controls, Cspg4/NG2^{CreERT2/+}::Plp1-CreERT2::*Fdft1^{fllox/fllox}* mutants and Plp1-CreERT2::*Fdft1^{fllox/fllox}* and *Fdft1^{fllox/fllox}* controls. *Cnp* null and *Plp1* null mice were crossbred to Thy1-EYFPnuc mice to generate CNP mutants (TYNC +/-, *Cnp* -/-, *Plp1* +/-) and PLP mutants (TYNC +/-, *Cnp* +/-, *Plp1* -/-) that were compared with TYNC +/- mice.

Tamoxifen induced recombination

Transgenic mice received tamoxifen either by oral administration, three times every second day at a concentration of 0.4 mg/g body weight dissolved in corn oil:ethanol (1:9) or by intraperitoneal injections on 5 consecutive days at a concentration of 75 µg/g body weight.

Experimental autoimmune encephalomyelitis (EAE)

MOG-EAE was induced by immunizing subcutaneously with 200 µg myelin oligodendrocyte glycoprotein peptide 35-55 (MOG35-55) in complete Freund's adjuvant (M. tuberculosis at 3.75 mg ml⁻¹) and i.p. injection twice with 500 ng pertussis toxin as described (Berghoff *et al.*, 2017b; Berghoff *et al.*, 2021). Animals were examined daily and scored for clinical signs of the disease. If disease did not start

within 15 days after induction or the clinical score rose above 4, animals were excluded from the analysis. The clinical score was: 0 normal; 0.5 loss of tail tip tone; 1 loss of tail tone; 1.5 ataxia, mild walking deficits (slip off the grid); 2 mild hind limb weakness, severe gait ataxia, twist of the tail causes rotation of the whole body; 2.5 moderate hind limb weakness, cannot grip the grid with hind paw, but able to stay on a upright tilted grid; 3 mild paraparesis, falls down from a upright tiled grid; 3.5 paraparesis of hind limbs (legs strongly affected, but move clearly); 4 paralysis of hind limbs, weakness in forelimbs; 4.5 forelimbs paralyzed; 5 moribund/dead.

Cuprizone

Cuprizone pathology was induced by feeding mice with 0.2% w/w cuprizone (Sigma-Aldrich) in powder chow. Mice received cuprizone for 'acute remyelination' (6 weeks) and 'chronic remyelination' (12 weeks followed by 2 weeks normal chow) paradigms. Chow was replaced three times a week. Age-matched untreated controls were fed powder chow without cuprizone.

Serum Analysis

Blood was collected by cardiac puncture, and serum was prepared after 4h clotting by centrifugation. Cholesterol measurements were done with the Architect II system (Abbott Diagnostics).

Open field

Exploratory activity in a novel environment was tested in an open field chamber (50x50x50 cm) at 20 lux light intensity. Individual female mice at the age of 22 weeks were placed into left bottom corner of the open field chamber. The exploratory behavior of the mouse was recorded for 10 min using an overhead camera system and scored automatically using the Viewer software (Bioobserve, St. Augustin, Germany). The overall traveled distance was analyzed as a parameter of general activity. Time, distance and visits in the center area (25x25 cm) was analyzed to measure behavior related to anxiety. Results were normalized to the mean of corresponding control animals and statistically analyzed using one-way ANOVA with Sidak's post-test.

Blood-brain barrier permeability

Measurements of BBB permeability were done as described (Berghoff *et al.*, 2017a). Tracers were i.v. injected (Evans Blue 50 mg/g body weight, sodium fluorescein 200 mg/g body weight). Animals were flushed with PBS. Brain samples were isolated, weighed, lyophilized at a shelf temperature of -56 °C for 24h under vacuum of 0.2 mBar (Christ LMC-1 BETA 1-16), and extracted with formamide at 57°C for 24h on

a shaker at 300 rpm. Integrated density of tracer fluorescence was determined in triplicates after 1:3 ethanol dilutions to increase sensitivity. Tracer concentration was calculated using a standard curve prepared from tracer spiked brain samples.

Flow cytometry

Single-cell suspensions from spinal cord were obtained via mechanical dissociation on a cell strainer. Immune cells were separated over a two-phase Percoll-density gradient by centrifugation. Staining of CD4⁺ T cells, CD8⁺ T cells and CD45/CD11b⁺ cells (macrophages/microglia) was performed using the following antibodies in a 1:200 dilution: anti-CD3e (clone 145-2C11, BioLegend), anti-CD4 (clone GK 1.5, BD), anti-CD8 (clone 53-6.7, BD), anti-CD11b (clone M1/70, BioLegend), anti-CD45.2 (clone 104, BioLegend). The addition of CaliBRITE APC beads (BD) allowed for cell quantification. Flow cytometry was performed using a CytoFLEX S (Beckman Coulter) operated by CytExpert software (Beckman Coulter, v2.4).

Magnetic cell isolation (MACS).

Glial cells and neurons were isolated according to the adult brain dissociation protocol (Miltenyi biotec) from corpus callosum and/or cortex. Antibody labeling was done according to the Microbead kit protocols (Miltenyi biotec) for oligodendrocytes (O4) or astrocytes (ACSA-2). Neurons were isolated by negative selection. Purity of cell populations was routinely determined by RT-qPCR on extracted and reverse transcribed RNA.

Expression analyses

For expression analyses of tissue samples, mice were killed by cervical dislocation. Samples were quickly cooled and region of interest prepared. RNA was extracted using RNeasy Mini kit (Qiagen). cDNA was synthesized with Superscript III (Invitrogen). Concentration and quality of RNA was evaluated using a NanoDrop spectrophotometer and RNA Nano (Agilent). RNA from MACS-purified cells was extracted using QIAshredder and RNeasy protocols (Qiagen). cDNA was amplified by Single Primer Isothermal Amplification (Ribo-SPIA® technology) using Ovation PicoSL WTA System V2 (NuGEN) following the manufactures protocol. Quantitative PCRs were done in triplicates using the GoTaq qPCR Master Mix (Promega, A6002) and the LightCycler 480 Instrument (Roche Diagnostics). Expression values were normalized to the mean of housekeeping genes. Quantification was done by applying the $\Delta\Delta C_t$ method, normalized to experimental controls (set to 1). All

primers (Table S1) were designed to fulfill optimal criteria e.g. length (18-22 bp), melting temperature (52-58°C), GC content (40-60%), low number of repeats, and amplicon length (<220 bp). All primers were intron-spanning.

Histochemistry

Mice were perfused with 4% formaldehyde (PFA). In case of cuprizone treated animals, brain samples were cut at Bregma 1.58 to account for regional specificity of cuprizone pathology. Tissue was postfixed overnight, embedded in paraffin and cut into 5 μ m sections (HMP 110, MICROM). For Gallyas silver impregnation, deparaffinized sections were incubated with a 2:1 mixture of pyridine and acetic anhydride for 30 min at room temperature (RT) to minimize background and increase myelin. Tissue was washed with ddH₂O, following heating in incubation solution (0.1% [w/v] ammonium nitrate, 0.1% [w/v] silver nitrate, 12% [w/v] sodium hydroxide pH 7.5) for 1 min (100 W) and further incubation for 10 min at RT. After washing with 0.5% [v/v] acetic acid three times for 5 min, sections were incubated in developer solution for 3-10 min. For reconstitution of the developer, 70 ml of solution B (0.2% [w/v] ammonium nitrate, 0.2% [w/v] silver nitrate, 1% [w/v] wolfram-silicic acid) was added to 100 ml of solution A (5% [w/v] sodium carbonate) with constant and gentle shaking and then slowly added to 30ml solution C (0.2% [w/v] ammonium nitrate, 0.2% [w/v] silver nitrate, 1% [w/v] wolfram-silicic acid, 0.26% [w/v] PFA). The reaction was stopped and fixed by washing in 1.0% [v/v] acetic acid and 2% [v/v] sodium thiosulfate. Tissue was dehydrated and mounted using Eukitt. For detection of apoptotic cells, a TUNEL assay was done according to the manufacturer (Promega G7130). Fluoro-Jade C staining (Sigma, AG 325) was done according to the manufacturers' instructions. Immunohistological stainings were done on deparaffinized sections followed by antigen-retrieval in sodium citrate buffer (0.01 M, pH 6.0). For chromogenic stainings, blocking of endogenous peroxidase activity with 3% hydrogen peroxide was performed followed by 20% goat serum block and incubation with primary antibodies. Detection was carried out with the LSAB2 System-HRP (anti-rabbit/mouse LSAB2 Kit Dako Cat#K0679, dilution 1:100) or the VECTASTAIN Elite ABC HRP Kit (Vector Labs, Anti-Rat IgG Vector Cat#BA-9400, dilution 1:100). HRP substrate 3,3'-diaminobenzidine (DAB) was applied by using the DAB Zytomed Kit (Zytomed Systems GmbH). Nuclear labeling was done by hematoxylin stain. For immunofluorescence detection, blocking was performed with serum-free protein block (Dako).

Primary antibodies were diluted in 2% bovine serum albumin (BSA)/PBS and incubated for 48 h followed by incubation with fluorophore-coupled secondary antibodies (Alexa488 donkey anti-mouse Invitrogen Cat #A-21202, dilution 1:1000; Alexa488 donkey anti-rabbit Invitrogen Cat #A-21206, dilution 1:1000; Alexa555 donkey anti-rabbit Invitrogen Cat #A-31572, dilution 1:1000). Stained sections were analyzed on an Axio Imager.Z1 (Zeiss) equipped with an AxioCam MRC3, x0.63 Camera Adaptor and the ZEN 2012 blue edition software using 10x objective (Plan Apochromat x10/0.45 M27) or 20x objective (Plan-Apochromat x20/0.8) and evaluated with Image J software. Quantification of areas (Gallyas, GFAP, MAC3) were done by applying semi-automated ImageJ software macro including thresholding and color deconvolution. Two to four sections per animal were analyzed.

Quantification of sterols

Sterol abundance was quantified by lipid gas chromatography coupled to mass spectrometry (GC-MS) in acutely isolated neurons and tissue samples (4-5 animals grouped for each replicate). Samples were lyophilized at a shelf temperature of -56 °C for 24 h under vacuum of 0.2 millibars (Christ LMC-1 BETA 1-16) and weighed for the calculation of water content and normalization. Metabolites were extracted in a two-phase system of 3:1 methyl-tert-butyl ether:methanol (vol/vol) and water, and pentadecanoic acid was added as an internal standard. The organic phase (10–200 µl) was dried under a stream of nitrogen, dissolved in 10–15 µl pyridine and derivatized with twice the volume of N-methyl-N-(trimethylsilyl) trifluoroacetamide (MSTFA) to transform the sterols and the standard to their trimethylsilyl (TMS) derivatives. Each sample was analyzed twice, with a higher split to quantify cholesterol and with a lower split to measure all other sterols. The samples were analyzed on an Agilent 5977N mass-selective detector connected to an Agilent 7890B gas chromatograph equipped with a capillary HP5-MS column (30 m × 0.25 mm; 0.25-µm coating thickness; J&W Scientific, Agilent). Helium was used as a carrier gas (1 ml/min). The inlet temperature was set to 280 °C, and the temperature gradient applied was 180°C for 1 min, 180–320°C at 5 K min⁻¹ and 320°C for 5 min. Electron energy of 70 eV, an ion source temperature of 230 °C and a transfer line temperature of 280°C were used. Spectra were recorded in the range of 70–600 Da/e (ChemStation Software D.01.02.16). Sterols were identified by the use of external standards.

Light sheet microscopy

PFA immersion fixed spinal cord segments were processed for whole mount immune-labelling and tissue clearing following a modified iDISCO protocol (Berghoff *et al.*, 2021). Briefly, samples were dehydrated in ascending methanol (MeOH)/PBS series followed by overnight bleaching /permeabilization in a mix of 5% H₂O₂/20% DMSO/MeOH at 4°C. Samples were further washed in MeOH and incubated in 20% DMSO/MeOH at RT for 2h. Then, samples were rehydrated using a descending methanol/PBS series and further washed with in PBS/0.2% TritonX-100 for 2h. The samples were then incubated overnight in 0.2% TritonX-100, 20% DMSO, and 0.3 M glycine in PBS at 37°C and blocked using PBS containing 6% goat serum, 10% DMSO and 0.2% Triton-X100 for 2 days at 37°C. Samples were retrieved, washed twice in PBS containing 0.2% Tween20 and 10µg/ml heparin (PTwH) and incubated with primary antibody solution (Iba1 1:500; PTwH/5%DMSO/3% goat serum) for 7 days at 37°C. After several washes, samples were incubated with secondary antibody solution (1:500 in PTwH/3% goat serum) for 4 days at 37°C. Prior to clearing, the samples were washed in PTwH and embedded in 2% Phytigel (Sigma Aldrich #P8169) in water. The embedded tissue was then dehydrated using an ascending series of Methanol/PBS and incubated overnight incubation in a mixture of 33% dichloromethan (DCM) and 66% MeOH at RT. Samples were further delipidated by incubation in 100% DCM for 40min and transferred to pure ethyl cinnamate (Eci; Sigma Aldrich #112372) as clearing reagent. Tissues became transparent after 15min in Eci and were stored at RT until imaging. Light sheet microscopy was performed using a LaVision Ultramicroscope II equipped with 2x objective, corrected dipping cap and zoom body. Spinal cords were mounted onto the sample holder with the dorsal/ventral axis facing down (z imaging axis = dorsoventral axis spinal cord). The holder was placed into the imaging chamber filled with Eci. Images were acquired in 3D multicolour mode with the following specifications: 5µm sheet thickness; 40% sheet width; 2x zoom; 4µm z-step size; one site sheet illumination; 100ms camera exposure time; full field of view. Autofluorescence was recorded using 488nm laser excitation (80% laser power) and a 525/40 emission filter and red fluorescence was recorded using 561nm laser excitation (30% laser power) and 585/40 emission filters. Images were loaded into Vision4D 3.0 (Arivis) and the image set was cropped to 500 - 2000 pixels corresponding to 2.2 mm of spinal cord length. The volume of the spinal cord was determined by performing an automatic intensity thresholding on the

autofluorescence channel. Phagocytes were detected by running a manual intensity thresholding on the 561nm channel and Iba1 cell accumulation with a volume of <1000µm³ was considered lesion positive. Then total lesion volume as well as the lesion volume fraction in respect to the total spinal cord volume were calculated. For 3D rendering, the autofluorescence and Iba1 channel were depicted in green and red pseudocolor, respectively. High-resolution images as well as videos were created using the Arivis 4D viewer.

Laser capture microdissection

Serial cryostat coronal brain sections at the level of Bregma 1 mm to 0.5 mm were prepared (Leica) for single cell isolation. 700 and 800 EYFP⁺ neurons for each individual sample were microdissected (Arcturus Veritas microdissection system with fluorescence package) from the motor and somatosensory cortex and captured in HS Transfer Cap (Molecular Devices). Cells were only collected if no adjacent nuclei were detected in close proximity. Successful cutting and collection steps were subsequently validated in bright-field and fluorescent mode on the quality control slot of the device. Microdissected cells were lysed in 100 µl of RNA lysis buffer (Qiagen, Hilden, Germany) and stored at -80°C until further use. All procedures were done under RNase-free conditions.

Microarray expression analysis

Total RNA of pooled single cells was resuspended with pretested T7-tagged dT21V oligonucleotides. Two-round T7-RNA polymerase-mediated linear amplification was performed according to optimized protocols for low-input RNA amounts (Small Sample Target Labeling Assay Version II, Affymetrix). Biotin-labeled second-round aRNA was generated with an NTP-mix containing Biotin-11-CTP and Biotin-16-UTP (PerkinElmer, Boston, MA) at 2 mM. Biotin-labeled amplified RNA (aRNA) size distribution and quantity was analyzed with the Agilent 2100 Bioanalyser using the RNA 6000 Nano LabChip kit (Agilent Technologies, Boeblingen, Germany). Samples with lower size compressed RNA products were discarded. At least 5 µg of labeled cRNA was fragmented by heating the sample to 95°C for 35 min in a volume of 20 µl containing 40 mM Tris acetate pH 8.1, 100 mM KOAc, and 30 mM MgOAc. Fragmentation was checked by alkaline agarose electrophoresis. Hybridization, washing, staining, and scanning were performed under standard conditions as described by the manufacturer. Mouse430A 2.0 genechips were used that contain over 22,600 probe sets representing transcripts and variants from over 14,000 mouse genes. Microarray raw data

were exported using Gene chip operating software (Affymetrix). Normalization and higher-level analysis were done in R (for packages see Key Resources table). Normalization was carried out using the Robust Multichip Average (RMA) model implemented in the R package Affy at default settings. The normalized microarray data was quality controlled (box-plot analysis, principal component analysis, and Spearman correlation tree) which led to the exclusion of two microarrays. The remaining data were re-normalized, log transformed and filtered based on absolute expression values (100 fold changed signal intensity cutoff). Probe sets with a fold change higher than 1.5 were included in further analysis for single gene analysis. A fold change threshold of 1.3 was applied for further pathway level analysis using gene set enrichment analysis (GSEA; www.broadinstitute.org/gsea/). GSEA was performed with 5214 different gene sets obtained from Molecular Signature Database (MSigDB) at the Broad Institute (MIT).

Human single-nuclei transcriptome sequencing datasets

Human single-nuclei RNA sequencing profiles were obtained from two available datasets, GSE118257 (Jäkel et al. 2019) and GSE124335 (Schirmer et al. 2019), and re-analyzed by R package Seurat v3.2.3. Both datasets were filtered and embedded according to parameters of original publications. Annotations of neurons, oligodendrocytes, and astrocytes were confirmed using marker gene expression of the different cell types (Figure S3). Subsequently, gene counts from neuron, oligodendrocyte and astrocyte subsets from both datasets were merged by applying Canonical Correlation Analysis (CCA) integration method. Uniform Manifold Approximation and Projection (UMAP) was used to visualize cell merging results. For each cell type, pairwise comparisons (MS lesion versus control and MS non-lesion versus control) of expression of genes related to cholesterol synthesis and metabolism were computed using normalized gene counts by Model-based Analysis of Single-cell Transcriptomics (MAST) R package v.1.12.0. Heatmap visualization was computed using R package pheatmap v.1.0.12 (Pretty Heatmaps).

Spinal cord co-cultures

Spinal cord co-cultures were established as described (Bijland et al., 2019) from embryonic day 13 mouse embryos. Cells were plated initially in 12.5 % horse serum and fed the following day and every second or third day thereafter with serum-free differentiation

medium. On day in vitro (DIV) 14 (before myelination commences around DIV 17), cultures were treated with cholesterol (10 µg/ml), cholesterol and tetrodotoxin (TTX) (1µM, Tocris), or 0.1% ethanol (vehicle control) for 3 days. On DIV 17, bromodeoxyuridine (BrdU; 10 µM) was added to the cultures for 2 hours. Cultures were fixed with PFA and washed in PBS. Cells were permeabilized for 10 minutes in 0.5% Triton X in PBS and incubated for 48 hours at 4°C in rabbit anti-NG2 (AB5320, Merck Millipore; 1:500) and rat anti-MBP (MCA409, Biorad, 1:500) in 10 % goat serum, 1 % bovine serum albumin in PBS. Following application of Alexa 596 anti-rabbit IgG and Alexa 488 anti-rat IgG (Invitrogen, 1:1000 for 1 hour), cells were fixed in 50:50 acetic acid and ethanol for 10 minutes and DNA was denatured in 2M HCl for 30 minutes. Then anti-BrdU (MCA2483T, Biorad; 1:500) was added in blocking buffer and incubated overnight. Alexa 647 anti-mouse IgG1 (Invitrogen, 1:1000) was added for ~1 hour at room temperature and coverslips were mounted in Mowiol with DAPI (2.5 µg/ml). 10 predefined locations were selected in the DAPI channel, and images were captured at 10x magnification using a Zeiss Axio Imager M.2 with an AxioCam MRm. Analysis of MBP positive area was performed by automated thresholding (Triangle, Image J). Quantification of the number of NG2 and BrdU double positive cells was done on binarized images and normalized to the DAPI-positive cell density with the particle analyzer plugin (Image J).

Whole cell current clamp and microelectrode arrays

Whole cell patch clamp recording was performed on DIV 21 cultures using an Axopatch 200B amplifier with a Digidata 1440A digital acquisition system and pClamp 10 software (Molecular Devices). Experiments were performed at 37°C in atmospheric air using an extracellular solution containing (in mM): 144 NaCl, 5.3 KCl, 2.5 CaCl₂, 1 MgCl₂, 10 HEPES, 10 mM glucose, pH 7.4. The pipette solution contained (in mM): 130 mM K⁺ gluconate, 4 mM NaCl, 0.5 mM CaCl₂, 10 mM HEPES, 0.5 EGTA pH 7.2. Borosilicate glass pipettes were pulled to a resistance of 3–8 MΩ. Liquid junction potentials were measured as 20 mV and traces were offset by this value. For microelectrode arrays, cultures were plated and maintained on commercial MEAs (60MEA200/30iR-Ti-gr; Multi Channel Systems, Reutlingen, Germany) as described previously (Bijland *et al.*, 2019). A fluorinated ethylene-propylene membrane (ALA MEA-MEM-SHEET) sealed the MEA culture dishes. The recordings were done in differentiation medium. Signals were digitally filtered at

3 Hz high pass filter, 1 kHz low pass filter and amplified up to x20,000. A digital notch filter was used to remove 60 Hz noise during recording. For data acquisition and analysis, spikes and potentials were sorted and counted from 3-minute gap-free recordings using the pCLAMP10 software (Molecular Devices Corporation, California, USA).

QUANTIFICATION AND STATISTICAL ANALYSIS

Number of animals for each experiment is provided in the figure legends. No statistical methods were used to pre-determine sample sizes but our sample sizes are similar to those reported in previous publications (Berghoff *et al.*, 2021). No inclusion or exclusion criteria were used if not otherwise stated. Studies were conducted blinded to investigators and/or formally randomized. Data are expressed as mean ± SEM unless otherwise indicated. For statistical analysis, unpaired two-sided Student's t-test, one-way ANOVA or two-way ANOVA with Sidak's or Tukey's post tests were applied. Normality was tested by using the Kolmogorov-Smirnov test. If the n was below 5, we assumed normal distribution. "Signal-to-Noise ratio" (SNR) statistics were used to rank genes for GSEA of microarray data. Linear model fitting and subsequent testing for differential expression by empirical Bayes variance moderation method implemented in R packaged limma v3.42.2 was applied to the 6-month neuron microarray data. Wilcoxon Rans Sum test was used for analysis of snRNAseq data material. Data analysis was performed using GraphPad Prism Software Version 6 (GraphPad) and the R software. A value of p<0.05 was considered statistically significant. Asterisks depict statistically significant differences (* p<0.05, ** p<0.01, *** p<0.001).

References

- Almeida, R.G., Williamson, J.M., Madden, M.E., Early, J.J., Voas, M.G., Talbot, W.S., Bianco, I.H., and Lyons, D.A. (2020). Synaptic vesicle fusion along axons is driven by myelination and subsequently accelerates sheath growth in an activity-regulated manner. *bioRxiv*, 2020.2008.2028.271593. 10.1101/2020.08.28.271593.
- Bacmeister, C.M., Barr, H.J., McClain, C.R., Thornton, M.A., Nettles, D., Welle, C.G., and Hughes, E.G. (2020). Motor learning promotes remyelination via new and surviving oligodendrocytes. *Nature neuroscience* 23, 819–831. 10.1038/s41593-020-0637-3.
- Berghoff, S.A., Duking, T., Spieth, L., Winchenbach, J., Stumpf, S.K., Gerndt, N., Kusch, K., Ruhwedel, T., Mobius, W., and Saher, G. (2017a). Blood-brain barrier hyperpermeability precedes demyelination in the

- cuprizone model. *Acta Neuropathol Commun* 5, 94. 10.1186/s40478-017-0497-6.
- Berghoff, S.A., Gerndt, N., Winchenbach, J., Stumpf, S.K., Hosang, L., Odoardi, F., Ruhwedel, T., Böhler, C., Barrette, B., Stassart, R., et al. (2017b). Dietary cholesterol promotes repair of demyelinated lesions in the adult brain. *Nature Communications* 8, 14241. 10.1038/ncomms14241.
- Berghoff, S.A., Spieth, L., Sun, T., Hosang, L., Schlaphoff, L., Depp, C., Dusing, T., Winchenbach, J., Neuber, J., Ewers, D., et al. (2021). Microglia facilitate repair of demyelinated lesions via post-squalene sterol synthesis. *Nat Neurosci* 24, 47-60. 10.1038/s41593-020-00757-6.
- Bijland, S., Thomson, G., Euston, M., Michail, K., Thummier, K., Mucklis, S., Crawford, C.L., Barnett, S.C., McLaughlin, M., Anderson, T.J., et al. (2019). An in vitro model for studying CNS white matter: functional properties and experimental approaches. *F1000Res* 8, 117. 10.12688/f1000research.16802.1.
- Borggrewe, M., Grit, C., Vainchtein, I.D., Brouwer, N., Wesseling, E.M., Laman, J.D., Eggen, B.J.L., Kooistra, S.M., and Boddeke, E. (2021). Regionally diverse astrocyte subtypes and their heterogeneous response to EAE. *Glia* 69, 1140-1154. 10.1002/glia.23954.
- Camargo, N., Brouwers, J.F., Loos, M., Gutmann, D.H., Smit, A.B., and Verheijen, M.H. (2012). High-fat diet ameliorates neurological deficits caused by defective astrocyte lipid metabolism. *FASEB journal : official publication of the Federation of American Societies for Experimental Biology* 26, 4302-4315. 10.1096/fj.12-205807.
- Cantoni, C., Bollman, B., Licastro, D., Xie, M., Mikesell, R., Schmidt, R., Yuede, C.M., Galimberti, D., Olivecrona, G., Klein, R.S., et al. (2015). TREM2 regulates microglial cell activation in response to demyelination in vivo. *Acta Neuropathol* 129, 429-447. 10.1007/s00401-015-1388-1.
- Crawford, D.K., Mangiardi, M., Xia, X., Lopez-Valdes, H.E., and Tiwari-Woodruff, S.K. (2009). Functional recovery of callosal axons following demyelination: a critical window. *Neuroscience* 164, 1407-1421. 10.1016/j.neuroscience.2009.09.069.
- Cunha, M.I., Su, M., Cantuti-Castelvetri, L., Muller, S.A., Schifferer, M., Djannatian, M., Alexopoulos, I., van der Meer, F., Winkler, A., van Ham, T.J., et al. (2020). Pro-inflammatory activation following demyelination is required for myelin clearance and oligodendrogenesis. *J Exp Med* 217, 10.1084/jem.20191390.
- Demerens, C., Stankoff, B., Logak, M., Anglade, P., Allinquant, B., Couraud, F., Zalc, B., and Lubetzki, C. (1996). Induction of myelination in the central nervous system by electrical activity. *Proceedings of the National Academy of Sciences of the United States of America* 93, 9887-9892. 10.1073/pnas.93.18.9887.
- Dietschy, J.M. (2009). Central nervous system: cholesterol turnover, brain development and neurodegeneration. *Biological chemistry* 390, 287-293. 10.1515/BC.2009.035.
- Dietschy, J.M., and Turley, S.D. (2004). Thematic review series: brain Lipids. Cholesterol metabolism in the central nervous system during early development and in the mature animal. *Journal of lipid research* 45, 1375-1397. 10.1194/jlr.R400004-JLR200.
- Edgar, J.M., McLaughlin, M., Werner, H.B., McCulloch, M.C., Barrie, J.A., Brown, A., Faichney, A.B., Snaidero, N., Nave, K.A., and Griffiths, I.R. (2009). Early ultrastructural defects of axons and axon-glia junctions in mice lacking expression of Cnp1. *Glia* 57, 1815-1824. 10.1002/glia.20893.
- Edgar, J.M., McLaughlin, M., Yool, D., Zhang, S.C., Fowler, J.H., Montague, P., Barrie, J.A., McCulloch, M.C., Duncan, I.D., Garbern, J., et al. (2004). Oligodendroglial modulation of fast axonal transport in a mouse model of hereditary spastic paraplegia. *J Cell Biol* 166, 121-131. 10.1083/jcb.200312012.
- Franklin, R.J.M., Frisen, J., and Lyons, D.A. (2020). Revisiting remyelination: Towards a consensus on the regeneration of CNS myelin. *Semin Cell Dev Biol* 10.1016/j.semcdb.2020.09.009.
- Fünfschilling, U., Jockusch, W.J., Sivakumar, N., Möbius, W., Corthals, K., Li, S., Quintes, S., Kim, Y., Schaap, I.A., Rhee, J.S., et al. (2012). Critical time window of neuronal cholesterol synthesis during neurite outgrowth. *The Journal of neuroscience : the official journal of the Society for Neuroscience* 32, 7632-7645. 10.1523/JNEUROSCI.1352-11.2012.
- Gibson, E.M., Purger, D., Mount, C.W., Goldstein, A.K., Lin, G.L., Wood, L.S., Inema, I., Miller, S.E., Bieri, G., Zuchero, J.B., et al. (2014). Neuronal activity promotes oligodendrogenesis and adaptive myelination in the mammalian brain. *Science* 344, 1252304. 10.1126/science.1252304.
- Hess, K., Starost, L., Kieran, N.W., Thomas, C., Vincenten, M.C.J., Antel, J., Martino, G., Huitinga, I., Healy, L., and Kuhlmann, T. (2020). Lesion stage-dependent causes for impaired remyelination in MS. *Acta Neuropathol* 140, 359-375. 10.1007/s00401-020-02189-9.
- Ioannou, M.S., Jackson, J., Sheu, S.H., Chang, C.L., Weigel, A.V., Liu, H., Pasolli, H.A., Xu, C.S., Pang, S., Matthies, D., et al. (2019). Neuron-Astrocyte Metabolic Coupling Protects against Activity-Induced Fatty Acid Toxicity. *Cell* 177, 1522-1535 e1514. 10.1016/j.cell.2019.04.001.
- Itoh, N., Itoh, Y., Tassoni, A., Ren, E., Kaito, M., Ohno, A., Ao, Y., Farkhondeh, V., Johnsonbaugh, H., Burda, J., et al. (2018). Cell-specific and region-specific transcriptomics in the multiple sclerosis model: Focus on astrocytes. *Proc Natl Acad Sci U S A* 115, E302-E309. 10.1073/pnas.1716032115.
- Jurevics, H., Largent, C., Hostettler, J., Sammond, D.W., Matsushima, G.K., Kleindienst, A., Toews, A.D., and Morell, P. (2002). Alterations in metabolism and gene expression in brain regions during cuprizone-induced demyelination and remyelination. *J Neurochem* 82, 126-136.
- Kassmann, C.M., Lappe-Siefke, C., Baes, M., Brugger, B., Mildner, A., Werner, H.B., Natt, O., Michaelis, T., Prinz, M., Frahm, J., and Nave, K.A. (2007). Axonal loss and neuroinflammation caused by peroxisome-deficient oligodendrocytes. *Nature genetics* 39, 969-976. 10.1038/ng2070.

- Korinek, M., Gonzalez-Gonzalez, I.M., Smejkalova, T., Hajdukovic, D., Skrenkova, K., Krusek, J., Horak, M., and Vyklicky, L. (2020). Cholesterol modulates presynaptic and postsynaptic properties of excitatory synaptic transmission. *Sci Rep* 10, 12651. 10.1038/s41598-020-69454-5.
- Lappe-Siefke, C., Goebbels, S., Gravel, M., Nicksch, E., Lee, J., Braun, P.E., Griffiths, I.R., and Nave, K.A. (2003). Disruption of *Cnp1* uncouples oligodendroglial functions in axonal support and myelination. *Nat Genet* 33, 366-374. 10.1038/ng1095.
- Linetti, A., Fratangeli, A., Taverna, E., Valnegri, P., Francolini, M., Cappello, V., Matteoli, M., Passafaro, M., and Rosa, P. (2010). Cholesterol reduction impairs exocytosis of synaptic vesicles. *J Cell Sci* 123, 595-605. 10.1242/jcs.060681.
- Marisca, R., Hoche, T., Agirre, E., Hoodless, L.J., Barkey, W., Auer, F., Castelo-Branco, G., and Czopka, T. (2020). Functionally distinct subgroups of oligodendrocyte precursor cells integrate neural activity and execute myelin formation. *Nature neuroscience* 23, 363-374. 10.1038/s41593-019-0581-2.
- Mathews, E.S., and Appel, B. (2016). Cholesterol Biosynthesis Supports Myelin Gene Expression and Axon Ensheathment through Modulation of P13K/Akt/mTOR Signaling. *Journal of Neuroscience* 36, 7628-7639. 10.1523/Jneurosci.0726-16.2016.
- Mauch, D.H., Nagler, K., Schumacher, S., Goritz, C., Muller, E.C., Otto, A., and Priege, F.W. (2001). CNS synaptogenesis promoted by glia-derived cholesterol. *Science* 294, 1354-1357. 10.1126/science.294.5545.1354.
- Miron, V.E., Boyd, A., Zhao, J.W., Yuen, T.J., Ruckh, J.M., Shadrach, J.L., van Wijngaarden, P., Wagers, A.J., Williams, A., Franklin, R.J.M., and Ffrench-Constant, C. (2013). M2 microglia and macrophages drive oligodendrocyte differentiation during CNS myelination. *Nature neuroscience* 16, 1211-1218. 10.1038/nn.3469.
- Miron, V.E., Rajasekharan, S., Jarjour, A.A., Zamvil, S.S., Kennedy, T.E., and Antel, J.P. (2007). Simvastatin regulates oligodendroglial process dynamics and survival. *Glia* 55, 130-143. 10.1002/glia.20441.
- Miron, V.E., Zehntner, S.P., Kuhlmann, T., Ludwin, S.K., Owens, T., Kennedy, T.E., Bedell, B.J., and Antel, J.P. (2009). Statin therapy inhibits myelination in the central nervous system. *Am J Pathol* 174, 1880-1890. 10.2353/ajpath.2009.080947.
- Mitew, S., Gobius, I., Fenlon, L.R., McDougall, S.J., Hawkes, D., Xing, Y.L., Bujalka, H., Gundlach, A.L., Richards, L.J., Kilpatrick, T.J., et al. (2018). Pharmacogenetic stimulation of neuronal activity increases myelination in an axon-specific manner. *Nature communications* 9, 306. 10.1038/s41467-017-02719-2.
- Nikic, I., Merkler, D., Sorbara, C., Brinkoetter, M., Kreutzfeldt, M., Bareyre, F.M., Bruck, W., Bishop, D., Misgeld, T., and Kerschensteiner, M. (2011). A reversible form of axon damage in experimental autoimmune encephalomyelitis and multiple sclerosis. *Nature medicine* 17, 495-499. 10.1038/nm.2324.
- Ortiz, F.C., Habermacher, C., Graciarena, M., Houry, P.Y., Nishiyama, A., Nait Oumesmar, B., and Angulo, M.C. (2019). Neuronal activity in vivo enhances functional myelin repair. *JCI Insight* 5, 10.1172/jci.insight.123434.
- Pfeiffer, F., Frommer-Kaestle, G., and Fallier-Becker, P. (2019). Structural adaption of axons during de- and remyelination in the Cuprizone mouse model. *Brain pathology* 29, 675-692. 10.1111/bpa.12748.
- Plemel, J.R., Liu, W.Q., and Yong, V.W. (2017). Remyelination therapies: a new direction and challenge in multiple sclerosis. *Nature reviews. Drug discovery* 16, 617-634. 10.1038/nrd.2017.115.
- Reich, D.S., Lucchinetti, C.F., and Calabresi, P.A. (2018). Multiple Sclerosis. *The New England journal of medicine* 378, 169-180. 10.1056/NEJMra1401483.
- Saab, A.S., and Nave, K.A. (2017). Myelin dynamics: protecting and shaping neuronal functions. *Current opinion in neurobiology* 47, 104-112. 10.1016/j.conb.2017.09.013.
- Saher, G., Brugger, B., Lappe-Siefke, C., Mobius, W., Tozawa, R., Wehr, M.C., Wieland, F., Ishibashi, S., and Nave, K.A. (2005). High cholesterol level is essential for myelin membrane growth. *Nat Neurosci* 8, 468-475. 10.1038/nn1426.
- Saher, G., Rudolph, F., Corthals, K., Ruhwedel, T., Schmidt, K.F., Lowel, S., Dibaj, P., Barrette, B., Mobius, W., and Nave, K.A. (2012). Therapy of Pelizaeus-Merzbacher disease in mice by feeding a cholesterol-enriched diet. *Nat Med* 18, 1130-1135. 10.1038/nm.2833.
- Scafari, A. (2019). MS progression is predominantly driven by age-related mechanisms - YES. *Multiple sclerosis* 25, 902-904. 10.1177/1352458518820633.
- Stassart, R.M., Mobius, W., Nave, K.A., and Edgar, J.M. (2018). The Axon-Myelin Unit in Development and Degenerative Disease. *Frontiers in neuroscience* 12, 467. 10.3389/fnins.2018.00467.
- Thelen, K.M., Falkai, P., Bayer, T.A., and Lutjohann, D. (2006). Cholesterol synthesis rate in human hippocampus declines with aging. *Neurosci Lett* 403, 15-19. 10.1016/j.neulet.2006.04.034.
- Thiele, C., Hannah, M.J., Fahrenholz, F., and Huttner, W.B. (2000). Cholesterol binds to synaptophysin and is required for biogenesis of synaptic vesicles. *Nat Cell Biol* 2, 42-49. 10.1038/71366.
- Trevisiol, A., Kusch, K., Steyer, A.M., Gregor, I., Nardis, C., Winkler, U., Kohler, S., Restrepo, A., Mobius, W., Werner, H.B., et al. (2020). Structural myelin defects are associated with low axonal ATP levels but rapid recovery from energy deprivation in a mouse model of spastic paraplegia. *PLoS biology* 18, e3000943. 10.1371/journal.pbio.3000943.
- Vance, J.E., Campenot, R.B., and Vance, D.E. (2000). The synthesis and transport of lipids for axonal growth and nerve regeneration. *Biochimica et biophysica acta* 1486, 84-96. 10.1016/s1388-1981(00)00050-0.
- Voskuhl, R.R., Itoh, N., Tassoni, A., Matsukawa, M.A., Ren, E., Tse, V., Jang, E., Suen, T.T., and Itoh, Y. (2019). Gene expression in oligodendrocytes during remyelination reveals cholesterol homeostasis as a therapeutic target in multiple sclerosis. *Proc Natl Acad*

Sci U S A 116, 10130-10139.
10.1073/pnas.1821306116.

Wehr, M.C., Laage, R., Bolz, U., Fischer, T.M., Grunewald, S., Scheek, S., Bach, A., Nave, K.A., and Rossner, M.J. (2006). Monitoring regulated protein-protein interactions using split TEV. *Nature methods* 3, 985-993. 10.1038/nmeth967.

Xu, Q., Bernardo, A., Walker, D., Kanegawa, T., Mahley, R.W., and Huang, Y. (2006). Profile and regulation of apolipoprotein E (ApoE) expression in the CNS in mice with targeting of green fluorescent protein gene to the ApoE locus. *The Journal of neuroscience : the official journal of the Society for Neuroscience* 26, 4985-4994. 10.1523/JNEUROSCI.5476-05.2006.

Zhao, C., Deng, Y., Liu, L., Yu, K., Zhang, L., Wang, H., He, X., Wang, J., Lu, C., Wu, L.N., et al. (2016). Dual regulatory switch through interactions of Tcf712/Tcf4 with stage-specific partners propels oligodendroglial maturation. *Nat Commun* 7, 10883. 10.1038/ncomms10883.

Acknowledgments

We cordially thank Annette Fahrenholz and Tanja Freerck for technical support. We thank Charles Stiles, John Alberta, Said Ghandour for generous gifts of antibodies. This work was funded by the Deutsche Forschungsgemeinschaft (SA 2014/2-1 to GS), the UK MS Society (Grant 127 to JE); Medical Research Scotland (PhD studentship 791-2014 to EB).

Author Contributions

SAB and GS planned and designed the study. SAB and LS were involved in all experiments. TS, YZ, and SBo performed reanalysis of human snRNAseq datasets. LH and FO did flow cytometry. TI and PS performed lipid mass spectrometry. MHV and AMS performed histology. CD and AOS did light sheet microscopy. DKB was involved in behavior experiments. SW, KAN, and MR analyzed genetic myelin mutants. JME conducted myelinating cell culture experiments. KM and EB conducted electrophysiology experiments on myelinating cell cultures. SAB and GS wrote and edited the manuscript. All authors approved the manuscript.

Declaration of Interests

The authors declare no competing financial interests.

LEAD CONTACT AND MATERIAL AVAILABILITY

Further information and requests for resources and reagents should be directed to and will be fulfilled by the Lead Contact, Gesine Saher (Saher@em.mpg.de). This study did not generate new unique reagents.

Appendix B. CV and list of publications



Ting Sun

CONTACT

✉ tsun@em.mpg.de
 in www.linkedin.com/in/ting-sun-66b785154/
 R^G www.researchgate.net/profile/Ting-Sun-23

LANGUAGES

English ● ● ● ● ● ● ●
 Mandarin ● ● ● ● ● ● ●
 German ● ● ● ● ● ● ●

RESEARCH INTERESTS

Myelin Genetics
Neurodegeneration
Bioinformatics
Single-cell sequencing
Precision medicine

ACTIVITIES

06/2019--10/2020 MPI-EM
 Internal PhD representative

11/2019--02/2020 MPG
 PhD-Net survey working group

SOFT SKILLS

Communication
Collaboration
Organization
Presentation
Supervision

Curriculum Vitae

EDUCATION

- 07/2017—present **PhD candidate**
 Max-Planck-Institute of Experimental Medicine
 Neurogenetics Department, K-A Nave group
Thesis title: Cell type specific transcriptomic characterization of myelin abnormalities
 Göttingen, Germany
- 09/2008—06/2015 **Bachelor & Master of Medicine**
 Beijing University of Chinese Medicine
 Faculty of Clinical Medicine
 Beijing, P. R. China
- 09/2002—06/2008 **High School Diploma**
 Beijing No.8 High School, Science major
 Beijing, P. R. China

PROFESSIONAL EXPERIENCES

- 01/2018—12/2020 **Collaboration student on PhD project**
 Center for Molecular Neurobiology Hamburg
 Institute of Medical System Biology, AG Bonn
 Hamburg, Germany
- 12/2017—11/2018 **Data annotation curator**
 Genevention GmbH
 Göttingen, Germany
- 01/2017—08/2017 **High resolution sequencing experiment & bioinformatics trainee**
 German Center for Neurodegenerative Diseases
 Computational System Biology group, AG Bonn
 Göttingen, Germany
- 09/2015—12/2016 **Research student**
 Universitätsmedizin Göttingen
 Prion Lab, AG Zerr
 Göttingen, Germany

CONFERENCES

- 17-19th March, 2021. **Keystone eSymposia Single Cell Biology**
 Poster presentation: *Single-cell resolution characterization of malfunctioning oligodendrocytes*
- 6th December, 2019. **5th Biennial Symposium Encephalon**
 Poster presentation: *Single-cell transcriptome profiling of mouse brain immune cells across brain region, gender and lifespan*

List of publications

Sun, T.*, Depp, C.*, Berghoff, S. A., Spieth, L., Sasmita, A. O., ... & Nave, K. (2021). Characterization of dysfunctional oligodendrocytes at single-cell resolution. *Manuscript prepared*.

Depp, C.*, **Sun, T.***, Sasmita, A. O., Spieth, L., Berghoff, S. A., Steixner-Kumar, A. A., ... & Nave, K. (2021). Ageing-associated myelin dysfunction drives amyloid deposition in mouse models of Alzheimer's disease. *bioRxiv*.

Berghoff, S.*, Spieth, L.*, **Sun, T.***, Hosang, L., Depp, C., Sasmita, A., ... & Saher, G. (2021). Neuronal cholesterol synthesis is essential for repair of chronically demyelinated lesions in mice. *bioRxiv*.

Gargareta, V.*, Reuschenbach, J.*, Siems, S.B.*, **Sun, T.*#**, Piepkorn, L., ... & Werner, H.B., (2021). Conservation and divergence of myelin proteome and oligodendrocyte transcriptome profiles between humans and mice. *Manuscript prepared*.

Berghoff, S. A., Spieth, L., **Sun, T.**, Hosang, L., Schlaphoff, L., Depp, C., ... Nave, K. & Saher, G. (2021). Microglia facilitate repair of demyelinated lesions via post-squalene sterol synthesis. *Nature neuroscience*, 24(1), 47-60.

Butt, U. J., Steixner-Kumar, A. A., Depp, C., **Sun, T.**, Hassouna, I., Wüstefeld, L., ... Nave, K. & Ehrenreich, H. (2021). Hippocampal neurons respond to brain activity with functional hypoxia. *Molecular Psychiatry*, 1-18.

Schepanski, S., Chini, M., Sternemann, V. Urbschat, C., Thiele, K., **Sun, T.**, Zhao, Y., ... Opatz, H. L. & Arck, P. C. (2021). Maternal immune cells shape the development of neuronal networks and cognitive abilities in offspring. *Manuscript under review*.

Jahn, O., Siems, S.B., Kusch, K., Hesse, D., Jung, R.B., Liepold, T., Uecker, M., **Sun, T.** & Werner, H.B., (2020). The CNS myelin proteome: deep profile and persistence after post-mortem delay. *Frontiers in Cellular Neuroscience*, 14, p.239.

Rahman, R.U., Liebhoff, A.M., Bansal, V., Fiosins, M., Rajput, A., Sattar, A., Magruder, D.S., Madan, S., **Sun, T.**, Gautam, A., ... & Bonn, S., (2020). SEAwab: the small RNA Expression Atlas web application. *Nucleic acids research*, 48(D1), pp.D204-D219.

Llorens, F., Kruse, N., Karch, A., Schmitz, M., Zafar, S., Gotzmann, N., **Sun, T.**, ... & Zerr, I. (2018). Validation of α -synuclein as a CSF biomarker for sporadic Creutzfeldt-Jakob disease. *Molecular neurobiology*, 55(3), 2249-2257.

Hatje, K., Rahman, R.U., Vidal, R.O., Simm, D., Hammesfahr, B., Bansal, V., Rajput, A., Mickael, M.E., **Sun, T.**, Bonn, S. & Kollmar, M., (2017). The landscape of human mutually exclusive splicing. *Molecular systems biology*, 13(12), p.959.

*shared first authorship

shared correspondence